Fluid-structure interactions on multistable pendular systems

Ariane Gayout

Numéro national de thèse : 2022LYSEN020

THESE DE DOCTORAT DE L'UNIVERSITE DE LYON

opérée par

l'Ecole Normale Supérieure de Lyon

Ecole Doctorale N° 52

Physique et Astrophysique de Lyon (PHAST)

Discipline : Physique

Soutenue publiquement le 29/06/2022, par :

Ariane GAYOUT

FLUID-STRUCTURE INTERACTIONS ON MULTISTABLE PENDULAR SYSTEMS

INTERACTIONS FLUIDE-STRUCTURE DE SYSTEMES PENDULAIRES MULTISTABLES

Devant le jury composé de :

BOREE, Jacques	Professeur des universités	ENSMA – Poitiers	Rapporteur
CADOT, Olivier	Professeur	Univ. of Liverpool	Rapporteur
DUBRULLE, Bérengère	Directrice de recherche	CNRS – CEA Saclay	Examinatrice
RAMANANARIVO, Sophie	Maîtresse de conférences	Ecole Polytechnique	Examinatrice
TUCKERMAN, Laurette	Directrice de recherche	CNRS – Sorbonne Univ.	Présidente
PLIHON, Nicolas	Directeur de recherche	CNRS – ENS de Lyon	Directeur de thèse
BOURGOIN, Mickaël	Directeur de recherche	CNRS – ENS de Lyon	Co-directeur de thèse

.

To Pépé Loup,
the only other Dr. in the family

ABSTRACT

When in a flow, an object deviates it and from this deviation are generated vortices and flow reaction forces, such as drag and lift. If the object is free to move, its movement can couple with the surrounding flow, falling into the domain of fluid-structure interactions. In this PhD thesis, the coupling between a pendular system and an air flow is studied both experimentally and theoretically. Placed in a wind tunnel, a disk pendulum presents bistability for a range of flow velocity, while a rectangular one does not. By varying the aspect ratio of such a rectangle and visualizing the wake behind a fixed disk, we propose an explanation on whether or not the bistability emerges, linking it to the phenomenon of stall. The influence of ambient turbulence on this phenomenon is then investigated together with the link between angular fluctuations and flow variations, both upstream and downstream. Going back to the bistability itself, spontaneous transitions between stable states are observed and a model inspired from the transition to turbulence suggests certain mechanisms in the wake that trigger such transitions, in particular rare aerodynamic events. Modifying the geometrical parameters of the pendulum enables the adjustment of the range of velocity for which bistability occurs, and with it, we could observe jumps between both stable states at the same flow rate. Finally, when the pendulum is balanced, its movement is only driven by the flow and while quasi-static model is not sufficient to describe the real dynamics of the pendulum, we introduce two ways of accounting for the dynamical retroaction of the flow in the equation of motion, one empirical and the other based on vortex-induced vibration theory.

RÉSUMÉ

Lorsqu'un objet est placé dans un écoulement, celui-ci est dévié et de cette déviation résultent l'apparition de tourbillons et la génération de forces de réaction du fluide, telles que la traînée et la portance. Si maintenant, l'objet en question est libre de se mouvoir, un couplage s'installe entre les mouvements de l'objet et de l'écoulement environnant, du domaine des interactions fluide-structure.
Dans cette thèse, le couplage entre un système pendulaire et un écoulement d'air est étudié expérimentalement et théoriquement. Placé dans une soufflerie, un pendule circulaire présente notamment une bistabilité sur une gamme de vitesse de vent, tandis qu'un rectangle n'en présente aucune. En variant le rapport d'aspect du pendule rectangulaire et en visualisant le sillage d'un disque fixe, nous proposons une origine à l'existence ou non de la bistabilité, en lien avec le phénomène de décrochage. L'influence de la turbulence incidente sur ce phénomène est ensuite approfondie ainsi que le lien entre les fluctuations d'angle du pendule et celles de l'écoulement, amont comme aval. En revenant à la bistabilité elle-même, des transitions spontanées d'un état stable à l'autre sont observées, dont le cadre de la transition vers la turbulence permet une modélisation et suggère certains mécanismes à l'œuvre dans le sillage, notamment des évènements aérodynamiques rares. La modification des paramètres géométriques du pendule permet de varier la plage de vitesses pour laquelle la bistabilité existe, et ainsi observer des sauts entre les deux positions, à même vitesse d'écoulement. Enfin, lorsque le pendule est équilibré, son mouvement est dicté par l'écoulement uniquement et alors qu'un modèle quasi-statique est insuffisant à la description de la dynamique réelle du pendule, nous établissons deux manières de prendre en compte la rétroaction dynamique de l'écoulement, l'une empirique et l'autre basée sur les vibrations induites par vortex.

ACKNOWLEDGMENTS

Among the various chapters and parts of a thesis, one could say that the hardest part to write is often also the one most read, which, in case of a PhD thesis, almost always happens to be the "Acknowledgments".

And as this part is also the one that friends from all horizons read, sometimes even the only part they read when not familiar nor comfortable with the physics of the remaining parts, I will try my best to write it in what I hope to be the best way to express my thanks, even if it means sometimes strange choice of language.Thus while most of the following will be written in French, some parts will also be in English.

Avant toute chose et avant d'oublier au milieu des différents remerciements, je tiens à remercier les membres de mon jury d'avoir accepté de relire mon manuscrit et de m'écouter parler pendant 45 minutes, car ce sont littéralement eux qui m'ont faite docteure aujourd'hui. Je remercie donc plus particulièrement Jacques Borée et Olivier Cadot pour avoir été les rapporteurs de ma thèse, Laurette Tuckerman pour avoir été la présidente de mon jury et la relectrice attentive de l'anglais de mon manuscrit, ainsi que Bérengère Dubrulle et Sophie Ramananarivo pour leur présence en tant qu'examinatrices lors de ma soutenance.

Pour la suite, je sais qu'il est souvent convenu de remercier sa famille en dernier, peut-être pour s'assurer qu'ils liront jusqu'au bout les différentes pages de remerciements. Toutefois, il est pour moi plus naturel de les remercier dès maintenant, parce qu'en me supportant (dans tous les sens du terme) depuis maintenant 25 ans, ils font partie des premiers contributeurs de l'achèvement du cycle éducatif, que représente la thèse. Que ce soit Papa ou Alexandre pour leur aide sur les différents déménagements (et on sait qu'il en reste à faire) ou Maman pour tout, et notamment pour la bonne cuisine (au pot et tout le temps en fait), si je suis docteure aujourd'hui, c'est en partie grâce à vous, même si ces 3 (25?) années n'auront pas toujours été simples avec surtout les 2 mois de cohabitation confinée.

Bien sûr, qui dit famille, dit aussi amis. Parmi eux, on retrouve ceux de (très) longue date tels que Math ou Emilie, ceux de prépa (parce que quiconque a fait prépa sait qu'on peut s'y faire des amis pour la vie) comme Arthur, Guillaume, Ludo, Clémence, Noranne et toutes les Magnifaïques, et ceux plus récents de l'ENS et de l'X, notamment Thomas, Maxen, Léo, Louison et Antoine, et encore ceux du labo, parmi lesquels Samuel, Laura, Jérôme, Hélène, Jérémy, Charles, Marcelo, Sebastian, Marc, Florencia, Simon,... pour ne citer qu'eux (Oui, il manque plein d'entre vous mais c'est pas parce que je ne vous aime pas, c'est juste parce que si j'essaie d'en faire une liste exhaustive, il en manquera toujours quelques uns).

Certains ont fait le déplacement jusqu'à Lyon, parfois de très loin, d'autres ont assister à mon one-woman show du 29 juin et tous je les en remercie mais je les remercie aussi pour tous les bons moments passés depuis qu'on se connaît, de leur soutien plus ou

moins important dans l'aventure que sont la thèse et les études plus généralement. J'espère qu'on pourra toujours arriver à se retrouver au gré des opportunités, même si on est éparpillé aux 4 coins de la France voire du monde (façon puzzle).

Parmi les amis du labo, certains ont eu plus particulièrement une tâche conséquente ces 4 dernières années (eh oui, j'aurais hanté les couloirs du laboratoire pendant exactement 4 ans 3 mois et 6 jours par le "gling gling" des clés qui manquent déjà à certains au point d'essayer de le reproduire, et le "tac tac" des bottes en hiver). Cette tâche, c'est d'avoir été mes co-bureaux et eux seuls savent à quel point ça peut être sportif... En particulier, je tiens à remercier Jason pour sa patience avec Lucas et moi alors qu'il finissait sa thèse, Lucas pour son bout-en-trainisme et ses injures envers son pc qui nous ont fait passer de bons fous-rires, Pono pour les diverses discussions sur les animaux et les plantes, Mamie pour tout (et surtout les Kinder) et Marceau pour la cohabitation très sympathique en milieu de thèse malgré le covid et les efforts pour les poils de chats.

Le M2 007 aura été un havre de paix discussions toujours plus folkoriques à l'instar des pauses café sur la passerelle et tout le monde sait qu'une bonne ambiance de bureau, ça change la vie au labo.

Parce que la vie au labo, ce n'est pas que des amis de son âge, c'est tout un monde qui nous facilite la vie (du moins en grande partie). Je souhaite donc remercier toutes les personnes que j'ai pu cotôyer au laboratoire durant ces 4 années, notamment Thierry et Jean-Christophe en tant que directeurs, le service Ingénierie mécanique avec Marc et Denis pour leurs aides sur les dispositifs expérimentaux, Pascal pour les discussions voyage du premier thé du matin, Angel pour le foot (même si je n'aurais pas été très assidue entre le covid et la 3e année...) et bien sûr le secrétariat sans qui rien ne tournerait rond dans le labo. Une dédicace spéciale quand même à Erika et Nadine pour leur appétit pour les gâteaux, crêpes et autres délicates sucreries. Et pour Fatiha, un grand merci pour tout, les problèmes de commandes, de missions, de voiture, etc... toujours finalement résolus et surtout avec le sourire!

Il y a quelque chose au labo dont on ne remarque l'importance qu'après avoir quitté le labo mais qui pourtant fait la richesse de la vie du labo, son ambiance et aide particulièrement au travail aussi paradoxalement que cela puisse paraître: la Pause! (thé, café ou chocolat selon les envies de chacun)

Ainsi au laboratoire, il y a certaines personnes qu'on croise systématiquement à la pause, et certains qu'on ne croise même qu'en pause, et même si les pauses prennent alors parfois des allures de journée complète, à la fin on aura été plus efficace sur la fin de la journée en voulant rattraper le temps perdu une fois la pause finie. Pour être toujours là pour une pause, je me dois de remercier Eric, Sylvain, Stéphane et l'Affine équipe (précédemment nommée individuellement) sans qui les pauses au labo ne sont pas vraiment des pauses; ce que le covid aura permis de vérifier.

Quatre ans dans un laboratoire, c'est court pour un chercheur mais long pour un étudiant, car notamment, on voit défiler des gens et on fait plein de rencontres, parmi lesquelles les stagiaires (dont certains arrivent même à être suffisamment efficaces pour qu'on mette leurs travaux en valeur dans le 1er chapitre), les postdocs, les visiteurs... Pour citer l'une des tirades les plus marquantes du cinéma français des années 2000, "si

je devais résumer ma vie aujourd'hui, je dirais que c'est d'abord des rencontres. Et c'est assez curieux de se dire que les hasards, les rencontres forgent une destinée..."

Pour moi, les rencontres ont commencé très tôt et si j'ai fini ma thèse aujourd'hui, c'est en partie grâce à elles. Je pense notamment à ma nounou, Tata Gilda, mes professeurs, M. Julien, M. Seguin, Mme. Bouchiat au lycée, M. Tosel et Mme. Dunlop en prépa, et de manière plus diffuse peut-être, l'équipe du Palais de la Découverte qui m'a introduite à la science durant l'enfance et dont j'ai eu la chance de faire partie pendant une petite année en 1ère année de thèse. Il y a aussi les rencontres autour, loin de l'école et loin du travail, comme le Bushindo, mon club de Kendo qui s'est connecté en masse à ma soutenance malgré la difficulté scientifique que représente une soutenance de thèse en physique même quand on essaie de vulgariser au maximum.

Enfin parmi toutes les rencontres que j'ai pu faire, il y en a une (ou deux suivant comment on la regarde) qui est responsable de cette thèse et en arrivant jusqu'ici, ils ont dû penser que j'allais les oublier mais non non. S'il y a bien deux personnes à qui je dois d'être moi aujourd'hui, ce sont bien mes directeurs de thèse Mica et Nico. I'll switch to English for convenience on my end because I doubt to be able to express myself with the right words in French.

When you called me to discuss science at the end of my M1 internship defense, I never expected I would sign up for 4 years with you a few months later. Yet, you had only one thing to say for me to say yes and you did say it: "on a retapé la soufflerie". From that point on, you gave me the most exciting subject I could ever dream of. Pendulums are among my favorite physical systems and having the opportunity to make it my once-in-a-lifetime research (in the sense that now I am no longer a student) has been one of the greatest joy of this PhD.

I have most likely not been the easiest PhD student, but you were always patient and caring, despite all your workload, which you however have the propensity to increase voluntarily. Covid time was very difficult, as everything got delayed and communication got complicated, through phone calls and Zoom... However, I knew that you would still try your best to come to the lab and discuss in person if something went wrong, which I know was not necessarily the case for everybody. Especially, I am really grateful that you would (almost) always leave the door open for me to come in and discuss science and results, because, even if sometimes you would feel as if you didn't do much, just having the opportunity to express my thoughts and try to make it understandable was enough for the thought to get shaped into an idea. You even went as far as accepting my PHOeBUS project, which obviously was not something you were ready for at first (me neither in fact).

Over the last years, you left me with much freedom while also making sure (or at least trying to) I wouldn't spread out to far in my thoughts and ideas so that my PhD would look like this final product. By asking me to rephrase many times when I would explain something, you helped me dissect my thoughts and refine them for a better global understanding of the physics behind, just like the first article and the second and... probably all the remaining ones. Throughout the years, you even managed to achieve an Ariane - rest-of-the-world translator, that possibly some people are going to be envious of in the coming years, as it is even better than DeepL or Google Translate. For all this (and more but I would probably never finish if I try to put it all down), I am truly grateful and hope that one day I can be the same kind of supervisor as you both

(with a little less extra work if possible).

I think that over these few pages, I have more or less expressed my thanks to most people, though probably a bit erratically. I still need to thank my collaborators on PHOeBUS, who accepted to join on this adventure of tracking the mysteries of butterfly flight in microgravity. I will not linger too much on this here as the adventure is only at its beginning. I just would like to thank Pr. Hao Liu for my stay in his lab at Chiba University this summer, which has been fruitful in many ways for project PHOeBUS.

Finally, I would like to thank David Lentink for the trust he has put in me for the coming years, and I am very pleased to join his lab to continue aerodynamic research and finally on birds. I am also thankful for his PhD manuscript that helped me a lot in the organization of mine, when I was struggling with how to arrange and articulate the various chapters together.

With all this said (or rather) written, I wish you a pleasant lecture of my work and hope you will enjoy it as much as I enjoyed doing it (not writing it though).

CONTENTS

Introduction

0 Introduction 3

0.1 A wind-swept pendulum 10
0.1.1 Definitions and aerodynamic considerations 11
0.1.2 Winding up pendulum-in-flow history 18
0.2 Thesis outline 21
0.3 How to use this thesis 22
0.4 Experimental setup and methodology 24
0.4.1 Experimental setup 24
0.4.2 PIV Methodology 33
0.4.3 Synthesis of the experimental setup 35
References 35

I Waking up

1 Describing the wake behind an inclined disk 43

1.1 Introduction 43
1.2 Mean flow field in the wake 45
1.3 Global vorticity considerations 47
1.3.1 Angular dependence of the wake vorticity structure 49
1.3.2 Connecting to the C_N coefficient? 50
1.3.3 Other vorticity properties of the wake 51
1.4 Perspectives 55
References 56

2 Shaping the bistability 59

2.1 Introduction 59
2.2 Experimental details 60
2.3 Results 62
2.3.1 Bistability existence and C_N coefficient 62
2.3.2 Complications around AR$\simeq$ 1 64
2.4 Discussion 67
2.4.1 Global evolution of C_N with aspect ratio 67
2.4.2 Evolution of the C_N stall angle with the aspect ratio 68
2.4.3 Wake interpretation 69
2.4.4 Polar curves 71
2.5 Perspectives 72
References 73

3 Solving the hole problem of the fly-swatter 75
3.1 Introduction ... 75
3.1.1 Natural porosity in Aerodynamics ... 75
3.1.2 An everyday object as a pendulum ... 77
3.2 Experimental setup ... 78
3.3 Results ... 81
3.3.1 Filling the holes concentrically ... 81
3.3.2 Curvature effects on C_N coefficient ... 82
3.3.3 Where stall starts ... 84
3.4 Discussion ... 86
3.4.1 Wake and stall entanglement ... 86
3.4.2 C_N perturbation at $\theta = 15°$ ... 87
3.5 Perspectives ... 88
References ... 89

II An eventful day

4 Taxonomy of the pendulum dynamics in the bistable region 93
4.0 Introduction ... 93
4.0.1 Multistability in fluid dynamics ... 93
4.0.2 Taming the bistability ... 94
4.0.3 Experimental setup ... 96
4.1 Spontaneous one-way transitions ... 97
4.2 Both-ways transitions ... 97
4.3 Unstable position visits ... 99
4.4 Overshoots ... 102
4.5 Excursions ... 103
4.6 Conclusion ... 105
References ... 105

5 Rare-event triggering for spontaneous transitions 107
5.1 Introduction ... 107
5.2 Experimental protocol ... 108
5.3 Waiting time probability ... 110
5.3.1 Survival function ... 110
5.3.2 Double-exponential distribution ... 112
5.4 Rare-event triggering model ... 113
5.4.1 Transition to turbulence ... 113
5.4.2 A model for the pendulum ... 114
5.4.3 What can we tell from this rare-event model ... 117
5.5 Precursors events in the wake? ... 118
5.5.1 Transition and PIV in the experiment ... 118
5.5.2 Wake structure on both sides of the transition ... 119
5.5.3 Events in the wake ... 119
5.6 Perspectives ... 122

References 124

III Back to sleep

6 The stabilization of wind-induced self-oscillations 129
6.1 Introduction 129
6.2 Material and Methods 131
6.2.1 Experimental setup 131
6.2.2 Momentum equation 134
6.3 Results 135
6.3.1 VIV-inspired time domain expansion 135
6.3.2 Dynamical C_N coefficient 137
6.4 Discussion 139
6.4.1 Physical interpretations to the models 139
6.4.2 Comparison of models 141
6.5 Perspectives 141
References 144

Conclusion

7 Conclusion 149
7.1 Perspectives 151
7.1.1 On the wake of the pendulum 151
7.1.2 On the model of the bistable dynamics 152
7.1.3 On the influence of turbulence 152
7.1.4 On flying itself 153
References 153

IV In the arms of Morpheus

8 PHOeBUS 157

Appendix

A Appendix: Shaping the bistability 161
A.1 Bird nomenclature 161
A.2 Effect of the square orientation on the angular bistability 161

B Appendix: Rare-event triggering for spontaneous transitions 163
B.1 Cumulative distribution function for $\delta\Gamma_{min/max}$ 163

C Appendix: The stabilization of wind-induced self-oscillations 165

Articles

INTRODUCTION

0 INTRODUCTION

"Flying might not be all plain sailing but the fun of it is worth the price."
Amelia Earhart

This quote, from one of the few women to have made a name for herself in the history of Aeronautics, could easily be extended to the understanding of flying itself, as this thesis will attempt to convey.

Before even trying to understand flight, one must know first-hand of its many shapes. From gliding like squirrels to hovering like hummingbirds, at least 6 different flying methods can be identified in the animal world, about 3 in the plant kingdom, and 6 in human technology.

In the Wiktionary[1], the first definition of flying in English and German is "traveling in the air, another gas or vacuum without being in contact of a grounded surface". So, in a sense, while running, humans do fly for a brief instant at each step. In French however, it is to stay in the air while flapping wings, which would mean that planes do not fly. In Japanese, flying (飛ぶ) is defined by the action of moving in mid-air, which though closer to the English and German definition does not require the absence of contact with a grounded surface. This linguistic excursion shows the ambiguity of defining what it means to fly, without even beginning to discuss how one flies.

From a physical point of view however, a possible definition of flight would be a combination of all three definitions. A requirement is the production of *lift* **L**, an upward force opposing gravity. If this lift is not sufficient to balance or dominate the weight $m\mathbf{g}$, then flight is assumed if the time in the air, without touching ground, is significantly higher than the equivalent time in free fall. Displacement mid-air is achieved by producing *thrust* **T** in the direction of motion. Yet, air resists in response to motion, inducing *drag* **D** opposing thrust. For a perfectly stable hovering kestrel, these 4 forces exactly balance each other (see Fig. 1).

In this thesis, our main model of a flying object is a simple plate pendulum placed in a wind tunnel. As such, only weight, drag and lift will be of interest and no active thrust is produced. Some of the various concepts presented hereafter through the example of flight will be useful for studying the pendulum and will be detailed one by one in section 0.1.

With this scientific definition of flight, it becomes easier to investigate how to fly by looking into all the possibilities of generating lift.

1 https://en.wiktionary.org/

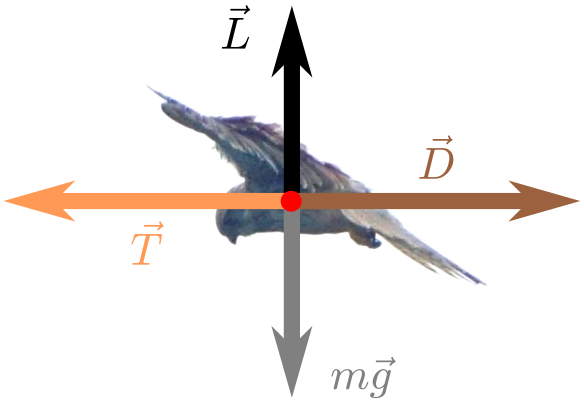

Figure 1: Forces acting on a hovering kestrel. Lift (L) compensates weight (mg) while thrust (T) balances drag (D).
(Photo: *Falco tinnunculus*, France, 2021)

Animal flight

In the animal world, a little-known fact is that a majority of animals flies [1]. Among warm-blooded vertebrates (birds and mammals), with about 10000 flying bird species and 1200 bats, the ratio of flying species to total species comes close to 80%. To this already consequent number of flying species, there are also about a million flying insects and a few tens of flying reptilians, amphibians and fishes. Yet only bats, birds and insects have independently acquired powered flight (and pterosaurs though now extinct), the others mostly relying on the wind and initial impulsion to soar through the air. Hence, within the here-presented of 6 flying methods of animals, 3 are powered while the other 3 are not (see Table 1).

Powered flight	Wind-induced flight
a) Flapping	b) Gliding
d) Hovering	c) Dynamic soaring
e) Clap and fling	f) Ballooning

Table 1: Different types of flight in the animal kingdom.

Birds use the 4 (a,b,c,d) first types of flight (see Fig. 2). All flying mammals glide, even bats [2], only they also flap and hover (a,b,d). Insects rely mostly on powered flight (a,d,e), with the exception of large butterflies that may use gliding on certain occasions [3]. Ballooning is very different from the 5 other flying techniques as we will see and is almost uniquely used by arachnids, with a few examples of lepidoptera larvae: caterpillars (31 confirmed species among more than 170000) [4].

"Flapping" and "gliding" flights are the most common flying methods. Bats and small birds favor flapping, while flying squirrels, flying lizards and large birds like raptors, have a propensity to gliding. The aerodynamics of both flying methods have been extensively investigated [5–7] but the diversity of flying species and the complexity of morphological variations of the animal in flight leave many stones to turn. *Flapping insect flight will be further detailed by the end in this thesis as a parallel project to the pendulum.*

Figure 2: a) Flapping flight: black kite (*Milvus migrans)*, Japan, 2018.
b) Gliding: white stork (*Ciconia ciconia*), France, 2021.
c) Dynamic soaring: northern fulmar (*Fulmarus glacialis*), Iceland, 2019.
d)Hovering;: green-throated carib (*Eulampis holosericeus*), France, 2021.

For simplicity, let us assume the flying animal to be a bird for a while.

For flapping flight, the lift is produced by pushing the air downwards in downstroke and then slightly backwards for thrust in upstroke (see Fig. 4.a). Through the repetition of wing motion, the asymmetry creates an time-averaged positive vertical force. However, structural torques on wings during flapping flight are important so that long and large wings are not suitable for such flight. Instead, wings of smaller size like that of starlings are flexible and resistant enough [8]. An important point in flapping flight, as in the later-described hovering flight, is the *wing-wake interactions*. While flapping wings at low speed, the vortices induced by the motion are not entirely advected by the time the stroke completes and as such strong coupling occurs between the vortex dynamics and the wing [9]. *This wing-wake coupling lies at the core of the pendulum system investigated in this thesis as we will see later in Chapter 5.*

The wake of an object is understood here as any flow structure behind the object that would not exist without the object itself. Behind an airfoil, it can separated into three different kinds of vortices as we will see later and is represented in Fig. 3.a.

In gliding flight, lift is morphological. Like for airplanes, which will be discussed later, the geometry of the wing generates lift by inducing a pressure difference between the upper side of the wing, the extrados, and the lower side, the intrados (see Fig. 3.b). To glide efficiently, a large surface area is needed and a perfect example of a gliding bird with extreme wing surface is the albatross. Raptors like condors and bearded vultures also present among the largest wing surface to body size ratios. Gliding is also enhanced by lifting *wingtip vortices* [10]. *Wingtip vortices develop due to finite span effects*

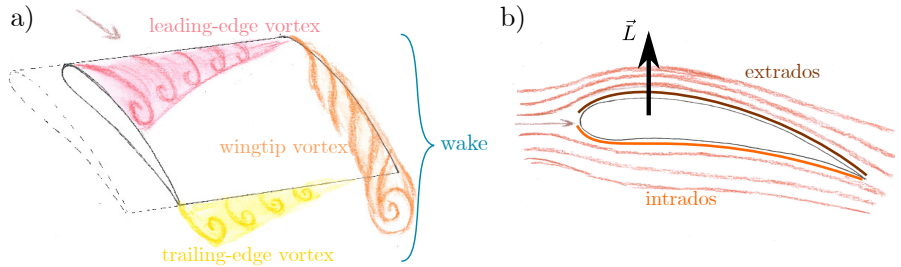

Figure 3: a) Schematic representation of the wake of a semi-infinite-span wing with leading-edge, trailing-edge and wingtip vortices. b) Flow around an airfoil. Lift is generated by the difference of flow velocity on both sides.

(Fig. 3.b) and the plate pendulums used in this thesis have been found to present such vortices close to the horizontal, as will be presented in Chapter 1.

While flapping flight produces thrust together with lift, gliding only generates lift. Thrust is provided mostly through wind currents, like thermals or by adding a horizontal component to lift by tilting the wing, so that the pressure resultant no longer only supports weight. The extreme of wind-current gliding is "dynamic soaring". Sea birds are experts for this kind of flight, in particular albatrosses and fulmars. They achieve horizontal acceleration by switching back and forth across a wind horizontal shear layer, taking advantage of the flow velocity difference and gravity [11].

However, birds sometimes wish to stay in one position but without losing altitude, like stationary flight. To achieve this feat, only a few bird families have evolved this flying technique, among which the best-known is the hummingbirds. Also referred to as "hovering" flight, stationary flight is practiced by kestrels for a certain range of wind speed [12] and occasionally by small passerines or sea gulls – calling stationary flight for kestrels hovering flight is a small leap, as the flapping pattern does not correspond to true hovering of hummingbirds or insects. While kestrels perform stationary flight mostly for hunting, hummingbirds hover almost constantly, for feeding, battling, courting, etc. They are also the only bird capable of hovering in still open air. This is possible thanks to a unique musculoskeletal adaptation: the humerus is shortened and almost perpendicular to the leading-edge thus enabling a greater laterality of the wing compared to other birds [13]. As such, their flapping motion can describe an ∞ in the air and thus produces lift by the asymmetrical vertical motion, while negating drag and thrust through the horizontal symmetry [14]. Hovering is a more common feature for insects such as hover flies or hawkmoths, whose flapping pattern is strikingly similar to that of a hummingbird [9].

In these 4 flying techniques, flight sustainability has for long been supposed to be achieved dynamically and morphologically, through morphological tuning and evolution. Though morphological tuning is observed to benefit the aerodynamics of flight, like feather spacing for gliding raptors [19], insect flight brought to light a particular trait in vertebrate flight, the *leading-edge vortex* (Fig. 3.a) [7, 20, 21]. This vortex develops at the leading edge of the wing and is stabilized through finite span effect and enhanced by the flapping motion [22]. Its main role in insect flight is lift production and its discovery refuted the apocryphal saying that bumblebees were flying defying Physics'

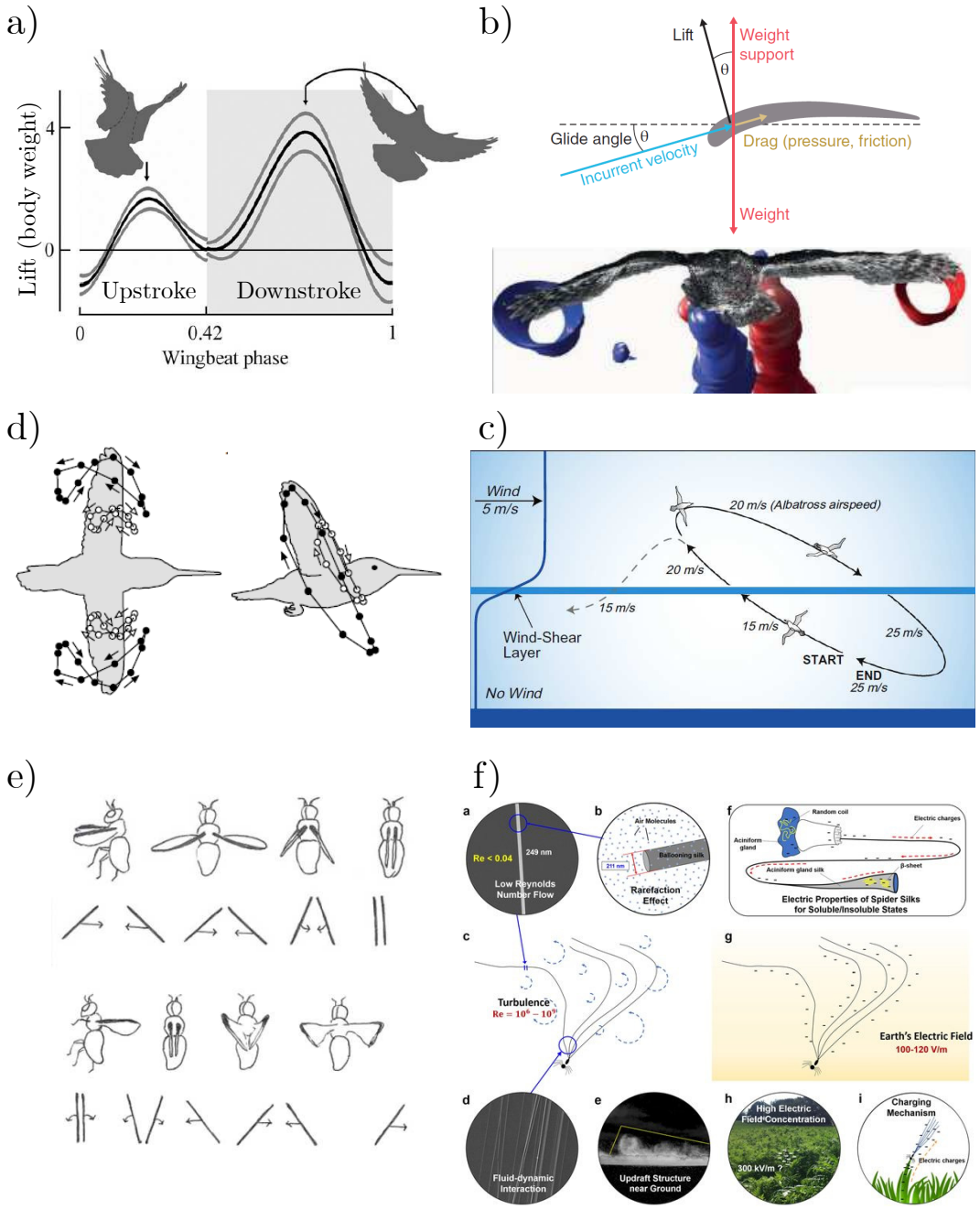

Figure 4: a) Flapping flight production of lift for a rock pigeon (*Columbia livia*) [15]. b) Gliding mechanism [16] and wingtip vortex generation behind a tawny owl (*Strix aluco*) [10]. c) Dynamic soaring schematic representation for an albatross [11]. d) Hovering flapping pattern of a humming bird in a wind at $10\,\mathrm{m}\cdot\mathrm{s}^{-1}$ [14]. e) Clap and fling schematic flapping pattern [17]. f) Ballooning representation, and the role of turbulence and electric field on the take-off [18].

law, saying that can be retraced to Antoine Magnan, professor at the Collège de France in 1934 [**Magnan1934**].

Due to their smaller size, insects are much more sensitive to vortex and viscous effects. Large insects have yet developed flying strategies close to birds as dragonflies flap their wings [23], butterflies glide like birds [3], and hover flies, as their name implies, hover like hummingbirds. For smaller insects however, like millimetric parasitic wasps (e. g. *Encarsia* genus), such options are not available as the flow offers more resistance and can be reversible if laminar. The equivalent to us would be to be moving in honey. They thus evolved the flapping pattern to "clap and fling", which bypasses the reversibility of the flow through an asymmetric motion (see Fig.4.e) [17]. As our interest lies more in the centimetric scale, we will not dwell further on clap and fling.

A last flying possibility observed in the animal kingdom is "ballooning". As we said before, it is mostly done by arachnids and this is due to the simple reason that it requires silk thread. Ballooning consists in extending one or multiple long silk threads and then once the vortex-induced lift on the thread is large enough, the arachnid takes off to be carried by the wind [18] (see Fig. 4.f). Like gliding, it is a form of airborne displacement but without any directional possibilities. It is thus only used for dispersal. Dispersal is also the reason plants take to the air.

Plant flying in the air

Plants, despite their inability to move when rooted, can also travel in the air, mostly as seeds. In particular, three types of flying apparatus have been observed in nature, some more widely spread than others: parachuting, autorotation and gliding.

As a child in Europe, it is indeed common to blow dandelions and watch the seeds taking off with their little feathery parachutes (Fig. 5.a) [24] or to throw maple samaras in the air to look at its rapidly spinning yet slow descent to the ground (Fig. 5.b) [25]. Rarely is it possible to play however with gliding seeds (Fig. 5.c)[26]. Yet all three mechanisms exist and are perfect examples of the complexity of flight.

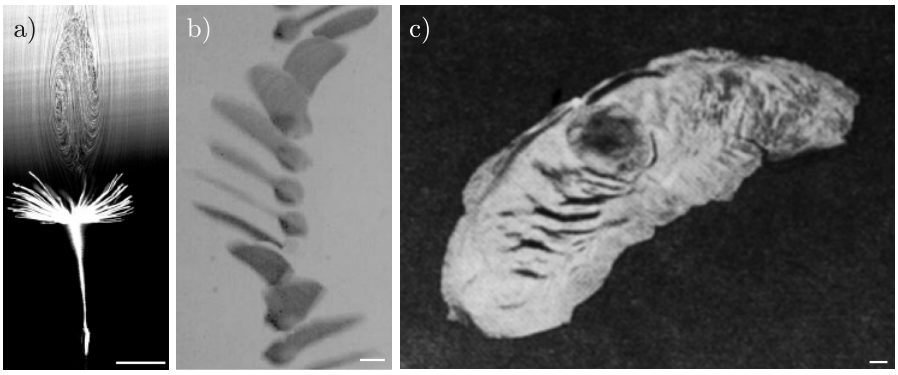

Figure 5: a) Dandelion (*Taraxacum officinale*) pappus in vertical wind tunnel and flow visualization, from [27]. b) Chronophotography of a falling maple samara (*Acer palmatum*) from [28]. c) Gliding seed (*Alsomitra macrocarpa*) from [26].

In particular, like for insects which rely on vortices to generate lift, dandelion seeds use enhanced vortices developing above their plumed top, the pappus. Such vortices indeed generate lift efficiently for small objects [27]. On the other hand, samaras are quite asymmetrical and always rotate in the same direction. Though rotation is enough

to induce lift to a certain extent, it has been shown that the stability of rotation and thus of lift production could be linked here again with a strong stable leading-edge vortex, like the one especially present in flapping flight for birds and bats [29]. Very little is known yet about plant flight as shows the example of the gliding seed of the Java cucumber vine *Alsomitra macropcarpa*. Apart from its excellent gliding properties, making it one of the most efficient gliders, the mechanisms behind such efficiency are still to be understood.

Human take-off

By looking at Nature, humans have since long dreamed to take to the skies. Like Icarus trying to fly with artificial wings or Leonardo da Vinci designing the first helicopter, one can feel how nature inspired people to fly. The first planes were also designed inspired by birds and bats, as shown in Fig. 6.a. However, flapping flight was not possible due to physical constraints, as the largest flapping birds are swans whose maximal mass is below 20 kg [6]. Above that mass, only gliding is possible for a short extent of time, as soaring is also limited [30]. Flight is a delicate balance between wing surface, wing structural resistance and weight.

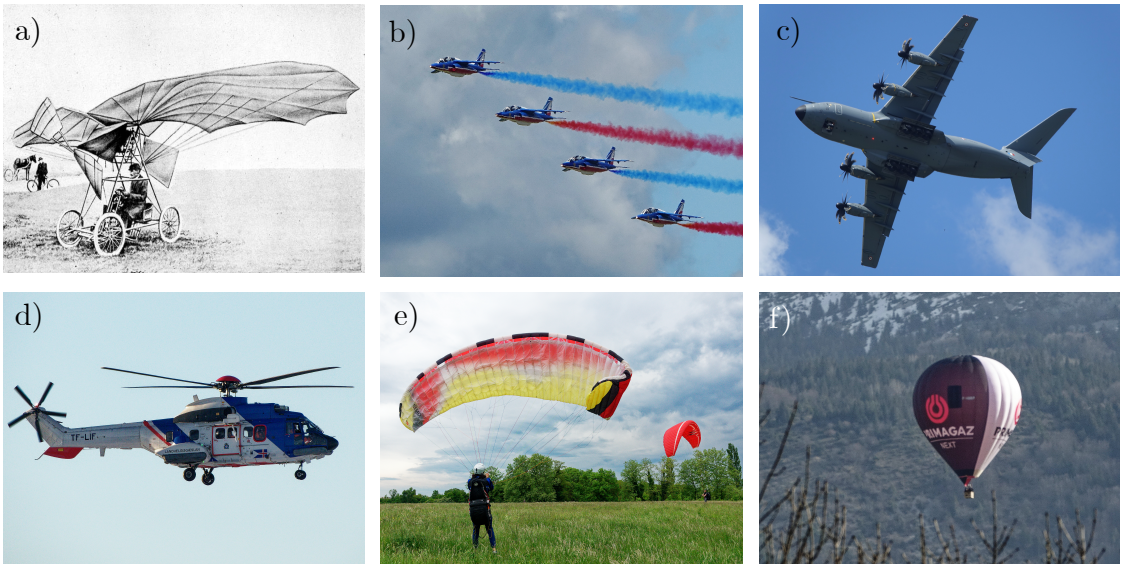

Figure 6: a) Traian Vuia in his plane, one of the fathers of aviation in Montesson, France, 1906 (Municipal archives). b) 4 Alpha jets of the *Patrouille de France*, France, 2019. c) Airbus A400M, France, 2019. d) Eurocopter AS332 Super Puma, Iceland, 2019. e) Paraglider, France, 2022. f) Hot-air balloon, France, 2021.

Humans thus developed their own means of flight, propelled (or powered) flight – this is not to be confused with the powered flight in animal flight which is any type of flight for which the thrust is produced by the animal. The most common means of propulsion for commercial airplanes are jet propulsion (Fig. 6.b) and propeller aircraft (Fig. 6.c). This provides the airplane with thrust and the lift is then produced as for animal gliders, by a pressure difference (Fig. 4.b) between the two sides of profiled wings. A whole variety of wing shapes has been tested through out the 20th century, among which is found the NACA 4-digits profiles, the profile NACA 0012 being one of the most studied [31–33]. A type of human powered flight is also performed by rotor

craft, better known as helicopters (see Fig. 6.d). These work like maple samaras and generate lift by driving the air below the rotor blades.

In addition to these 3 powered flight techniques, 2 types of non powered-flight are also found in human technologies, gliders and balloons. Gliders, like paragliders (Fig. 6.e), are similar to that found in nature in their flying method, while balloons take advantage of buoyancy rather than lift to elevate in the air (Fig. 6.f).

A last flying technology developed by mankind is found in unmanned air vehicles (UAV) which have taken flight in the recent years and with them the mechanical constraint on flapping flight, with mass below 20 kg. Bio-inspired UAV have been developed based on the comprehension of bird and insect flapping flight, like the Pigeonbot [34] or flapping micro-air-vehicles [35]. These recent developments expanded unsteady aerodynamics research of pitching and heaving airfoils as well as animal flight understanding. *These two themes will be met again later in Chapter 6 and Chapter 8.*

Pendulum flight?

By observing the diversity of flight, both in nature and technology, the importance of flow-wing and vortex-wing interactions stands out. As physicists, the spontaneous reaction to try to understand a problem is by simplifying the system. Reducing the whole flight problem into a single simple system to investigate a particular point is key to grasp the phenomenology behind it and then develop entire models that take into consideration its complexity. The core of this thesis is the coupling between a moving object and its wake. The simplest object for such study is then a rigid pendulum. Placed in a wind tunnel facing the flow, its equilibrium position depends on the flow velocity and its leading-edge vortex exists in the plane of motion, so that it directly interacts with the dynamics of the pendulum. Yet before going further into this thesis, with experiments and results, a few concepts are properly defined in order for the journey to be smoother.

0.1 A WIND-SWEPT PENDULUM

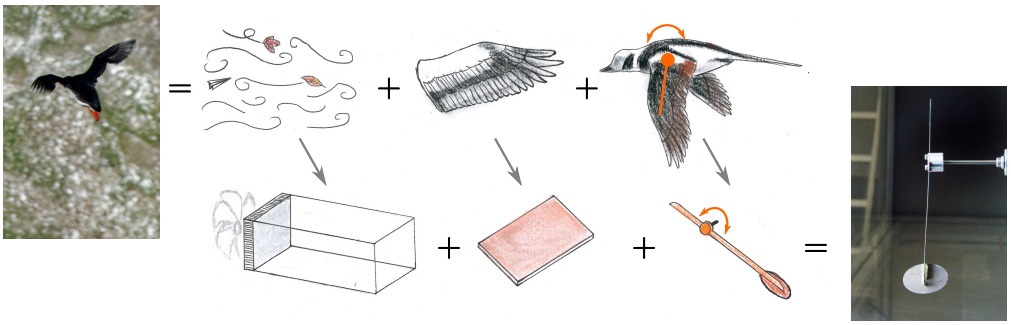

Figure 7: Analogy and decomposition from animal flight to pendulum study. Left: Atlantic puffin (*Fratercula arctica*), Iceland, 2019. Right: Pendulum in the wind tunnel, Lyon. From left to right: Natural wind is simplified into a controlled air flow in a wind tunnel. The wing (redrawn from an Egyptian vulture, *Neophron percnopterus*) is replaced by a thin plate. The pivot point of the wing to the bird body (represented on a long-tailed duck, *Clangula hyemalis*) is set as a pendulum in the experiment.

In this thesis, the pendulum is used as a model to investigate various aspects of flight. By replacing the natural turbulent and unsteady wind by a controlled air flow in a

wind tunnel, and the complex shape of a bird or insect wing by a plate and a perfect pivot connection, the main flight mechanisms that we try to understand are wing-wake interactions and unsteady coupling (see Fig. 7). This phenomenon is also important in the context of *fluid-structure interactions*, such as wind-induced oscillations of bridges or cables.

Though both animal flight and wind-induced oscillations are interactions between an air flow and a structure, fluid-structure interaction will be, in the following, meant as the study between man-made structures and wind, as in civil engineering.

0.1.1 *Definitions and aerodynamic considerations*

The pendulum equation, known to all scientists, is one of the basic equations taught in undergraduate classes to learn how to solve differential equations. This particularity makes the pendulum very interesting to study complex couplings from electromagnetism to aerodynamics.

As a standard application of the conservation of the angular momentum, its most general form, projected onto the direction normal to the plane of motion, is the following:

$$J\ddot{\theta} = -mgl\sin(\theta) + \sum \mathbf{r} \times \mathbf{F}_{\text{ext}} \cdot \mathbf{e}_\mathbf{y} \tag{0.1}$$

with J the moment of inertia, m the mass of the pendulum, l the distance between the swivel and the center of mass, g the local acceleration of free fall, and $\mathbf{r} \times \mathbf{F}_{\text{ext}}$ the various external torques, such as aerodynamic torque coming from drag and lift.

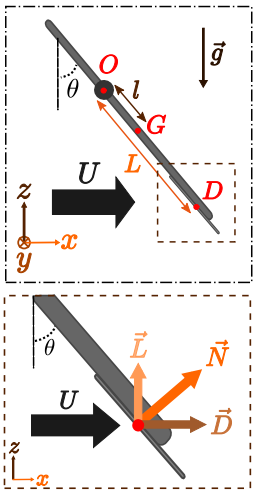

In the following, the flow is considered along the $\mathbf{e_x}$ *and the object motion in the* $(\mathbf{e_x}, \mathbf{e_z})$*-plane.*

This thesis focuses on the torque resulting from fluid interactions and the pendulum dynamics is used as a mean towards their understanding. However, external torques can take many forms, from electric forcing to torsion spring or magnetic torque.

Fluid interactions are commonly separated between *drag* $\mathbf{D}$, in the direction of the fluid motion, and *lift* $\mathbf{L}$, perpendicular to it, as we defined earlier for flight. These two forces result from the pressure p and the shear stress $\overline{\overline{\tau}}$ at the surface of the object, defined as in Eq. 0.2. Drag can also be divided into two main components, pressure drag $\mathbf{D}_P$ from the pressure forces, encompassing geometric drag and lift-induced drag and viscous drag $\mathbf{D}_\mu$ from viscous friction on the object.

$$\mathbf{F}_{\text{fluid}} = \underbrace{-\iint_S p\mathbf{n}\,dS}_{\mathbf{L}+\mathbf{D}_P} + \underbrace{\iint_S \overline{\overline{\tau}} \cdot \mathbf{n}\,dS}_{\mathbf{D}_\mu} \tag{0.2}$$

To have a better grasp of these two forces, dimensional analysis can be useful. Let us perform such an analysis on a sphere of surface S (and diameter d) in a flow of

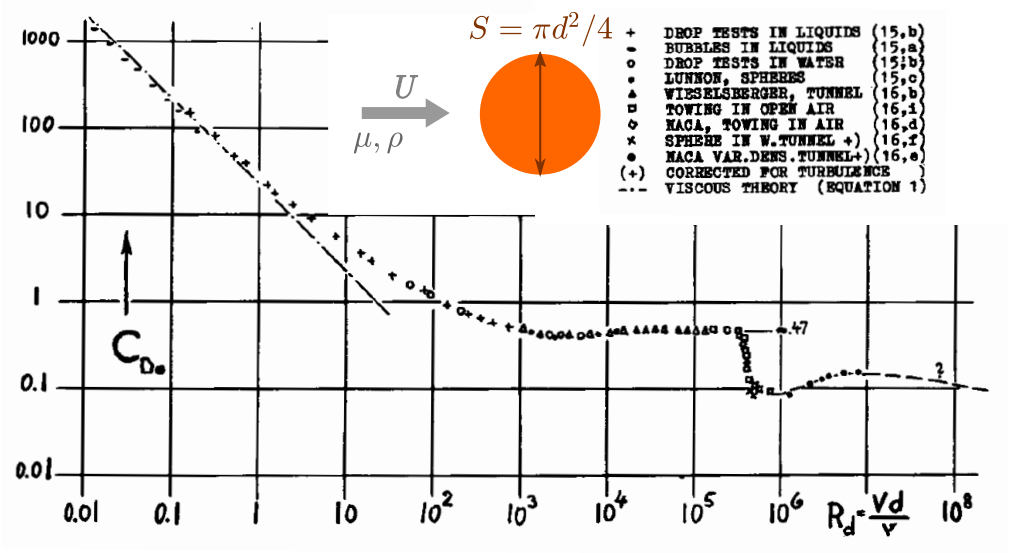

Figure 8: Drag coefficient of a sphere as a function of the Reynolds number. Extracted from [36]

velocity U, density ρ and viscosity μ. Due to symmetry, only the drag D acts on a sphere placed in a flow. In total, there are 5 independent values for 3 different units. Using the Buckingham Π theorem, two dimensionless parameters are sufficient to describe the system. One is the well-known *Reynolds number* $\mathrm{Re} = \frac{\rho U d}{\mu}$ and the other is the drag coefficient C_D, such that:

$$D = \frac{1}{2}\rho U^2 S C_D(\mathrm{Re}) \tag{0.3}$$

The lift coefficient C_L can be defined the same way, so that in a general fashion for an incoming horizontal flow, drag and lift can be rewritten as follows::

$$\mathbf{D} = \frac{1}{2}\rho U^2 S C_D \mathbf{e_x}, \quad \mathbf{L} = \frac{1}{2}\rho U^2 S C_L \mathbf{e_z} \tag{0.4}$$

In Eq. 0.3, it can be noticed that the drag coefficient C_D is function of the Reynolds number Re. Indeed dimensional analysis allows for dimensionless parameters to be interdependent. An example of this dependence is the drag coefficient of our aforementioned sphere of diameter d [36]. At low Reynolds number ($\mathrm{Re} < 10^2$), i. e. for slow and viscous fluids, the drag coefficient C_D is proportional to $1/\mathrm{Re}$, and the expression for the drag is taken as $\mathbf{D} = -3\pi\mu d\mathbf{U}$, which is no longer proportional to the square of the flow velocity. In contrast, for intermediate Reynolds number $\mathrm{Re} \sim 10^3 - 10^5$, C_D is almost constant, fitting the description of the drag in Eq. 0.4. After this range, there is the drag crisis, a sudden drop in the drag coefficient as the Reynolds number increases. This region is however not explored in this thesis as the considered Reynolds numbers are around 10^4, as we will discuss in the experimental setup description.

Based on these considerations, our pendulum equation Eq. 0.1 can be rewritten using Eq. 0.4, taking L as the distance between the aerodynamic center and the swivel of the pendulum, with U the flow velocity relative to the pendulum:

$$J\ddot{\theta} = -mgl\sin(\theta) + \frac{1}{2}\rho U^2 S L \underbrace{(C_D\cos(\theta) + C_L\sin(\theta))}_{C_N} \tag{0.5}$$

This equation 0.5 lays the groundwork of this thesis and was introduced in a similar disk configuration by Obligado et al. *in 2013 [37].*

For a sphere, due to its symmetries, no lift is produced ($C_L = 0$) while the drag coefficient C_D is known from experiments as in Fig. 8. The normal force is then expressed using the normal aerodynamic coefficient $C_N = C_D \cos(\theta)$. It results that rigidly (and horizontally) towed spheres are inclined from the vertical to an angle θ_{eq} simply given by $\theta_{\text{eq}} = \operatorname{atan}\left(\frac{\rho S}{2mg} C_D U^2\right)$, if the rod mass is negligible compared to that of the sphere and for Reynolds numbers between 10^3 and 10^5.

0.1.1.1 *Wind-swept plate and bistability*

When replacing the sphere by a 2D-plate, a new variable comes into play, the angle of attack α, also known as AoA in Aerodynamics. The angle of attack quantifies the orientation of the plate with respect to the flow, and as such can be defined by $\alpha = \frac{\pi}{2} - \theta$ for the pendulum. It is especially important for a plate because of its lack of rotational symmetry along the $\mathbf{e_y}$ direction. As drag and lift result mostly from the pressure distribution on the object, they depend strongly on the angle of attack as the flow around the plate varies drastically from the vertical to the horizontal as shown for a disk in Fig. 9.

In such configuration, replacing the sphere by a disk in the previous towing motion, the equilibrium position is much more complex than the arc-tangent previously obtained. θ_{eq} is defined by $mgl \sin(\theta_{\text{eq}}) = \dfrac{\rho S L}{2} C_N(\theta_{\text{eq}}) U^2$. Depending on the shape of C_N, this equation may not accept a unique solution, which could lead to a multistability, a central point to this thesis.

To illustrate this, the disk pendulum is particularly suited [37]. In Fig. 9, the disk aerodynamic coefficients C_D, C_L and C_N are represented. The measures used for this figure are the ones obtained by Flachsbart in 1932 [38]. The disk C_N coefficient, shown in Fig. 9, presents a sharp discontinuity, which separates a drag-predominance at low θ angles and a lift one at high θ. Because of this particularity, at intermediate flow velocity, three positions of equilibrium exist, two stable and one unstable in-between – this will be referred to as a *bistability*, as the unstable position is difficult to gauge based on the C_N coefficient measurements [38]. At low velocity, only one position in the drag-dominated domain is stable and at high velocity, only one in the lift-dominated region. This is particularly visible on the intersection of the weight torque Γ_{weight} and the aerodynamic torque Γ_{aero} in Figure 10.

In this particular case, at low velocity ($5\,\mathrm{m \cdot s^{-1}}$), there is only one stable fixed point ($\theta = 25°$). At large velocity ($8\,\mathrm{m \cdot s^{-1}}$) ,there is also only one stable fixed point ($\theta = 66°$). At intermediate velocities ($6.2\,\mathrm{m \cdot s^{-1}}$), there are however two stable fixed points ($\theta = 43°$ and $\theta = 58°$) and one unstable fixed point $\theta = 50°$.

A energy-based model of double-well potential is sufficient to reconstruct the equilibrium positions observed experimentally presented in Obligado *et al.* 2013 [37]. A point discussed in the article but which we will not detail now is the dependence of the C_N coefficient on the turbulence rate in the incoming flow. In particular, it smooths the discontinuity to the point that the bistability disappears at high turbulence rate.

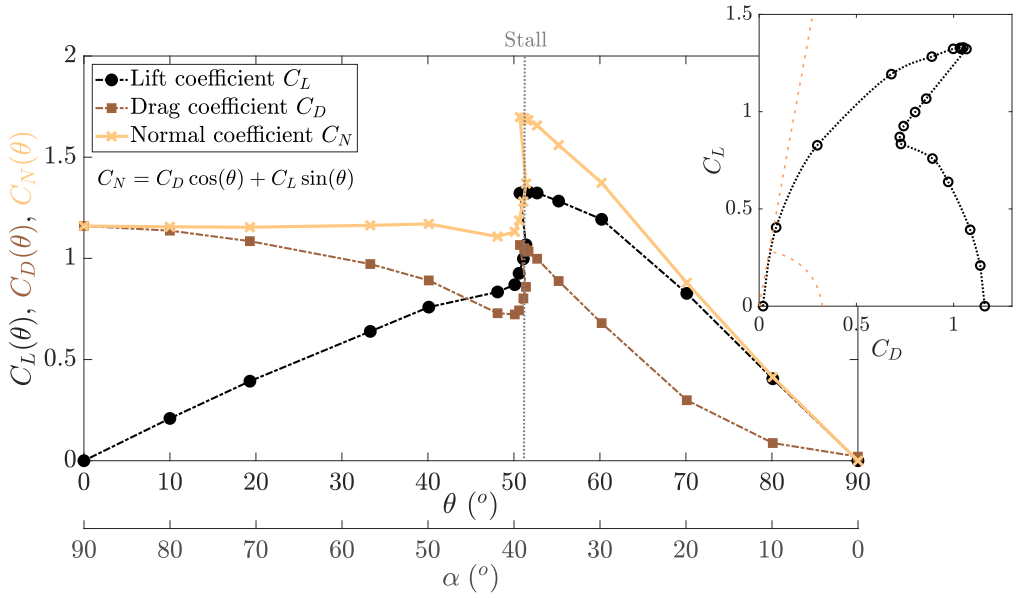

Figure 9: Angular dependence of the drag and lift coefficients C_D and C_L for an disk (redrawn from [38]. The normal contribution of both coefficients gives the normal coefficient C_N which will be used throughout this thesis. A particular feature of these curves is the sharp discontinuity around $\theta = 52°$, identified as the stall angle. Inset: polar curve of the disk. The maximal efficiency is attained at the dotted orange line. The corresponding angle is $\theta_{max} \simeq 80°$.

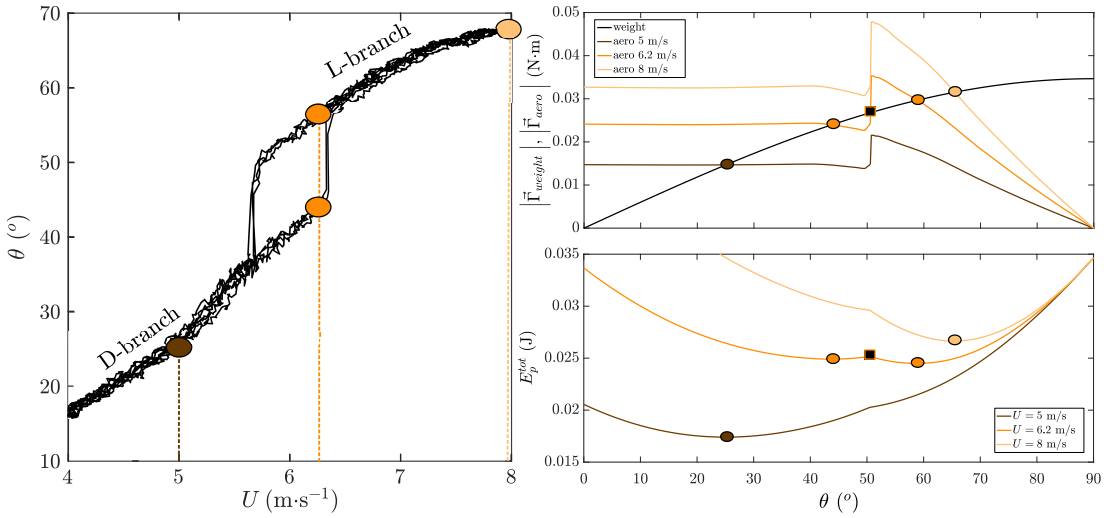

Figure 10: a) Equilibrium position θ_{eq} as a function of the flow velocity U. b) Weight and aerodynamic torques as a function of θ for different flow velocities U. c) Potential energy approach to investigate the stability of each position of equilibrium identified by the intersection of torques (circles for stable and square for unstable positions). Figures from [37].

0.1.1.2 *Quasi-steady wake description*

In this disk configuration, the angle of attack plays a central part in the aerodynamic coefficients. In Aeronautics also, the angle of attack is of particular importance, due to the presence of *stall*, a sudden drop of lift for a slight angular difference. As neither wings nor aircraft are spherical or cylindrical, their drag and lift coefficients depend

strongly on the angle of attack, like a plate, but stall is especially dangerous and subject to caution. Yet another parameter is closely watched, the lift to drag ratio C_L/C_D, which represents the efficiency of an aircraft: the higher the ratio, the more efficient the aircraft. To determine the maximum efficiency of a particular plane, it is common to look at the drag polar, that corresponds to the (C_D,C_L) curve (inset of Fig. 9), parametrized by the angle of attack. The maximal efficiency is then defined by the point for which the tangent to the polar curve goes through the origin – and of minimal drag if multiple points verify this condition – represented by the orange dotted-line in Fig. 9 (inset).

As we know that aerodynamic coefficients result from the pressure and shear distribution on the surface of the object (Eq. 0.2), we can expect great changes in the wake between the lift and drag branches of the C_N coefficient in Fig. 9. For simplicity, we will first assume a infinite-span thin plate for consideration in the plane of motion. The flow is deviated differently depending on the angle of attack as we would expect as shown in Fig. 11.

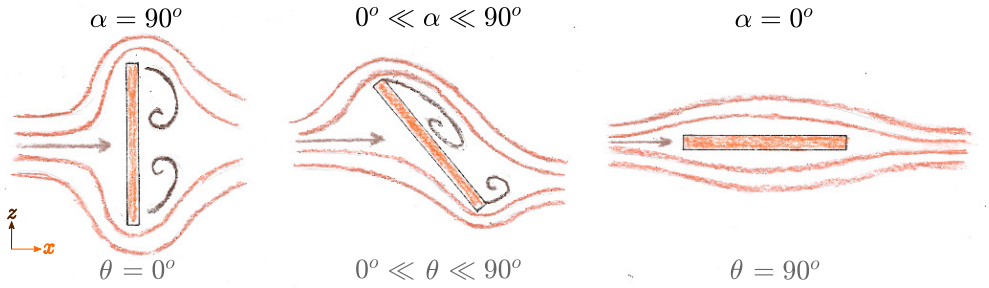

Figure 11: Schematic representation of how the flow deviates when encountering a thin plate at various angles. For $\alpha = 90°$ and $\alpha = 0°$, the downstream flow is symmetric and so only drag is produced. For intermediate configurations, the flow is no longer symmetric and the resulting pressure map on the surface favors both drag and lift through its asymmetrical distribution.

As the angle of attack increases (from right to left in Fig. 11), the flow detaches at the top of the plate leading to the formation of a recirculation bubble (in brown). Once the bubble grows enough, it induces the sudden drop of lift known as stall – the stall angle for a disk is represented in Fig. 9 by the dotted gray line. The growth of the recirculation bubble is highly dependent on the shape of the plate, in particular on its edge. While sharp edges are easy to manufacture, they induce a detachment at the leading edge at even the smallest angle of attack. This detachment increases the drag compared to a smoother edge that initiates detachment at a higher angle of attack due to flow reversal at the surface. The condition for stall is reached when the recirculation bubbles covers the entire plate. Though a recirculation bubble is a depression and induces lift, when it covers the whole plate, it can no longer enhance lift and stall occurs. This condition is true for thin airfoils, like the plates we use in this thesis, but other criteria for stall exist for intermediate to thick airfoils [39].

0.1.1.3 *Non-stationary wake evolution*

The description in Fig. 11 corresponds to a quasi-time-averaged flow. When the temporal dimension is also considered, periodic shedding occurs for the vortices growing in the recirculation bubbles.

First observed as an experimental fact, the mechanism behind this shedding is still under investigation. A possible interpretation though hand-waving comes from a naive approach of the system, and is presented here. When first encountering an inclined plate, the flow rolls up at the edge and creates the recirculation bubble. As it induces a depression, more fluid gets rolled up by the pressure difference in the recirculation bubble that grows up to a certain size. At that size, the recirculation no longer deviates enough the flow to grow but instead the more fluid is added, the more the bubble detaches from the surface, as the flow velocity increases by rotation. The bubble is at the same time advected by the incoming flow above it and a new bubble forms below. A schematic representation of the phenomenon is shown in Figure 12. As the recirculation bubbles take almost always the same time to form, this process produces a periodic oscillation in both aerodynamic forces and vorticity at the surface. This is known as *vortex shedding*, and is well-known by the trace it leaves downstream, called the von-Kármán street. For an inclined plate, it can be separated, as asymmetry arises, into the *leading-edge vortex* (LEV) and the *trailing-edge vortex* (TEV) (defined as in Fig. 3.a, and identified in Fig. 12).

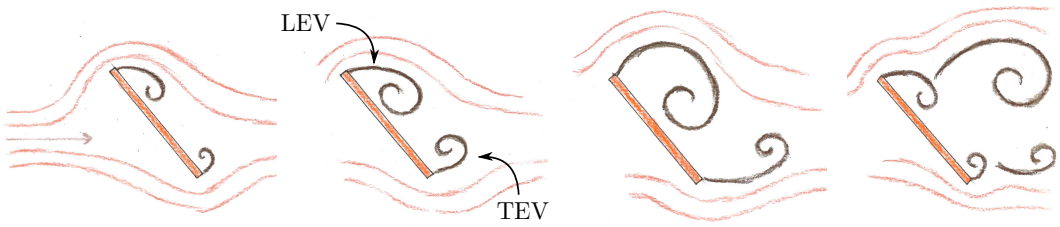

Figure 12: Representation of vortex shedding development on an inclined plate.

From the periodic vortex shedding, another dimensionless quantity is defined that will be of interest to us, the *Strouhal number* $\mathrm{St} = \frac{f_{vs} D}{U}$, with U and D defined as in the Reynolds number and f_{vs} the frequency of the vortex shedding. This number will be important throughout the following and depends mostly on the shape of the object. Once the Strouhal number is calibrated, the vortex shedding frequency can be used for flow velocity estimation. Flow anemometers work on this design, for instance a typical order of magnitude for the Strouhal number is 0.2 for a sphere.

0.1.1.4 *Finite-size effects*

All the aforementioned considerations were described for wings (plates/airfoils) of infinite span. When the span is finite, the aspect ratio comes into play and the wake becomes three-dimensional. In particular, the flow rolls not only in a von-Kármán street, but also transversely to its plane of motion, from the wingtips. These wingtip vortices, also known as trailing vortices, first develop from a vortex sheet to a counter-rotating vortex pair, rolling-up under its self-induced velocity field [40]. A well-known simplified

model of the wingtip vortices is the horseshoe vortex, which assumes the distribution of vorticity to be uniform along the wing span. Despite its simplicity, it captures the flow dynamics far from the aircraft, given an effective wing span $b' = \pi/4\ b$. A model closer to reality as it takes into consideration the vortex sheet, is Prandtl lifting-line theory. As the vorticity in the lifting-line theory is a function of the lift coefficient, models have been developed for the characteristic distance to the roll-up of the vortex sheet using this dependency [40]. The coupling between the von Kármán street and the trailing vortices can generate vortex rings and complex behaviors in the near wake.

The aspect ratio in Aeronautics is defined as the ratio between the squared span b over the surface area S, $\mathrm{AR}_{\mathrm{aero}} = \frac{b^2}{S}$. *For simplicity, here the aspect ratio will be defined as the ratio between the span b and the chord length c,* $\mathrm{AR} = \frac{b}{c}$. *For rectangular plates, both ratios are equal but not for disks, for which they differ by a factor* $1/\pi$.

For instance, depending on the interactions between leading-edge (LEV), trailing-edge (TEV) and wingtip vortices, the wake can present various configurations. A good example for this is the disk, whose aspect ratio of 1 gives close-to-equal importance to the 4 vortices. Large Eddy Simulations (LES) at low Reynolds number provide a qualitative description of the wake structure at different angles [41, 42].

- At the vertical, the disk presents an annular stable wake, due to its symmetry, detaching only through the destabilization of the ring close to the plate.
- When tilted, the LEV becomes more important than the TEV, which gradually shrinks as it is advected more easily due to its position. The wingtip vortices still connect both LEV and TEV forming a ring vortex and the shedding occurs from the upper center of the ring vortex, the rest of the ring being entirely detached ahead of the shedding.
- As the angle of attack is reduced, the LEV becomes more constrained by the flow. Yet the wingtip vortices are free to roll up, especially with this reduction of the LEV. Hence, the wake is similar to that of an airplane, with two long trailing vortices and the LEV and TEV are almost non existent.
- At the horizontal, due to the symmetry between the upper and lower parts, the wingtip vortices do not have a preferred rolling direction, so the wake will be mostly determined by defects on the plate.

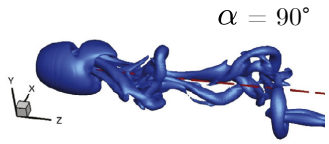

0-isovorticity **[Tian *et al.* 2017]**

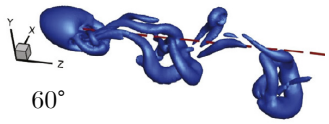

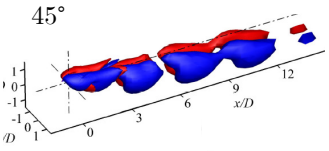

+/- isovorticity **[Gao *et al.* 2018]**

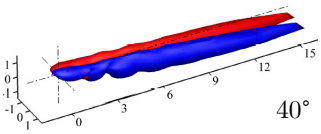

This overview of the wake shape will be further detailed in Chapter 1 with the visualization performed on the disk pendulum.

Returning to the disk as a pendulum, the functional form of the C_N coefficient presented in Fig. 9 might be linked with the description of the wake and a first sim-

plification would be that for angles of attack $\alpha < \alpha_{stall}$, the wake can be considered that of an aircraft and below, a ring vortex. Linking it with the predominance of drag and lift would change the previous perception of stall. Indeed in 2D, stall occurs due to expansion of the recirculation bubble, while in 3D, it might come from a wake reconfiguration, as we will see in Chapters 1 and 2.

This should cover most of the aerodynamic considerations that will arise throughout this thesis and any lack will be filled when needed.

0.1.2 *Winding up pendulum-in-flow history*

As the idea of simplifying a flying object into a plate pendulum might seem old-fashioned (for engineers and even physicists) or too simplistic (for biologists and engineers), a good knowledge of the previous pendulum-in-flow situations as well as fluid-structure-interaction history is necessary not to fall into the traps of previously-studied phenomena.

Pendulums in flows have, indeed, a long-standing history and while this thesis explores particular configurations (of disks, fly-swatters and rectangles), records of more standard configurations, such as spheres or cylinders, are found way before the 21st century and the following is here to pay tribute to the forgotten work of scientists from another era, viewed in the light of current knowledge. Our literature review traces back to the 18th century for spherical pendulums and to the 17th century for inclined plates. Even as early as the 15th century, pendulums have been used as anemometers (see Fig. 13), by Leon Battista Alberti, Leonardo da Vinci[2] and later Robert Hooke in the 17th century [43].

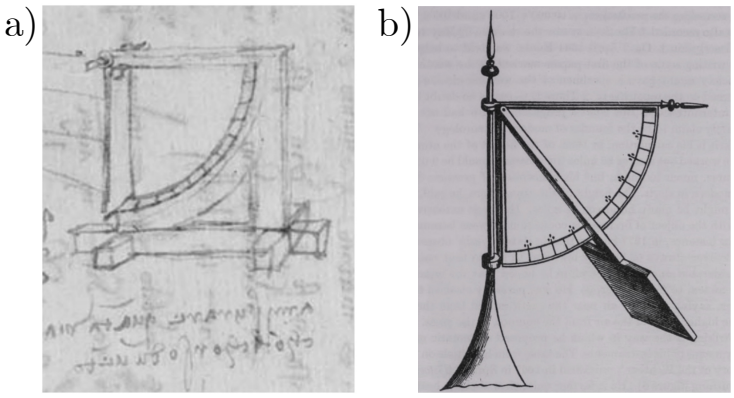

Figure 13: a) Da Vinci pendulum anemometer. b) Hooke anemometer [43].

In 1752, ∂'Alembert measured the resistance of air using the oscillations of a pendulum [44]. His work discussed the resistance of the fluid, which is now referred to as drag, and showed the proportionality of this resistance to the square flow velocity through the decrease in amplitude of the pendulum oscillations. In conclusion of his work, he mentioned the presence of a constant term in the resistance at low flow velocity. This

2 *Codex Atlanticus*, p. 675, 1486, original drawing by Leonardo da Vinci, http://www.codex-atlanticus.it/

could relate to the predominance of viscous drag D_μ on lift-induced drag D_L at low Reynolds number, which was not yet understood. ∂'Alembert also reported similar experiments conducted in the first half of the century by Newton, Bernoulli and Hutton.

The 19th century has been particularly active on the characterization of fluid resistance and pendulums have become standard for this investigation. Measures in various pressure environments, in particular in void chambers, were done by Baily in 1832 [45] and Stokes presented a review of these measurements together with other contemporary works, such as Bessel's, in an article in 1850 [46]. In particular, mathematicians, like Poisson in 1831 and Plana in 1835, have computed theoretically, based on the later-called potential flow theory, the necessary added mass for a sphere moving in a flow [47, 48]. These 19th-century works have mostly documented the viscosity of gas and set the base to the investigation of fluid-particle interactions, as the pendulum was only moving in the fluid at rest. After this thorough investigation, the pendulum has been more or less forgotten in the study of fluid-structure interactions, giving way to airfoils and bluff bodies with the development of aviation.

As most pendulum bobs for the study of air resistance were spheres, angle-of-attack and aspect-ratio issues were not tackled in that community and were however developed in a whole different context. Indeed, the study of flow resistance to moving plates goes back to an even earlier time than that of pendulums in flows, since such configurations are found in watermill systems. In the late 18th century, Abbé Bossut did experiments on the pressure on plates in canals and documented the movement of wheels driven by water [49]. Later, the angle between the plate and the flow was varied by Vince in 1798 and Colonel Duchemin in 1842 [50, 51]. They both observed a great change in pressure response between plates struck at low angle of incidence and at high angle of incidence. Despite the lack of theoretical development after these observations, they propose that the relative aspect ratio of the plate seen by the flow would be of importance to the pressure response, which we will see in the following is an interesting conjecture.

With the development of aviation, many wind tunnels and water tunnels were built in the early 20th century, leading to both the extension to the study of inclined plates and visualization techniques. In 1910 and 1911, Eiffel and Otto Föppl (son of August Föppl, of the Föppl-von Kármán equations) investigated the effect of shape, in particular aspect-ratio on the normal aerodynamic coefficient C_N [52, 53]. *These aspects will be investigated for the pendulum in Chapter 2.* From this, emanated a series of experimental measurements of any shape in flows, spanning from the ellipsoid to the half-sphere, empty or filled [54]. Through the installation of sewers and running water, studies on pipe flows and pressure drops added to the understanding on drag coefficients for grids and confined objects [55]. Until 1965, drag and lift coefficients were an important subject of research and Hoerner brought almost all existing research into a single book, which served as the standard for Mechanical and Aeronautical Engineering up to now [36].

Parallel to this development of Aeronautics, fluid-structure interactions have gained a lot of interest through the study of structural instabilities. A trigger to that was the incident of the Takoma Narrows Bridge in 1940 (Fig. 14.a). The fluttering instability developing on the deck led to the complete destruction of the bridge and it became the standard example of coupling between mechanical and aerodynamic responses.

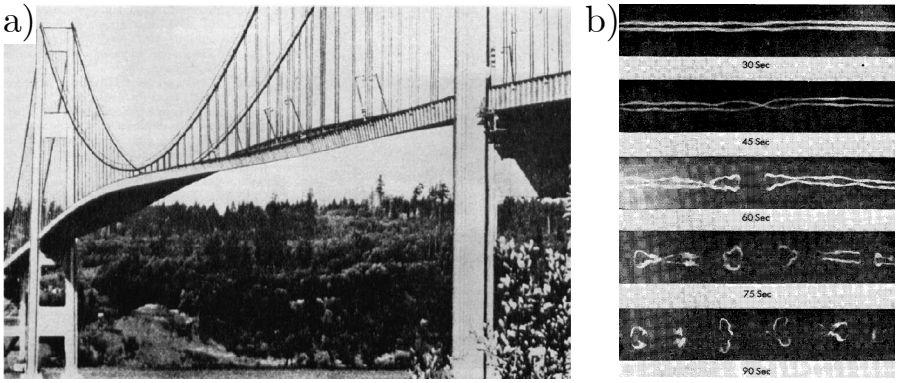

Figure 14: a) Tacoma Narrows Bridge under flutter instability [64]. b) Crow instability developing on a pair of trailing vortices [61].

First observed in 1841 by Russell [56], bridge deck flutter was only theorized in the 20th century, with Fung in 1955 [57] and then Blevins in 1975 among the precursors [58]. Flutter does not only occur on bridge decks but also on transmission lines. Ice-rigged transmission cables are indeed subject to strong wind-induced vibrations and the development of telegraphs and telephone boosted the study on such vibrations, initiated by den Hartog in 1932 [59], and more broadly on any built structure with Scruton and Rogers in 1971 [60].

This led to the expansion of the field of *aeroelasticity*, that relates to the mutual interaction between inertial, elastic, and aerodynamic forces acting on structures in airflow. In particular, other instabilities like galloping, divergence or buffeting arise in this field. *Fluid-structure considerations based on the pendulum are presented in Chapter 6.*

Instabilities are yet not limited to fluid-structure interactions. In the wake of airplanes in particular, composed mostly of two wingtips vortices, the Crow instability develops and destabilizes the trailing vortices into vortex rings (see Fig. 14.b). This instability was thoroughly investigated as trailing vortices can be stable for a long time in the sky depending on the atmospheric conditions. In the two World Wars, planes could be detected and their trajectory known due to these vortices. The Crow instability is fundamental to initiate the decay of the trail and once as a vortex ring, another instability adds to the decay, the Widnall instability. The theoretical formulation of both instabilities took place in the 1970s [61, 62], while the development of the trailing vortices was investigated from the first half of the century [40, 63]. *The wake instability and development of the trailing vortices are discussed in Chapter 1.*

The study of flow instabilities and the aim at improving the lifting properties of airfoils and understanding the wake naturally incited aerodynamicists to pursue flow visualization parallel to the theoretical investigation[3]. Flow visualization thus came to with a variety of techniques, some of which can be found early in the 20th century. A collection of flow visualization examples is the Album of Fluid Motion by van Dyke in 1982[65].Among this diversity of techniques, are dye, aluminum dust in oil, smoke, optical techniques such as shadowgraph, Schlieren or interferogram, etc. In the

3 Aerodynamics has the particularity of stimulating many senses (hearing, touch and smell), only lacking in eyesight, which is not the case for hydrodynamics with surface eddies for instance

case of a disk, that interests us here, a first study of the vortex rings in the wake is found in 1931 by Marshall and Stanton [66]. This first visualization for a disk normal to the flow was expanded by Calvert in 1967 [67] for an inclined disk. Both studies were done in water tunnel using dye, while smoke was later introduced in wind tunnels.

The development of cameras and computers in the second half of the 20th century gave rise to two quantitative estimations of flow properties, Particle Image Velocimetry (PIV) and Computational Fluid Dynamics (CFD). As computational fluid dynamics relies not on experiments but on numerical simulations, in order to reproduce truthfully experimental dynamics, some well-understood experiments were brought back to fashion. Among those are for instance the flow past a sphere in 2000 [68], flow separation behind a NACA 0012 airfoil in 1993 [69] or more recently the wake of a disk normal to the flow in 2008 [70].

Together with the new understanding of fluid dynamics brought by numerical simulations, pendular systems regain interest from the research community experimentally in the last decade, as freely-moving objects in flows are still difficult to investigate numerically. The coupling between fluid forces and pendulum motion can take many forms from vortex-ring emissions [71], bob-wake galloping instability [72], bob-wake stabilization [73] or even bistability [37]. This diversity makes the pendulum still a fruitful and mysterious subject for research, as despite its simplicity, it has yet to reveal all its physics.

This overview of the pendulum-in-flow and fluid-structure-interaction history is here to pay tribute to the many researchers that have worked for centuries on the kind of problems we explore in this thesis. It is of course not exhaustive as it is impossible in one life to read all the literature on the subject nor is this thesis a thesis in the field of history of science.

0.2 THESIS OUTLINE

Throughout this thesis, various aspects and phenomena of aerodynamic coupling and dynamical systems are explored, with a wind-swept pendulum to investigate them as their common feature.

Among the diversity of questions we propose to answer in the following thesis, some tackle fundamental issues in Aerodynamics, on the correspondence between the aerodynamic coefficients and the wake. Others belong to the domain of stochastic processes and multistability analysis.

To present these interrogations and their development, we have chosen to divide this work into 6 chapters, grouped in 3 parts.

The first part (Part i: *Waking up*) focuses on the characterization of the static aerodynamic coefficient C_N from different angles. This part includes the following 3 chapters.

Chapter 1 presents the visualization of the wake behind an inclined disk and aims at understanding how the wake structure influences the drag or lift dominance in the C_N coefficient.

Chapter 2 investigates the influence of the aspect ratio on the aerodynamic coefficient. In particular, one of its objectives is to understand and predict stall for finite-span rectangular plates.

Chapter 3 studies the influence of yet another geometrical parameter of the plate on the C_N coefficient: the porosity. To this end, the object of interest in the chapter is a fly-swatter.

The second part (Part ii: *An eventful day*) concentrates on the dynamics of the pendulum in its bistable zone. This part gathers the following 2 chapters.

Chapter 4 provides an overview of the various possibilities of behavioral response of the pendulum to bistability. Among these, spontaneous transitions and excursions are of particular interest.

Chapter 5 digs into the phenomenology of spontaneous transitions. It proposes a model inspired by the transition to turbulence to explain the temporal statistics of these events.

The third part (Part iii: *Back to sleep*) centers on the unsteady aspects of the coupling between the pendulum and the wind. This part is composed of a single chapter.

Chapter 6 examines the stabilization dynamics of a weathercock (a balanced pendulum). One aspiration is to define a dynamic C_N coefficient in the particular case of wind-induced self-oscillations.

In addition to the organization detailed above, each part possesses a common thread between the chapters with regards to the literature and unique to the part. In Part i, the various addressed questions are connected to bird flight and natural considerations. In Part ii, a common ground to many of the detailed dynamics is less alive, with a main comparison with dynamical systems presenting hydrodynamic bifurcations. Lastly in Part iii, the chapter is placed in the context of fluid-structure interactions and thus aeronautical and civil engineering.

0.3 HOW TO USE THIS THESIS

To complement the aforementioned outline, here are some comments on how to read and use this thesis.

- ▷ All parts are independent and standalone and can thus be read in any order.
- ▷ All chapters are also independent but some connections can be made between them.
- ▷ All photographs presente, identified by the location and date in their caption, were taken by the author.
- ▷ Wake structure schemes, as presented in Chapters 2 and 3, are simplified visual suggestions and do not represent verified reality in particular on the reattachment of the wake.
- ▷ Each chapter starts with a question identified as follows:

Question: What is a pendulum?

▷ In a chapter, some interludes will be found. These present methods, theoretical developments or anecdotes that are in connection with the chapter but not relevant results, strictly speaking. They are recognizable as follows:

Interlude

The equation system governing a double-pendulum motion without the point mass assumption is presented hereafter, given the conventions on the right. The only hypothesis is the alignment of the center of mass G_1 from the first pendulum to the swivels of the two pendulums (O and I).

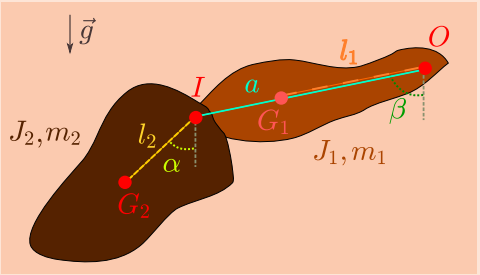

$$J_2\ddot{\alpha} = -m_2 g l_2 \sin(\alpha) + \dot{\alpha}\dot{\beta} m_2 l_2 a \sin(\alpha - \beta)$$
$$(J_1 + J_2 + m_2 a^2 + 2 m_2 l_2 a \cos(\alpha))\ddot{\beta} = -g((m_1 l_1 + m_2 a)\sin(\beta) + m_2 l_2 \sin(\alpha))$$

As all parts and chapters are independent, one can decide on the order in which to read them. The order chosen in the thesis is a personal arrangement and the reader is free to decide on his/her own.

For instance, the unfolding detailed in Section 0.2 has been designed around the idea of a passing day. The morning of our journey is the starting point of the thesis, the static understanding of the bistability. Afterwards, the active part of the day covers the dynamics in the bistable zone, while the evening investigates how the pendulum returns to its rest position when balanced like a weathercock. After the conclusion, the night is also embraced with the description of project PHOeBUS expanding the present study in a new direction of more intrinsic aerodynamic coupling between living butterflies, vortex and lift.

Some other suggestions are detailed hereafter. They are centered around similarities in the chapters either in the method, subject or experimental setup.

As examples, the following pools of chapters are possible:

- PIV measurements are presented in Chapters 1, 5 and to a lesser extent in Chapter 3.
- Aerodynamic unsteadiness is central in Part ii and iii, in particular in Chapters 5 and 6.
- Stall existence is discussed in Chapters 2 and 3 as function of the pendulum geometry.
- Models have been developed based on neighboring Fluid Dynamics fields in Chapters 5 and 6.
- C_N coefficients are computed from the experimental data in Chapters 2, 3 and 6.
- Chapters 1, 5 and 6 focus only on the disk pendulum.
- A fly-swatter is used as the pendulum in Chapters 3 and 4.

- Pendulum shape has been modified in Chapters 2 (aspect-ratio), 3 (porosity) and 6 (diameter).

The above list is not exhaustive and the reader is invited to find other commonalities between chapters and design one's route to go through them.

0.4 EXPERIMENTAL SETUP AND METHODOLOGY

In this thesis, the main experimental subject is a disk pendulum placed in a wind tunnel (see Fig 15). Across the chapters however, some changes to this particular setup will be made. Such changes will be discussed only in the relevant chapters and here is presented the basis of the experiment, which is assumed in any chapter unless otherwise mentioned. In addition to this description, the governing equation of the system is presented as part of the common methods used throughout the thesis and Particle Image Velocimetry (PIV) is introduced both in its setup and its methodology.

0.4.1 *Experimental setup*

The experimental setup can be divided into 4 main elements:

i. the wind tunnel,

ii. the pendulum,

iii. the swivel system of the pendulum,

iv. the PIV-measurement structure.

0.4.1.1 *Wind tunnel description*

Overview

The wind tunnel used for the experiments in this thesis is located at the Laboratoire de Physique in the ENS de Lyon. It is a hand-crafted closed-loop wind tunnel constructed in the late 1980s, with a few upgrades since then.

It is a "blowing" wind tunnel, meaning that the flow is generated by a wind turbine ahead of the test section. "Sucking" wind tunnels are usually open-looped like the Eiffel wind tunnel. The turbine is driven by a motor, for which we control the rotation frequency. This imposes the turbine angular velocity and with it the flow velocity. The conversion rate between the motor frequency and the flow velocity depends on the pressure drop in the wind tunnel. Thus, a calibration is required to set a given flow velocity after each modification of the test section.

The maximal flow velocity U in the wind tunnel is around $20\,\mathrm{m}\cdot\mathrm{s}^{-1}$, while only velocities up to $10\,\mathrm{m}\cdot\mathrm{s}^{-1}$ have been explored in this thesis. The maximal (over-estimated here) Reynolds number in the wind tunnel is about 3×10^5, and the maximal Reynolds number in the experiments only comes to 7×10^4, the minimal Reynolds number is about 2×10^3. Over this range, as introduced in Section 0.1, the drag and lift coefficients can be considered constant and depending only on the geometry.

The wind tunnel is automated by controlling the motor frequency and synchronized with the acquisition of the various measured variables, through a National Instrument

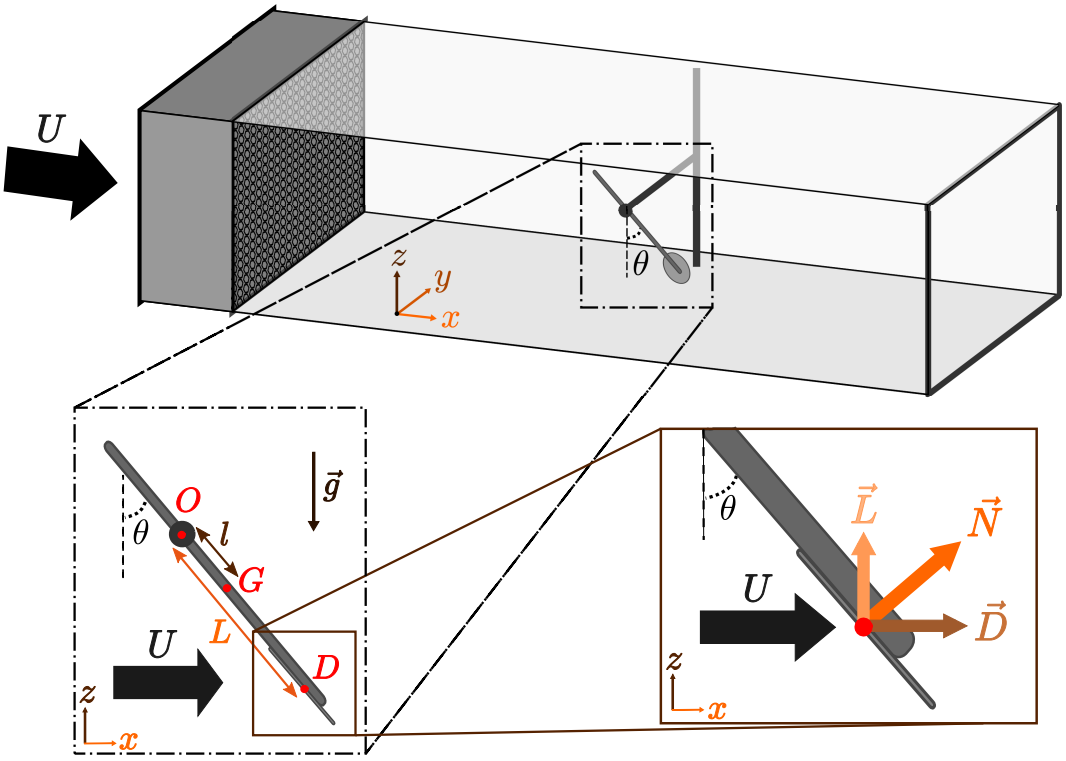

Figure 15: Schematic view of the test section of the wind tunnel. Details on the pendulum and how the aerodynamic forces are defined.

(NI) PXI-chassis, using PXI modules NI-4472 and NI-6229. This feature enables for a variety of experimental protocols that will be detailed in the relevant chapters.

Structural details

The test section is square over 3 m stream-wise and has a section of $51 \times 51\,\mathrm{cm}^2$. The total volume of air in the wind tunnel is estimated to about $8\,\mathrm{m}^3$. With a Norcan® structure and plexiglas panels, the test section can be modulated from close to open section and rails enable the displacement of measuring instruments such as the Pitot tube or the hot-wire, detailed later.

Before entering the test section, the air is conditioned through a honeycomb of 6 mm-width. The honeycomb has been changed during this thesis due to the heterogeneity of the flow downstream. The first honeycomb was 50 cm-thick, composed of multiple 5 cm-thick panels, and conditioned the flow to about 1.5% of turbulence intensity with however great spatial heterogeneity in the mean flow velocity. The *turbulence rate (or intensity)* is defined by the ratio $\frac{u_{\mathrm{rms}}}{U_{\mathrm{mean}}}$, u_{rms} the standard deviation of the flow velocity and U_{mean} its mean value. As it was changed early, only the results presented in Chapter 5 were made using this first honeycomb. The second honeycomb, a Polycarbonate CEL Components® honeycomb, is only 30 cm-thick, but in one block, removing any flow heterogeneity due to panel mismatches as the previous honeycomb showed. This however elevates slightly the turbulence rate to about 2.5% in the flow. The only remaining inhomogeneity in the wind tunnel is a light horizontal and vertical gradient that arises from the lack of guide vanes in the bend ahead of the honeycomb.

Flow measurements

The flow characteristics are measured using a Pitot tube and hot-wire anemometry. The Pitot tube is connected to a manometer Furness Control FCO318, from which is measured the dynamic pressure ΔP. This dynamic pressure is proportional to the square of the flow velocity U, $\Delta P = 1/2\rho U^2$ (ρ the air density). This measurement thus provides the flow velocity U and the calibration of the wind tunnel, which is controlled by the frequency of the motor, as the motor drives the turbine which set the flow velocity. As mentionned before, the wind tunnel is not controlled by the Pitot measurement, leaving the dynamic pressure subject to drift in case the air density varies, as it will be detailed later in Chapter 4. To refine the velocity measurement, in particular on the fluctuations, a hot-wire is placed closed to the Pitot tube. This hot-wire, operated in constant anemometry mode, provides the fluctuations of velocity which enables the estimation of the turbulence rate inside the wind tunnel. For more information on hot-wire anemometry, a complete review is found in [74]. In the wind tunnel in Lyon, two hot-wire anemometers are used, both Constant Temperature Anemometers, TSI IFA100 and TSI CTA module 1750.

In addition to these flow measurement systems, a barometer FCO342 measures the atmospheric pressure P in the room and a thermocouple, the temperature T inside the wind tunnel. These complementary measurements have been installed for refining the flow velocity estimation from the Pitot tube, as the air density ρ is given by $\rho = \frac{PM}{RT}$, with M the molar mass of dry air and R the universal gas constant.

0.4.1.2 *Standard pendulum*

The second fundamental element in the experimental setup is naturally the pendulum. While different pendulums have been used for the various experiments presented in this thesis, one particular configuration has been most thoroughly investigated and is assumed unless otherwise mentioned.

A common trait in all studied pendulums is the rod, which consists of a sanded saw-blade of thickness 1 cm and width of 1 mm. Its length is 31 cm. Only when Particle Image Velocimetry is done to investigate the pendulum wake dynamics, a shorter rod is used, of about 20 cm, but the total length of the rod is not relevant unless for the moment of inertia calculation.

At the end of the rod, a thin aluminum disk is glued. The main disk is 0.3 mm-thick and of diameter $d = 4$ cm. It is attached asymmetrically on one end of the rod, so that 3 cm are covered by the rod, leaving 1 cm of free surface behind (see Figure 16). The disk is then placed facing the flow, with the rod behind it. This asymmetry of the disk-rod swivel is deliberate as symmetry in Aerodynamics is very sensible. Even the slightest flaw can bring asymmetry to the wake structure, making it difficult to separate experimental bias to real asymmetrical behavior.

Some important parameters on the pendulum in addition to the disk diameter are its mass m, the distances l and L between the swivel O and the center of mass G and aerodynamic center D, and its moment of inertia J.

- The total mass is $m = 17.0$ g, divided into 1.26 g for the disk and 15.75 g for the rod.
- The distance to the center of mass $OG = l$ is $l = 5.7$ cm, calculated from the balance of masses and double-checked using the plumb line method.

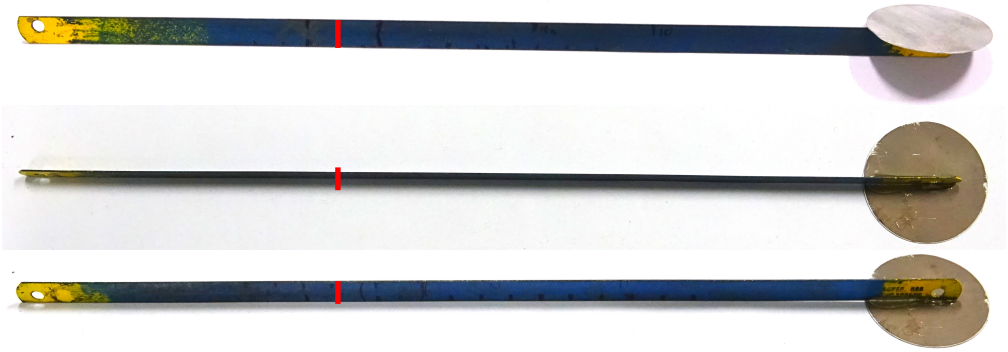

Figure 16: Multiple views of the 4 cm-wide disk pendulum. The red line indicates the position of the swivel in the standard configuration.

- The distance to the aerodynamic center $OD = L$ is taken as the distance to the center of the disk. Since we cannot access the exact position of the center of pressure on the disk, it is a reasonable approximation, all the more as $L \gg d$. This brings to $L = 19.5\,\text{cm}$.
- The moment of inertia J is calculated using Huygens formula for a compound pendulum, $J = 1.48\ \ 10^{-4}\ \ \text{kg/m}^2$. Another estimation can be provided by leaving the pendulum oscillate without wind, for which the pulsation is $\sqrt{\frac{mgl}{J}}$.

0.4.1.3 *swivel of the pendulum*

Now that the wind tunnel is presented and the main object of interest is described, a last fundamental point that still needs to be discussed is how the pendulum is attached in the wind tunnel. Like for the wind tunnel honeycomb, this swivel system has been changed during this thesis.

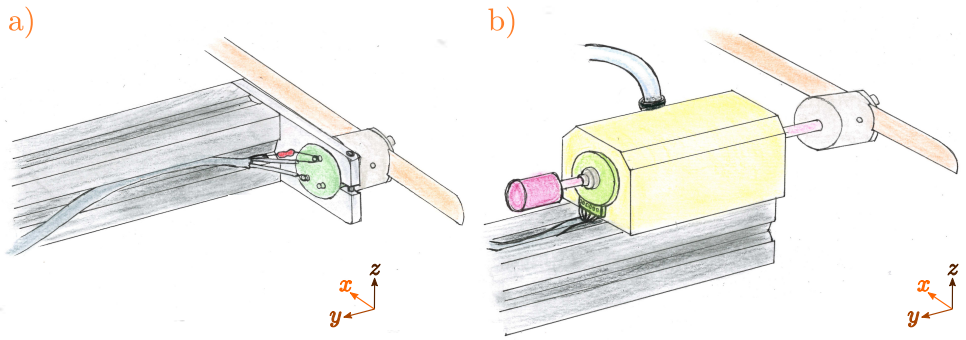

Figure 17: a)Potentiometer setup. The potentiometer is in green and the resistance of the voltage divider in red.
b)Frictionless swivel. The air bearing in yellow is provided with compressed air in blue. The electric encoder is in green, the shaft in pink and the counterweight in magenta.
For both figures, the pendulum is represented in brown with only its rod continuing in the x-direction.

The first swivel system, used in Chapters 1 (for the dynamical visualization) and 5, is a potentiometer. Through a voltage divider, it measures the angle by the variation of resistance with analog acquisition. A schematic view of the setup is presented in Fig. 17.a. The potentiometer has the advantage of being simple both in its use and installation. It yet needs calibration to retrieve what angle corresponds to which voltage. Moreover, due to inner bearings, solid friction arises, especially when the other forces on the pendulum are not particularly important. The solid friction coefficient was estimated at $0.72\,\mathrm{s}^{-2}$, for a natural pulsation of the pendulum of about $6.7\,\mathrm{s}^{-1}$ (black line in Fig. 18. Another drawback of the potentiometer is its sensitivity to electromagnetic noise, which requires the data to be filtered to some extent.

To compensate the aforementioned flaws, we changed the swivel into a frictionless system. Instead of the potentiometer, the support is an OAV air-bushing, OAV $16 \times 4\,\mathrm{mm}$ thrust air bushing. The pendulum is mounted on a shaft going through the bushing and suspensed frictionless on compressed air, maintained at a pressure of about 80 psi, described in Fig. 17.b. To measure the angular position, a Netzer® DS-25 17-bit digital encoder is appended to the end of the air bushing. This encoder provides with absolute angular measurement, however through digital acquisition, which had to be considered in the acquisition system controlled in LabView®. In particular, synchronicity between the analog and digital acquisition was achieved by imposing a master clock 40 times higher than the acquisition frequency to communicate to the encoder and get the 17 bits of data on the ticks of the master clock , set off by a slave clock at the frequency of acquisition. The delicate alignment of the encoder and the bushing may cause a bit of solid friction at some positions, though way lower than the one of the potentiometer.

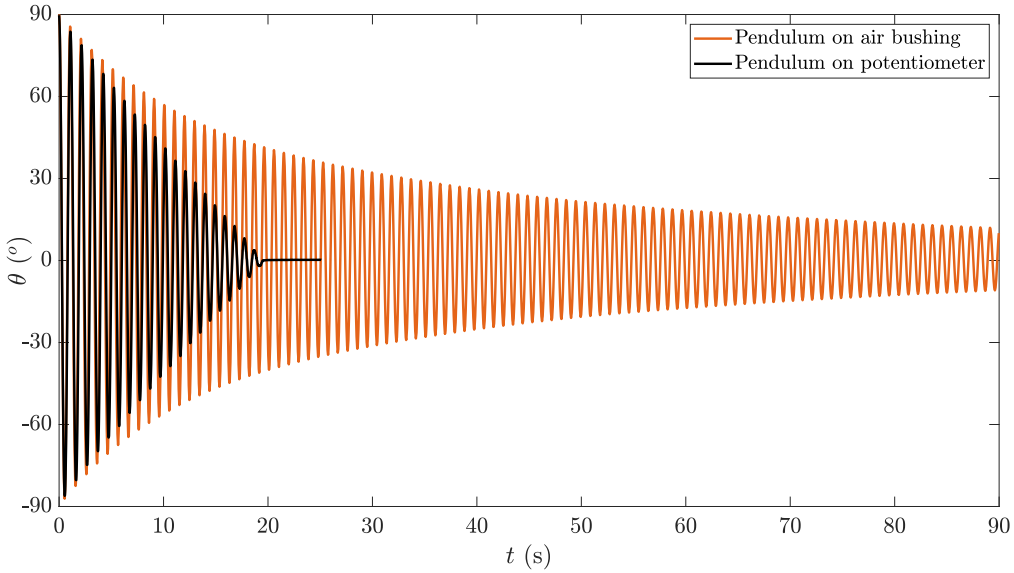

Figure 18: Pendulum dynamics without wind for both configurations, with potentiometer and with air bushing. With the potentiometer, the solid friction is highlighted by the linear decrease of the oscillation amplitude. On the contrary, the air bushing induces a light exponential damping.

The pendulum dynamics without the flow though only present fluid damping (about $0.05\,\mathrm{s}^{-1}$ at its maximum) as shown in Fig. 18. It is however difficult to conclude on the origin of the fluid damping as it can either emanate from the air bushing or from

the movement of the pendulum itself. A slight change of slope is observed on the exponential decrease thus leading us to consider that both damping terms play a role on the dynamics though not in the same amplitude range. A possible explanation would be that at high amplitude, the movement of the pendulum induces more drag that at low amplitude. The air bushing damping however kicks in as the motion become steadier and of smaller amplitude.

Due to the swivel system becoming larger, thus making more fluctuations downstream, the pendulum is deported slightly and a counterweight is added to the shaft to minimize its bending and support the alignment.

0.4.1.4 *Noise reduction on signal acquisition*

Discussing the swivel of the pendulum, we mentioned that electronic noise was observed on the potentiometer and removed by changing to the digital encoder. However, a few other steps have been taken to reduce the potentiometer sensitivity to noise, prior to changing the whole swivel of the pendulum. A time series example of the electronic noise faced by the potentiometer is presented in Fig. 19.a. The signal shows great amplitude of fluctuations with periodic intensity and beat as superposition of multiple noise frequencies. It is difficult from this signal to differentiate the electronic fluctuations from real oscillations of the system. It was thus important to reduce the noise to a point where the true signal would be evident and only minimal filtering would be necessary to get angular velocity and acceleration.

As electronic noise can be radiating from a device or directly polluting the electrical ground, multiple approaches can be followed to reduce it. A first reduction can be achieved by using armored cables from the potentiometer to the acquisition device, with the armor connected to the ground as a protection against radiative noise. This was not conclusive and, as we identified the motor controller to be the main source of noise, we went a step further by dissociating the potentiometer acquisition from the motor control, which was aiming from the same NI PXI-chassis. This is particularly important when the electronic noise is suspected on the ground and cannot be countered through a floating ground and ground loops are unavoidable.

To dissociate the electrical circuits, various options are available, like opto-isolators or inductive isolation amplifiers. In both cases, the incoming signal is modulated into a LED or current signal then transmitted to a separated circuit for demodulation. The separation is physical, with a dielectric barrier. For opto-isolators, the signal is received by a phototransistor which then reconstruct the initial signal on the new circuit. In the case of inductive isolation, the signal is transmitted by induction as in transformers. In both cases, the noise is reduced by galvanic isolation between the acquisition and control circuit. In Fig. 19.b), we implemented a Texas Instruments ISO124P isolation amplifier between the potentiometer and the acquisition system, which drastically reduced the noise on the signal.

This method, though quite efficient if we compare Fig. 19.a) and b), has the disadvantage of requiring constant voltage sources for the amplifiers and separated from the motor controller. The voltage sources we decided on were thus electric batteries but as they get consumed, the signal would no longer get transmitted entirely and it was not a sustainable solution against the noise – the batteries needed change approximately

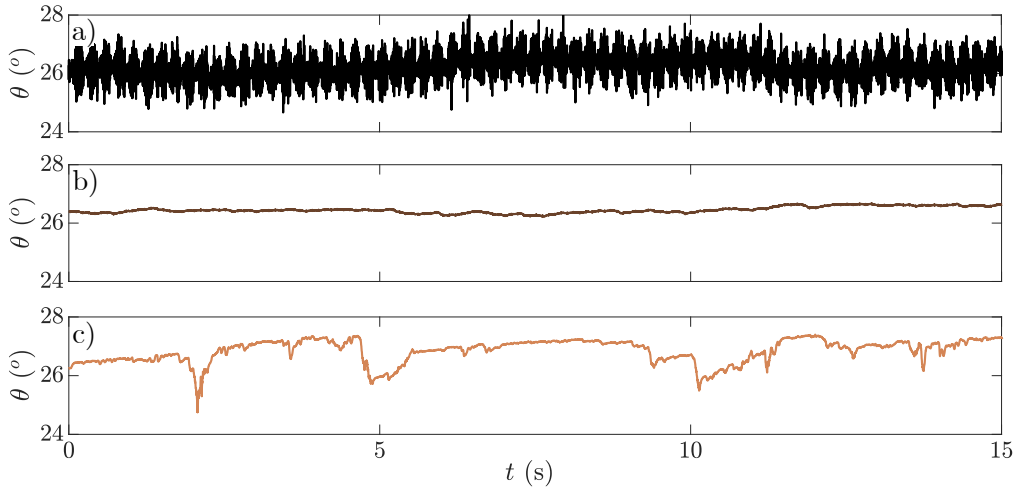

Figure 19: Angular time series examples at fixed flow velocity, for $\theta \simeq 26.5°$ acquired in different experimental conditions with the potentiometer. a) Potentiometer with initial motor controller and without any protection. b) Potentiometer with initial motor controller and protection through isolation amplifier. c) Potentiometer with final motor controller and without any protection.

every 3 weeks of constant use, as could happen when investigating the pendulum transitions in part ii.

Hence, among the various changes brought to the wind tunnel during this thesis, the motor controller was also replaced for a better isolated one and in particular less-radiating. As can be observed in Fig. 19.c, the level of electrical noise after the change of controller and without any protection is the same as when protected by the isolation amplifier (Fig. 19.b). The difference in the amplitude of fluctuation is due to the time series corresponding to a different (larger) pendulum than the 2 first signals. This last signal reinforced the principal origin of the noise faced at the start of this thesis (Fig. 19.a) to be the motor controller.

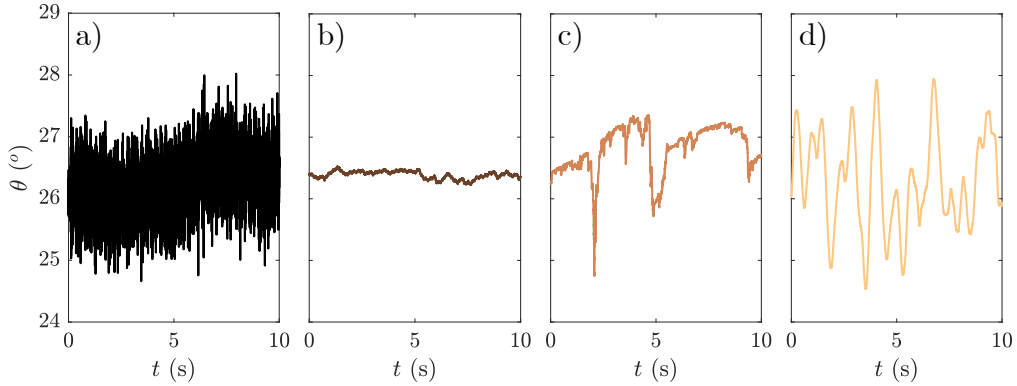

Figure 20: Angular time series examples at fixed flow velocity, for $\theta \simeq 26.5°$ acquired in different experimental conditions with the potentiometer. a) Potentiometer with initial motor controller and without any protection. b) Potentiometer with initial motor controller and protection through isolation amplifier. c) Potentiometer with final motor controller and without any protection. d) Netzer DS-25 17-bit digital acquisition.

With the potentiometer, the signal is still electrically noisy as in Fig. 19, no signal is really smooth. This is however not the case with the digital encoder as presented in Fig. 20. Here, not only is the signal smoother, it also shows greater low frequency dynamics. This results from the removal of the solid friction on the swivel through the air bushing which was illustrated in Fig. 18. Fig. 20.c) also present higher low frequency fluctuations as the disk used for this signal is larger, thus providing a greater aerodynamic torque and thus less affected by solid friction.

0.4.1.5 *PIV setup*

In addition to the angular recording and the time-averaged flow measurements, Particle Image Velocimetry (PIV) has been implemented in the wind tunnel to enable flow visualization in the wake of the pendulum. This flow visualization is done in the transverse (y, z) plane. This choice was in particular motivated by the tri-dimensionality of the wake for pendulums of aspect ratio close to 1 [42].

This methodology largely used in research and industry consists in visualizing the flow by seeding it with particles and calculating their displacement between two (or more) consecutive images. Here is only discussed the PIV setup (see Figure 21) and further details on the method and how to proceed with PIV measurements will be presented later in this introduction.

To do PIV in air flows, one of the difficulties is the choice of the seeding particle. As we want to trace down flow structures, the ideal seeding particles are small and iso-dense. A dimensionless parameter, the Stokes number gives a criterion on the choice of tracer particles: $\mathrm{S_t} = \frac{d^2 \rho_p}{18 \nu \rho_f} \ll 1$, with d the diameter of the particle, ρ_p its density, ν the kinematic viscosity of the fluid and ρ_f its density. Usually in the air, two types of particles are chosen from, smoke droplets, which size a few microns, and helium bubbles, of about $100\,\mu$m, which both verify the aforementioned condition on $\mathrm{S_t}$. In this thesis, only smoke has been used, as the flow velocity is high enough to sustain them long enough to get homogeneously spread, despite their density higher than air. Helium bubbles can be achieved to be iso-dense, so very useful in still air, but require a more complex experimental setup. The smoke is produced by a smoke machine, like that of a discotheque.

To see the particles in a plane, we illuminate them with a laser sheet. This sheet is produced by aligning a high-power (5 W) blue laser LED and a Powell lens with a 30° fan angle. To enhance the light intensity, such setup is placed and aligned on both sides of the wind tunnel, totaling a light power of 10 W.

For the visualization, a high-speed camera (Phantom v26.40) films the particles flowing in the laser-sheet plane, which can film at up to 24 000 fps in full frame. As we chose to visualize the transverse flow (in the y, z-plane), the particles only last a brief instant in the sheet and as such the frame rate is however constrained by the flow velocity, the thickness of the plan and the light intensity.

When looking at the transverse structure in a forward flow, especially seeded with particles, it is usually unwise to place the camera perpendicular to the plane of sight, for two reasons. One is that the camera will then most likely be inside the wind tunnel (or water tunnel) which can be quite hazardous for the camera guarantee. The other is

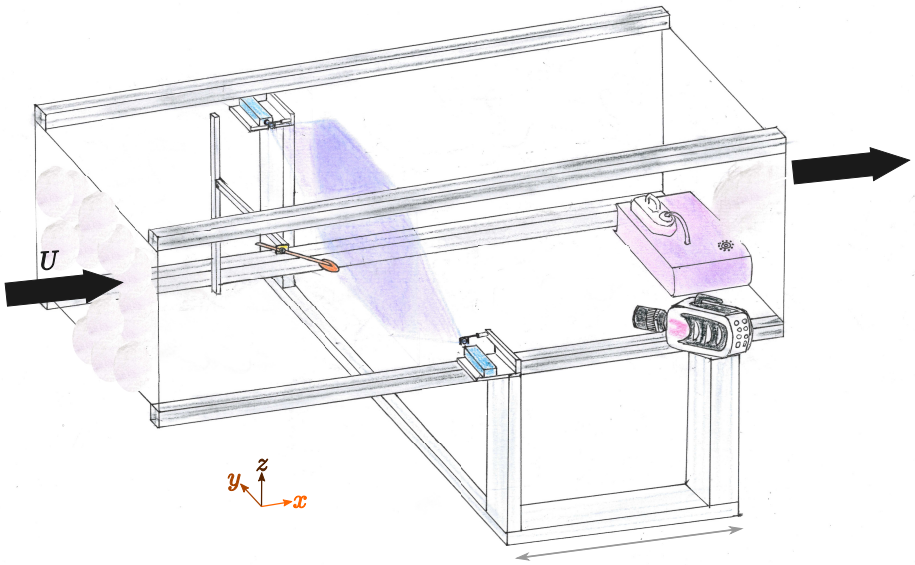

Figure 21: Schematic view of the PIV setup. The laser sheet (in violet-blue) is joined together with the camera and mounted on a translating platform. This enables a longitudinal scan of the wake without changing the optical settings nor calibration. The smoke (light violet) is produced behind the pendulum and directly advected by the flow. It comes around as the wind tunnel is closed and goes through the honey comb and diffuses enough to be considered homogeneous after experiencing such conditioning about 3 to 4 times.

that due to forward scattering by the particle, the maximal light intensity is not found facing the laser sheet. Hence, the camera is placed outside of the wind tunnel, with an angle to the plane of view, as presented in Fig. 21. This however induces an optical difficulty, the plane of focus is not parallel to the laser sheet anymore.

This problem can be solved in two manners. The first one is to close the diaphragm to enlarge the depth of field to the projected thickness of the sheet orthogonal to the plane of focus. Yet such option is only desirable when there is an excess of light as well. Since we already commented on the constraint in light intensity, this solution is not satisfying. The second option uses an optical principle, the Scheimpflug principle, named after Austrian army captain T. Scheimpflug who spread it for aerial photography, though not the initial discoverer. By tilting the lens, and thus making an angle not only between the camera sensor and the laser sheet but also between the camera sensor and the lens, the plane of focus is no longer parallel to the sensor. Hence by adjusting the angle between the lens and the camera sensor, it is possible for the plane of focus to collapse on the laser sheet with maximal aperture on the lens. The condition for such adjustment is that the planes of the laser sheet, the sensor and the lens coincide on one line.

As such, the optical setup for the PIV consists in a 100 mm lens appended through a Scheimpflug structure to the Phantom v26.40 high-speed camera. Mainly two acquisition frequencies have been selected for the study, 2000 fps at low flow velocity and 4000 fps at higher flow velocity.

0.4.2 *PIV Methodology*

To reconstruct the flow field from the video, a few steps are required. The principle behind Particle Image Velocimetry is the estimation of the local displacement through the correlation of two consecutive images. By subdividing the image into small interrogation windows, the average particle displacement $(\Delta x, \Delta y)$ is determined by cross-correlation with the localization of the correlation peak (see Fig. 22). The velocity components (u, v) are retrieved by a calibration which we detail hereafter.

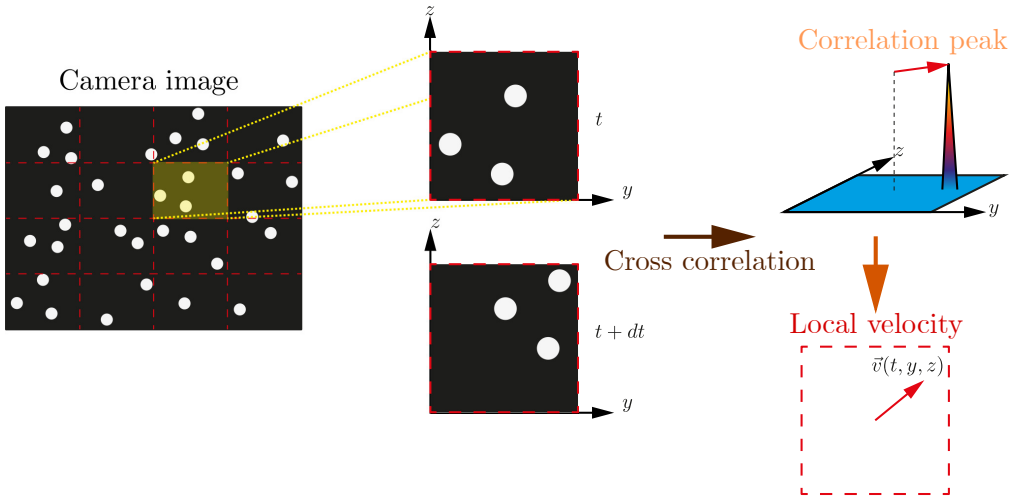

Figure 22: Schematic representation of the algorithm used for Particle Image Velocimetry. (Courtesy: Samuel Bera)

Before even starting the PIV algorithm, a pre-treatment of the video is necessary. Indeed, as shown in Fig. 23.a), the original image has a low ratio signal over noise due to the presence of the background. To enhance this ratio, the mean image (over the whole duration of recording) is subtracted to all images, which gives Fig. 23.b. After this subtraction, a two-dimensional gaussian filter is applied to further smooth the background and bring out the particles. On this image, the particles are quite visible individually, thus enabling a better correlation for the PIV than with the initial images.

Once the pre-treatment is done on the whole video, the PIV is then conducted on the Matlab toolbox uvmat developed at the LEGI in Grenoble. This toolbox provides with a two-steps PIV, with a refining of the grid between both correlations. For instance, the used parameters in the different PIV results we will present in the following chapters are for the first PIV: grid boxes of 25×25 px^2 with a correlation zone of 55×55 px^2. The second PIV refines the grid to boxes of 21×21 px^2, with a correlation zone of only 27×27 px^2 however located in the direction of the displacement estimation from the first PIV. In between the two PIV computations, false vectors are also removed to help the second PIV and the flow is interpolated in such regions of false vectors. The obtained raw flow field is shown in Fig. 23.c.

Without any calibration, the flow field provided by the PIV algorithm presents velocities of pixels per time step (which are by no mean units of the International System). While the correspondence in time step is simple once the frequency of acquisition is

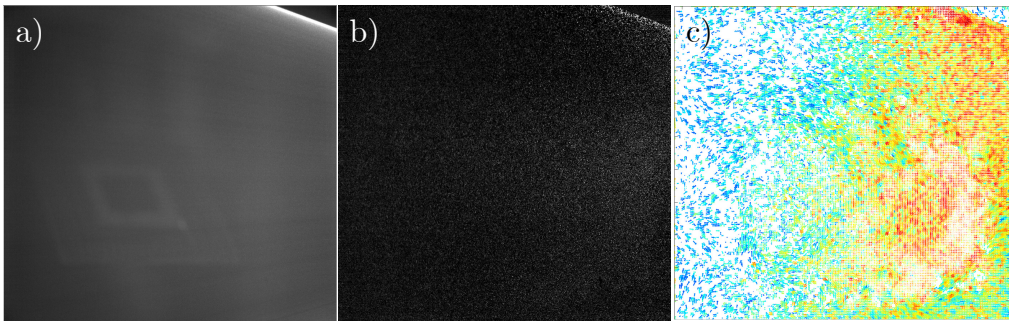

Figure 23: a) Original image from the camera. b) Pre-treated image, subtracting the mean value over the whole video. c) Correlated image resulting from Matlab toolbox uvmat.

known, the spatial calibration needs a bit more work. To achieve it, we use a calibration plate on which is patterned with an array of regularly spaced dots. This calibration plate is placed in the visualization plane for a calibration image done before the first experiment. In case a possible modification on the visualization setup during the experiments is suspected, a second calibration can be done afterwards to ensure the best possible conversion from pixels to coordinates in the real world.

Once the flow is calibrated, it might still need some filtering in particular to compute vorticity or acceleration. A gaussian filtering has been proceeded with for instance in Chapter 1 to estimate the intensity of the wingtip vortices behind the disk. Another post-treatment on the calibrated flow is the removal of mean background flow field. In particular, because of the thickness of the laser sheet and the plane of focus not parallel to it, the horizontal displacement presents a drift v_{par} of about $1\,\mathrm{m}\cdot\mathrm{s}^{-1}$ for a flow velocity of about $2\,\mathrm{m}\cdot\mathrm{s}^{-1}$. This drift is due to parallax. To remove this drift, an acquisition without the pendulum has been done. This estimation of the drift is however not perfect due to the velocity drop behind the disk. As such, the acquisition without the pendulum overestimates the drift as it is proportional to the local streamwise flow velocity. This drift is mostly inconvenient when calculating vorticity due to a slight horizontal gradient over the span of visualization. Figure 24 presents an example of the drift and the filtering of the horizontal velocity v ahead of the calculation of vorticity presented in Chapter 1.

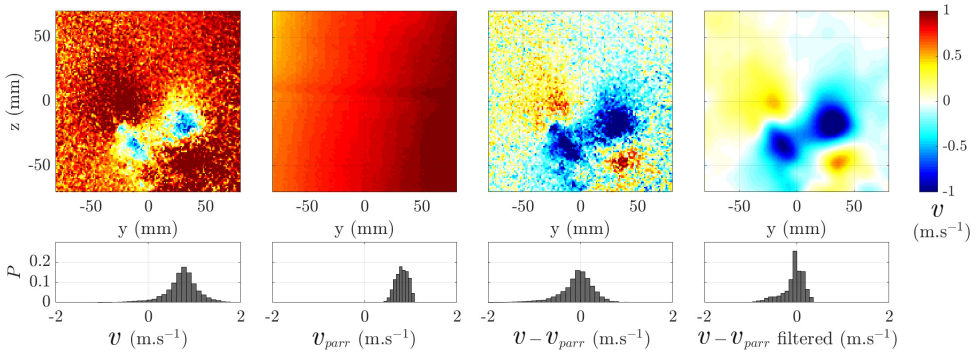

Figure 24: Different stages of the pre-treatment for the horizontal velocity v field before the computation of vorticity, with the subtraction of the parallax contribution v_{par} and gaussian filtering. (Courtesy: Samuel Bera)

The various methods of exploiting the PIV measurements will be discussed in the relevant chapters, in particular 1 and 5.

As we mentioned before, the description of the experimental setup presented here only covers the commonalities throughout the chapters and each modification to it will be notified at the beginning of the concerned chapter.

0.4.3 *Synthesis of the experimental setup*

As we will present various experiments throughout this thesis, a summary of the configurations that were used in each chapter is presented hereafter in Tab. 2 and we invite the reader to refer to it whenever he has a doubt on the exact experimental setup for a particular chapter.

Chapter	1	2	3	4	5	6
4 cm-pendulum (standard)				★	★	★
6 cm-pendulum on short rod (PIV)	★			★		
Other pendulums		★	★	★		★
Potentiometer	★			★	★	
Air bushing		★	★	★		★
Particle Image Velocimetry	★		★		★	

Table 2: Configurations of pendulum, support and PIV setups used in the different chapters. The configurations used in one chapter are indicated by a ★ symbol.

REFERENCES

[1] W. Shyy et al. *Aerodynamics of Low Reynolds Number Flyers*. Cambridge: Cambridge University Press, 2008.

[2] A. D. Ruck. "Gliding in Bats." In: *Nature* 157 (1946), p. 304.

[3] C. Le Roy et al. "Adaptive evolution of flight in Morpho butterflies." In: *Science* 374.6571 (Nov. 2021), pp. 1158–1162.

[4] J. Bell et al. "Ballooning dispersal using silk: world fauna, phylogenies, genetics and models." In: *Bulletin of Entomological Research* 95.2 (2005), pp. 69–114.

[5] V. A. Tucker and G. C. Parrott. "Aerodynamics of Gliding Flight in a Falcon and Other Birds." In: *Journal of Experimental Biology* 52.2 (Apr. 1970), pp. 345–367.

[6] C. P. Ellington. "Limitations on Animal Flight Performance." In: *Journal of Experimental Biology* 91 (1991), pp. 71–91.

[7] D. D. Chin and D. Lentink. "Flapping wing aerodynamics: From insects to vertebrates." In: *Journal of Experimental Biology* 219.7 (2016), pp. 920–932.

[8] I. J. Lovette and J. W. Fitzpatrick. *Handbook of Bird Biology*. Cornell Lab of Ornithology. Wiley, 2016.

[9] S. P. Sane. "The aerodynamics of insect flight." In: *Journal of Experimental Biology* 206.23 (Dec. 2003), pp. 4191–4208.

[10] J. R. Usherwood et al. "High aerodynamic lift from the tail reduces drag in gliding raptors." In: *The Journal of experimental biology* 223 (2020).

[11] P. L. Richardson. "How do albatrosses fly around the world without flapping their wings?" In: *Progress in Oceanography* 88.1-4 (Jan. 2011), pp. 46–58.

[12] J. Videler and A. Groenewold. "Field Measurements of Hanging Flight Aerodynamics in the Kestrel Falco Tinnunculus." In: *Journal of Experimental Biology* 155.1 (Jan. 1991), pp. 519–530.

[13] D. Warrick et al. "Hummingbird flight." In: *Current Biology* 22.12 (June 2012), R472–R477.

[14] B. W. Tobalske et al. "Three-dimensional kinematics of hummingbird flight." In: *Journal of Experimental Biology* 210.13 (July 2007), pp. 2368–2382.

[15] I. G. Ros et al. "Pigeons steer like helicopters and generate down- and upstroke lift during low speed turns." In: *Proceedings of the National Academy of Sciences* 108.50 (Dec. 2011), pp. 19990–19995.

[16] B. W. Tobalske. "Avian Flight." In: *Handbook of Bird Biology, 3rd Edition*. Cornell Lab of Ornithology. Wiley, 2016, pp. 149–167.

[17] L. A. Miller and C. S. Peskin. "A computational fluid dynamics of 'clap and fling' in the smallest insects." In: *Journal of Experimental Biology* 208.2 (Jan. 2005), pp. 195–212.

[18] M. Cho. "Aerodynamics and the role of the earth's electric field in the spiders' ballooning flight." In: *Journal of Comparative Physiology A* 207.2 (2021), pp. 219–236.

[19] V. A. Tucker. "Gliding Birds: Reduction of Induced Drag by Wing Tip Slots between the Primary Feathers." In: *Journal of Experimental Biology* 180.1 (July 1993), pp. 285–310.

[20] C. P. Ellington et al. "Leading-edge vortices in insect flight." In: *Nature* 384.6610 (Dec. 1996), pp. 626–630.

[21] J. J. Videler, E. J. Stamhuis, and G. D. E. Povel. "Leading-Edge Vortex Lifts Swifts." In: *Science* 306.5703 (Dec. 2004), pp. 1960–1962.

[22] D. Lentink and M. H. Dickinson. "Rotational accelerations stabilize leading edge vortices on revolving fly wings." In: *Journal of Experimental Biology* 212.16 (Aug. 2009), pp. 2705–2719.

[23] Z. J. Wang and D. Russell. "Effect of Forewing and Hindwing Interactions on Aerodynamic Forces and Power in Hovering Dragonfly Flight." In: *Physical Review Letters* 99.14 (Oct. 2007), p. 148101.

[24] D. F. Greene and E. A. Johnson. "The Aerodynamics of Plumed Seeds." In: *Functional Ecology* 4.1 (1990), pp. 117–125.

[25] A. Rosen and D. Seter. "Vertical Autorotation of a Single-Winged Samara." In: *Journal of Applied Mechanics* 58.4 (Dec. 1991), pp. 1064–1071.

[26] A. Azuma and Y. Okuno. "Flight of a samara, Alsomitra macrocarpa." In: *Journal of Theoretical Biology* 129.3 (Dec. 1987), pp. 263–274.

[27] C. Cummins et al. "A separated vortex ring underlies the flight of the dandelion." In: *Nature* 562.7727 (Oct. 2018), pp. 414–418.

[28] S. J. Lee, E. J. Lee, and M. H. Sohn. "Mechanism of autorotation flight of maple samaras (Acer palmatum)." In: *Experiments in Fluids* 55.4 (Apr. 2014), p. 1718.

[29] D. Lentink et al. "Leading-Edge Vortices Elevate Lift of Autorotating Plant Seeds." In: *Science* 324.5933 (June 2009), pp. 1438–1440.

[30] H. J. Williams et al. "Physical limits of flight performance in the heaviest soaring bird." In: *Proceedings of the National Academy of Sciences* 117.30 (July 2020), pp. 17884–17890.

[31] W. J. McCroskey, L. W. Carr, and K. W. McAlister. "Dynamic stall experiments on oscillating airfoils." In: *AIAA J.* 14.1 (1976), p. 57.

[32] M. La Mantia and P. Dabnichki. "Added mass effect on flapping foil." In: *Engineering Analysis with Boundary Elements* 36.4 (2012), pp. 579–590.

[33] N. Chiereghin, D. J. Cleaver, and I. Gursul. "Unsteady lift and moment of a periodically plunging airfoil." In: *AIAA Journal* 57.1 (2019), pp. 208–222.

[34] E. Chang et al. "Soft biohybrid morphing wings with feathers underactuated by wrist and finger motion." In: *Science Robotics* 5.38 (Jan. 2020).

[35] T. Nakata et al. "Aerodynamics of a bio-inspired flexible flapping-wing micro air vehicle." In: *Bioinspiration & Biomimetics* 6.4 (Dec. 2011), p. 045002.

[36] S. F. Hoerner. *Fluid-Dynamic Drag*. 1965.

[37] M. Obligado, M. Puy, and M. Bourgoin. "Bi-stability of a pendular disk in laminar and turbulent flows." In: *J. Fluid Mech.* 728 (2013), R2.

[38] O. Flachsbart. "Messungen an ebenen und gewölbten Platten." In: *Ergebnisse der Aerodynamischen Versuchsanstalt zu Göttingen - IV. Lieferung*. München und Berlin: Verlag von R. Oldenburg, 1932, pp. 96–100.

[39] G. B. McCullough and D. E. Gault. *Examples of three representativ types of airfoil-section stall at low speed*. Tech. rep. National ADVISORY Committee For Aeronautics, 1951, p. 52.

[40] J. R. Spreiter and A. H. Sacks. "The Rolling Up of the Trailing Vortex Sheet and Its Effect on the Downwash Behind Wings." In: *Journal of the Aeronautical Sciences* 18.1 (Jan. 1951), pp. 21–32.

[41] X. Tian et al. "Flow around an oscillating circular disk at low to moderate Reynolds numbers." In: *Journal of Fluid Mechanics* 812 (2017), pp. 1119–1145.

[42] S. Gao et al. "Flow around an inclined circular disk." In: *J. Fluid Mech.* 851 (Sept. 2018), pp. 687–714.

[43] E. N. d. C. Andrade. "Wilkins Lecture - Robert Hooke." In: *Proceedings of the Royal Society of London. Series A. Mathematical and Physical Sciences* 201.1067 (May 1950), pp. 439–473.

[44] J. l. R. D'Alembert. "Manière de déterminer par les expériences du pendule la résistance des Fluides, lorsque la vitesse est fort petite." In: *Théorie de la résistance des fluides*. 1752, pp. 115–122.

[45] F. Baily. "On the Correction of a Pendulum for the Reduction to a Vacuum: together with Remarks on some anomalies observed in Pendulum experiments." In: *Philosophical Transactions of the Royal Society of London* 122 (1832), pp. 399–492.

[46] G. G. Stokes. "On the Effect of the Internal Friction of Fluids on the Motion of Pendulums." In: *Mathematical and Physical Papers*. Vol. 88. 2208. Cambridge: Cambridge University Press, 1912, pp. 1–10.

[47] S. D. Poisson. "Mémoire sur les mouvements simultanés d'un pendule et de l'air environnant." In: *Mémoires de l'Académie Royale des Sciences de l'Institut de France*. Vol. 11. 1831, pp. 521–581.

[48] G. A. A. Plana. *Mémoire sur le mouvement d' un pendule dans un milieu résistant*. Turin: Á L' Imprimerie Royale, 1835, 167 p.

[49] A. Bossut. *Traité théorique et expérimental d'hydrodynamique (tome second)*. Imprimerie. Paris, 1787.

[50] S. Vince. "The Bakerian Lecture . Experiments upon the Resistance of Bodies Moving in Fluids ." In: *Philosophical Transactions of the Royal Society of London* 88 (1798), pp. 1–14.

[51] N. C. Duchemin. "Recherches expérimentales sur les lois de la résistance des fluides." In: *Mémorial de l'Artillerie n° V*. Bachelier, 1842.

[52] G. Eiffel. "Sur la résistance des plans rectangulaires frappés obliquement par le vent." In: *Comptes-rendus hebdomadaires des séances de l'Académie des Sciences* 151 (1910), pp. 979–981.

[53] O. Föppl. "Windkräfte an ebenen und gewölbten Platten." PhD thesis. Berlin, Heidelberg: Königlichen Technischen Hochschule zu Aachen, 1911.

[54] L. Prandtl and A. Betz. *Ergebnisse der Aerodynamischen Versuchsanstalt zu Göttingen - IV. Lieferung*. Ed. by L. Prandtl and A. Betz. Vol. 7. Göttinger Klassiker der Strömungmechanik. Göttingen: Göttingen University Press, 1935.

[55] I. E. Idel'chik. "Handbook of hydraulic resistance (3rd edition)." In: *Handbook of hydraulic resistance* (1960), p. 517.

[56] J. S. Russell. "On the Vibration of Suspension Bridges and other Structures; and the Means of preventing Injury from this Cause." In: *Transactions of the Royal Scottish Society of Arts*. 1841, pp. 304–314.

[57] Y. C. Fung. *An Introduction to the Theory of Aeroelasticity*. Dover Books on Aeronautical Engineering. Dover Publications, 2008.

[58] R. D. Blevins. *Flow-induced Vibration*. Van Nostrand Reinhold, 1990.

[59] J. P. D. Hartog. "Transmission Line Vibration Due to Sleet." In: *Transactions of the American Institute of Electrical Engineers* 51.4 (Dec. 1932), pp. 1074–1076.

[60] C. Scruton and E. Rogers. "Steady and unsteady wind loading of buildings and structures." In: *Philosophical Transactions of the Royal Society of London. Series A, Mathematical and Physical Sciences* 269.1199 (May 1971), pp. 353–383.

[61] S. C. Crow. "Stability theory for a pair of trailing vortices." In: *AIAA Journal* 8.12 (Dec. 1970), pp. 2172–2179.

[62] S. E. Widnall, D. B. Bliss, and C.-Y. Tsai. "The instability of short waves on a vortex ring." In: *Journal of Fluid Mechanics* 66.1 (Oct. 1974), pp. 35–47.

[63] H. Muttray. *Investigations on the amount of downwash behind rectangular and elliptical wings*. Tech. rep. National Advisory Committee for Aeronautics, 1932, p. 24.

[64] C. Scruton. "Wind Effects on Structures." In: *Proceedings of the Institution of Mechanical Engineers* 185.1 (June 1970), pp. 301–317.

[65] M. van Dyke. *An Album of Fluid Motion*. The Parabolic Press, 1982, p. 177.

[66] D. Marshall and T. E. Stanton. "On the Eddy System in the Wake of Flat Circular Plates in Three Dimensional Flow." In: *Proceedings of the Royal Society A: Mathematical, Physical and Engineering Sciences* 130.813 (Jan. 1931), pp. 295–301.

[67] J. R. Calvert. "Experiments on the flow past an inclined disk." In: *Journal of Fluid Mechanics* 29.04 (Sept. 1967), pp. 691–703.

[68] A. G. Tomboulides and S. A. Orszag. "Numerical investigation of transitional and weak turbulent flow past a sphere." In: *Journal of Fluid Mechanics* 416 (Aug. 2000), pp. 45–73.

[69] C. M. Rhie and W. L. Chow. "Numerical study of the turbulent flow past an airfoil with trailing edge separation." In: *AIAA Journal* 21.11 (Nov. 1983), pp. 1525–1532.

[70] A. R. Shenoy and C. Kleinstreuer. "Flow over a thin circular disk at low to moderate Reynolds numbers." In: *Journal of Fluid Mechanics* 605 (June 2008), pp. 253–262.

[71] D. Bolster, R. E. Hershberger, and R. J. Donnelly. "Oscillating pendulum decay by emission of vortex rings." In: *Physical Review E* 81.4 (Apr. 2010), p. 046317.

[72] A. Orchini, H. Kellay, and A. Mazzino. "Galloping instability and control of a rigid pendulum in a flowing soap film." In: *Journal of Fluids and Structures* 56 (2015), pp. 124–133.

[73] V. Mathai et al. "Dynamics of heavy and buoyant underwater pendulums." In: *J. Fluid Mech* 862 (2019), pp. 348–363.

[74] C. G. Lomas. *Fundamentals of Hot Wire Anemometry*. Cambridge University Press, 2011, p. 224.

Part I

WAKING UP

1

DESCRIBING THE WAKE BEHIND AN INCLINED DISK

Knowing the structure of the wake, what information on the aerodynamic coefficients can we extract?

1.1 INTRODUCTION

"Tell me what your wake is and I will tell you who you are."

This aphorism is the aspiration of many aerodynamicists, hydrodynamicists and engineers. It still remains a pipe dream as our understanding of the wake is still far from sufficient. The closest living thing to being able to say this is in fact the true seal. True seals (from the *Phocidae* family) are indeed capable of identifying and following preys from their sole wake signature, as they often live and hunt in turbid waters [1, 2]. This characteristic comes from a specific evolution of their whiskers. In particular, the shape of a seal whisker presents a wavy structure that has been observed to cut down self-generated vortex-induced vibration [3]. This enables the seal to keep a high signal-to-noise ratio on sensory clues even when moving around in the water. Though the sensory mechanism to distinguish different preys or predators is still under investigation, bio-inspired flow control devices have been emerging over the last decade for reducing vortex-induced vibration [4].

Far from these marine considerations, the wake is an important feature to characterize any object moving in a flow, from a fish to a vehicle or a bird. While it is undeniable that wake and aerodynamic efforts are strongly coupled together, the understanding of their coupling is still in its early stages, in particular the influence of coherent structures on lift and drag coefficients [5]. Part of the difficulty to understand the wake development and structure comes from its intrinsic simplicity and yet fundamental complexity. A wake is mostly constituted by three types of vortices, as already introduced in Fig. 3:

- the leading-edge vortex,
- the trailing-edge vortex,
- the wingtip vortices, also known as trailing vortices.

Due to the semantic similarity between "trailing vortices" and "trailing-edge vortex", in the following, the term wingtip vortices *will be preferred to avoid any confusion on that regard.*

The simplicity comes from the fact that with this elementary decomposition, all wakes are quite similar in their overall shape. The complexity of the wake arises from the plurality of its shedding frequencies, the complex self-evolution or interactions between the vortices, such as recombination, breakup, etc.

In animal flight, we already mentioned the importance of the leading-edge vortex for insects and flight stability for birds and mammals [6, 7]. The leading-edge vortex is particularly prominent for wide-spanned object, which can be considered almost $2D$ like glider wings. Lift estimates from the leading-edge vortex have been proposed both empirically and following the Kutta-Joukowski theorem for flow circulation [8, 9]. However, when the tri-dimensionality of the wing or object comes into play, the wake structure incorporates the wingtip vortices and the leading-edge vortex loses intensity to them.

Especially evident at low angles of attack with two intense vortices in the transverse plane, the importance of the wingtip vortices is fully considered in Prandtl lifting-line theory for finite-span wings. This theory extends the Kutta-Joukowski theorem to the circulation in the wingtip vortices linked with the leading-edge vortex into a large horseshoe vortex [10]. The estimation of the lift coefficient is then possible depending on the wing spanwise shape, the *wing loading*.

In bird flight, knowing the wake of a bird can help understand its behavior and the evolutionary adaptations that have conducted to the selection of a certain type of flight among those presented in Chapter 0. To probe it, mostly two techniques are available, Particle Tracking Velocimetry (as in Fig. 1.1.a) and Particle Image Velocimetry (PIV), the technique we also use in this chapter. While, in gliding flight, the wake is almost reduced to the wingtip vortices (see Fig. 1.1.a) [11], this is not true in flapping flight. The wake then depends on the flapping motion (upstroke in red or downstroke in blue) but also on the flow velocity, as shown in Fig. 1.1.b) for a thrush nightingale [12]. Because of these dependencies, standard lift calculations based on wake models may differ greatly from experimental measurements [13].

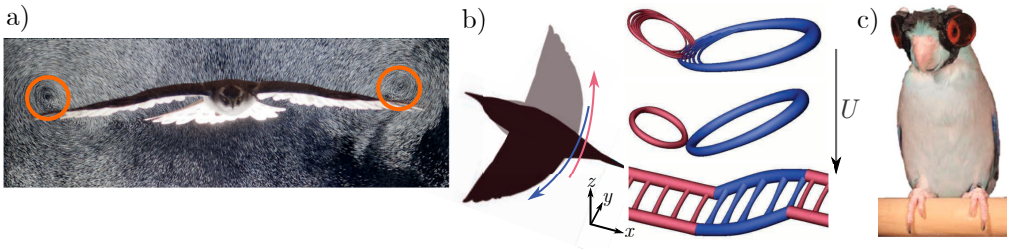

Figure 1.1: a) Wake behind a gliding goshawk (*Accipiter gentilis*), wingtip vortices are highlighted by orange circles [11]. a) Wake structure, represented by isovorticity contours, behind a flapping thrush nightingale (*Luscinia luscinia*) with increasing flow velocity from top to bottom [12]. Red represents the upstroke wake, blue is the downstroke wake. c) Pacific parrotlet (*Forpus coelestis*) with laser safety goggles [13].

As for other bluff bodies like vehicles [14], choosing the plane of visualization, when 2D PIV is performed, is fundamental to reconstruct the wake to its best accuracy. While it is rather simple to change planes with fixed objects, working with living animals makes it much more complicated. In particular, to have the animal fly through a laser sheet for PIV, not only does it require a lot of training but also ethical considerations on possible blinding and harm come into play. As such, most studies on bird wake prefer longitudinal and out of the center planes or have developed special adaptations for transverse wake visualization [15]. For instance, only the far wake is investigated with a second light sheet ahead of the laser, to act as a security – if the bird crosses it, the laser

turns off [16]. Laser goggles have also recently been designed for birds to safely cross laser sheets (see Fig. 1.1.c) [13].

In the context of the PhD work reported in this thesis, the situation is hopefully much easier, since pendulums are inert objects. They only require small adjustments due to their mobility to change the plane of visualization. For instance, if we were to visualize longitudinal flow structures, the motion of the pendulum creates a fluctuating shadow which might reduce the liability of some measurements. Adjustments like mirrors to ensure a total lighting coverage of the system even during motion would thus be required. Within the time frame of this PhD, such adaptations have not been conducted, and only transverse flow considerations will be discussed as introduced in Chapter 0. To get insights on the longitudinal component of the wake, the distance D_{pl} between the pendulum and the laser sheet has been varied (see Chapter 0, Fig. 21) and spatio-temporal diagrams can be exploited in particular for the trailing-edge vortex, as we will present in Chapter 5. Unless D_{pl} is mentioned otherwise, the default distance between the pendulum and the PIV plane is 10 cm.

To study the wake of our disk pendulum, two main directions are presented. First, the mean flow field provides information on the location of the interesting structure. Secondly, the vorticity can be extracted from the flow field to reconstruct wake coherent structures through iso-surfaces, as obtained from numerical simulations [17, 18] and similar to what is observed in water experiments using dye [19–21].

In this chapter, we used a 6 cm-wide disk appended to a 20 cm-long rod. The distance L between the center of the disk and the center of attach has been varied throughout the experiments to change the mean angle of the pendulum while keeping the flow velocity constant for the PIV measurements (typically $2\,\mathrm{m}\cdot\mathrm{s}^{-1}$). The mean field results presented in the following section were obtained with the mobile disk attached with the potentiometer. This mobile disk configuration was first developed to investigate the correlation between the pendulum dynamics and the flow response but this part is still under investigation and will not be discussed here. Only preliminary results of this kind will be presented in section 5.5. For the rest of the chapter, and thus the vorticity considerations, we will consider the case when the pendulum is blocked; the disk is attached at a distance $L = 20\,\mathrm{cm}$ from the support at a fixed angle which can be varied. This allows to investigate the wake of an inclined disk with limited influence of the support. This was necessary to study the whole range of angles from $\theta = 0^\circ$ to $\theta = 90^\circ$, as the latter angle, corresponding to the horizontal, is inaccessible for the pendulum due to the limit $U \to \infty$ as $C_N \xrightarrow{\theta \to 90^\circ} 0$.

1.2 MEAN FLOW FIELD IN THE WAKE

In the case of a wake with two main wingtip vortices, the mean transverse flow field is clearly recognizable as the two vortices are in the transverse plane, as is identified in Fig. 1.1.a. As such, a first overview of the wake structure is naturally to observe the mean flow field for different angles of the pendulum, as shown on the left column in Fig. 1.2. As the angle increases from $\theta = 20^\circ$ to $\theta = 60^\circ$, a slight evolution of the mean flow field is visible, with the intensification of a downward motion, the *downwash*, for coordinates $y \simeq 0$ and $z \in [-30, 0]$. More information on the wake can be extracted in

Fig. 1.2 from the velocity fluctuations v_{rms} along the y-axis (middle column) and w_{rms} (right column) along the z-axis.

In particular, as the wingtip vortices pulse due to the shedding and the trailing-edge and leading-edge vortices induce large fluctuations when crossing the transverse plane, it is possible to identify large structure by the sole velocity fluctuations.

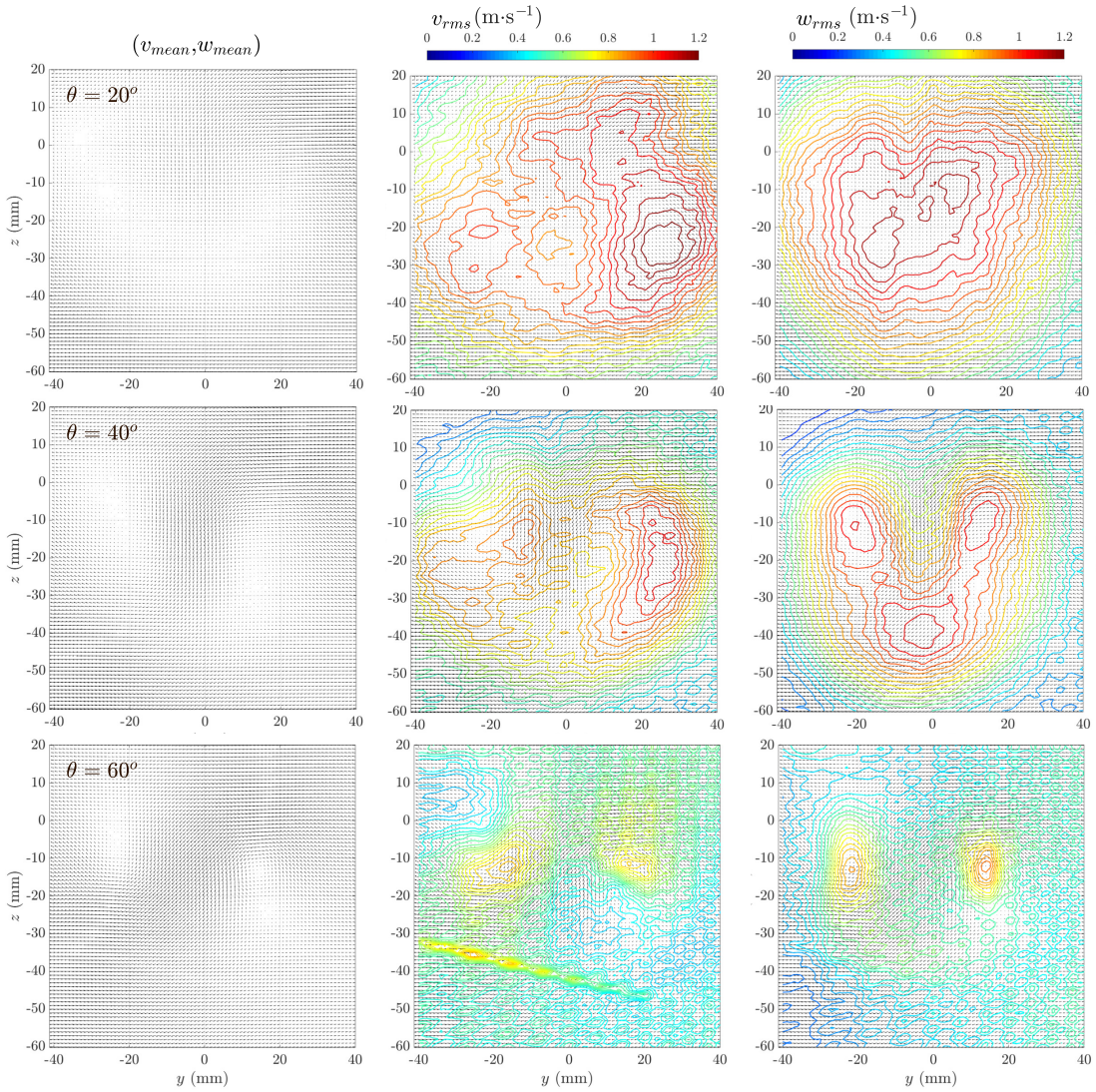

Figure 1.2: Evolution of the wake mean field and fluctuations with the angle of the pendulum θ. From top to bottom: $\theta = 20°$, $\theta = 40°$ and $\theta = 60°$. From left to right: mean field (v_{mean},w_{mean}), transverse velocity fluctuations v_{rms},vertical velocity fluctuations w_{rms}.

For instance, for $\theta = 20°$ (Fig. 1.2 top row), we observe a large almost axisymmetric zone of intense fluctuations (in red) for both transverse and vertical velocities. This observation supports the assumption of a ring vortex structure which sheds from the center of the disk as observed at low Reynolds number in numerical simulations [18].

When $\theta = 40°$ (Fig. 1.2 middle row), the fluctuations are more restrained to two large lobes for the transverse velocity, almost vertically symmetric. On the vertical velocity, the high fluctuations cover a horseshoe region, intersecting with the two lobes of the transverse velocity fluctuations. These two lobes are signatures of the shedding of the

wingtip vortices, as it will be confirmed from the time-evolution of the vorticity. On the other hand, the bottom region of the horseshoe for the vertical velocity marks the existence of a strong trailing-edge vortex. These two considerations suggest an oblique ring vortex which is shed either by its sides or bottom part.

At even higher angles, $\theta = 60°$ for instance (Fig. 1.2 bottom row), the fluctuations for both velocities are concentrated in two small spots at equal distance from the vertical symmetry axis. This seems to point towards a plane-like wake with only the two wingtip vortices.

As the angle θ increases, the fluctuation intensity decreases, especially between $40°$ and $60°$. We will come back on this later, when discussing vorticity evolution with θ. Overall, the shape seems to almost change continuous through the smoothing of its middle vertical line from top to bottom.

Two details were not commented here, on the transverse velocity fluctuations v_{rms}.

The first one is for $\theta = 60°$, a diagonal line of fluctuation is observed from $(y, z) = (-40, -30)$ to $(y, z) = (20, -50)$. This was identified to be experimental artifacts, as during this measurement, a light protection from the laser fell down and a small reflection was later observed on the video.

The second point is the left-right asymmetry of the horizontal fluctuations for $\theta = 20°$ and $\theta = 40°$. Various factors might explain this asymmetry, one physical and three more experimental. As $\theta = 20°$ is close to the vertical, the disk can resemble a bluff body from the flow perspective. It is well-documented that bluff bodies present spontaneous symmetry breaking of the wake with one side predominant over the other [22, 23] and possible switches between each side [24], which will be encountered again in Chapter 4. To verify this possibility, more acquisitions in this configuration would be necessary as we only have 3 s to 6 s of flow dynamics per acquisition.

It might otherwise come from the experimental setup itself. In particular, a possibility is the link between the rod and the disk that could be slightly off the center, enough for the flow to settle in one asymmetrical configuration. Another possible explanation might come from the inhomogeneity of the laser sheet as the flow field is less well-defined on the left part of the image. Due to this, it may underestimate the velocity fluctuations.Finally, it is possible that the left field fluctuations are less intense as the mean value is also lower, due to the non-parallelism of the plane of visualization and the camera sensor, which induces a small gradient of transverse flow velocity as we commented in Chapter 0.

From the mean flow field, other information may be extracted, especially from spatio-temporal diagrams. Yet, the most common way of studying the wake of an object is still to compute the vorticity and discuss its evolution, which is the topic of the following.

1.3 GLOBAL VORTICITY CONSIDERATIONS

The vorticity field Ω is computed from the velocity field (v, w). Ω is the off-plane vorticity component (along the x-axis), as the vorticity vector ω is the curl of the velocity ($\omega = \nabla \times \mathbf{u} = \nabla \times (u, v, w)$)and we have only access to v and w with our PIV setup, thus rendering the other components of the vorticity field not measurable.

In Fig. 1.3, we illustrate the analysis of the vorticity for one particular angle $\theta = 40°$ at an arbitrary time, to define some characteristic variables, that we will further study in the following.

An instantaneous flow field is thus represented in Fig. 1.3.a) and 1.3.b) with the corresponding vorticity field in Fig. 1.3.c. To compute the vorticity, as we mentioned in Chapter 0, a gaussian filter (of standard devation of 10 px, corresponding to 1 mm in real units) is applied to ensure a smooth spatial derivation of the velocity fields.

From the vorticity field, we observe two intense vortices and extract the extremal values Ω_{max} and Ω_{min} and the iso-contours corresponding to $\frac{\overline{\Omega_{min}}}{\sqrt{2}}$ and $\frac{\overline{\Omega_{max}}}{\sqrt{2}}$, presented in Fig. 1.3.d. $\overline{\Omega_{min}}$ and $\overline{\Omega_{max}}$ are the time-averaged values for Ω_{min} and Ω_{max} over one realization. Note that $\Omega_{min} \simeq -\Omega_{max}$, as expected from a counter-rotating vortex pair. In addition to estimating the maximum vorticity and its location, we can define the distance d between the vortices and thanks to the aforementioned iso-contours, the average vortex radius R of both vortex tubes, as shown in Fig. 1.3.e.

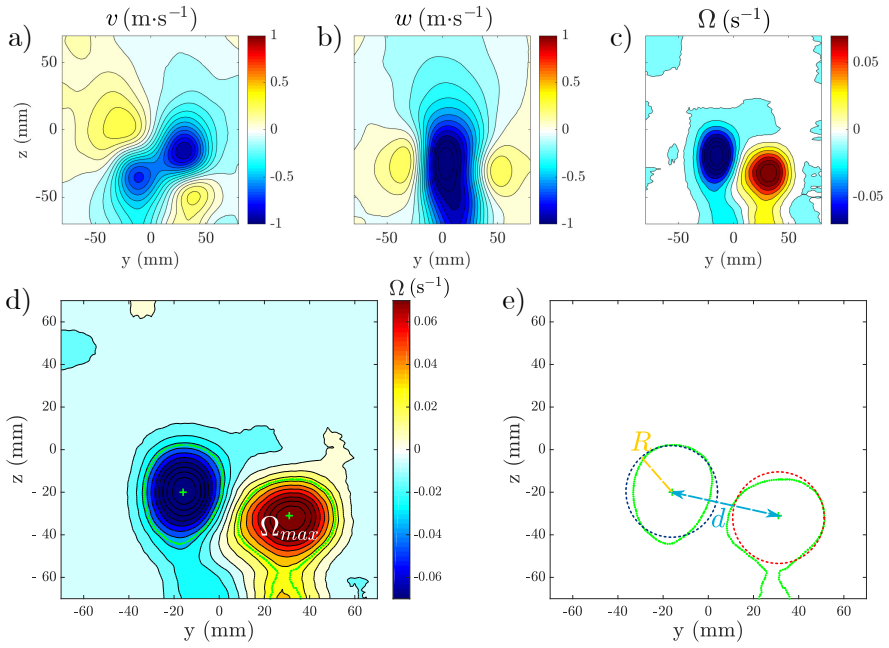

Figure 1.3: a) Instantaneous horizontal velocity v field after gaussian filtering. b) Instantaneous vertical velocity w field after gaussian filtering. c) Vorticity Ω field. d) Identification of the maximum of vorticity Ω_{max} and detection of the vortices with the condition $|\Omega| > \frac{\Omega_{max}}{\sqrt{2}}$ in green. e) Definition of the mean vortex radius R and the distance between the vortices d.

By doing the same analysis over the whole PIV recording, we can obtain the temporal evolution of all the variables (Ω_{max}, d and R) and recreate iso-surfaces of vorticity in the 3D spatio-temporal space (t,y,z), as we will discuss right after.

1.3.1 *Angular dependence of the wake vorticity structure*

Figure 1.4 presents the wake evolution over time and space for angles from $\theta = 0°$ to $\theta = 90°$. The wake is represented by the iso-surfaces defined in the previous section, $\Omega = \frac{\overline{\Omega_{max}}}{\sqrt{2}}$ and $\Omega = \frac{\overline{\Omega_{min}}}{\sqrt{2}}$. The top row represents the spatial projection of the wake over 1 s, while below is the temporal evolution of the wake projected on the y-axis.

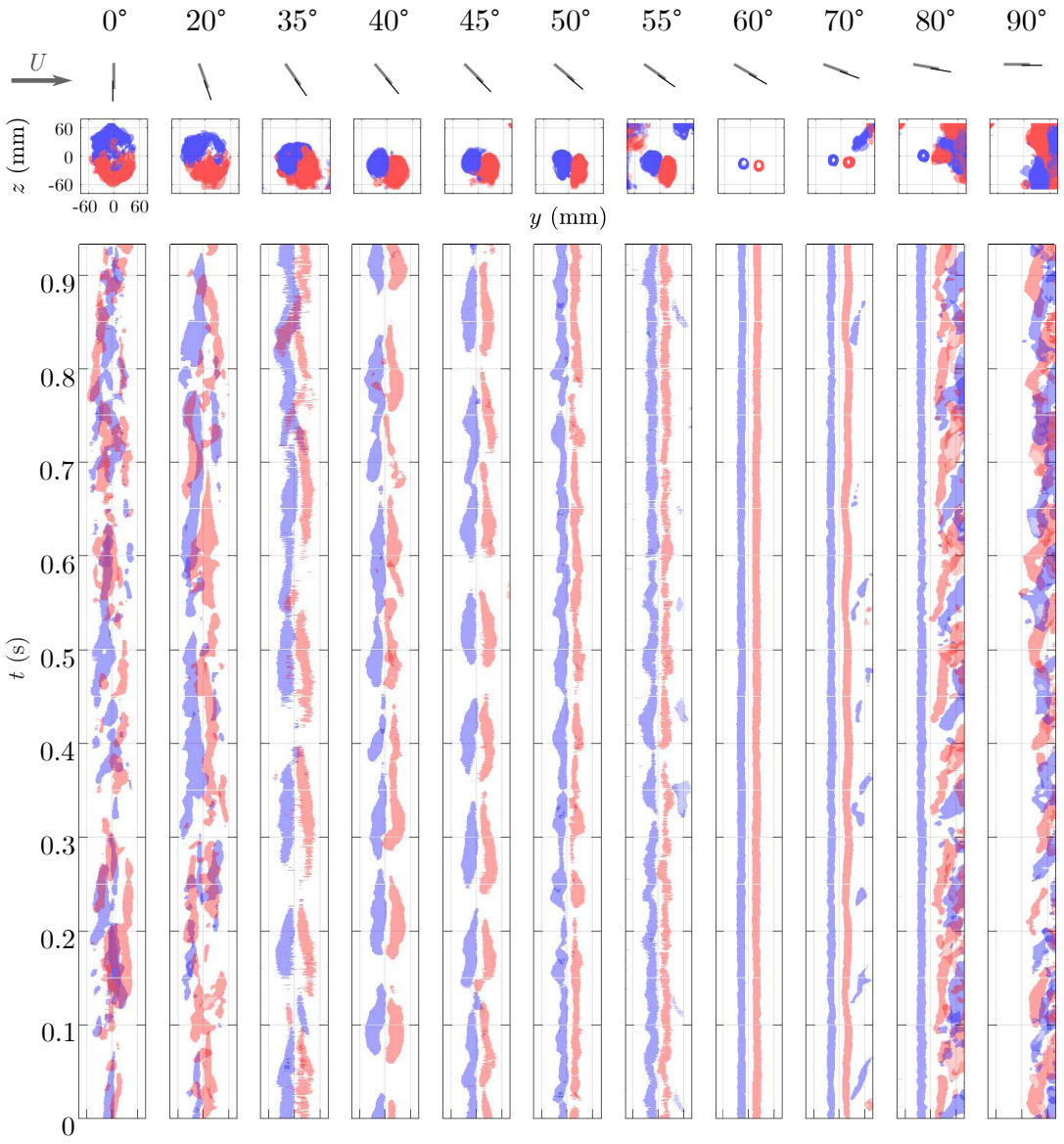

Figure 1.4: Evolution of the wake from the vertical $\theta = 0°$ to the horizontal $\theta = 90°$. Each column corresponds to the wake at the angle specified at the top of it. For each angle, the projection of the spatio-temporal diagram of the vorticity iso-contours is shown below, in the (y,z)-plane (top) and in the (y,t)-plane (bottom). Positive vorticity corresponds to the red surfaces and negative to the blue surfaces.

In Fig. 1.4, we observe a continuous stabilization of the wake from $\theta = 0°$ to $\theta = 70°$. In particular, disorganized puffs of vorticity settle down into almost straight cylinders. To achieve this stabilization, the vorticity first gets quasi-periodic oscillations and

its region of fluctuations condenses by $\theta = 40°$. Then for angles between $\theta = 40°$ and $\theta = 55°$, the spatial expansion keeps almost constant, while the frequency of the oscillations increases and their amplitude decreases with increasing angle. From $\theta > 60°$, the wake spatial expansion reduces again and is stable with very little fluctuations.

For the higher angles $\theta \geq 80°$, the vorticity measurements of the wake is polluted by the wake of the support as the pendulum is almost aligned to the horizontal and directly in the wake of the support for $y > 0$. Hopefully, this direct observation of the interference by the support is only visible for these high angles and confirms that it does not exist for lower angles, which are central to our study.

For the lower angles $\theta \leq 20°$, the wake is not well defined by the chosen vorticity contour, due to the vorticity being mostly contained in the visualization plane (y,z) and thus $\Omega \sim 0$.

While this overview of the wake structure is mostly qualitative, the observed behaviors are in agreement with previous findings in the literature for the wake of the disk in low Reynolds number numerical simulations [18].

1.3.2 *Connecting to the C_N coefficient?*

One of the aims of this thesis is to understand the difference between the lift and drag states of the disk pendulum. Due to the intrinsic coupling between the wake and the aerodynamic coefficients, we attempt here to draw a parallel between the vorticity structure and the C_N coefficient of the disk (see Section 0.1.1.1) at least qualitative and maybe quantitative as well.

From the qualitative observations (see Fig. 1.4) of spatio-temporal diagrams in the previous section, the wake seems to radically change between $\theta = 45°$ and $\theta = 50°$ and its spatial structure between $\theta = 55°$ and $\theta = 60°$. Coming back to the C_N coefficient, the change of regime, from drag to lift predominance, occurs at $\theta = 50°$. From the wake point of view, as we already proposed in Chapter 0, the drag-dominant regime ($\theta \lesssim 45°$) would be related to a ring vortex structure with a well-defined shedding. The lift-dominant state ($\theta \gtrsim 55°$) on the contrary is constituted with two stable wingtip vortices. In-between ($\theta = 50°$ and $\theta = 55°$), we observe, in Fig. 1.4, an hybrid state, where the shedding[1] is almost non existent with however strong fluctuations of position of the wingtip vortex centers. It is possible that this particular angular region possesses two possible wake structures, leading to two C_N coefficients, as was reported for a few angles in this range by Flachsbart in 1932 [25].

To further link the wake and the C_N coefficient, it would be interesting to compute the lift coefficient using the Kutta-Joukowski theorem, linking the normal lift coefficient and thus C_N to the circulation Γ_0 and the span b for an elliptic wing loading: $C_N = \frac{\pi b \Gamma_0}{SU}$ [26]. The difficulty here is the estimation of the circulation Γ_0 as $\Gamma_0 = \oint_{\mathcal{C}} \mathbf{u} \cdot \mathrm{d}\mathbf{l}$, with $\mathcal{C}$ a contour to be determined, usually taken as the edge of the vortex. Though the Stokes theorem links the circulation to the vorticity, $\Gamma_0 = \iint_{\mathcal{S}} \omega \cdot \mathrm{d}\mathbf{S}$, the surface of

1 Here, we understand the shedding as a temporal discontinuity of the vorticity iso-surface, corresponding to a diminution of $|\Omega|$ below $\frac{\overline{\Omega_{max}}}{\sqrt{2}}$.

integration $\mathcal{S}$ is also to be defined appropriately. Note that $\mathcal{C}$ is the closed contour of the surface $\mathcal{S}$, so once we know one, the other is also determined. As the results presented here are preliminary, we will not discuss the circulation but only the mean maximal vorticity $\overline{\Omega_{max}}$, which presents the advantage of not requiring the choice of any arbitrary threshold as it is a direct output from the vorticity field.

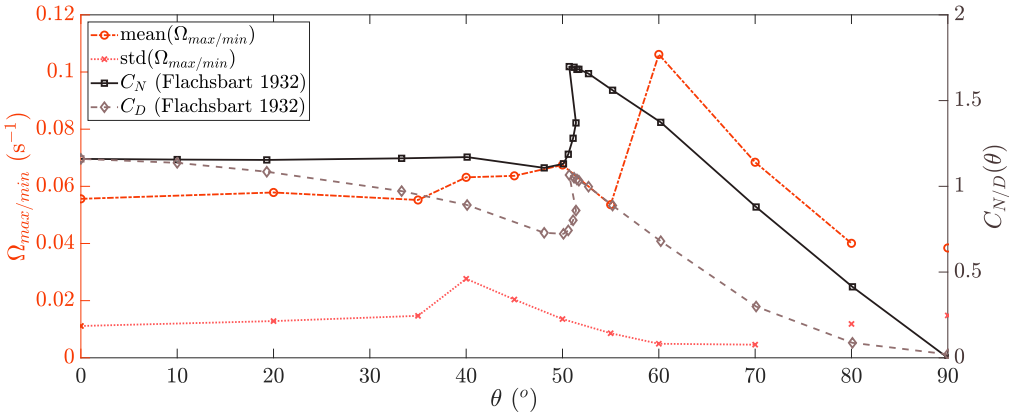

Figure 1.5: Evolution of the time-averaged maximal vorticity mean(Ω_{max}) = $\overline{\Omega_{max}}$ and its standard deviation std($\Omega_{max/min}$) with the angle of the pendulum θ. For comparison, the angular evolution of C_N and C_D coefficients is also represented on the right axis.

In Fig. 1.5, the time-averaged maximal vorticity is compared to the C_N coefficient, over the angle θ. The shape of both curves is quite similar with a plateau at low angles and a linear decay towards 0 at $\theta = 90°$ for angles $\theta > 60°$. This similarity is hindered by a slight shift for the maximum of the curves ($\theta = 60°$ for Ω_{max} and $\theta = 50°$ for C_N). A possibility for this shift is the uncertainty on the measured angles, we estimated it at about $\pm 3°$, as the angle was fixed for these data sets and the protractor was not particularly precise. It is thus possible that the angle $\theta = 55°$ is in fact $\theta = 52°$ and thus be one of the angle of two C_N coefficients [25]. As an indication, the standard deviation of Ω_{max} is also represented in Fig. 1.5, and slightly resemble the drag coefficient C_D in its evolution, though the difference is much greater than between C_N and $\overline{\Omega_{max}}$.

This likeness between the C_N coefficient and the vorticity $\overline{\Omega_{max}}$ of the wingtip vortices is still to be further investigated in order for us to understand the reason behind it, as a direct proportionality would mean that the diameter of the wingtip vortices would remain constant over the whole range of angles.

1.3.3 *Other vorticity properties of the wake*

In addition to the qualitative and time-averaged analysis conducted so far, we can investigate the temporal dynamics of the wake, such as the time evolution of the vortex intensity Ω_{max}, the distance between the vortices d and their radius R. From Fig. 1.4, we expect quasi-periodic fluctuations of the distance between the vortices and of the radius.

In the following, we present a temporal analysis for a single angle $\theta = 50°$ and distance $D_{pl} = 5\,\text{cm}$, and only comment by the end of this section the influence of the

angle θ on the vortex dynamics.

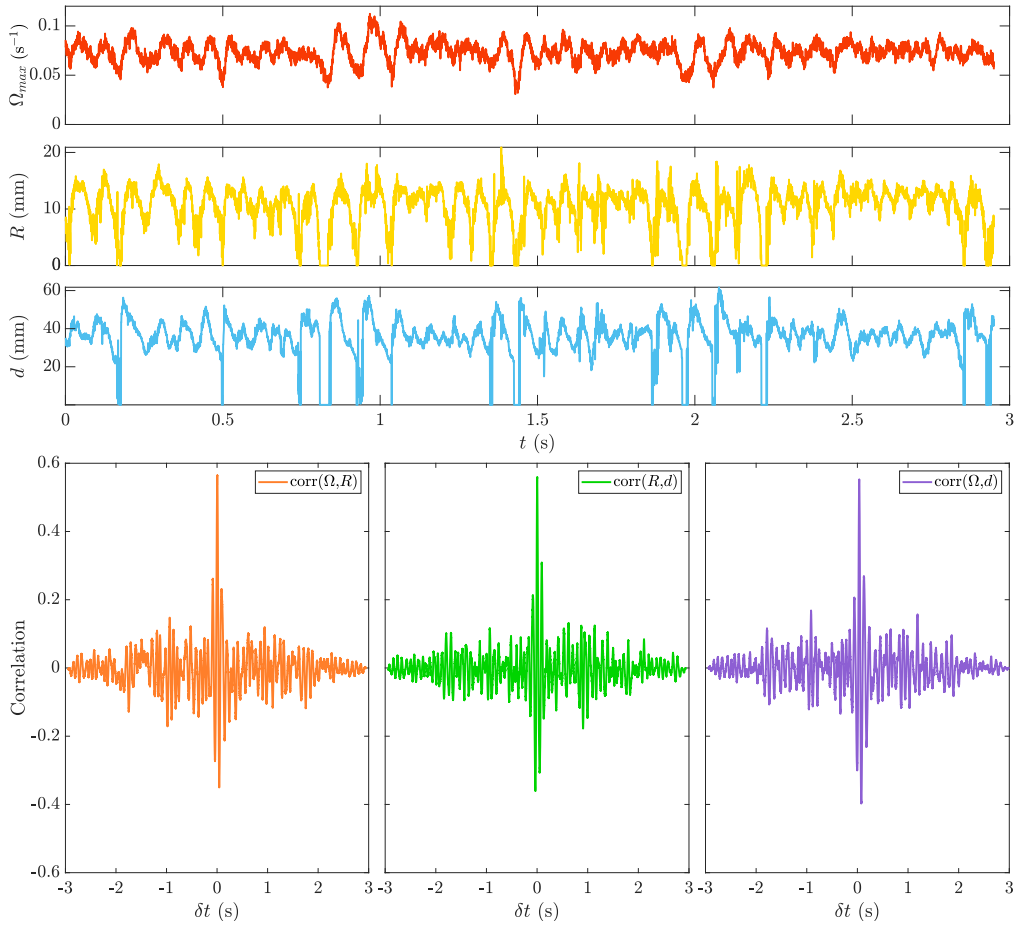

Figure 1.6: Top: time series of the vortex intensity Ω_{max}, the vortex radius R and the distance between the vortices d. Bottom: cross-correlations between each couple (Ω_{max}, R), (R, d), (Ω_{max}, d) as a function of the phase difference δt.

Figure 1.6 depicts the temporal evolution of the three variables Ω_{max}, R and d. Each variable presents well defined oscillations, which appear to be synchronous. This confirmed by the lack of phase shift for the maximal cross correlation in Fig. 1.6. The maximal values of the cross-correlation, ζ_i^j, are significant and almost all equal to 0.6 in this particular configuration of $(\theta, D_{pl}) = (50°, 5\,\text{cm})$. This means that as the vortex intensity increases so does the expansion of the vortex, which suggests that the process at play is not simply due to vortex stretching. However, we only observe the longitudinal component Ω of the vorticity and this expansion might result from a shift in the vorticity orientation. The correlation between the distance and the radius is understood by the fact that larger vortices also need a larger space and as such the flow region in the middle may be seen as incompressible, as the region of maximum downwash from the vortices.

As the distance D_{pl} is varied, the vortex intensity $\overline{\Omega_{max}}$ decreases monotonously, and almost linearly over 20 cm, as shown in Fig. 1.7.a. On the contrary, the distance $\overline{d}$ between the two vortices is almost constant, as is the vortex radius $\overline{R}$. The constancy of the radius $\overline{R}$ may reflect a lack of spatial expansion of the vortex as it propagates

and diffuses. If we suppose a gaussian distribution of vorticity around the center of the vortex, which is close to the experimental measurements, R is proportional (by a factor $1/\sqrt{2}$) to the full width at half maximum. If it remains constant with D_{pl}, this means that the vortex intensity decreases in a uniform manner in the transverse plane. This diminution of vorticity might be directly linked with the viscous dissipation ϵ through the relation $\epsilon = \frac{\mathrm{d}u^2}{\mathrm{d}t} \propto -\Omega^3 R^2$, with $\frac{\mathrm{d}u^2}{\mathrm{d}t}$ the variation of kinetic energy. To do a robust estimation of the dissipation in the wake, the Taylor hypothesis of frozen turbulence is needed, yet the wingtip vortices have been observed to reconnect sporadically at various distances D_{pl}, mostly through their destabilization by the Crow instability [27]. This could explain the slowdown of dissipation by $D_{pl} = 25\,\mathrm{cm}$ in Fig. 1.7.a.

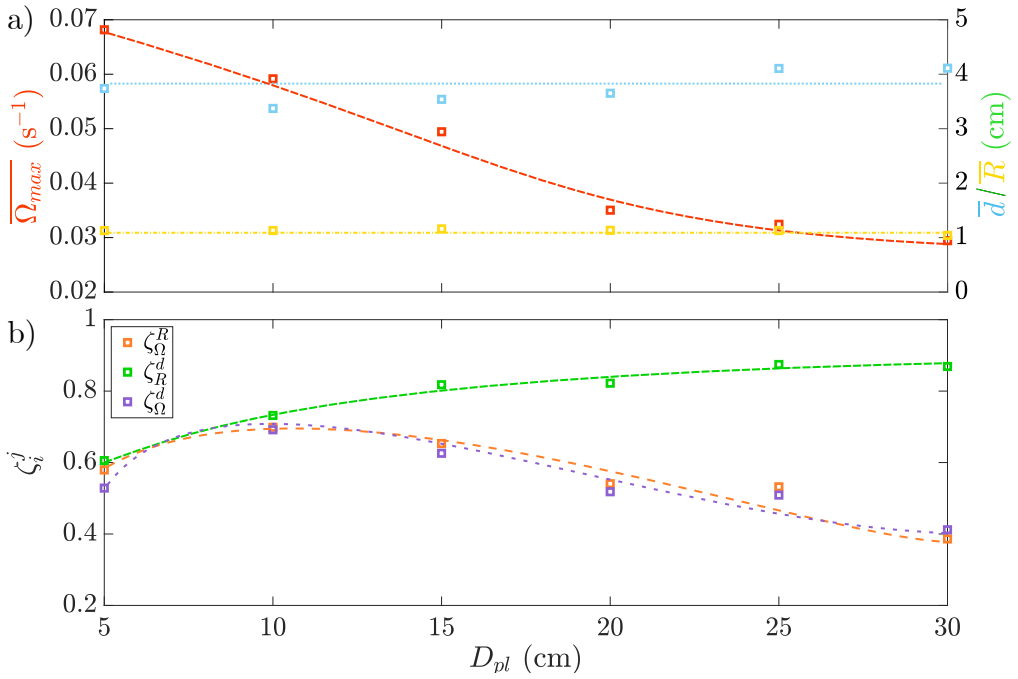

Figure 1.7: a) Evolution of the vortex intensity $\overline{\Omega_{max}}$, the vortex radius $\overline{R}$ and the distance between the vortices $\overline{d}$ as a function of the distance D_{pl} between the pendulum and the wake plane. b) Evolution of the cross correlation maxima ζ_i^j as a function of the distance D_{pl} between the pendulum and the wake plane: ζ_Ω^R, ζ_R^d, ζ_Ω^d. Dashed and dotted lines serve as eye guides.

In addition to the mean values of Ω_{max}, R and d, we can also look at the evolution of their correlation with the distance D_{pl}. In Fig. 1.7.b, the evolution of the maximum of correlation ζ_i^j for the three pairs of variables is presented as a function of the distance D_{pl}. The correlations with the vorticity Ω_{max} tend to decrease with the distance, with however a peak around $D_{pl} = 10\,\mathrm{cm}$. While the decrease might be related to the overall decrease of vorticity, thus increasing the sensitivity to ambient turbulent noise in the fluctuations, the first increase between $D_{pl} = 5\,\mathrm{cm}$ and $D_{pl} = 10\,\mathrm{cm}$ may come from the roll-up of the wingtip vortices. If the vortices are not entirely rolled up, it is possible that the size of the vortex is also growing from incoming flow deviated from the plate and not only from vorticity transfer from the transverse to the longitudinal component as we mentioned earlier as a possible explanation of the high correlation between the vorticity and vortex radius. On the contrary, the correlation between the distance

between the vortices and their radius ζ_R^d is gradually increasing with the distance to the pendulum D_{pl}. Though we may not have an explanation to this phenomenon for the moment, it seemed like an interesting observation to be made, which would require more investigation as to its implications.

A similar correlation behavior is observed for angles from $\theta = 35°$ to $\theta = 55°$, for which a study on the effect of the distance has been conducted. For the other angles, the distance was kept constant at $D_{pl} = 10\,\text{cm}$. In Fig. 1.8.a), the correlation maxima are presented for the different angles θ of the pendulum. The shape of the C_N coefficient is again somehow retrieved with the maximum value of the correlation reached at $\theta \simeq 40°$. In Fig. 1.8.b), we can see that the correlation maximum is attained at synchronicity ($\delta t_{corr} = 0$) for almost all angles, thus suggesting that this property is independent of the shape of the wake itself.

For angles $\theta > 70°$, the correlation is increasing again, however the cross-correlation signals present no clear peak of correlation possibly due to the turbulent noise emanating from the support. Similar difficulties are found for $\theta < 20°$, which there translates into an artificial phase shift on the correlation.

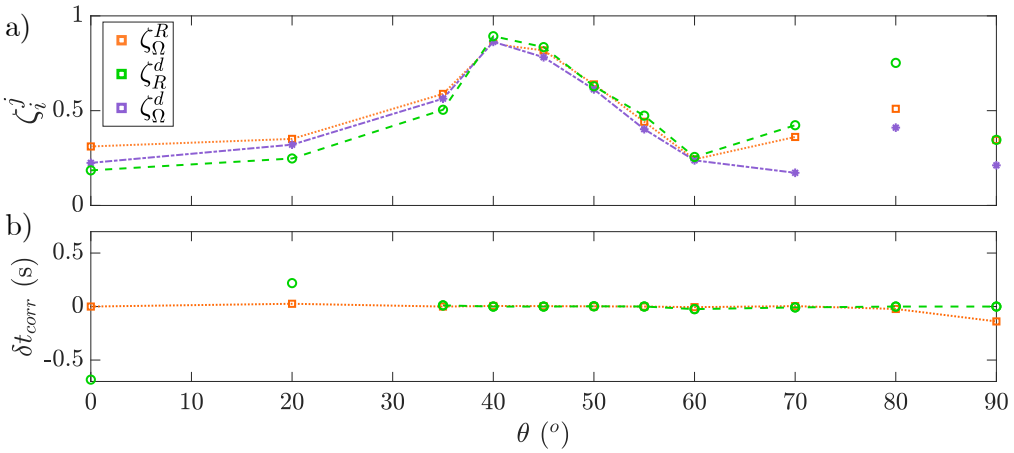

Figure 1.8: a) Evolution of the cross correlation maxima ζ_i^j as a function of the angle θ: ζ_Ω^R, ζ_R^d, ζ_Ω^d. b) Temporal shift between the two signals δt_{corr}, corresponding to the δt for which the correlation is equal to ζ_i^j, for ζ_Ω^R, ζ_R^d.

Many more properties of the wake can be extracted from the present signals but are beyond the scope of this Chapter. Some, like the evolution of the absolute position of the vortices or the analysis of the power density spectrum of the time series for the vorticity, are developed in the report from Samuel Bera, a Master 1 student intern that I supervised during my PhD [28].

In particular, there is an increase with the angle θ of the Strouhal number $\text{St} = \frac{f_{vs} d_{disk}}{U}$ defined on the frequency of oscillation of the vortex radius.

Another interesting point is the downwash of the vortices observed by scanning the longitudinal direction D_{pl}. The average descent angle is estimated to be about -6°, which might be further checked by integrating the vorticity over the central horizontal axis but could not be done in the time frame of this PhD.

1.4 PERSPECTIVES

In this Chapter, we have presented an overview of the angular dependence of the transverse wake behind a disk, which overall coincides with numerical simulations at lower Reynolds numbers [18]. This is accompanied by a few properties we observed when studying the details of the wake from different points of view, in particular the cross-correlations between the different wake characteristics. This kind of investigation has yet been seldom pursued in previous works and the cross-correlation is usually conducted between one wake variable and a force measurement on the object under study [29], leaving little grounds for comparison for our findings.

The isovorticity structure, as shown in Fig. 1.4, is more commonly spread to present a qualitative general outlook of the wake. In particular, the temporal evolution of the transverse wake vorticity structure has been investigated for different birds and mammals [30–32]. For animals, flapping flight results in a ring vortex wake close to what we observe in the drag branch of the disk ($\theta < 50°$), while gliding flight is closer to the disk wake at high angles in the lift branch ($\theta > 50°$), as compared in Fig. 1.9.

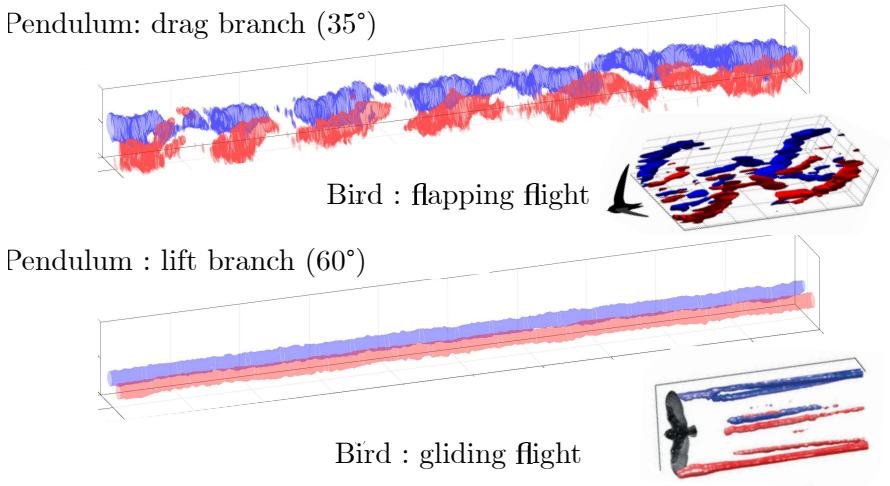

Figure 1.9: Comparison of the wake of the pendulum in the drag (top) and lift (bottom) branche with the wake of birds in flapping and gliding flight. Flapping flight wake of a swift (*Apus apus*) from [33] and gliding flight wake of a barn owl (*Tyto alba*) from [11].

Many more questions remain, that would require a whole set of new experiments and analysis, in particular on the coupling between the wake and the angular fluctuations, when the pendulum is released, that has only started during this thesis. Another point is whether the wake changes observed around the stall angle $\theta = 50°$ are continuous and could be modelled using a first-order or second-order phase transition. Investigations closer to the disk would also be interesting in order to observe the roll-up of the wingtip vortices and the role of it in the stability of the wake. A theoretical estimation of the roll-up distance has been proposed by Spreiter and Sacks in 1951 from the aerodynamic coefficients. It is possible that the mechanism of rolling-up is at the core of the coupling between the wake structure and the stall, as the roll-up distance is inversely proportional to the lift coefficient C_L. Thus were C_L be too high, the roll up would be close enough

to the disk for the wingtip vortices to reconnect to the trailing-edge vortex and with this form a ring vortex as observed in the drag-dominated regime.

REFERENCES

[1] G. Dehnhardt et al. "Hydrodynamic Trail-Following in Harbor Seals (Phoca vitulina)." In: *Science* 293.5527 (July 2001), pp. 102–104.

[2] N. Schulte-Pelkum et al. "Tracking of biogenic hydrodynamic trails in harbour seals (Phoca vitulina)." In: *Journal of Experimental Biology* 210.5 (2007), pp. 781–787.

[3] W. Hanke et al. "Harbor seal vibrissa morphology suppresses vortex-induced vibrations." In: *Journal of Experimental Biology* 213.15 (July 2010), pp. 2665–2672.

[4] A. Rinehart, V. Shyam, and W. Zhang. "Characterization of seal whisker morphology: Implications for whisker-inspired flow control applications." In: *Bioinspiration and Biomimetics* 12.6 (2017).

[5] L. Fiabane. "Méthodes analytiques de caractérisation des structures cohérentes contribuant aux efforts aérodynamiques." PhD thesis. 2011, p. 141.

[6] C. P. Ellington et al. "Leading-edge vortices in insect flight." In: *Nature* 384.6610 (Dec. 1996), pp. 626–630.

[7] J. J. Videler, E. J. Stamhuis, and G. D. E. Povel. "Leading-Edge Vortex Lifts Swifts." In: *Science* 306.5703 (Dec. 2004), pp. 1960–1962.

[8] C. W. Pitt Ford and H. Babinsky. "Lift and the leading-edge vortex." In: *Journal of Fluid Mechanics* 720 (Apr. 2013), pp. 280–313.

[9] T. Jardin, J. Choi, and T. Colonius. "An empirical correlation between lift and the properties of leading-edge vortices." In: *Theoretical and Computational Fluid Dynamics* 35.4 (Aug. 2021), pp. 437–448.

[10] J. D. Anderson. *Fundamentals of Aerodynamics*. 6. McGraw-Hill Higher Education, 2011, p. 1154.

[11] J. R. Usherwood et al. "High aerodynamic lift from the tail reduces drag in gliding raptors." In: *The Journal of experimental biology* 223 (2020).

[12] G. R. Spedding, M. Rosén, and A. Hedenström. "A family of vortex wakes generated by a thrush nightingale in free flight in a wind tunnel over its entire natural range of flight speeds." In: *Journal of Experimental Biology* 206.14 (July 2003), pp. 2313–2344.

[13] E. Gutierrez et al. "Lift calculations based on accepted wake models for animal flight are inconsistent and sensitive to vortex dynamics." In: *Bioinspiration and Biomimetics* 12.1 (2017), pp. 1–15.

[14] S. Ahmed, G. Ramm, and G. Faltin. "Some Salient Features Of The Time-Averaged Ground Vehicle Wake." In: *SAE Technical Paper*. SAE International, Feb. 1984.

[15] A. J. Kirchhefer, G. A. Kopp, and R. Gurka. "The near wake of a freely flying European starling." In: *Physics of Fluids* 25.5 (May 2013), p. 051902.

[16] van Griethuijsen et al. "Vortex wakes of birds: recent developments using digital particle image velocimetry in a wind tunnel." In: *Animal Biology* 56.4 (2006), pp. 535–549.

[17] X. Tian et al. "Flow around an oscillating circular disk at low to moderate Reynolds numbers." In: *Journal of Fluid Mechanics* 812 (2017), pp. 1119–1145.

[18] S. Gao et al. "Flow around an inclined circular disk." In: *J. Fluid Mech.* 851 (Sept. 2018), pp. 687–714.

[19] D. Marshall and T. E. Stanton. "On the Eddy System in the Wake of Flat Circular Plates in Three Dimensional Flow." In: *Proceedings of the Royal Society A: Mathematical, Physical and Engineering Sciences* 130.813 (Jan. 1931), pp. 295–301.

[20] J. R. Calvert. "Experiments on the flow past an inclined disk." In: *Journal of Fluid Mechanics* 29.04 (Sept. 1967), pp. 691–703.

[21] P. Szaltys et al. "Nonlinear evolution of instabilities behind spheres and disks." In: *Journal of Fluids and Structures* 28 (Jan. 2012), pp. 483–487.

[22] A. Evrard et al. "Fluid force and symmetry breaking modes of a 3D bluff body with a base cavity." In: *J. Fluid Struct.* 61 (2016), pp. 99–114.

[23] J. M. Lucas et al. "A numerical investigation of the asymmetric wake mode of a squareback Ahmed body - Effect of a base cavity." In: *Journal of Fluid Mechanics* 831 (2017), pp. 675–697.

[24] R. D. Brackston et al. "Stochastic modelling and feedback control of bistability in a turbulent bluff body wake." In: *Journal of Fluid Mechanics* 802 (2016), pp. 726–749.

[25] O. Flachsbart. "Messungen an ebenen und gewölbten Platten." In: *Ergebnisse der Aerodynamischen Versuchsanstalt zu Göttingen - IV. Lieferung*. München und Berlin: Verlag von R. Oldenburg, 1932, pp. 96–100.

[26] G. R. Spedding. "The Wake of a Kestrel (Falco Tinnunculus) in Gliding Flight." In: *Journal of Experimental Biology* 127.1 (Jan. 1987), pp. 45–57.

[27] S. C. Crow. "Stability theory for a pair of trailing vortices." In: *AIAA Journal* 8.12 (Dec. 1970), pp. 2172–2179.

[28] S. Bera. "Visualisation du sillage d'un pendule en soufflerie." MA thesis. ENS de Lyon, 2021, p. 27.

[29] X.-B. Li et al. "On the correlation between aerodynamic drag and wake flow for a generic high-speed train." In: *Journal of Wind Engineering and Industrial Aerodynamics* 215.December 2020 (Aug. 2021), p. 104698.

[30] T. Y. Hubel et al. "Time-resolved wake structure and kinematics of bat flight." In: *Experiments in Fluids* 46.5 (May 2009), pp. 933–943.

[31] F. T. Muijres et al. "Comparative aerodynamic performance of flapping flight in two bat species using time-resolved wake visualization." In: *Journal of The Royal Society Interface* 8.63 (Oct. 2011), pp. 1418–1428.

[32] L. C. Johansson and A. Hedenström. "The vortex wake of blackcaps (Sylvia atricapilla L.) measured using high-speed digital particle image velocimetry (DPIV)." In: *Journal of Experimental Biology* 212.20 (Oct. 2009), pp. 3365–3376.

[33] P. Henningsson, F. T. Muijres, and A. Hedenström. "Time-resolved vortex wake of a common swift flying over a range of flight speeds." In: *Journal of The Royal Society Interface* 8.59 (June 2011), pp. 807–816.

2

SHAPING THE BISTABILITY

Can the existence of the bistability and the presence of sharp stall be inferred from the sole aspect ratio of a rectangular plate?

2.1 INTRODUCTION

When looking at birds, a striking feature is the diversity of shape. Not only is the body morphology different, when comparing for instance a European robin (*Erithacus rubecula*) and a rose-ringed parakeet (*Psittacula krameri*) (see Fig. 2.1.a-b), but even the wing form itself varies greatly from one bird to the other. Millions of years of evolution have shaped the wings of each bird to its particular flight. From the triangular wing of a starling to the crescent wing of a tern and the elongated wing of a northern gannet, each shape is adapted to the body morphology and the flight strategies adopted.

A common starling (*Sturnus vulgaris*, Fig. 2.1.c) migrates mostly on land, with many perch possibilities and its small profiled body (20 cm for a total wingspan of 40 cm) makes it more efficient to flap-bound flight, a technique that combines flapping flight and flexed-wing leaps [1]. Arctic terns (*Sterna paradisaea*, Fig. 2.1.d) on the contrary migrate over extreme distances, more than 14 000 km a year, going back and forth between the polar circles by the sea, with a typical size of 30 cm for a total wingspan of 80 cm. Crossing the Equator, flapping flight is necessary due to the intertropical convergence zone, known to sailors as the doldrums because of the lack of wind. Their crescent wing shape enables for both gliding and flapping flight. Northern gannets (*Morus bassanus*, Fig. 2.1.d), while also sea birds, rely almost entirely on gliding and soaring, and elongated wings provide them with enhanced lift to drag ratio, with their large size of 90 cm and a total wingspan of 180 cm.

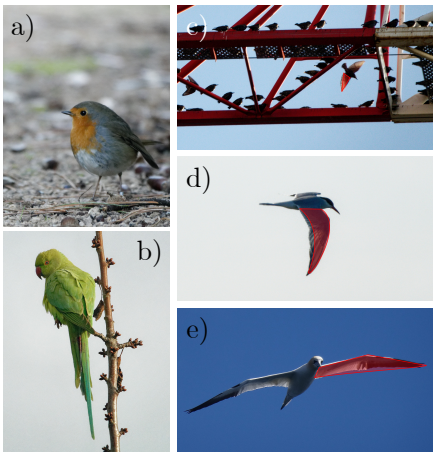

Figure 2.1: a) European robin, France, 2021.
b) Rose-ringed parakeet, France, 2021.
c) Common starling, France, 2019.
d) Arctic tern, Iceland, 2019.
e) Northern gannet, Atlantic ocean, 2019.
Wing shape is colored red for highlighting.

Within a given family, such as the *Accipitridae* (one of the major raptor families), smaller variations are observed. Their wing shape looks quite invariant almost rectangular and with the tip (primary) feathers spread out, yet the Aspect Ratio (AR) of the wing is found to be quite changing depending on the species, spanning from 2 to about 3.5[1]. For instance, while both are gliders, bearded vultures, *Gypaetus barbatus* (Fig.

1 A standard measure of the aspect ratio for a bird in ornithology guides is based on the entire wingspan from one wingtip to the other, rather than on the span of a single wing as we chose here.

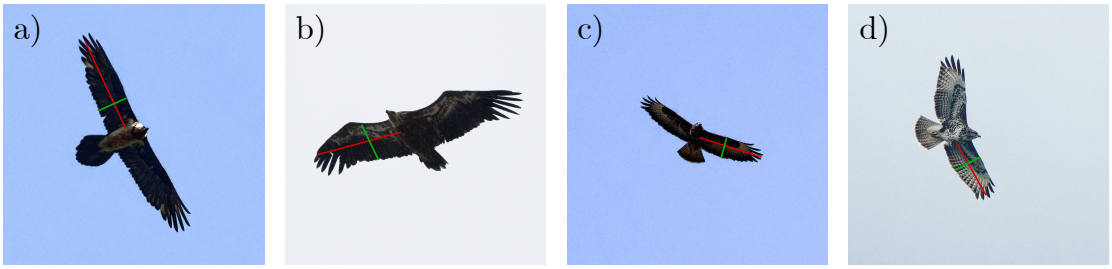

Figure 2.2: a) Bearded vulture, France, 2021. b) Griffon vulture, France, 2021. c) Common buzzard, France, 2021. d) Short-toed snake eagle, France, 2021. Wing span (red) and chord (green) are indicated by lines on each bird.

2.2.a), and griffon vultures, *Gyps fulvus* (Fig 2.2.b), present quite different aspect ratios, respectively about 3.1 and 2.3. Their respective aspect ratios are closer to all-rounder flyers such as common buzzards, *Buteo buteo* (Fig. 2.2.c) of estimated aspect ratio 3.2, and short-toed snake eagles, *Circaetus gallicus* (Fig. 2.2.d) of estimated aspect ratio 2.2.

The study of the role of aspect ratio in bird flight is still only at its infancy [2], as most studies have been morphological [3, 4] and not aerodynamically oriented.

Aspect ratio is also very important in Aeronautics and has been, in this context on the contrary, extensively studied from the early 20th century [5–7]. In particular, aspect ratios close to 1 present an important stall while aspect ratios either smaller or larger than 1 tend to have smoother change between lift and drag predominance [5]. Lift coefficient at angles of attack lower than the stall angle is also reported to increase with aspect ratio [8], which could link to the propensity of gliding birds to have high aspect ratio. The wake of rectangular plates of different aspect ratios has also been investigated numerically and experimentally [9, 10] and the description of it will be detailed later in this chapter when discussing the implications on it from the aerodynamic coefficients.

2.2 EXPERIMENTAL DETAILS

As we are interested here in the aspect ratio AR, a disk is not necessarily the best companion to investigate such a problem, an ellipsoid neither for practical reasons. Hence, for simplicity, we will use in the following of this chapter rectangular plates fixed at the end of the pendulum rod. A total of 4 PVC plates, of thickness $e = 0.8\,\mathrm{mm}$, has been used, providing us with 8 different aspect ratios depending on the direction of the maximal length, in the plane of motion or orthogonal to it. Just like for the disk pendulum presented in Chapter 0, as we will considerably use the momentum equation at equilibrium (given again by Eq. 2.1), a few geometrical parameters are required to go back to the C_N coefficient, that are the distance to the center of mass l, the distance to the aerodynamic center L, the total mass of the pendulum m and its surface $S = bc$ with b the span and c the chord as defined in Fig. 2.3 – the aspect ratio (defined in Chapter 0) is here $\mathrm{AR} = b/c$. An overview of the various pendulums used hereafter is presented in Table 2.1. The equilibrium equation is then:

$$mgl\sin(\theta) = \frac{1}{2}\rho U^2 bcLC_N(\theta) \tag{2.1}$$

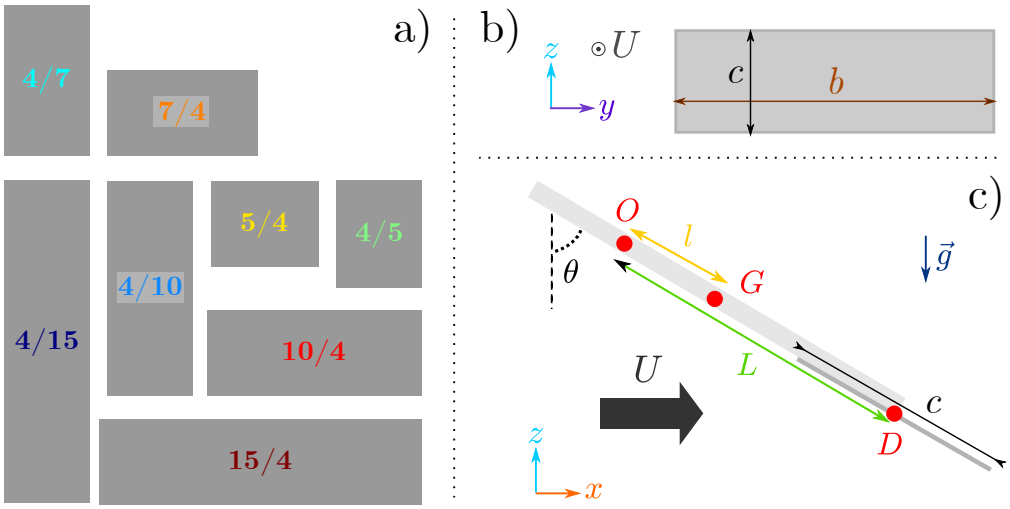

Figure 2.3: a) Different plate configurations used in the experiment, true scaling. b) Definition of span b and chord c in the experimental coordinate system. c) Schematic view of the rectangular pendulum in the wind tunnel.

Aspect ratio AR (cm)	4/15	4/10	4/7	4/5	5/4	7/4	10/4	15/4
Chord c (cm)	15	10	7	5	4	4	4	4
Span b (cm)	4	4	4	4	5	7	10	15
Mass m_{plate} (g)	8.76	5.84	4.17	2.92	2.92	4.17	5.84	8.76
Total mass m (g)	22.0	19.1	17.4	16.2	16.2	17.4	19.1	22.0
Distance l (cm)	4.5	3.9	3.5	3.1	3.5	4.0	4.5	5.3
Distance L (cm)	10.3	10.3	10.3	10.3	12.3	12.3	12.3	12.3

Table 2.1: Physical characteristics of the different rectangular plates used in the experiment. 8 configurations were tested using 4 different plates with one of the dimension equal 4 cm, which is the diameter of the disk presented in Chapter 0.

The experimental setup is the one presented in Chapter 0. No hot-wire measurements will be reported here as only the mean flow velocity U was relevant for this study.

The experimental protocol for investigating the influence of the aspect ratio on the aerodynamic coefficient, and thus on the bistability, is a step by step sweep of the flow velocity over a wide range. This method, used by [11], takes advantage of the weight torque from Equation 2.1 to reconstruct the aerodynamic coefficient. Due to natural oscillations of the system, the flow velocity is only increased and then decreased step by step and the angular equilibrium position is time-averaged over 15 to 120 s depending on the observed fluctuations. When the equilibrium position was not well-defined, as for instance a jump was observed yet without bistability, a refined stepping was done. As such, in total for the 8 different configurations, 24 cycles were executed, which amounted to more than 3200 flow velocity steps, with about 1600 while increasing the flow velocity U, from $0\,\mathrm{m}\cdot\mathrm{s}^{-1}$ to about $10\,\mathrm{m}\cdot\mathrm{s}^{-1}$, and the same amount decreasing U, from about $10\,\mathrm{m}\cdot\mathrm{s}^{-1}$ to $0\,\mathrm{m}\cdot\mathrm{s}^{-1}$.

2.3 RESULTS

2.3.1 *Bistability existence and C_N coefficient*

Inspired by Obligado et al. 2013 [11], when confronted with a new pendulum shape, the first thing we do is always to look at the angular response to a flow velocity cycle, thus resulting in a $\theta(U)$ portrait. Once this portrait is drawn, it is then possible to get the aerodynamic coefficient C_N by inverting Eq. 2.1 knowing the flow velocity and the equilibrium position. In the following, we have decided to first present the aspect ratios greater than 1 and lower than 1 separately as the pendulum configuration slightly changed between both cases, in particular on the distance L between the swivel and the aerodynamic center. Only in the discussion will all configurations be compared as a whole.

2.3.1.1 *AR*> 1

Looking back at Figures 2.1 and 2.2, the most common aspect ratios found in nature are above 1, at least for birds – insects also present mostly aspect ratios above 1 but we will not detail it further here. As such, the first case to investigate is naturally the aspect ratios greater than 1.

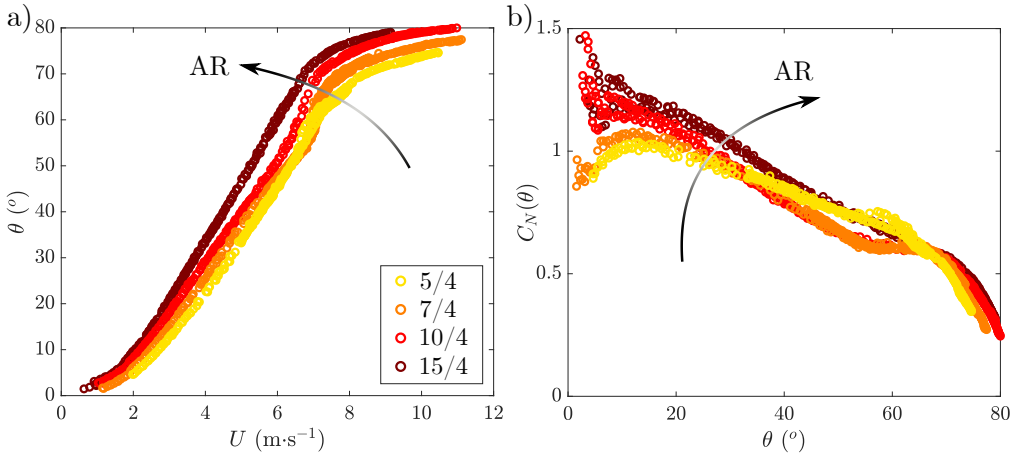

Figure 2.4: a) Angular equilibrium position as a function of the flow velocity. b) Reconstructed aerodynamic coefficient C_N as a function of the angle θ. Color codes for the aspect ratio: the darker the color, the higher the aspect ratio, here above 1.

In Figure 2.4.a), the evolution of the $\theta(U)$ portrait is presented for increasing aspect ratio AR from 5/4 in yellow to 15/4 in maroon. A first observation is the quick uptake in angle at low velocity for the larger AR. A second point is the appearance of the bistability in the range $\theta \in [50°, 60°]$, known for the disk pendulum, only for the smallest AR. The $\theta(U)$ bistability, slightly more visible on the C_N coefficient with the bump at $\theta \simeq 60°$, is however not as clearly defined as the one for the disk presented in Fig. 9, while a bistability of the C_N coefficient itself seems to appear for this aspect ratio, with two values of C_N for the same angle. This will be further detailed in section 2.3.2, as it is not only observed for AR $= 5/4$. Apart from this, the shape of the $\theta(U)$ portrait does not change much over the range of aspect ratio tested. Regarding the C_N coefficient, presented in Fig. 2.4.b), neither is there any drastic evolution for the 3

higher aspect ratios, especially between AR = 7/4 (orange) and AR = 10/4 (red). As the aspect ratio is decreased, the normal coefficient around 60° first diminishes, forming a plateau over more than 5°, before increasing again for AR = 5/4 when the bistability appears. On the contrary, the drag-dominated part of the C_N coefficient at low angles, $\theta < 30°$ is constantly increasing with the aspect ratio and so does the lift-dominated part for high angles, $\theta > 70°$. Another particularity of the C_N coefficient for these aspect ratios is the absence of sharp stall apart from AR = 5/4, which will be discussed in more details in Section 2.4.2.

2.3.1.2 *AR*< 1

Aspect ratios below 1 are also present in nature however much rarer than ones larger than 1. Such aspect ratios are found in the tail of birds and in their feathers, in particular secondary feathers[2] and tail feathers.

In Figure 2.5, the aspect ratio is varied from 0.8 (green) to 0.27 (dark blue). A striking feature on the $\theta(U)$ portrait (Fig. 2.5.a) is the presence of the bistability and a large band of forbidden angles for AR = 4/7 (cyan). Bistability is also observed for AR = 4/10 (light blue) and AR = 4/5. For the latter however, the bistability is less marked, for the same reason as for AR = 5/4, which will be detailed in section 2.3.2. The bistability seems to emanate from the inflection point of the $\theta(U)$ curve, as we see from the change between AR = 4/15 and AR = 4/10.

As the aspect ratio tends to 1, the value of C_N increases with the aspect ratio when lift dominates but its stall angle also increases (Fig. 2.5.b). The stall angle for the smallest aspect ratio is not well defined, as not as sharp as for the other aspect ratios. It can be however estimated around $\theta = 30°$, at the edge of the plateau observed for θ between 30° and 40°. An interesting point on the C_N coefficient is also the non uniform evolution of its peak value, whose maximum is attained for AR = 4/7 in our study. This was already observed in the literature as we will discuss later in section 2.4.1.

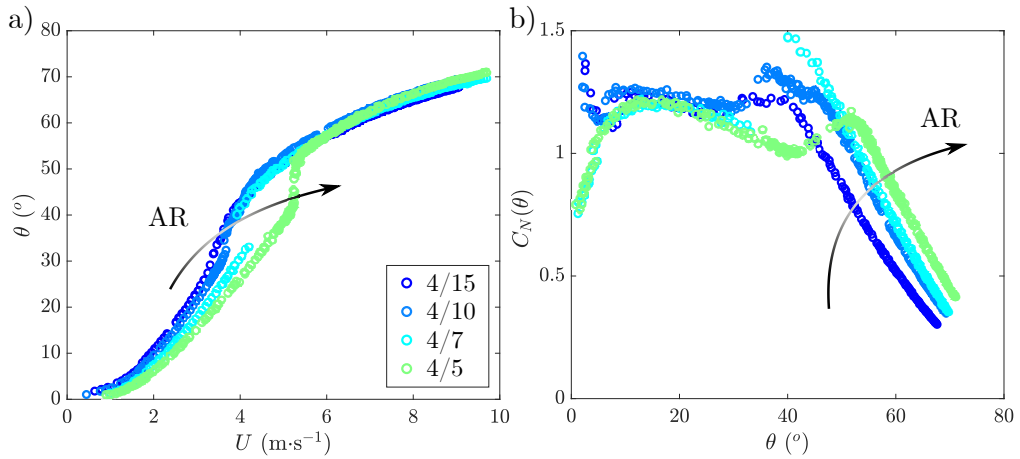

Figure 2.5: a) Angular equilibrium position as a function of the flow velocity. b) Reconstructed aerodynamic coefficient C_N as a function of the angle θ. Color codes for the aspect ratio: the darker the color, the smaller the aspect ratio, here below 1.

2 Secondary feathers are flight feathers in the middle of the wing, a scheme of bird nomenclature in presented in Annex A.1

A more discreet observation that can be done from Figure 2.5.a), is that despite the great discrepancy in surface and mass between the plates (Table 2.1), all pendulums attain the same position of equilibrium for flow velocity higher than $6\,\mathrm{m}\cdot\mathrm{s}^{-1}$. It even goes to the point that for large angles (above 60°), all $\theta(U)$ portraits collapse on a single curve. It results from it and Eq.2.1, as the span is constant at 4 cm, the following relation:

$$\frac{cL}{ml}C_N(\theta) = \mathrm{Cst}(\theta) \tag{2.2}$$

for $\theta > 60°$. This relation has only been observed for this particular case of constant 4 cm-span and no explanation is being proposed for now, as it would require more investigation in particular with different spans to ensure it not be a coincidence.

At low flow velocity, on the contrary, the higher the aspect ratio, the lower is the angle for the same velocity in Fig. 2.5.a. This comes from the fact that the surface $S = bc$ diminishes as the aspect ratio increases from $4/15$ to $4/5$. Indeed in Fig. 2.5.b), the C_N coefficient stays almost constant with the aspect ratio for angles $\theta \in [10°, 30°[$, which is quite different from the results for aspect ratios greater than 1, described in section 2.3.1.1.

2.3.2 *Complications around AR$\simeq$ 1*

As we mentioned previously, for aspect ratios close to 1, the bistability seems difficult to observe on time-averaged $\theta(U)$ portraits as presented in Fig. 2.4.a) and 2.5.a). To get a better idea of the bistability for such aspect ratios, a possibility is to look not only at the time-averaged angle θ but also at its distribution. Some positions, that were considered to be attained by the pendulum, are in fact only time-averaging artifacts and the result of a pondered mean of two equilibrium positions, while the pendulum keeps switching back and forth between both. The probability density function (pdf) is then bimodal and well-approximated by the sum of two Gaussian distributions as shown in Fig. 2.6.

At first glance, the cycle described by the pendulum for these aspect ratios seems to turn clockwise, which is theoretically not possible for a hysteretic cycle based on subcritical bifurcations, as such cycles are normally traveled across counterclockwise. This questions the stability of the equilibrium positions defined by Eq. 2.1. The hysteretic cycle for the disk results from the C_N coefficient, which is considered to be a function of θ, *i.e.* for any angle θ, the C_N coefficient is uniquely defined or does not exist.

If the C_N coefficient is no longer a function, and can admit 2 values for a given angle, then an angle can be attained for two different flow velocities and the bistable zone may be explored in a more exotic way than a simple hysteresis. In the literature, such behavior on the C_N coefficient has been observed, in particular for the squareas shown in Fig. 2.7.a [7]. Similarly NACA profiles may also present C_N bistability [12], even without even adding to the dynamic stall which is intrinsically hysteretic [13].

A possible explanation for the observed clockwise (red in Fig. 2.7.b) hysteretic cycle is then that it is part of a larger hysteresis (green in Fig. 2.7.b) that can be divided into 2 smaller hysteresis (blue in Fig. 2.7.b) at its edge. The existence of these smaller hysteresis may arise from the bistability of the C_N coefficient. The exotic cycle faced in

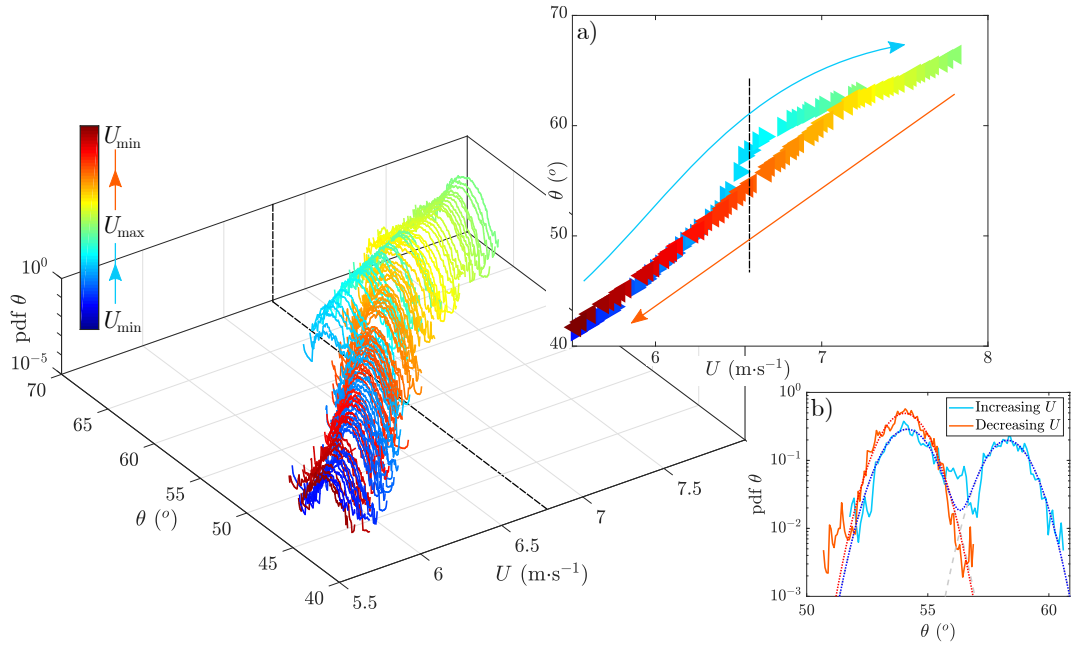

Figure 2.6: Details of the hysteretic cycle $\theta(U)$ for aspect ratio AR = 5/4, with probability density functions (pdf) of angular time series. From blue to green, the flow velocity is increased. From green to red, the flow velocity is decreased.
a) Time-averaged equilibrium angles as function of flow velocity.
b) Details of the pdf for $U = 6.5\,\mathrm{m}\cdot\mathrm{s}^{-1}$.

the experiment could then be the upward transition of the first cycle and the downward one from the second, thus resembling a clockwise hysteresis.

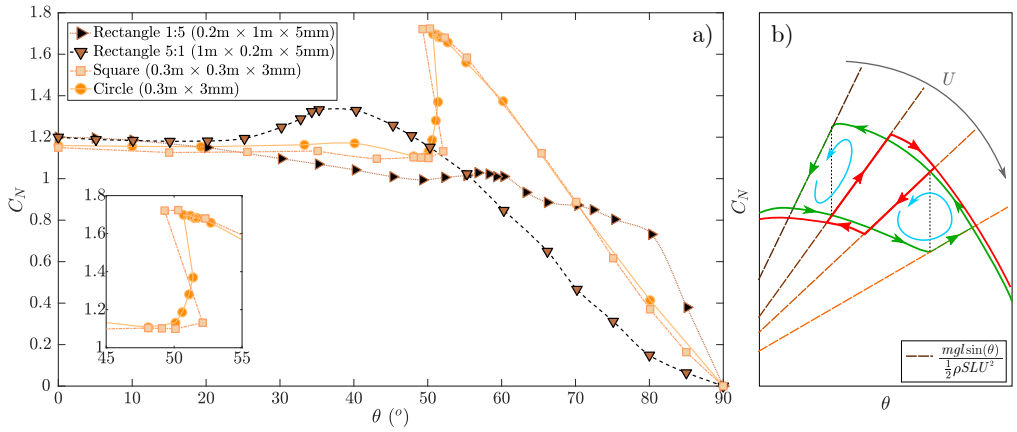

Figure 2.7: a) Detailed C_N coefficient from Flachsbart 1932 [7]. For the square and the circle, a hysteresis inherent to the C_N is observed. b) Schematic representation of the $\theta(U)$ bistability evolution (in red) in case of a bistable C_N coefficient. The clockwise hysteresis may result from the expression of two normal hysteresis (in blue) that are less likely to be observed experimentally, inside a larger hysteresis (in green).

This hypothesis could not be tested in the current experiment as we cannot measure the C_N coefficient directly and we are dependent on the stability of the equilibrium position to measure its C_N. To try our conjecture, the pendulum angle should be fixed and the pendulum attached to an aerodynamic scale, in order to measure both lift and drag. Such aerodynamic scale can be either a three-axis piezoelectric force sensor or a

more traditional setup with two scales, one for lift and the other for drag using a pulley to redirect the force to the vertical.

The particular case of AR = 1 has not been tested with the same PVC plate and thus will not be discussed here. *Examples of the obtained hysteretic cycle for square plates are presented in Annex A.2 for* 2 *configurations, the chord being the side of the square or the chord being the diagonal. The plate was thinner (about* 600 µm*-thick) and larger (*6 cm*-wide).*

In the literature, this case is covered by Eiffel, Föppl, Flachsbart and Winter [5–7, 14], thus providing us with a reference framework for the comparison of our results. Note that, in Chapter 3, the fully taped fly-swatter presents an aspect ratio AR = 1, which could also serve as reference.

Interlude

A natural question emanating from the discussion on the existence of the $\theta(U)$ bistability is whether there exists a mathematical criterion to the possibility of such bistability.
The sole equation of equilibrium of the pendulum (Eq. 2.1) is not sufficient to predict the existence of one or multiple solutions to it. In dynamical systems, a way of checking such existence is to investigate the stability of the possible solutions through their derivative – the curvature of the potential energy. If there exists a solution for which the derivative is positive, it is unstable and with Poincare-Bendixon theorem as there is at least one stable solution, there are another one for each unstable position. For the bistability to be unattainable, all possible equilibrium positions need to be stable and thus verify the following condition:

$$\forall \theta, U, \quad mgl\cos(\theta) > \frac{1}{2}\rho S L U^2 \frac{\mathrm{d}C_N}{\mathrm{d}\theta}$$

This is only verified for all θ and U if $\frac{\mathrm{d}C_N}{\mathrm{d}\theta} < 0$. As long as there is one angle θ for which $\frac{\mathrm{d}C_N}{\mathrm{d}\theta} > 0$, there exists a pendulum configuration and a flow velocity for which this angle can be unstable. However, it is necessary but not sufficient as this angle may never be attained as the equilibrium position is set by $mgl\sin(\theta_{eq}) = \frac{1}{2}\rho S L U^2 C_N(\theta_{eq})$

The limit case of existence of the bistability requires the metastability of at least one equilibrium position which verifies the following equation:

$$\frac{\mathrm{d}C_N}{\mathrm{d}\theta}|_{\theta_{meta}} = C_N(\theta_{meta})\cot(\theta_{meta})$$

As $\cot(\theta)$ and $C_N(\theta)$ are both positive, a metastable position exists also only if an angle presents a positive derivative of C_N, $\frac{\mathrm{d}C_N}{\mathrm{d}\theta} > 0$. This provides with a second condition coupling C_N and its derivative for the existence of a bistability, as it can exist only together with two metastable positions.

2.4 DISCUSSION

2.4.1 *Global evolution of C_N with aspect ratio*

To present the results, we decided to separate aspect ratios between those greater and lower than 1, for the reasons we detailed in section 2.3.1. Yet it is also possible to look at the overall evolution of C_N over the whole range of aspect ratios, as was done by Eiffel in 1910, as shown in Fig. 2.8.a [5]. To do so though, the C_N coefficients are rescaled for better comparison with Eiffel's work. While Eiffel chose $\theta = 0°$ for its rescaling, we choose $\theta = 15°$ due to the difficulty of correct estimation of C_N at low angles and low velocity (see Fig. 2.8.b). This difficulty may be related to the higher sensitivity to turbulent noise at low flow velocity when the mean aerodynamic torque is very low as well. Another possibility could be the irregularity of the sharp edges of the plates as edges play an important role in the estimation of aerodynamic coefficients close to symmetrical configurations such as the horizontal or vertical.

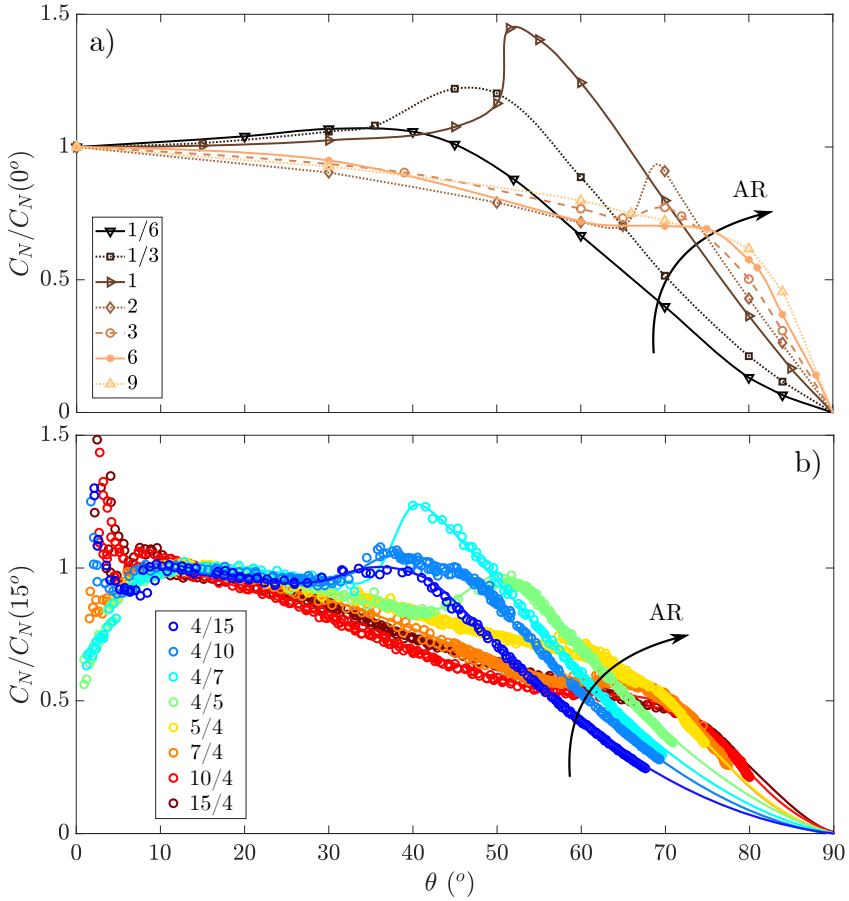

Figure 2.8: a)C_N measurements on rectangular plates of variable aspect ratios in 1910 (redrawn from [5]). b) Rescaled C_N coefficients as function of θ and aspect ratio. Color codes for the aspect ratio with green for AR = 1.

When comparing the evolution of C_N from Eiffel, measured using an aerodynamic scale, and ours, reconstructed from the pendulum, in Fig. 2.8, a qualitative agreement is observed. The same tendency is visible as we vary the aspect ratio from large to low. In particular, the variation of the C_N slope around $\theta = 90°$ is the same and

the displacement of the C_N inflection point shows a similar evolution. However, the results differ quantitatively on two aspects. First, the shape agreement between 1910 measurements and ours is not found for the same aspect ratios, in particular for high aspect ratios. Our AR $= 7/4 = 1.75$ presents a closer shape to AR $= 6$ for Eiffel than AR $= 2$. The second aspect that differs greatly between our results and the ones from Eiffel is the maximum value of C_N. While in Fig. 2.8.a) the maximum value of C_N is found for AR $= 1$, it is only attained for AR $= 4/7$ in Fig. 2.8.b). This quantitative variability can be attributed to the presence of the pendulum rod which may interact with the wake of the plate and artificially modify its C_N coefficient. Other factors, such as the turbulence rate, the sharpness of the edges of the plates or confinement effects from the closed test-section, might also play a role in the quantitative fluctuation.

Overall, this points to the high sensitivity of the C_N coefficient on many external factors.

2.4.2 *Evolution of the C_N stall angle with the aspect ratio*

A interesting feature from the C_N evolution described above is the variation of the stall angle position. As stall can be difficult to estimate for aspect ratio far from 1, we consider the C_N stall angle θ_{stall} to be the point of maximal curvature of the C_N coefficient ($\frac{\mathrm{d}^2 C_N}{\mathrm{d}\theta^2}$). For aspect ratios close to 1, this corresponds to the conventional stall angle, as described in Chapter 0.

This angle θ_{stall} is found to increase monotonously with the aspect ratio, as shown in Fig 2.9.a. Despite the previous lack of quantitative agreement between the measurements made by Eiffel and ours, the position of the stall angle seems far more robust as both data sets collapse on a single curve over their common range of aspect ratios. From this first observation, the nature of the guiding curve is to be determined, in particular to try understand what drives this C_N stall.

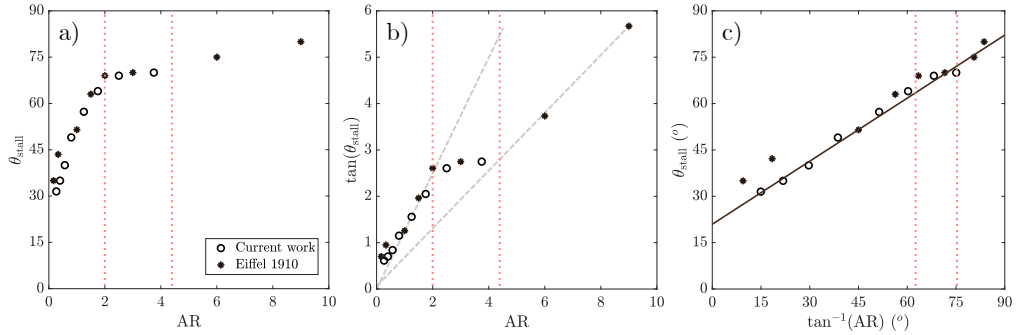

Figure 2.9: a) Angle of C_N stall θ_{stall} as a function of the aspect ratio AR. b) $\tan(\theta_{\text{stall}})$ as a function of the aspect ratio. Dashed lines represent proportionality tendency at low AR and high AR. c) θ_{stall} as a function of atan AR. A linear function is fitted to the experimental data.

Looking first at the tangent of the stall angle with respect to the aspect ratio, three *behaviors* stand out (Fig 2.9.b). At low aspect ratios, up to 2, $\tan(\theta_{\text{stall}})$ increases rapidly and linearly with the aspect ratio, $\tan(\theta_{\text{stall}}) \simeq \frac{5}{4}\text{AR}$. It then comes to a plateau for aspect ratios from 2 to 4 at an angle of about 70° and finally increases linearly again with a smoother slope, $\tan(\theta_{\text{stall}}) \simeq \frac{5}{8}\text{AR}$. The ratio 1/2 between the slopes might be a

coincidence. An interesting point is that most birds present wing aspect ratios between 2 and 4, for instance hummingbirds present aspect ratios comprised between 3.2 and 4.4 [2]. As such, it would mean that despite the variations, the stall angle remains relatively constant. This could be important for flight stability especially during the molting of the flight feathers, molting which has been observed to be a possible strong constraint on the maximal size of flying birds [15].

Looking the other way round, not at the tangent of the stall angle but rather as the arc-tangent of the aspect ratio, another tendency comes out, as presented in Fig. 2.9.c. The stall angle follows a linear function of $\mathrm{atan}(\mathrm{AR})$. With a non-zero origin, it seems that rectangular plates always present a C_N stall no matter how elongated in the direction of the flow ($\mathrm{AR} \to 0$), at an angle $\theta_{\mathrm{stall}} = 20°$, corresponding to an angle of attack of 70°. When $\mathrm{AR} \to \infty$, the stall angle does not attain 90° but only about 82°. It means that an infinite-span plate of finite chord stalls at an angle of attack of about 8°. This is not far from the obtained estimation of 9° for a 2D-plate (of infinite span) [16]. With this consideration, the angle of stall could be approximated for any aspect ratio by the following equation:

$$\theta_{\mathrm{stall}} \simeq 20° + 0.68\,\mathrm{atan}(\mathrm{AR}) \tag{2.3}$$

This simple relation does not catch the particularity of the plateau between $\mathrm{AR} = 2$ to $\mathrm{AR} = 4$ but provides a first estimate to the stall angle. It can also be noticed that the plateau occurs around the particular point for which θ_{stall} and $\mathrm{atan}(\mathrm{AR})$ are equal, at about 70°. Though no explanation can be given at this stage, it resembles a lock-in, similarly to the frequency lock-in observed in vortex-induced-vibrations or flutter [17].

2.4.3 *Wake interpretation*

The wake behind the plate is intrinsically linked with the C_N coefficient, as we introduced in Chapter 0 and further discussed in Chapter 1. In particular, for finite-span wings, the drag and lift predominance is bound with the interactions between the leading-edge vortex and the wingtip vortices. Numerical simulations have been done in the recent years on plates of various aspect ratios to try understanding the influence of the angle of attack on the wake structure [9, 10].

Despite the lack of flow visualization in our experiment, the evolution of the wake with θ can be inferred from numerical simulations [9]. Figure 2.10 represents a schematic evolution of the wake as the angle of attack increases, going from a lift predominant regime ($\theta > 70°$) to the drag dominated regime ($\theta < 30°$). At intermediate angle around $\theta = 50°$, the plate of aspect ratio greater than 1 is already past stall, while the one lower than 1 is still lifting.

For low angles of attack (top panel of Fig. 2.10), the wake can be likened to the sole wingtip vortices as a strong pumping of the surface flow from the leading-edge reinforce these two vortices. For such angles of attack, the leading-edge vortex can only expand on a small height before separating and getting advected by the flow and is thus mostly unstable. As the angle of attack increases, the leading-edge vortex has more vertical space to develop and with it the wingtip vortices can no longer monopolize the leading-edge surface flow. The roll-up distance of these two vortices also diminishes up to the point that their rolling occurs before the trailing-edge. If the diameter of the wingtip vortices is much smaller than the distance between them, this enables the

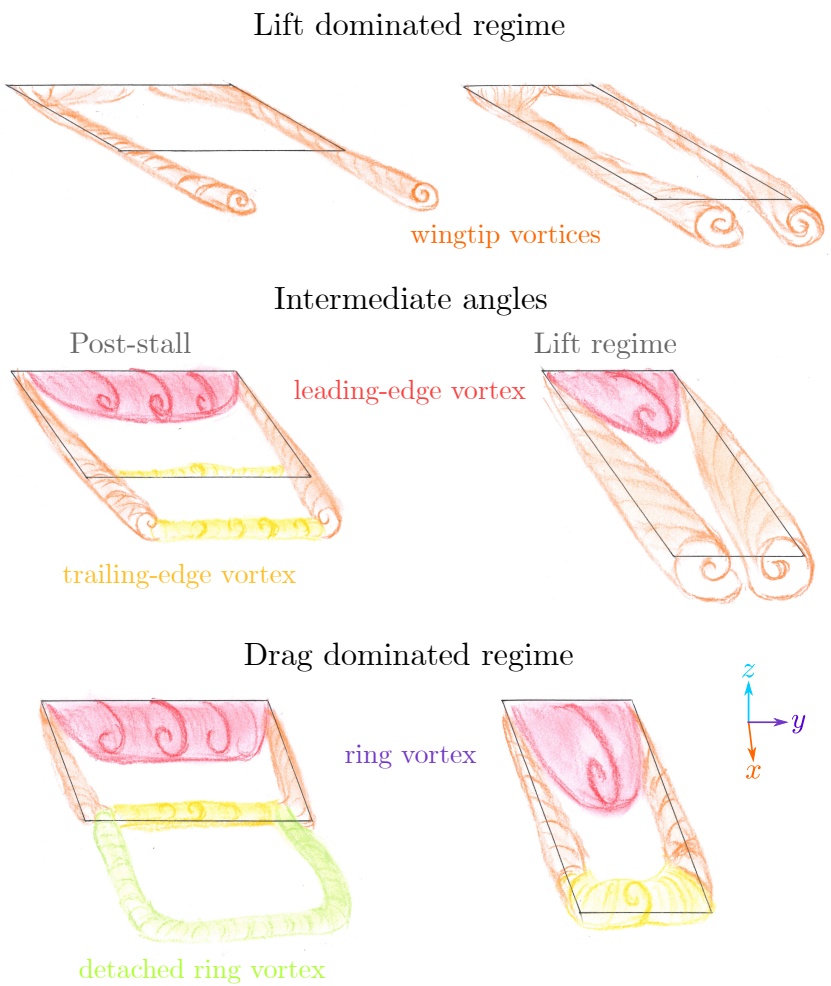

Figure 2.10: Left: AR > 1. Right: AR < 1. From top to bottom: $\theta > 70°$, $\theta \simeq 50°$, $\theta < 30°$. The wake evolves in both cases from two wingtip vortices to a ring vortex. For AR > 1, the transition occurs early in terms of angle of attack, and the ring vortex easily detaches. On the contrary, for AR < 1, the wingtip vortices remain predominant for a long range of angles and the then-formed ring vortex is quite stable as leading-edge and trailing-edge vortices attach on a wide area stream-wise. Partially redrawn from [9].

formation of the trailing-edge vortex, which as it connects to the wingtip vortices creates the ring vortex.

For AR > 1, the wingtip vortices are thin compared to the span due to their spacing. Because of this, leading-edge and trailing-edge vortices can develop easily and the ring vortex can be achieved at low angles of attack. On the contrary, for AR < 1, the wingtip vortices occupy almost the entire plate completely rolled-up and impair the development of the trailing-edge vortex. As the chord is long, the pumping of vorticity from the leading-edge is not the main provider of vorticity. Only at high angles of attack is the leading-edge vortex strong enough to push around the wingtip vortices, which leaves space for the trailing-edge vortex to expand and connect to the ring vortex.

2.4.4 *Polar curves*

In addition to the C_N coefficient, the main interest for aerodynamicists are lift and drag coefficients. With only the normal C_N coefficient, it is not possible to reconstruct the real lift and drag coefficients, that also require the measurement of the tangential (radial) force. However, by using the expression of the lift-induced drag as $D_L = L\cot(\theta)$, the polar curve defined by $C_L = C_N \sin(\theta)$ and $C_{D_L} = C_N \cos(\theta) = C_L \cot(\theta)$ is at least qualitatively correct, if not quantitatively. For instance, for the disk, using the measurements from Flachsbart 1932 [7], the drag corresponds to the lift-induced drag and the lift estimated by $C_L = C_N \sin(\theta)$ collapses onto the original lift measurements. In that case, no tangential contribution is observed and the quantitative agreement is even reached, also supported by further experiments by Winter in 1936 [14]. In our case however, as no experimental verification has been done on the tangential force, we will not presume the quantitative character of the lift and drag coefficients.

In Fig. 2.11, the polar curves for both AR < 1 and AR > 1 are presented. A first observation is that drag or lift predominance is not entirely separated by stall. In particular, for all tested aspect ratios above 1, lift predominance lasts to much higher angle of attacks than the stall angle (Fig 2.11.b). In fact, when coming back to the expression $D_L = L\cot(\theta)$, the lift or drag predominance changes at $\theta = 45°$ no matter the configuration. Hence, it is not because stall occurs that lift is not higher than drag, at least in the plate configuration. On the contrary, for aspect ratios below 1, stall occurs after drag takes over lift in terms of angle of attack (Fig 2.11.a). *It could also be noticed that the extension of the definition of stall from section 2.4.2 can be interpreted as the angle from which the lift coefficient stops increasing and either attends a plateau or drops suddenly for aspect ratios greater than* 1.

Another interesting trait is how the lift varies in the lifting part for a fixed drag coefficient. For instance, for $C_D < 0.2$, the lift coefficient increases with the aspect ratio, like in animal flight [18, 19].

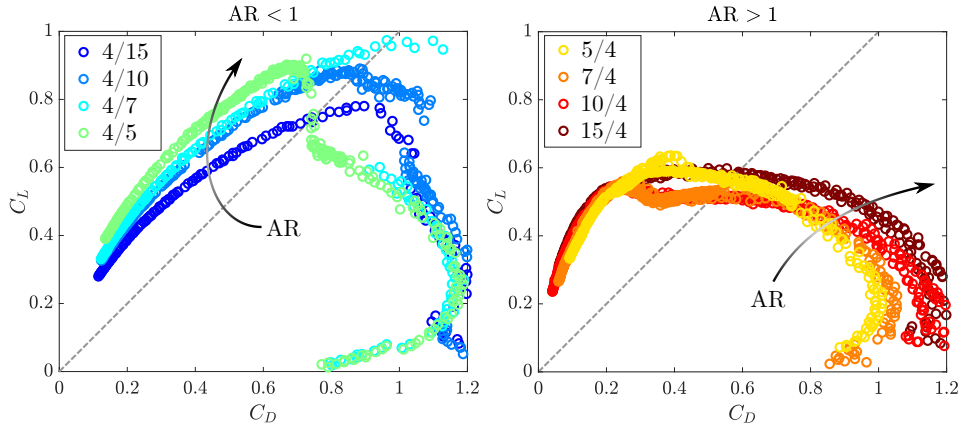

Figure 2.11: a) Polar curves for aspect ratios below 1. b) Polar curves for aspect ratios above 1. Color codes for the aspect ratio, with dark blue the lower and maroon the higher. Dashed line corresponds to the identity $C_L = C_D$.

2.5 PERSPECTIVES

This chapter investigates the depths of the aspect ratio on the aerodynamic coefficient through the use of the pendulum. As far as this chapter goes, a strong coupling intrinsic to the wake seems to be at the core of the stall. By switching wake configurations from two main wingtip vortices to a ring vortex, lift reaches a plateau or decreases abruptly while drag increases almost continuously. As such, the study of the aspect ratio influence on the C_N coefficient opens many questions on the overall dynamics of the wake and the relative importance of each vortex in the production of lift or drag.

The link between the angle of stall and the aspect ratio may be key to the understanding of the stall mechanism in 3D. In particular, the surface flow structure, like the angle that delimits the leading-edge vortex and the wingtip vortex, is observed in the literature to strongly depend on the angle of attack [20]. Visualizing the surface flow on the various rectangles for different angles of attack would be ideal to further our comprehension and understand how the angle of attack translates into a wake structure.

Another remaining question, that we did not comment on yet, is how the C_N coefficient at the stall angle varies with the aspect ratio. For both Eiffel and our measurements, as the aspect ratio increases, the C_N coefficient at θ_{stall} first increases and then decreases with a maximum around AR $= 1$. This non monotonic evolution hints at complex aerodynamic mechanisms in particular in the light of the change of the leading-edge- and wingtip-vortex stability with the aspect ratio.

The lock-in of the stall angle for aspect ratios around 3 is also a first observation that needs to be investigated, especially in the context of flight. For instance, two questions that might arise from this are the following:

- To what extent is the stall angle important in the dynamics of flapping flight?
- Has evolution favored aspect ratio in the lock-in region for flight stability?

REFERENCES

[1] J. R. Usherwood. "Physiological, aerodynamic and geometric constraints of flapping account for bird gaits, and bounding and flap-gliding flight strategies." In: *Journal of Theoretical Biology* 408 (2016), pp. 42–52.

[2] J. W. Kruyt et al. "Hummingbird wing efficacy depends on aspect ratio and compares with helicopter rotors." In: *Journal of The Royal Society Interface* 11.99 (Oct. 2014), p. 20140585.

[3] C. H. Greenewalt. "The Flight of Birds: The Significant Dimensions, Their Departure from the Requirements for Dimensional Similarity, and the Effect on Flight Aerodynamics of That Departure." In: *Transactions of the American Philosophical Society* 65.4 (1975), p. 1.

[4] F. Hertel and L. T. Ballance. "Wing Ecomorphology of Seabirds from Johnston Atoll." In: *The Condor* 101.3 (Aug. 1999), pp. 549–556.

[5] G. Eiffel. "Sur la résistance des plans rectangulaires frappés obliquement par le vent." In: *Comptes-rendus hebdomadaires des séances de l'Académie des Sciences* 151 (1910), pp. 979–981.

[6] O. Föppl. "Windkräfte an ebenen und gewölbten Platten." PhD thesis. Berlin, Heidelberg: Königlichen Technischen Hochschule zu Aachen, 1911.

[7] O. Flachsbart. "Messungen an ebenen und gewölbten Platten." In: *Ergebnisse der Aerodynamischen Versuchsanstalt zu Göttingen - IV. Lieferung*. München und Berlin: Verlag von R. Oldenburg, 1932, pp. 96–100.

[8] Y. C. Liu and F. B. Hsiao. "Aerodynamic investigations of low-aspect-ratio thin plate wings at low reynolds numbers." In: *Journal of Mechanics* 28.1 (2012), pp. 77–89.

[9] K. Taira and T. Colonius. "Three-dimensional flows around low-aspect-ratio flat-plate wings at low Reynolds numbers." In: *Journal of Fluid Mechanics* 623 (2009), pp. 187–207.

[10] T. Linehan and K. Mohseni. "Leading-edge flow reattachment and the lateral static stability of low-aspect-ratio rectangular wings." In: *Physical Review Fluids* 2.11 (2017), pp. 1–23.

[11] M. Obligado, M. Puy, and M. Bourgoin. "Bi-stability of a pendular disk in laminar and turbulent flows." In: *J. Fluid Mech.* 728 (2013), R2.

[12] S. Mittal and P. Saxena. "Prediction of hysteresis associated with the static stall of an airfoil." In: *AIAA journal* 38.5 (2000), pp. 933–935.

[13] I. A. Angulo and P. J. Ansell. "Influence of aspect ratio on dynamic stall of a finite wing." In: *AIAA Journal* 57.7 (2019), pp. 2722–2733.

[14] H. Winter. *Flow Phenomena on plates and airfoils of short span*. Tech. rep. National Advisory Commiittee for Aeronautics, 1936, p. 31.

[15] S. Rohwer et al. "Allometry of the duration of flight feather molt in birds." In: *PLoS Biology* 7.6 (2009).

[16] A. Fage and F. C. Johansen. "On the flow of air behind an inclined flat plate of infinite span." In: *Proceedings of the Royal Society of London. Series A, Containing Papers of a Mathematical and Physical Character* 116.773 (Sept. 1927), pp. 170–197.

[17] E. de Langre. "Frequency lock-in is caused by coupled-mode flutter." In: *Journal of Fluids and Structures* 22.6-7 (2006), pp. 783–791.

[18] U. M. Norberg. "Gliding Flight." In: *Vertebrate Flight*. Springer-Verlag, 1990, pp. 65–75.

[19] J. W. Kruyt et al. "Power reduction and the radial limit of stall delay in revolving wings of different aspect ratio." In: *Journal of The Royal Society Interface* 12.105 (Apr. 2015), p. 20150051.

[20] M. S. Genç et al. "Interaction of tip vortex and laminar separation bubble over wings with different aspect ratios under low Reynolds numbers." In: *Proceedings of the Institution of Mechanical Engineers, Part C: Journal of Mechanical Engineering Science* 232.22 (2018), pp. 4019–4037.

3

SOLVING THE HOLE PROBLEM OF THE FLY-SWATTER

How do holes influence the 3D-structure of the wake of a square?

3.1 INTRODUCTION

In addition to aspect ratio, shape and profile, another parameter can greatly affect the aerodynamic properties of an object: *porosity*. In this chapter, through the example of a fly-swatter, we aim at understanding how the presence of holes impacts on the wake of a flat plate.

3.1.1 *Natural porosity in Aerodynamics*

Porosity is defined by the fraction of "void" in a material. In Aerodynamics, this translates into the proportion of empty spaces in an airfoil/object into which the air can rush. The common consideration is thus holes. Among porous media in Aerodynamics, many are found in Nature and some have already been presented in Chapter 0.

A first example of natural "holes" is the molt of birds, mentioned in Chapter 2. Apart from some sea birds which molt all their flight feathers simultaneously, most birds molt step by step with only a few feathers growing at the same time [1]. Molting has been repeatedly observed to have strong aerodynamic implications [2–5] and the complexity of the molting pattern of some birds shows how gaps in wings may handicap flight [1, 6]. For instance, a marabout stork (*Leptoptilos crumenifer*) may molt two distant primary feathers simultaneously (see Fig. 3.1.a) and then a secondary feather alone, centered in the middle of the wing (see Fig. 3.1.b). As the secondary feathers constitute the major part of the trailing-edge, it is possible that their molting impacts more on the aerodynamic properties of the wing than the primary feathers.

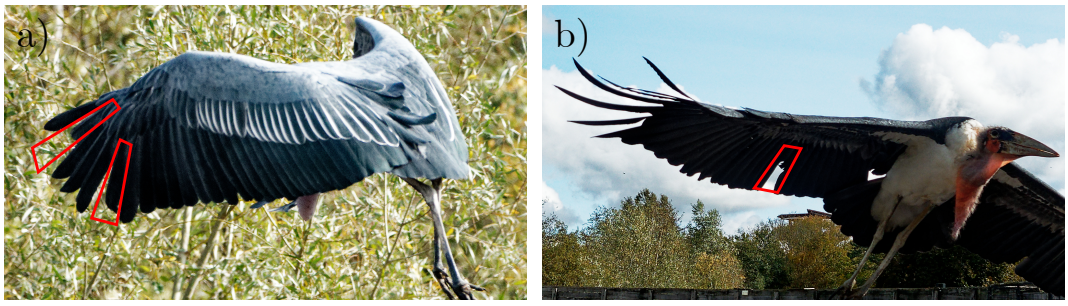

Figure 3.1: Marabou stork during molting. a) Primary feather molting (P6 and P10). b) Secondary feather molting (S10) (See A.1 for the nomenclature of bird feathers).

Another possibility for holes in bird wings is wing-feather damage, whose origin may span from predatory attempts to accidental collisions. Feather damage is usually

compensated by a molt but some birds cannot afford to molt due to a bad nutritional state for instance and have thus to fly with badly shaped wings. Despite the observation of such increased damage in owl populations, a quantitative estimate on the impact on their flight performance is yet to be done, in order for instance to understand whether bad nutritional state may become a vicious cycle [7].

Not all holes in bird wings are of the same size as those resulting from the molt. The structure itself of the wing is a porous medium, and in particular its feathers. Feathers are constituted with arrays of barbs and barbules with small hooks (see Fig. 3.2 that act like unidirectional Velcro® [8]. This almost fractal structure of the feather leaves a great deal of free space for the air to pass through and it has been observed that air permeates better in secondary feathers than in primary feathers, with a great discrepancy between the two sides of the feathers (inner vane vs outer vane) [9]. In addition to this micro-structural porosity, some flight feathers also present slight holes at the contact between the barbs and the rachis. These holes have been observed to enhance the lift to drag ratio by reducing drag with a functionality possibly similar to that of slats (leading-edge flaps) on airplane wings [10]. In contrast, small holes elsewhere on the feathers lead to reduced aerodynamic performance like acceleration and velocity, with no effects on maneuverability [11].

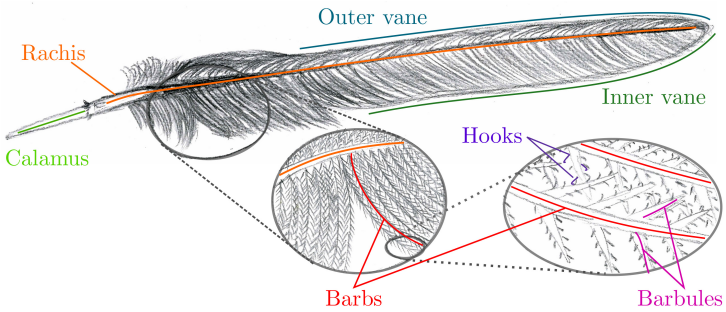

Figure 3.2: Anatomy of a flight feather. Drawing of a primary feather (P10) of a great cormorant *Phalacrocorax carbo* (personal collection).

Micro-structural porosity is found in yet other contexts, apart from feathers, in nature. One of the best examples is the dandelion seed which we presented in Chapter 0. The *pappus*, the small parachute that tops the seed, is composed of thin feathery bristles. The porous disk formed by these bristles drastically enhances drag when facing the flow compared to standard parachutes by inducing a strong stable ring vortex [12]. Compared to a solid disk, the ring vortex behind the porous disk is steadier as it is constrained by the flow going through the holed edges of the disk [13]. Some insects also use the same principle to fly with bristled wings [14–16].

Depending on the size of its empty spaces, porosity shows quite different aerodynamic effects. Small-scale pores tend to increase lift (equivalent to drag for parachutes) at small Reynolds numbers. Large holes however are prone to weaken aerodynamic performance.

3.1.2 *An everyday object as a pendulum*

Holes thus appear to have contradictory effects in Aerodynamics. To investigate the effect of porosity on the pendulum, we needed an object with holes, not too deformable and for which it would be easy to modify the porosity by filling the holes, for instance, or varying their diameter.

It would have certainly been possible to pierce holes in the disk plate, just as a hole of various diameters as was used to study the effect of holes on tumbling in free fall [17]. However, our daily life presents the ideal object for such study: the *fly-swatter*.

Patented in 1900 by Montgomery, the first modern fly-swatter, the "Fly-Killer", was composed of a rectangular wired net [18]. The use of wire-netting was introduced for durability and elasticity but no reference on the aerodynamic advantage of such netting is mentioned in the patent. In the later patents of Gatch in 1927 [19] and Brownson in 1938 [20], improvements on the fly-swatter mostly cover the handle, to facilitate the killing motion. In 1939, Baker patented a different kind of fly-swatter, made of a rubber surface with a few holes, which is supposed to act a pocket to trap the fly with the elastic recoil from the surface killing the fly without crushing it [21]. This change was motivated by avoiding property damage and traces when battling with and killing a fly. Here again however, no aerodynamic considerations are presented in the patents and it seems that holes were added empirically, to either reduce costs or increase elasticity.

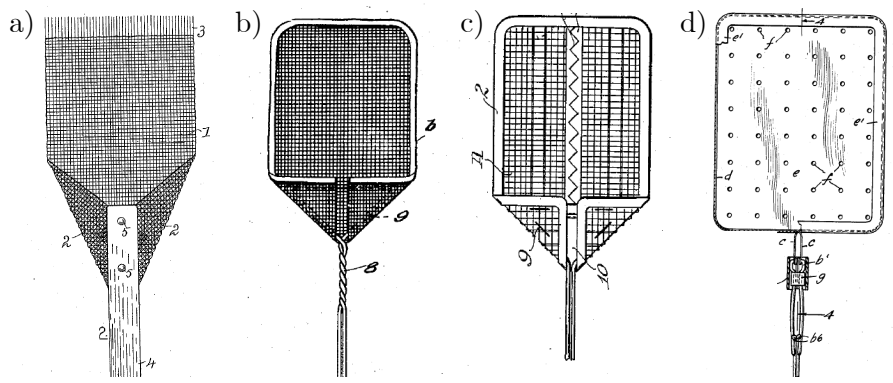

Figure 3.3: a) Fly-killer in 1900 from [18]. b) Fly-swatter in 1927 from [19]. c) Fly-swatter in 1938 from [20]. d) Fly-swatter in 1939 from [21].

The question is then if there is a particular aerodynamic advantage to having holes. A naive approach gives a partial answer. By having holes, the fly-swatter allows the air in front to go through it when it is swept. If it were solid, the air would be pushed away and the fly as well. This only gives a partial answer to our question as it does not take into account the size of the holes nor their aerodynamic properties.

The holes of a fly-swatter, about 2 mm-wide, are small enough to avoid the fly going through and escaping in the unlikely event of it making contact right at the hole. At this size, a hole is almost equivalent to a small vortex and small vortices are particularly advantageous for destabilizing large 3D vortex structures. By adding this consideration to the wake of a square plate and the link between the C_N coefficient and the wake structure from Chapters 1 and 2, it seems natural for the holes to greatly modify the lift and drag production of a fly-swatter, through the modification of the wake compared

to that of a square plate. In particular the C_N coefficient is observed for the fly-swatter to present an absence of sharp stall, as observed in Fig. 3.4.

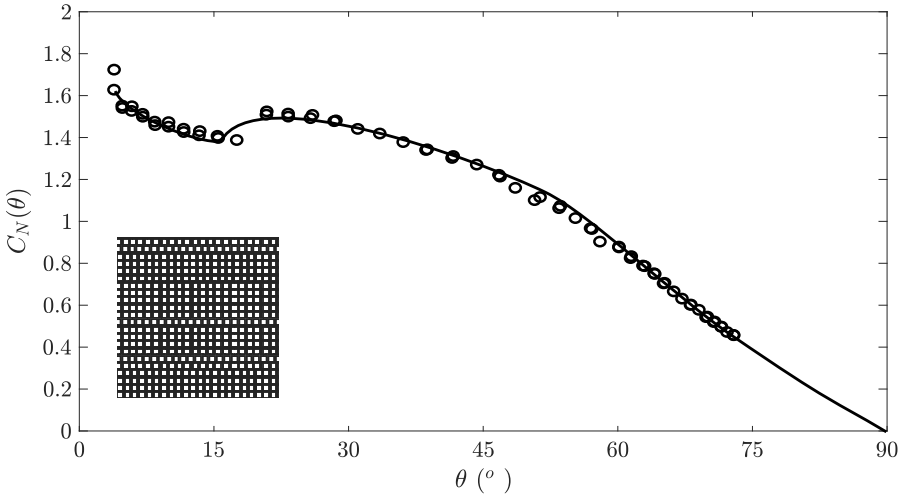

Figure 3.4: Aerodynamic C_N coefficient of the fly-swatter.

Preliminary observations of the transverse wake of a fly-swatter (Fig. 3.5) shows no significant evolution of the mean field nor standard deviations on both the vertical (w) and transverse (v) velocity with the angle of attack. As the fly-swatter is placed like a pendulum, we consider the angle θ with respect to the vertical, rather than the true angle of attack $\alpha = 90° - \theta$. The angle θ is also more relevant in the case of the fly-swatter, as the fly-swatter is meant to face the flow it sweeps in. For comparison, the reader is invited to refer to the evolution of the wake of a disk with the angle of attack presented in Chapter 1, in Fig. 1.2.

The lack of evolution of the wake from $\theta = 20°$ to $\theta = 80°$ is most likely due to the presence of the hole array in the fly-swatter. To understand how holes achieved such an effect on a square plate, the rest of this chapter will focus on how filling the holes modifies the C_N coefficient of the fly-swatter. In particular, the C_N coefficient of the fly-swatter shows no sharp stall, with only a slight stagnation below 20° as shown in Fig. 3.4 while for a solid square plate, Eiffel observed an especially sharp stall at about $\theta = 51°$ (see Fig. 2.8.a) [22]. Holes therefore seem to restructure the wake in a way that absorbs stall.

3.2 EXPERIMENTAL SETUP

To investigate the effect of the holes on the fly-swatter, we placed a square silicon fly-swatter[1] of size $a = 10\,\text{cm}$ in the wind tunnel in place of the standard disk pendulum (details of the pendulum are found in Chapter 0). The holes are squares of size 2.4 mm equally spaced at a distance of 1.8 mm. Each row and column of holes contains 22 holes, and in total 484 holes are present on the fly-swatter (see Fig. 3.6.a). The resulting porosity is $\dfrac{\text{surface of the holes}}{\text{surface of the whole square}} = \dfrac{484 \times 2.4 \times 2.4\,\text{mm}^2}{10 \times 10\,\text{cm}^2} \simeq 30\%$.

1 The exact reference of this particular fly-swatter has unfortunately been lost when it was bought on Amazon among other fly-swatters.

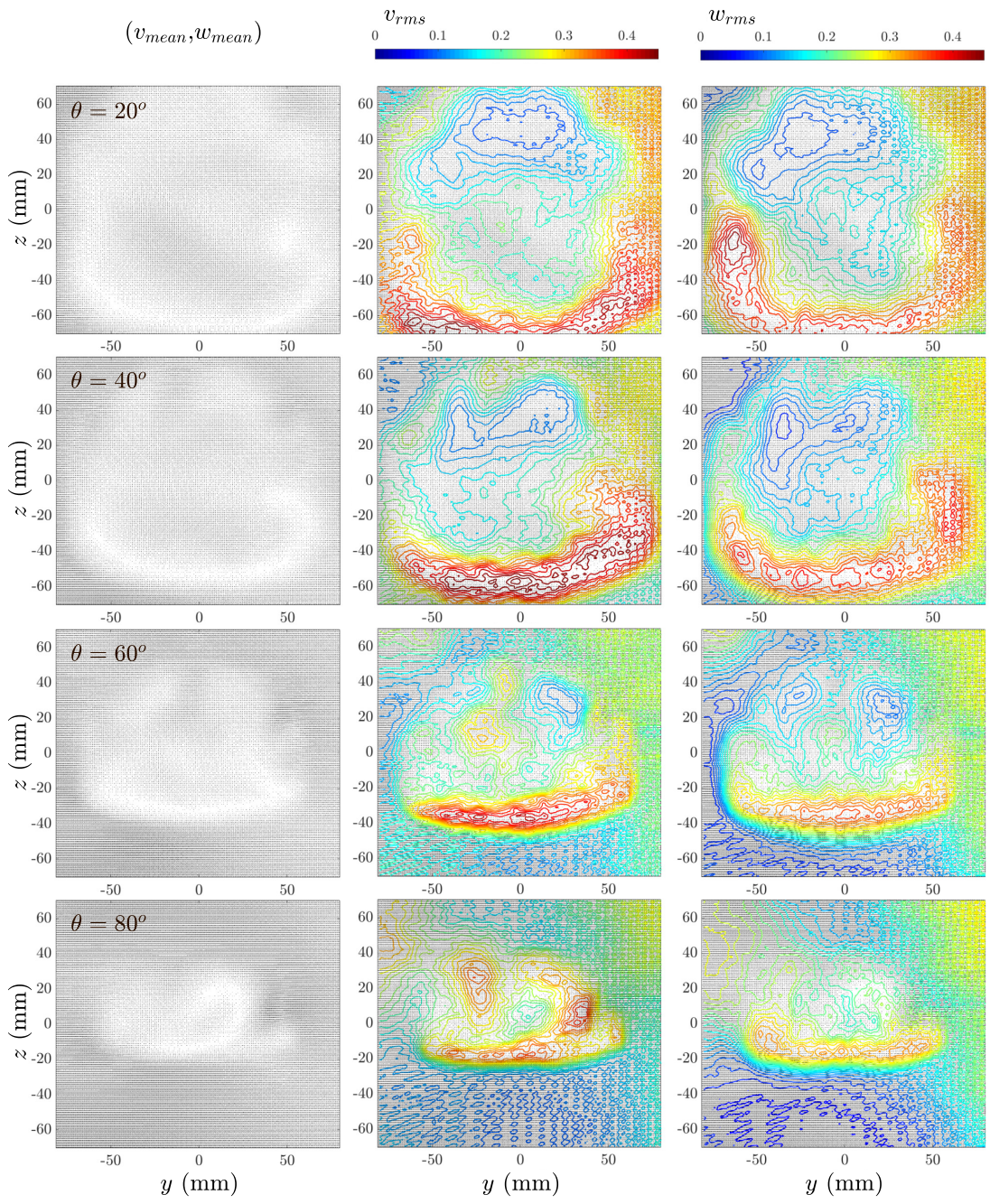

Figure 3.5: Mean wake transverse field of a square fly-swatter for different angles θ. From left to right: mean flow field (v_{mean},w_{mean}), transverse velocity fluctuations v_{rms}, vertical velocity fluctuations w_{rms}. From top to bottom: $\theta = 20°$, $\theta = 40°$, $\theta = 60°$, $\theta = 80°$

The aforementioned preliminary observations on PIV measurements were conducted on this fly-swatter.

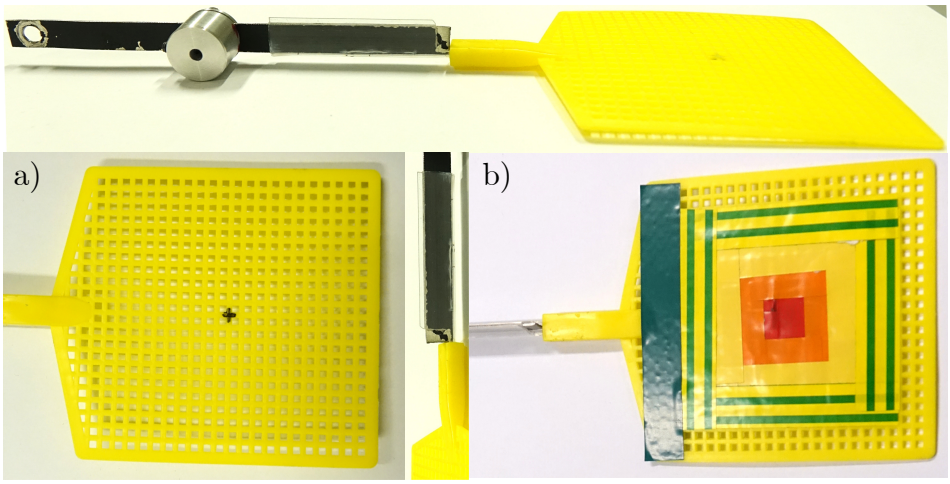

Figure 3.6: Fly-swatter used in the experiment from every angle, in original state (a) and partially covered in tape (b). The taped configuration corresponds to the minimal tested cover for the angular bistability to appear.

For the fly-swatter to move in a pendular fashion, it is placed facing the flow, at the end of a rod as demonstrated in Fig. 3.6 and attached to the air bearing, acting as the swivel. The distance between the pivot point and the center of the fly-swatter is $L = 17.3\,\text{cm}$.

To seal the holes of the fly-swatter, we use vinyl tape of width 1 cm. Vinyl tape adheres well on silicon and no peeling was observed over the various experiments. The vinyl tape was placed so that only rows or columns of 2-hole width were sealed by one piece of tape. An example of a taped configuration is shown in Fig. 3.6.b.

A total of 18 different configurations of the hole-filling of the fly-swatter was tested. For 11 of them, due to a slight curvature of the fly-swatter, two sets of measurements were carried out, one with the curvature facing upstream and the other downstream, as will be presented in section 3.3.2.

For each configuration, the experimental protocol is the same as in Chapter 2, the flow velocity is first increased step by step and then decreased the same way. The mean angle is measured over 15 s to 2 h for each flow velocity and then the C_N coefficient is computed from the following static equilibrium equation:

$$mgl\sin(\theta) = \frac{1}{2}\rho U^2 a^2 L C_N(\theta) \tag{3.1}$$

In Eq. 3.1, we made the choice of ignoring the filling fraction for the area a^2 of the fly-swatter, as we expect it to not be a simple proportionality factor due to the aerodynamic coupling of holes in the array. This choice is also supported by the fact that all data collapses at low angles ($\theta < 15°$) as we will see in the following section on experimental results. In contrast, the mass m has been measured for each configuration, due to the vinyl tape adding up to 2 g to the fly swatter in full fill.

3.3 RESULTS

Of the 2^{484} possible configurations for the fly-swatter to be partially filled, we decided to choose only 18 respecting some symmetry. A common trait of all the tested configurations described hereafter is for instance left-right symmetry. For simplicity, we started concentrically filling the fly-swatter.

3.3.1 *Filling the holes concentrically*

The fly-swatter can be filled concentrically in two different ways, either from the center towards the edges or the reverse. Each filling step adds a two-hole wide square band to the preceding step, as indicated in Fig. 3.7.

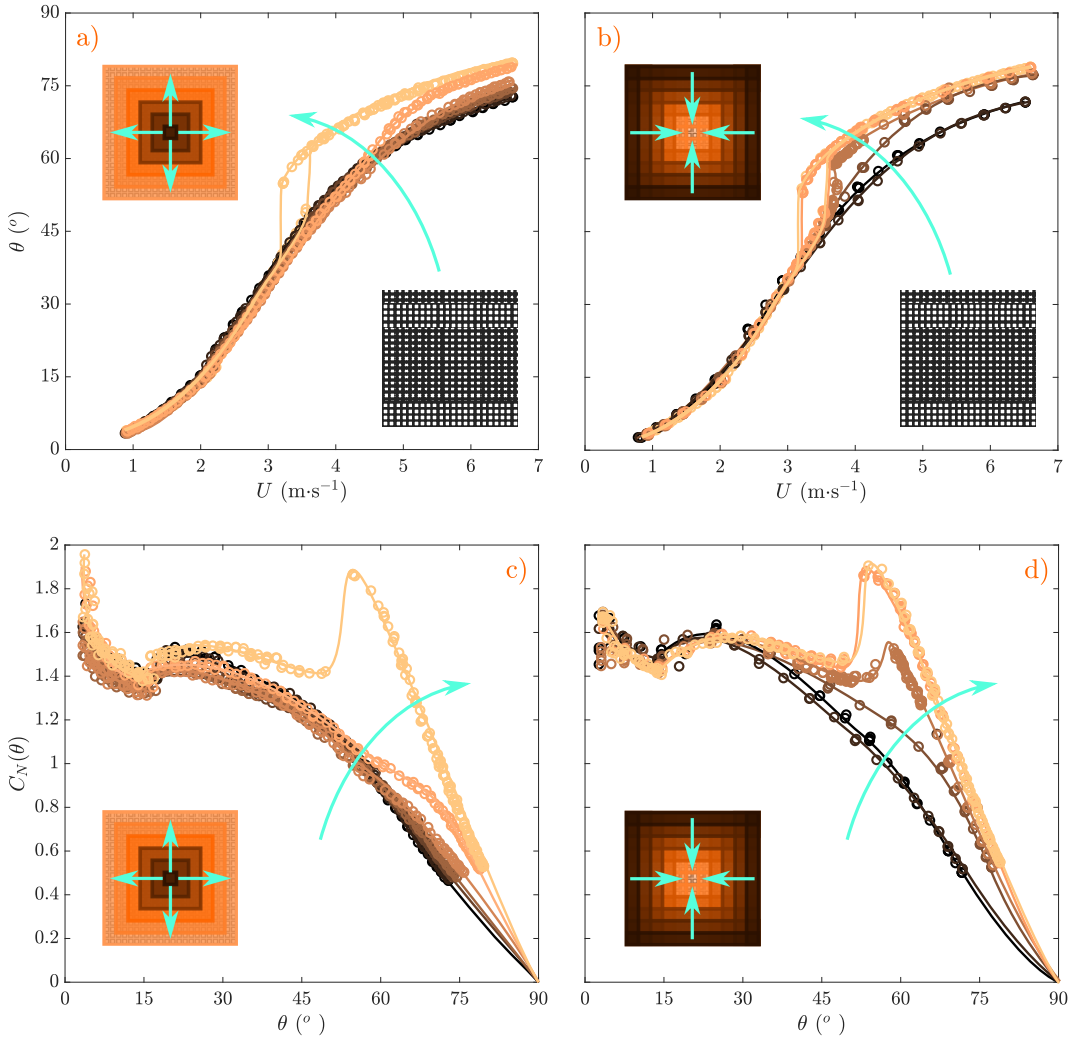

Figure 3.7: Influence of the concentric sealing of holes on the angular equilibrium positions and the C_N coefficient. Top (a,b): $\theta(U)$ portraits for different hole-sealing configurations. Bottom (c,d): associated C_N coefficient reconstructed using Eq. 3.1. Left (a,c): concentric filling starting from the center towards the edges. Right (b,d): concentric filling from the edges towards the center. Color codes for the configuration: the lighter the color, the more holes sealed.

Starting from the center, in Fig. 3.7.a, the $\theta(U)$ portrait does not vary much until the filling of the two last lines of holes at the edges. In particular, bistability is only present for the fully taped configuration. In contrast, in Fig. 3.7.b, when starting from the edges towards the center, an angular bistability appears from the 4th configuration, with a 6×6-hole square left unfilled. In both cases, the solid square (all holes filled) presents a large bistability. The reconstructed C_N coefficient (from Eq. 3.1) presents a sharp stall at $\theta = \theta_{stall} \simeq 53°$, quite close to that observed by Eiffel ($\theta_{stall} \simeq 51°$ in Fig. 2.8.a) and Flachsbart ($\theta_{stall} \simeq 49°$ in Fig. 2.7.a) [22, 23].

No significant changes are observed on $\theta(U)$ in Fig. 3.7.a) nor the C_N coefficient in Fig. 3.7.c) as the filling fraction is increased from the center, until the last fill. A slight increase of C_N at high angles ($\theta > 75°$), close to the horizontal, is observed for the second-to-last fill, for which only a band of 2 holes is left open at the edge. For the centerwise filling, in Fig. 3.7.d), the C_N coefficient evolves initially in the lift-dominated regime at high angles ($\theta > 60°$). Once this part of the C_N coefficient reaches its final value of the fully filled (solid) configuration, the separation of the drag and lift branches is initiated and grows to its maximal extent in the solid configuration. Almost no difference is observed between the solid case and the case when a 2×2-hole square is left open at the center.

From these results, it appears that for a sharp stall to exist, edges cannot be holed while the center has to be covered to a certain extent. In order to understand where exactly the sharp stall stems from, the filling of the edges lines has been refined. Before discussing it, we first observed that the fly-swatter could present a natural curvature, which would affect its aerodynamic response as we expose in the following section.

3.3.2 *Curvature effects on C_N coefficient*

When testing whether the side that is filled by the tape influences the appearance of the bistability, a collateral change has been observed. The fly-swatter is slightly curved and curvature can have a strong effect on aerodynamic properties, as observed already by Flachsbart in 1932 [23].

In the following, we will refer to the intrados as the concave part of the fly-swatter. When the intrados is facing the flow, it is the configuration in Fig. 3.8.a.

To test the influence of the side on which the tape is added, four sets of experiments were done per concentric filling configurations, two with the intrados on the same side of the tape and two with the tape opposite to the intrados. In the end, no influence of the tape was observed, while the orientation of the intrados seems to greatly alter the C_N coefficient as shown in Fig. 3.8.

In Fig. 3.8.a-b), the evolution of $\theta(U)$ with the filling is similar but a few small differences come to light. In particular, the bistable zone is much narrower when the intrados faces downstream (b) than upstream (a). For the same flow velocity, for instance $U = 6\,\mathrm{m} \cdot \mathrm{s}^{-1}$, the angle attained is much higher in the latter configuration, leading to a higher C_N coefficient for high angles, as observed in Fig. 3.8c-d. By looking at

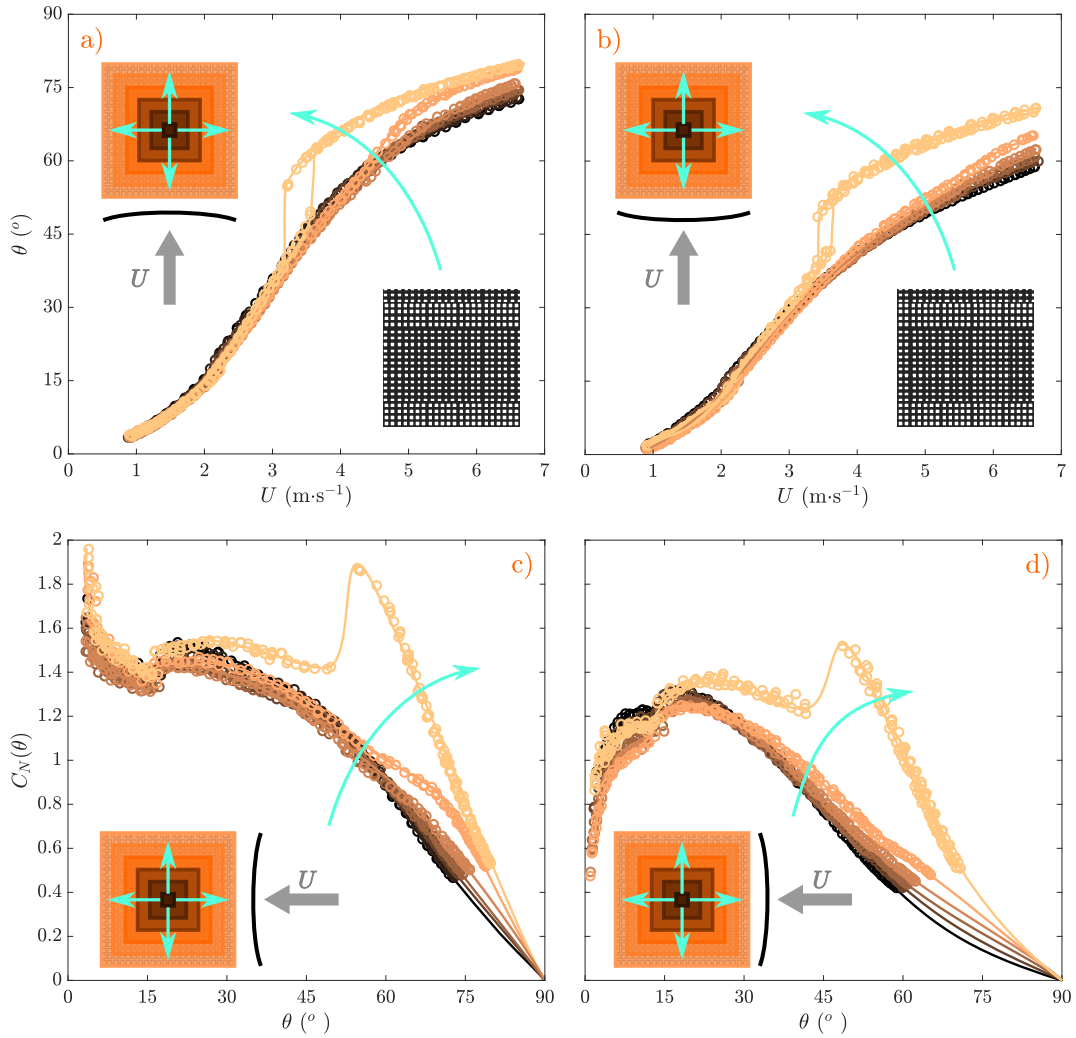

Figure 3.8: Influence of curvature on the aerodynamic response of the partially filled fly-swatter. Top (a,b): $\theta(U)$ portraits for two curvature configurations with concentric filling starting from the center towards the edges. Bottom (c,d): associated C_N coefficient reconstructed using Eq. 3.1. Left (a,c): Intrados facing upstream. Right (b,d): Intrados downstream-oriented. Color codes for the configuration, same as in Fig. 3.7.a) and 3.7.c.

angles instead of flow velocity, the difference is much smaller than anticipated. When the orange filling attains $\theta = 60°$ for both configurations, the solid case reaches $\theta = 68°$ for the downstream-facing intrados and $\theta = 70°$ in the upstream configuration. This impression of dissimilarity is more of an optical illusion due to the difference in flow velocity.

It is on the C_N coefficient (Fig. 3.8.c-d) that the difference between both curvature configurations is the most visible. On average, for all configurations and all angles, the C_N coefficient is much higher for the intrados facing upstream. A striking observation is on the sharpness of the stall. For the fully-filled fly-swatter, the stall is indeed much smaller when the intrados is facing downstream (d) than upstream (c), with a factor of two for the amplitude of the discontinuity.

Furthermore, in the low-angle region, in Fig. 3.8.c), C_N appears to diverge, while in Fig. 3.8.d), it seems to fall to 0. This is true whatever the filling configuration, which supports the conjecture that this is an effect of curvature. To better understand how such a difference arises, visualization of the wake and pressure measurements would be interesting. However it would require much more experiments and could not be done within the time frame of my PhD project.

Hence, in the following, as in the previous section, only the case of the intrados facing upstream (Fig. 3.8.a and c) is considered. Similar results are likely to be obtained in the other configuration, as has been verified for the concentric filling.

3.3.3 *Where stall starts*

From section 3.3.1, we know that bistability emerges only when filling the last two lines of holes on the periphery if the inner holes are all sealed. To understand the emergence of bistability in this final step, seven configurations with a partially filled periphery were tested.

We present in Figure 3.9, the configurations that expand the bistability. In Figure 3.10, the configurations, that despite a similar filling fraction present no bistability, are described.

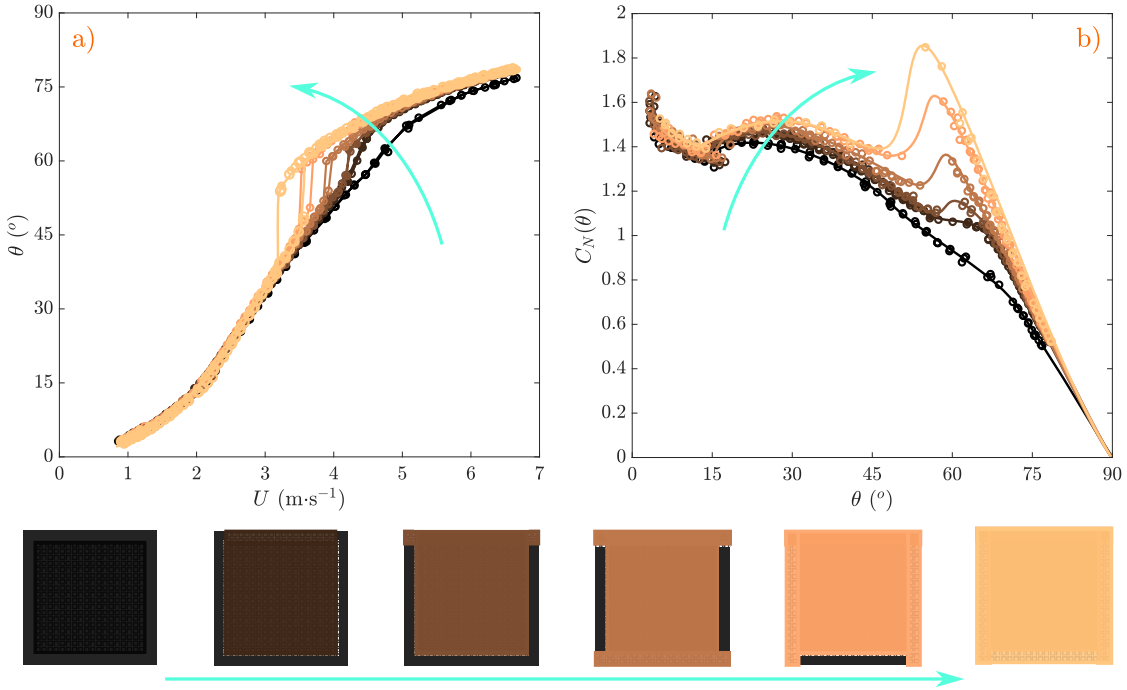

Figure 3.9: Expanding the bistability by partially filling the outer rows of holes on the fly-swatter. Color codes for the configuration, described at the bottom. a) $\theta(U)$ portrait. b) C_N coefficient reconstructed from a) and Eq. 3.1.

In Fig. 3.9.a), the two first configurations do not present any bistability, while it develops from the four others. From the third configuration, the range of bistable positions increases with the filling fraction. The bistability thus first arises, when in

addition to the center of the fly-swatter, the top two rows are covered with tape in their entirety in the third configuration. The filling of the two top corners seems fundamental, as, if they remain uncovered as in the second configuration, bistability does not exist.

In Fig. 3.9.b), the same increase is observed for the C_N coefficient, with a higher increase for angles above 60°, seemingly correlated with the separation of the lift and drag branches of the C_N coefficient. More precisely, we can see that the filling of the two corners only brings a modification of the C_N coefficient for a few angles between 63° and 67°. This slight increase is nonetheless sufficient to induce a "sharp" stall as all other values remain the same, as an inflection point appears on the C_N coefficient. It marks the separation between the drag- and lift-dominated regimes. When the filling fraction increases, the lift-dominated part of the C_N coefficient gains ground in angle while the drag branch recedes.

A possibly coincidental characteristic, common between all these C_N coefficient with a $\theta(U)$ bistability, is the gap of unattained angles remaining quasi-constant. Indeed, despite the growth of the bistable region in flow velocity and in angles, it seems that the range of "forbidden" angles is almost constant, about 6°, while the stall angle shifts towards 50°. This observation is for now not understood and if not an experimental artifact, may be linked with wake properties unknown to us at this stage.

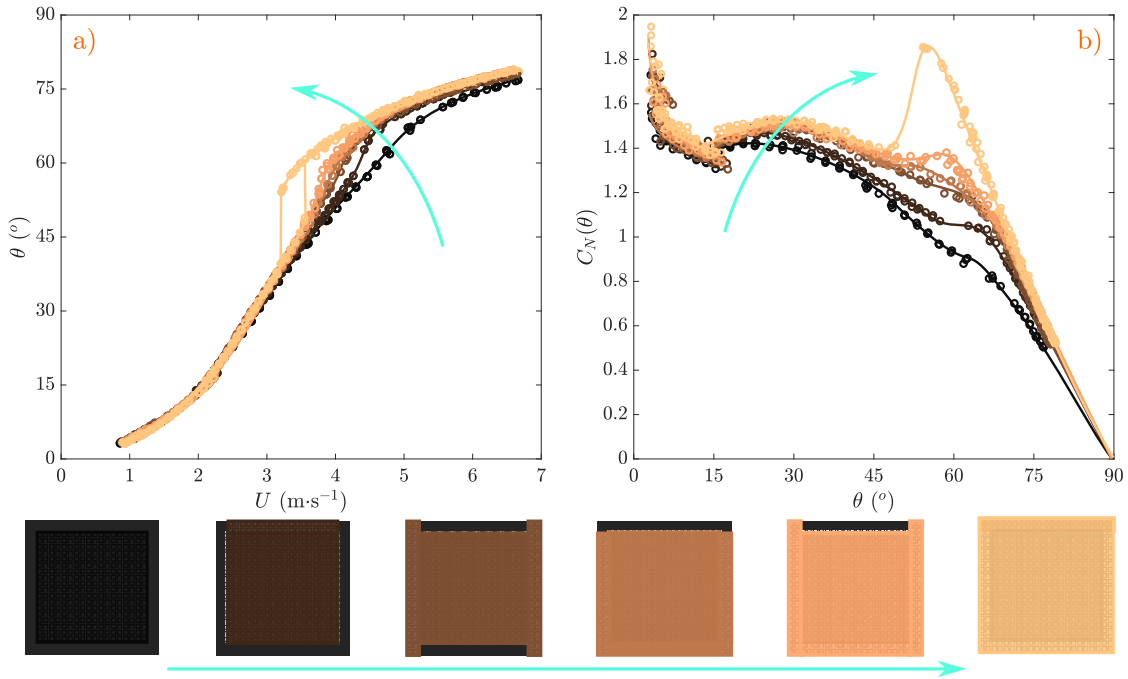

Figure 3.10: Partially filling the outer rows of holes on the fly-swatter without achieving bistability. Color codes for the configuration, described at the bottom. a) $\theta(U)$ portrait. b) C_N coefficient reconstructed from a) and Eq. 3.1.

For non-bistable configurations, in Fig. 3.10.a), no bistability is observed for any configuration apart from the fully filled one. The overall shape of the $\theta(U)$ portrait does not vary but to attain high angles like $\theta = 60°$, the flow velocity required is lower as is the filling fraction. A particularity of all non-bistable configurations tested thus far is the presence of holes on the upper rows.

Looking at the C_N coefficient (Fig. 3.10.b), the sharp stall is only present for the solid case (last configuration) and most of the variation between the configurations occurs in the range of angles $\theta \in [45°, 70°]$. Over the three last configurations of increasing filling fraction before the solid configuration, the C_N coefficient is observed to only slightly increase at $\theta = 60°$, while otherwise remaining the same. In particular, the addition of the two upper corners shifts $\frac{dC_N}{d\theta}$ from negative to positive at $\theta = 58°$ between the fourth and fifth configurations.

By matching the C_N coefficient evolution with the filling pattern of the fly-swatter, it appears that filling the lateral edges is sufficient for obtaining the C_N coefficient of the solid case on the drag branch ($\theta < 45°$) and on part of the lift branch ($\theta > 70°$). However, the region in which the sharp stall occurs for the solid case remains smooth if the whole of the upper rows is not covered.

This detailed study of the filling of the last two rows of the fly-swatter suggests that a necessary condition for the existence of the bistability is the filling of the upper rows from edge to edge. It is sufficient for the inner part of the fly-swatter to be covered as well, but not if only the edges are, as in Fig. 3.7.b. The minimal bistable configuration we have tested is thus the third one in Fig. 3.9, with the whole center covered and the two upper rows sealed as well in their entirety. It is possible that it is not the absolute minimal hole configuration , as $2^{484} - 18$, i. e. more than 4.9×10^{145}, filling possibilities remain.

3.4 DISCUSSION

3.4.1 *Wake and stall entanglement*

From section 3.3.3, knowing the filling fraction of the fly-swatter is not sufficient to predict the existence of bistability, as configurations with the same filling fraction (for instance: Fig. 3.9 4th configuration and Fig. 3.10 3rd configuration) present quite different behaviors and C_N coefficient. The filling fraction plays a quite distinct role on the C_N coefficient from that of the aspect ratio developed in Chapter 2.

The position of the sealed holes is key to understanding how the bistability and the sharp stall develop. As we already mentioned, a small hole can be seen as a small vortex and small vortices tend to destabilize large 2D structures when stabilizing 3D vortices. Therefore, when the upper rows of the fly-swatter are left open, it is likely that the leading-edge vortex, which is most a 2D vortex, cannot form properly (see Fig. 3.11 left). Similarly, when the side lines are not covered, it is more difficult for wingtip vortices to grow (see Fig. 3.11 middle). In particular, the wingtip vortex formation requires an anchor point for the roll-up, as they result from the finite span of the fly-swatter. When this anchor point is available but the sides remain holed, the wingtip vortices may be "lifted" above the fly-swatter (see Fig. 3.11 right) thus not acting to their full extent on the fly-swatter in terms of forces.

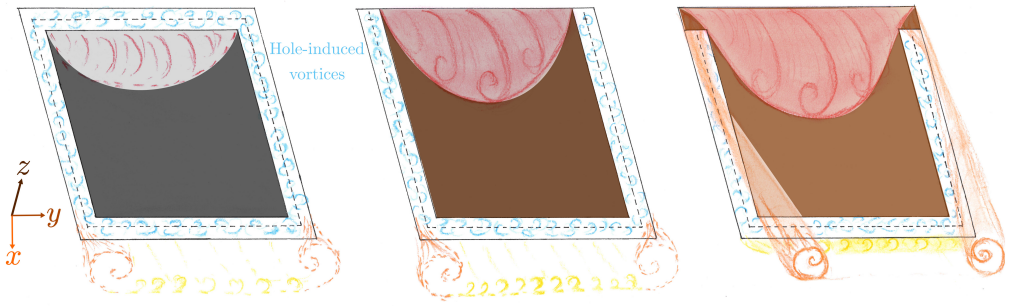

Figure 3.11: Schematic representation of the wake behind partially-sealed fly-swatters in the three first configuration of 3.9. The trailing-edge vortex is represented in yellow, the leading-edge vortex in red and the wingtip vortices in orange (same colors in Fig. 3). In blue are represented the hole-induced vortices.

Note that this is hand-waving phenomenology and a thorough PIV analysis is required to fully explain the aerodynamic mechanism at work in the process of stall for porous plates.

3.4.2 C_N *perturbation at* $\theta = 15°$

At $\theta = 15°$, the C_N coefficient presents a discontinuity whatever the hole configuration, as can be observed in Figures 3.7, 3.8, 3.9 and 3.10. To try to explain this phenomenon, two possibilities come to mind: one extended from Chapter 2 and the other from the literature.

As the discontinuity exists even when the fly-swatter square is completely sealed, it seems unrelated to holes. From Chapter 2, for θ about 20°, a longitudinal flat plate stalls. Since the fly-swatter is attached to a rod, resembling a longitudinal flate plate, the discontinuity might be an experimental artifact resulting from the interaction of the wake of the rod and of the fly-swatter. However, as the same rod was used for both the fly-swatter and the rectangles, we would expect the same perturbation on the C_N to be visible on the rectangle data, which is not the case as shown in Fig. 2.8.b.

In fact, when we consider the fully filled fly-swatter, there remain a few holes open at the extreme top, as the fly swatter is not strictly square, as presented in Fig. 3.6. Thus the discontinuity might be related to the holes in some fashion. To look for possible aerodynamic mechanisms from holes that could explain the bistability, perforated plates are a system quite similar to our fly-swatter [24].

In the case of perforated plates, when flow penetrates in the holes, a recirculation bubble is created in each hole and its size grows as the plate gets closer to the horizontal (Fig. 3.12). A conjectured estimate of the occupation ratio s/D of the recirculation bubble in the pore is given by:

$$\frac{s}{D} = \sin^{1.3}(\theta) \tanh\left(4\frac{t}{D}\right) \tag{3.2}$$

with t/D the aspect ratio of the pore defined in Fig. 3.12, formula adapted from [24].

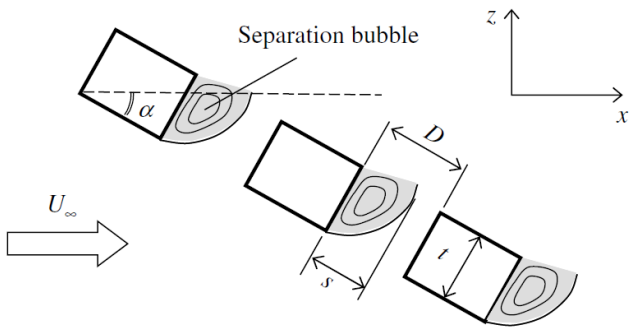

Figure 3.12: Schematic representation of the inner wake of a perforated plate, from [24].

For $\theta = 15°$, the occupation ratio of the recirculation bubble is estimated at $s/D \simeq 17\%$, which does not seem to present any particularity , as we would expect $s/D \sim 1$ to trigger a C_N discontinuity. This equation 3.2 however was formulated in [24] for a 2D plate and the exponent 1.3 and the factor of four are determined empirically. Hence, it would be presumptuous to fully consider this a correct estimation in our particular case.

3.5 PERSPECTIVES

By sealing holes on a fly-swatter, we observe the emergence of bistability. In all tested configurations that present a bistability, the upper rows are filled and a major part of the holes around the center are also sealed off.

Seen in a different light, the bistability of a square plate disappears as soon as holes are open on the upper rows, without impairing the lift production for angles $\theta > 70°$. Leading-edge porosity may thus be interesting for dampening stall. Surface porosity close to the leading-edge on airfoils has also been observed to reduce pressure load due to wing-vortex interactions [25].

An aspect we have not investigated here is the noise reduction by the holes on the fly-swatter. Indeed, porosity at the leading- and trailing-edge is often associated with noise reduction [26]. The small vortices induced by the pores destabilizes the two leading- and trailing-edge vortices, which are responsible to a large extent for the sound noise production of planes.

This effect of porosity was, in fact, first observed in Nature [27] and biomimetic concerns spread it to aerospace engineering [28].

Owls are particularly known for their silent flight and recent studies have shown how the particular structure of their flight feathers enables this feat [29]. The owl feather presents serrations at its leading-edge, and sometimes also throughout the inner vane. Serrations are an ultra-thin comb of barbules and increase the porosity of the feather. The comb breaks the two-dimensionality of the leading-edge vortex which is no longer sustained [30].

While a complete study on the noise produced by the fly-swatter depending on its number of holes is way beyond the scope of this thesis, the reader is invited to do a small experiment at home. The experiment consists in listening to the sweep of the fly-swatter both in its original perforated condition and with all its holes sealed.

REFERENCES

[1] E. S. Bridge. "Influences of morphology and behavior on wing-molt strategies in seabirds." In: *Marine Ornithology* 34.1 (2006), pp. 7–19.

[2] J. P. Swaddle and M. S. Witter. "The effects of molt on the flight performance, body mass, and behavior of European starlings (Sturnus vulgaris): an experimental approach." In: *Canadian Journal of Zoology* 75.7 (July 1997), pp. 1135–1146.

[3] P. Chai. "Hummingbird hovering energetics during moult of primary flight feathers." In: *Journal of Experimental Biology* 200.10 (1997), pp. 1527–1536.

[4] A. Hedenström and S. Sunada. "On the aerodynamics of moult gaps in birds." In: *Journal of Experimental Biology* 202.1 (Jan. 1999), pp. 67–76.

[5] S. Rohwer et al. "Allometry of the duration of flight feather molt in birds." In: *PLoS Biology* 7.6 (2009).

[6] A. E. Edwards and S. Rohwer. "Large-Scale Patterns of Molt Activation in the Flight Feathers of two Albatross Species." In: *The Condor* 107.4 (Nov. 2005), pp. 835–848.

[7] P. Piedrahita et al. "Integrity of and damage to wings, feather vanes and serrations in barn owls." In: *Zoology* 147.August 2020 (2021), p. 125930.

[8] L. Y. Matloff et al. "How flight feathers stick together to form a continuous morphing wing." In: *Science* 367.6475 (2020), pp. 293–297.

[9] W. Müller and G. Patone. "Air transmissivity of feathers." In: *Journal of Experimental Biology* 201.18 (1998), pp. 2591–2599.

[10] H. Eder, W. Fiedler, and X. Pascoe. "Air-permeable hole-pattern and nose-droop control improve aerodynamic performance of primary feathers." In: *Journal of Comparative Physiology A: Neuroethology, Sensory, Neural, and Behavioral Physiology* 197.1 (2011), pp. 109–117.

[11] P. Matyjasiak et al. "Feather holes and flight performance in the barn swallow Hirundo rustica." In: *Animal Cells and Systems* 22.2 (2018), pp. 124–131.

[12] C. Cummins et al. "A separated vortex ring underlies the flight of the dandelion." In: *Nature* 562.7727 (Oct. 2018), pp. 414–418.

[13] Y. Dong et al. "The steady vortex and enhanced drag effects of dandelion seeds immersed in low-Reynolds-number flow." In: *AIP Advances* 11.8 (Aug. 2021), p. 085320.

[14] S. Sunada et al. "Fluid-dynamic characteristics of a bristled wing." In: *Journal of Experimental Biology* 205.17 (2002), pp. 2737–2744.

[15] A. Santhanakrishnan et al. "Clap and fling mechanism with interacting porous wings in tiny insect flight." In: *Journal of Experimental Biology* 217.21 (2014), pp. 3898–3909.

[16] D. Kolomenskiy et al. "Aerodynamic performance of a bristled wing of a very small insect: Dynamically scaled model experiments and computational fluid dynamics simulations using a revolving wing model." In: *Experiments in Fluids* 61.9 (2020), pp. 1–13.

[17] L. Vincent, W. S. Shambaugh, and E. Kanso. "Holes stabilize freely falling coins." In: *Journal of Fluid Mechanics* 801 (2016), pp. 250–259.

[18] R. R. Montgomery. *Fly killer*. 1900.

[19] M. W. Gatch. *Fly swatter*. 1927.

[20] P. J. Brownson. *Fly swatter*. 1938.

[21] D. Baker. *Fly swatter*. 1939.

[22] G. Eiffel. "Sur la résistance des plans rectangulaires frappés obliquement par le vent." In: *Comptes-rendus hebdomadaires des séances de l'Académie des Sciences* 151 (1910), pp. 979–981.

[23] O. Flachsbart. "Messungen an ebenen und gewölbten Platten." In: *Ergebnisse der Aerodynamischen Versuchsanstalt zu Göttingen - IV. Lieferung*. München und Berlin: Verlag von R. Oldenburg, 1932, pp. 96–100.

[24] J. Xiong et al. "Body force model for the aerodynamics of inclined perforated surfaces." In: *AIAA Journal* 50.11 (2012), pp. 2525–2535.

[25] E. Eljack, I. AlQadi, and M. Khalid. "Numerical simulation of surface porosity in presence of wing-vortex interaction." In: *Aircraft Engineering and Aerospace Technology* 87.5 (2015), pp. 443–453.

[26] M. Zhang and T. P. Chong. "Experimental investigation of the impact of porous parameters on trailing-edge noise." In: *Journal of Sound and Vibration* 489 (2020), p. 115694.

[27] R. R. Graham. "The Silent Flight of Owls." In: *The Journal of the Royal Aeronautical Society* 38.286 (Oct. 1934), pp. 837–843.

[28] C. Rao et al. "Owl-inspired leading-edge serrations play a crucial role in aerodynamic force production and sound suppression." In: *Bioinspiration & Biomimetics* 12.4 (July 2017), p. 046008.

[29] T. Ikeda et al. "Morphology Effects of Leading-edge Serrations on Aerodynamic Force Production: An Integrated Study Using PIV and Force Measurements." In: *Journal of Bionic Engineering* 15.4 (2018), pp. 661–672.

[30] C. Rao and H. Liu. "Aerodynamic robustness in owl-inspired leading-edge serrations: a computational wind-gust model." In: *Bioinspiration & Biomimetics* 13.5 (July 2018), p. 056002.

Part II

AN EVENTFUL DAY

4 TAXONOMY OF THE PENDULUM DYNAMICS IN THE BISTABLE REGION

What temporal dynamics does the pendulum present in the bistable zone?

4.0 INTRODUCTION

This chapter is quite different from the others as it presents a variety of behaviors observed in the bistable region of the pendulum, without trying to understand them at this point. Some will be encountered again and explained in Chapter 5 and others have been described in Chapter 2. As such, the chapter will be divided in sections each corresponding to a "taxon" of behavior. A total of 5 different behaviors are documented here and not only can they be investigated for this particular pendulum, they can also be found in other bistable systems, as we will see in the following. The wind-swept pendulum used in this thesis may thus be used as a model system to understand in greater depth particular dynamics of dynamical bistable systems. The 5 events discussed here are the following:

1. Spontaneous one-way transitions,
2. Both-ways transitions,
3. Unstable position visits,
4. Overshoots,
5. Excursions.

4.0.1 *Multistability in fluid dynamics*

In Physics, and in particular in both Solid and Fluid Mechanics, the stability of any equilibrium state is always a central question for any studied system.

A standard example for this in Solid Mechanics is the number and stability of equilibrium positions for a homogeneous solid.
Though V. I. Arnold conjectured that the minimal number of equilibrium positions for a homogeneous solid would be 2 in 1995, it was only in 2006 that a solid verifying this conjecture would be constructed by Várkonyi and Domokos: the Gömböc [1, 2], and also exists in Nature as the shell of the Indian Star Tortoise (*Geochelone elegans*).

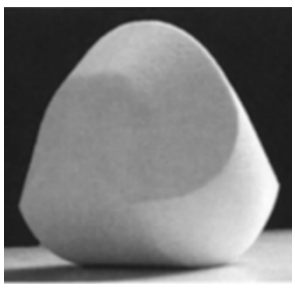

In Fluid Dynamics, the Navier-Stokes equations are still fully understood, even less so solved, as only the existence of multiple weak solutions in particular configurations has been mathematically proved [3–5]. From this on, multistability of flows is almost a given, which experiments and numerical simulations tend to confirm this.

Among common multistable flows, some arise from flow instabilities like Rayleigh-Bénard convection [6], while others are due to the presence of a solid-fluid boundary like the wake behind bluff bodies [7]. Fluid multistability is often geometrical, in the sense that the flow structure presents different equilibrium states (e. g.1-cell/2-cell configurations in Von Kármán flows). When this structure can not be observed, due to the lack of visualization possibilities for instance, other flow-derived quantities can be found to be multistable, such as the magnetic field in dynamo experiments [8], the torque difference between the rotating disks of von Kármán flows [9] or the wall shear stress in a rotating spherical Couette flow [10].

Other examples of multistable flows are found in climate sciences, such as flow streams, both zonal jets and ocean currents [11, 12]. Geometrical multistability is even observed in standard flow configurations like Taylor-Green vortices [13] or Taylor-Couette flows [14]. The transition to turbulence may be also seen as a bistable system, as for the same Reynolds number, both laminar and turbulent flows can exist [15].

In this plethora of multistable systems in Fluid dynamics, the aerodynamic bistability of the pendulum may be only one system among others [16]. However, its simplicity coupled with the diversity of its dynamics make it an ideal candidate to investigate some aspects of stochastic multistable phenomena. This chapter will thus present an overview of which aspects are explorable in our particular pendular system.

4.0.2 *Taming the bistability*

In the context of dynamical systems, bistability often occurs with a subcritical bifurcation.

In the pendulum case presented here, two parameters control the shape of the bistable zone in the (U,θ) space, both of them geometric. The first one is the shape of the pendulum itself, as discussed in Chapters 2 and 3. By changing the shape, one can influence the angular dependence of the C_N coefficient and thus the resulting bistability. As there is yet no common parameter to quantify the effect of the plate shape on the C_N, the first control parameter for the bistability is taken as the C_N coefficient itself, provided it is either referenced or can be known otherwise. The second parameter, once the overall shape is fixed, comes from the equilibrium equation (from Eq. 0.5), which can be rewritten as:

$$\frac{\sin(\theta_{eq})}{C_N(\theta_{eq})} = \frac{1}{2}\frac{\rho}{g}\frac{SL}{ml}U^2 = \gamma U^2 \tag{4.1}$$

The control parameter is then $\gamma = \dfrac{1}{2}\dfrac{\rho SL}{mgl}$ which is fixed by geometrical constraints such as the distance L between the swivel and the disk and the distance l between the swivel and the center of mass. As we know from Chapter 0, bistability occurs when, for one value of the flow velocity U, Eq. 4.1 has at least two solutions – three when one is unstable. At fixed shape, hence for a given $C_N(\theta)$, the bistable zone, in the (U, θ) space, can only deform in the flow velocity direction and not in the angular one.

Figure 4.1.a) presents the particular case of a disk that will interest us in the following. In this figure, the solutions of Eq. 4.1, the angles θ_{eq}, are plotted against the variable γU^2. For the range of γU^2 identified by γU^2_{min} and γU^2_{max} (dotted lines), 3 possible equilibrium positions θ_{eq} exist. U_{max} is the highest flow velocity for which bistability exists, and U_{min} the equivalent minimal flow velocity.

While this range $\gamma U^2_{max} - \gamma U^2_{min}$ (thus in the γU^2 space) is constant for a given shape, the range of flow velocity ΔU for which bistability occurs can be tuned via $\gamma U^2_{max} - \gamma U^2_{min} = \gamma \Delta U (U_{max} + U_{min})$. By varying only γ, it is possible to thus narrow or broaden the bistable range of the flow velocity.

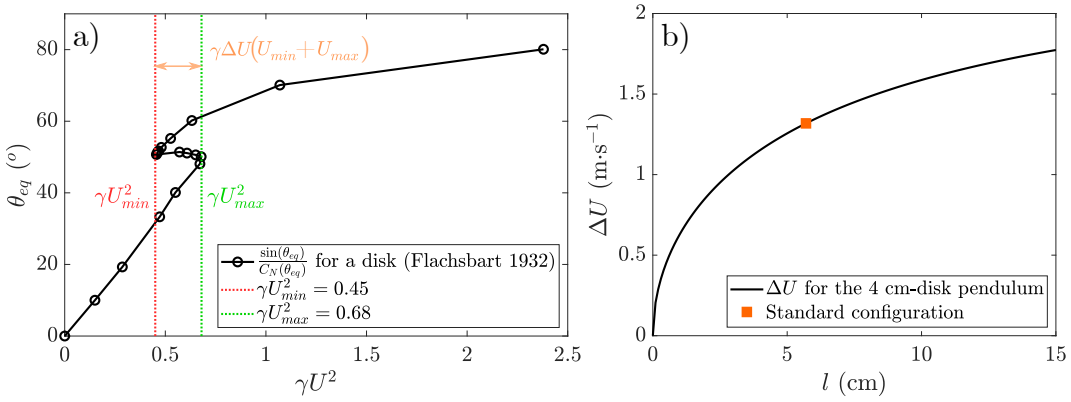

Figure 4.1: a) Solutions θ_{eq} to Eq. 4.1 as a function of γU^2 for a disk. The bistability range is delimited by the dashed lines. b) Theoretical ΔU as a function of the distance l between the pivot point and the center of mass for the standard 4 cm disk pendulum. The value for the standard configuration of $l = 5.7$ cm is shown by an orange square.

For a disk, the upper limit of multistability is $\gamma U^2_{max} = 0.68$ and the lower limit is $\gamma U^2_{min} = 0.45$, as shown in Fig. 4.1.a. Assuming the gravitational acceleration and the air density constant, respectively at $9.81\,\mathrm{m}\cdot\mathrm{s}^{-2}$ and $1.18\,\mathrm{kg}\cdot\mathrm{m}^{-3}$, it results that ΔU is a function of $\frac{ml}{SL}$ as:

$$\Delta U = U_{max} - U_{min} \simeq \sqrt{\frac{1}{\gamma}}(\sqrt{0.68} - \sqrt{0.45}) \simeq 0.62\sqrt{\frac{ml}{SL}} \tag{4.2}$$

This calculated ΔU is a theoretical estimate. In the experiment, the "real" ΔU is smaller due to ambient noise which destabilizes the extreme equilibrium positions and the turbulence rate which tends to smooth out the C_N coefficient.

To illustrate this, let us take the example of the standard 4 cm disk pendulum, which we can attach to different lengths, so that the distances from the swivel to the disk L and to the center of mass l vary, while keeping the distance $L - l$ between the disk and the center of mass constant. In this configuration, the ratio l/L can be rewritten as $\frac{l}{l + (L - l)}$, and thus only a function of l. Figure 4.1.b) presents the typical values of ΔU obtained for the standard 4 cm disk pendulum, used in the experiments and described in Chapter 0. The particular configuration that was used to study the transitions in this chapter and in Chapter 5 is marked by the square.

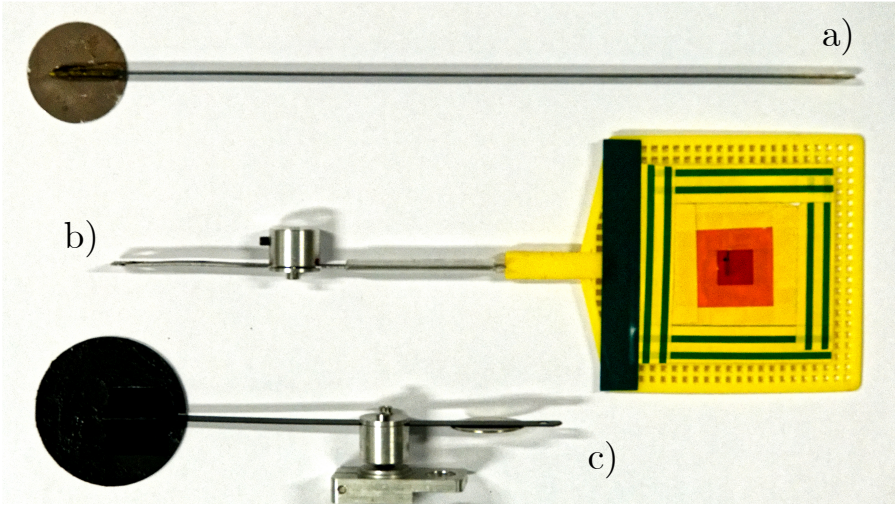

Figure 4.2: a) Standard 4 cm-pendulum. b) Fly-swatter in minimal bistable configuration (see Chapter 3). c) PIV 6 cm-pendulum.

A third way to modify the bistability, through the C_N coefficient, is to make use of the turbulence rate. It has been shown that incoming turbulence can modify the angular dependence of the C_N coefficient up to the disappearance of the bistability [16]. This will not be investigated here as such a study requires a specific apparatus in the wind tunnel. A few preliminary results, extended from [16], will only be briefly mentioned in Chapter 7.

4.0.3 *Experimental setup*

In this chapter, to investigate the different behaviors, three different pendulums have been used in Fig. 4.2

a) the *standard pendulum* with a disk of 4 cm diameter (details in Chapter 0), whose ΔU is represented in Fig. 4.1.b by the square.

b) the *fly-swatter* pendulum of minimal bistability (see Chapter 3),

c) and the *PIV pendulum* with a disk of 6 cm diameter used for the PIV measurements (details in Chapter 1).

An estimate of the maximal ΔU from Eq. 4.2 for the two disk pendulums is $\Delta U_4 \leq 1.3\,\mathrm{m}\cdot\mathrm{s}^{-1}$ for the standard pendulum and $\Delta U_6 \leq 0.72\,\mathrm{m}\cdot\mathrm{s}^{-1}$ for the PIV pendulum. The bistable velocity range is thus for the PIV pendulum only half the size of the one of the standard pendulum.

For the fly-swatter, as we have no measurements of C_N at fixed angles, it is difficult to estimate the extremal values of the C_N required in Eq. 4.2. In particular, extremal points are usually unreachable experimentally due to natural fluctuations. We have therefore no theoretical estimate of ΔU for the fly-swatter, though thz experimental ΔU is close to that of the PIV disk.

4.1 SPONTANEOUS ONE-WAY TRANSITIONS

When ΔU is large, as it is for the standard pendulum, only *one-way transitions* are observed, close to U_{min} and U_{max}. As we will see in Chapter 5, it is not that the reverse transition is not possible, but that it takes an infinitely long time on average to achieve. For instance, if we do a 3 h-long experiment with the highest flow velocity for which the bistability is observed $U \sim U_{max}$, only one upward D→L transition will be recorded, usually occurring in the first few minutes.

In Fig. 4.3, typical time series of recorded transition events are presented. The angle oscillates for a variable waiting time around an initial position, with fluctuations of about $1-2^\circ$ before suddenly jumping to another angle, whose value is substantially outside that of natural fluctuations. For an upward transition, the initial angle is about 47° for a final angle around 56°. For downward transitions, initial angles are about 53° with final angles about 43°. The waiting time ahead of the transition spans from a few seconds to more than a thousand seconds. This does not change whether the pendulum is attached using the potentiometer or the air bearing, only the intensity of fluctuations around each initial and final position varies from one configuration to the other (with damped fluctuations when the potentiometer is used due to the additional solid friction).

This particular one-way transition is the central event investigated in Chapter 5, so that we will no linger more on the subject. Similar one-way transitions are also observed in other systems, such as for instance von Kármán flows [9].

4.2 BOTH-WAYS TRANSITIONS

When ΔU is small, for instance $\Delta U < 1\,\mathrm{m}\cdot\mathrm{s}^{-1}$, transitions in both directions may occur for a given flow velocity.

For instance, with the fly-swatter, we can record bistable angular signals at constant flow velocity (see Fig. 4.4), for which the two equilibrium positions are switching back and forth over small characteristic time scales. In Fig. 4.4, 41 transitions between the two states are observed in a one-hour experiment. Such *both-ways transition* behavior has never been observed for the standard pendulum as presented in Fig. 4.1.

In addition to having a small velocity range for the bistability, the angular range of the bistability of the fly swatter is also much narrower, with a difference between the two stable positions less than 4°. While one may think this could be a reason for such jumpy behavior, the PIV pendulum also exhibits the same bistable switching. In Fig. 4.5, an angular time series is presented, with increasing the flow velocity step by step (about $\delta U \simeq 0.02\,\mathrm{m}\cdot\mathrm{s}^{-1}$) every hour. As shown on the probability density function (pdf) of the angle θ, the bistability evolves with the flow velocity U, with a strong bimodality of the pdf. The predominance of one position on the other changes from the lower position ($\theta \simeq 47^\circ$) one at low velocity to the higher position ($\theta \simeq 54^\circ$) for high flow velocity. While the relative proportion of each position over a given time varies with U, the difference $\theta_f - \theta_i$ between the upper and lower positions is almost constant, at about 6°.

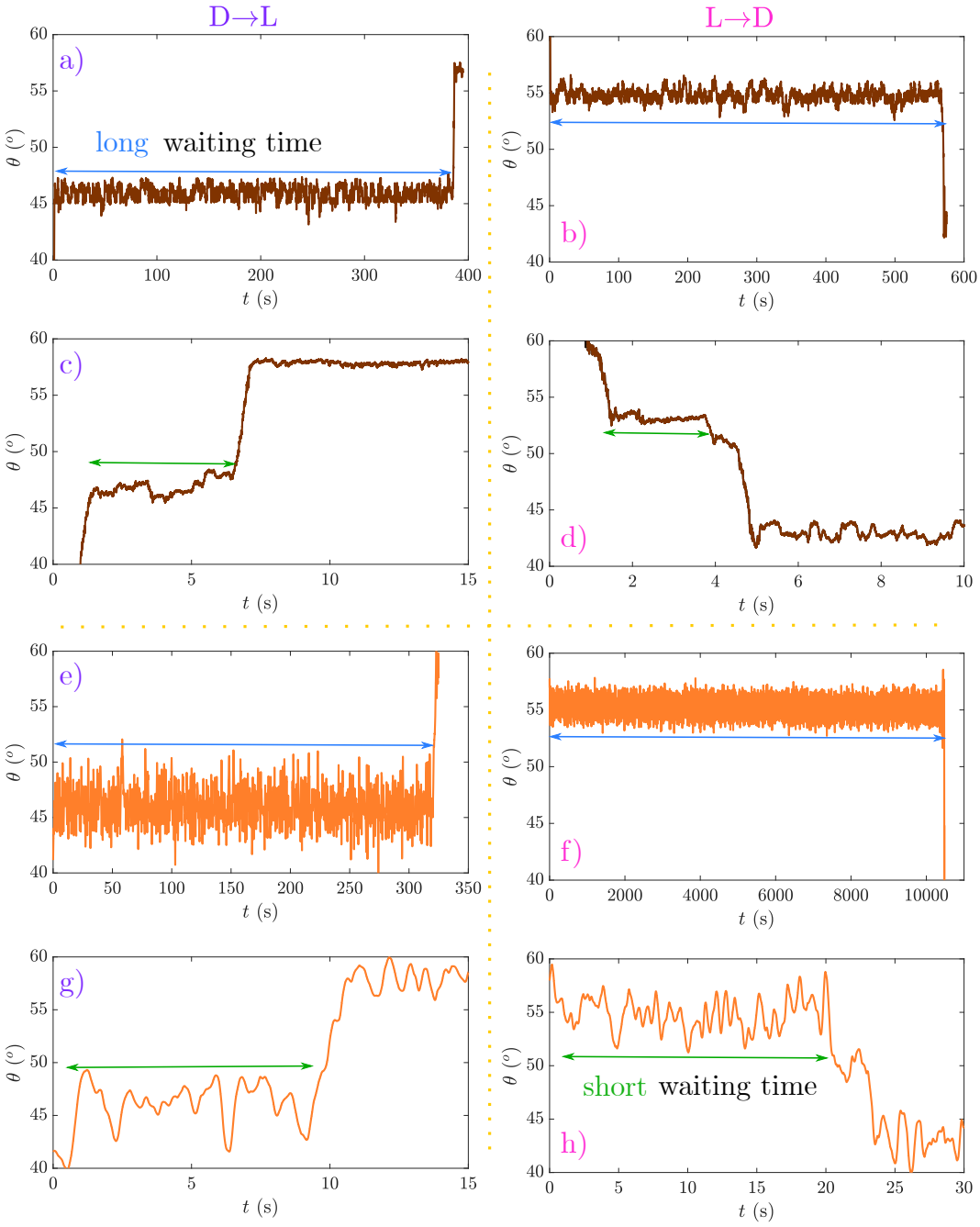

Figure 4.3: Examples of one-way transitions. a-d) Experiments conducted with the potentiometer. e-h) Experiments conducted with the air bearing. a,c,e,g: upward D→L transitions. b,d,f,h: downward L→D transitions. Both long and short waiting times ahead of transition are observed for all configurations.

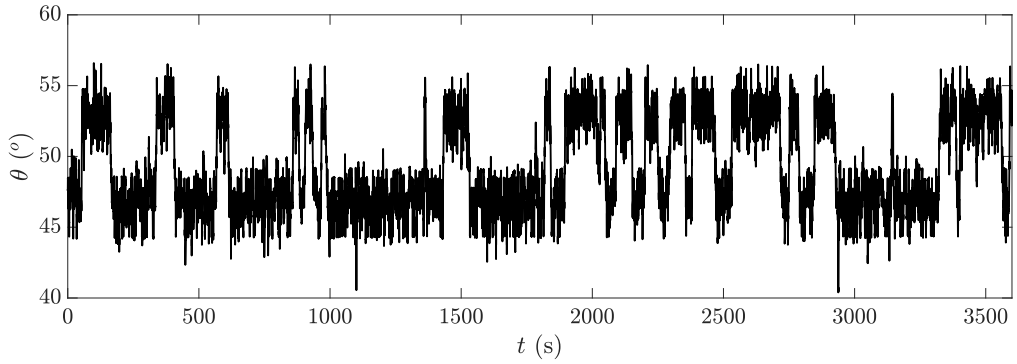

Figure 4.4: One-hour long angular time series $\theta(t)$ for the fly-swatter at constant flow velocity. The fly-swatter switches 41 times between two equilibrium positions, at $\theta = 48°$ and $\theta = 52°$.

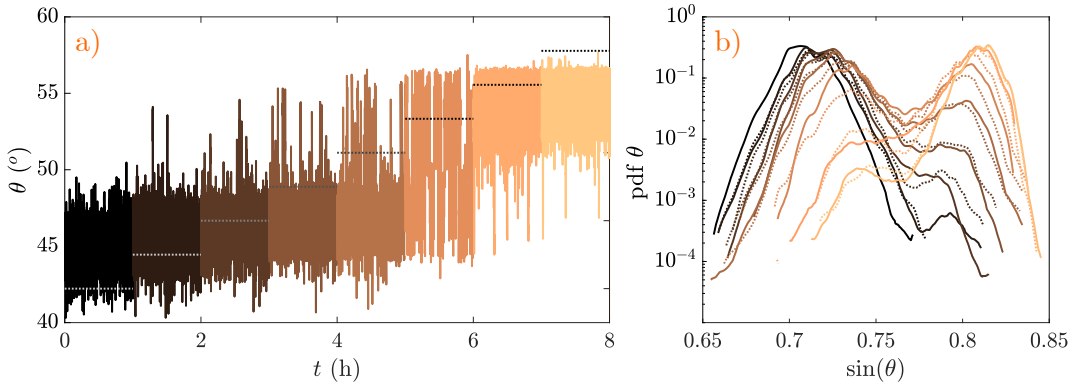

Figure 4.5: a) Angular time series $\theta(t)$ obtained with a step by step increase in flow velocity after each hour. b) Corresponding probability density functions (pdf). Color codes for the flow velocity. Dotted lines represent the same experiment with decreasing flow velocity. Experiments conducted with the 6 cm-pendulum used for the PIV measurements in Chapter 1.

Such bistable switching is observed in many fluid systems. In particular, geometrical bistabilities are especially susceptible to this kind of behavior. For instance, bluff body wakes present left-right reversals in their vortex structure [17], while magnetic field switches direction in dynamo experiment and simulation like in the Earth [18, 19].

4.3 UNSTABLE POSITION VISITS

During a transition, if an unstable equilibrium position exists between the two positions, sometimes the system may visit a brief instant this position. Such a position may not exist if at least one position is metastable. For a system with two stable positions resulting from a subcritical bifurcation, an unstable position is required to exist by the Poincaré-Bendixon theorem.

When the standard pendulum is placed in almost laminar flow (below 1% turbulence)[1], it may visit its unstable position during any transition, by slowing down at a particular angle as it transits. In Fig. 4.6.a), an example of such *slowdown* is presented for the angular time series. This phenomenon is best shown in the phase portrait $(\theta,\dot{\theta})$ in Fig. 4.6.b. Indeed, the phase portrait provides a complementary approach in particular as $\dot{\theta}$ directly translates the slowdown by first increasing as the transition starts, then returning close to 0 and increasing again to leave the unstable position and finish the transition. In Fig. 4.6.b), the slowdown is notably visible as all curves are two-lobed, while a direct transition is only one-lobed.

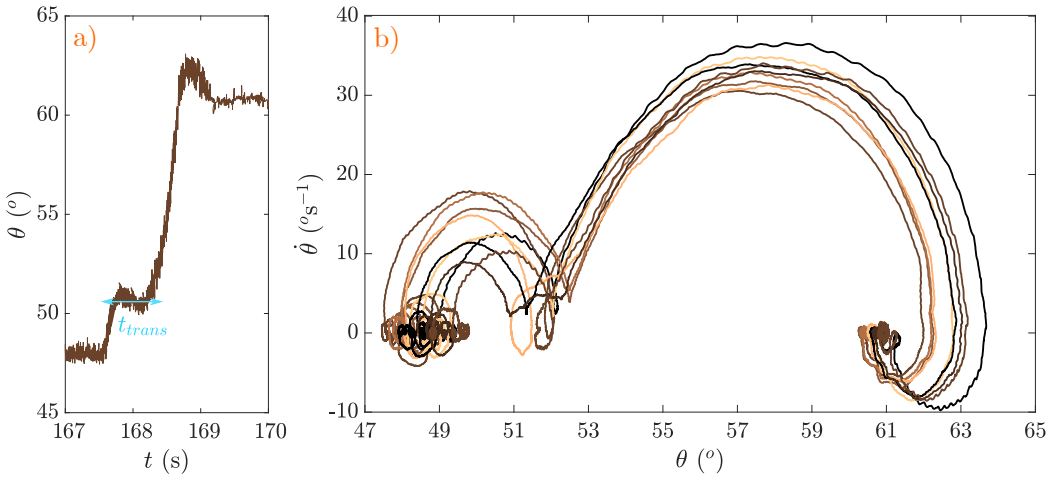

Figure 4.6: a) Angular time series $\theta(t)$ at the moment of transition. b) Phase portrait $(\theta,\dot{\theta})$ of various transitions. Experiments performed with the standard pendulum from Chapter 0 in the wind tunnel at LEGI in Grenoble.

Looking at the slowdown time t_{trans} (see Fig. 4.6) for each transition, it appears that this time t_{trans} spent in the unstable position follows an exponential law as shown by its cumulative distribution function in Fig. 4.7. Even with as few as 14 transitions, a characteristic time of transition τ_{trans} of about 0.55 s seems a good estimate for an exponential distribution for this particular set of experiments. It might be possible to reconstruct part of the energetic landscape using this time τ_{trans} and the characteristic time (τ_c^T, see Chapter 5) preceding transition in both directions, through for instance Kramers relations [20]. However, due to the separation of time scales between the upward and downward transition for the standard pendulum (about 6 to 8 orders of magnitude between the two times $\tau_c^{L\to D}$ and $\tau_c^{D\to L}$ for a given γU^2), this approach could not be pursued in the framework of this PhD thesis. Other configurations might be more interesting for this study, like the fly-swatter with its both-ways transitions.

The unstable position is not always visited during a transition. For instance, natural fluctuations may bring the pendulum close to the unstable position before returning to its initial position. For the fly-swatter that jumps intensively back and forth, the unstable position can be visited multiple times as shown in Fig. 4.8.a. The unstable position is represented in yellow.

1 The experiments in laminar flow were conducted in the wind tunnel of the LEGI in Grenoble, a wind tunnel similar to the one in Lyon though with much lower turbulence rate thanks to the presence of guide vanes and contraction ahead of the test section.

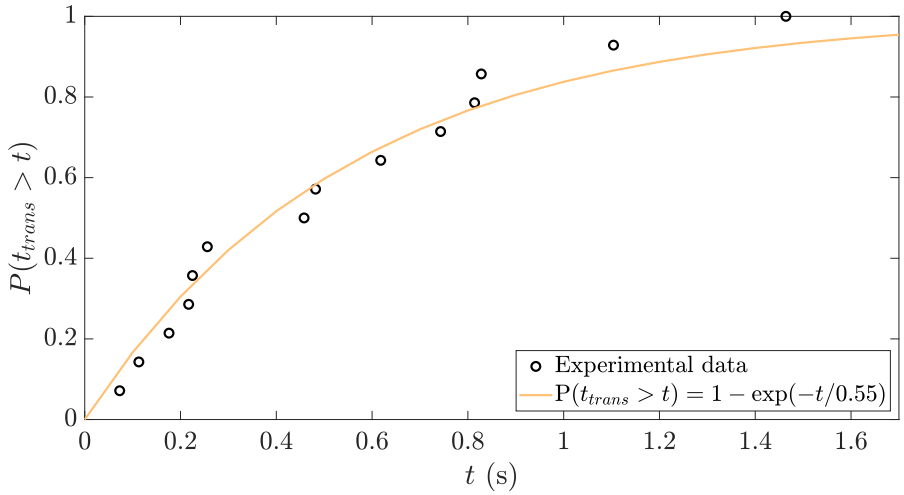

Figure 4.7: Cumulative distribution function of the time of transition t_{trans} for a set of 14 upward transitions in laminar flow. Experiments performed in the wind tunnel at the LEGI in Grenoble.

We see that, for instance at $t \simeq 500\,\mathrm{s}$ and $t \simeq 900\,\mathrm{s}$, the unstable position is visited first from the upper position and then from the lower. In both cases, the fly-swatter returns to its origin position right after. At $t \simeq 660\,\mathrm{s}$, a slowdown during a transition is also observed, like the one for the standard pendulum.

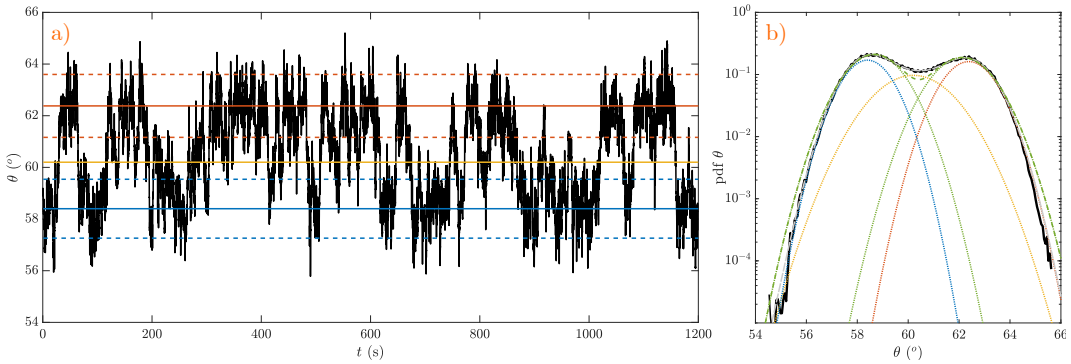

Figure 4.8: a) 20-minute long time series of the fly-swatter angle $\theta(t)$. Three angles are highlighted: the lower equilibrium position, the upper equilibrium position and the unstable position. b) Associated probability density function (pdf) with two fits: a sum of two gaussian distributions and a sum of three gaussian distributions, corresponding to the positions highlighted in a).

To better quantify the importance of the unstable position for the fly-swatter, we can look at its angular probability density function (pdf) in Fig. 4.8.b. It exhibits two well-separated modes of almost equal prominence. However when fitting this pdf with the sum of two gaussian functions, in green, the probability of the intermediate position is not well estimated by almost a factor of two compared to the experimental pdf in black. By adding a third gaussian to the fit, in grey, we completely recover the experimental pdf. The mean lower equilibrium angle, determined by the blue gaussian in Fig. 4.8.b, is represented by the full blue line in Fig. 4.8.a) with its standard deviation in dotted lines. Similarly, the red lines in Fig. 4.8.a) correspond to the upper equilibrium position.

The unstable equilibrium position (yellow in Fig. 4.8) presents a higher standard deviation than the equilibrium positions as the fly-swatter does not stay a long time near it with only flybys. Statistical convergence of the probability for this position is thus more difficult to achieve.

In the case of bluff body wakes, when the wake reverses from a large recirculation flow towards the left to its mirror equilibrium towards the right, the system goes through a weak symmetric state, which corresponds to the unstable position [21, 22].

4.4 OVERSHOOTS

In the transition presented in Fig. 4.6.a), two features are highlighted. The first one is the slowdown about which we commented previously in section 4.3 and the second one is the subject of this section: the presence of an *overshoot*. An overshoot occurs when the pendulum exceeds for a short time its final position at the end of its transition. These tend to represent an excess in kinetic energy for crossing the energy barrier between the two stable equilibrium positions. Examples of overshoots are visible in Fig. 4.9.a.

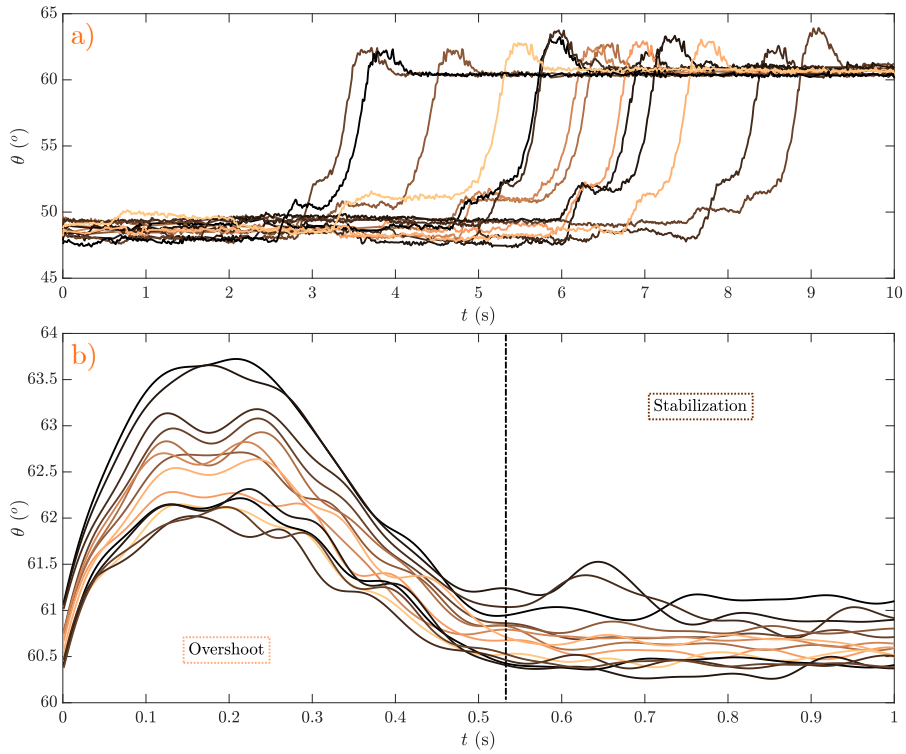

Figure 4.9: a) Examples of transitions in laminar flow presenting overshoots. b) Superposition of the overshoots observed in a), all overshoots last approximately the same time, beforethe stabilization of the pendulum is achieved. Experiments performed in the wind tunnel at LEGI in Grenoble.

Stacking all the overshoot events synchronized by their start as in Fig. 4.9.b), it appears that all overshoots take approximately the same time to complete $t_{over} \simeq 0.5\,\mathrm{s}$. Compared to the exponential distribution from the slowdowns (section 4.3), overshoots seem to follow a gaussian distribution with a small standard deviation ($\mathrm{std}(t_{over}) \simeq 0.1\,\mathrm{s}$).

This particularity, resembling an overdamped second-order oscillator, might result from the pendulum characteristics rather than from aerodynamic considerations. Indeed, overshoots are only observed for experiments conducted with the potentiometer and none were observed for the air bearing (in the latter configuration, the angular natural fluctuations are much stronger with the lack of solid friction). The threshold for determining an overshoot with the air bearing is much more difficult to estimate, just like for downward transitions as the pendulum also presents higher fluctuations on the lower (drag-dominated) branch.

Hence, overshoots may be experimental artifacts due to the potentiometer, but even so their presence may help us understand how solid friction impacts on the overall dynamics of the system.

4.5 EXCURSIONS

In section 4.3, we mentioned the possibility of visiting the vicinity of the unstable position, without going all the way through the transition, thus going back to its original position. Such an event can be defined as an *excursion*. In general, the excursion is not necessarily constrained to the unstable position and we will extend its definition to any incursion into the hysteretic cycle without concluding in a change of equilibrium positions. Examples of such excursions for the standard pendulum in laminar flow are presented in Fig. 4.10.

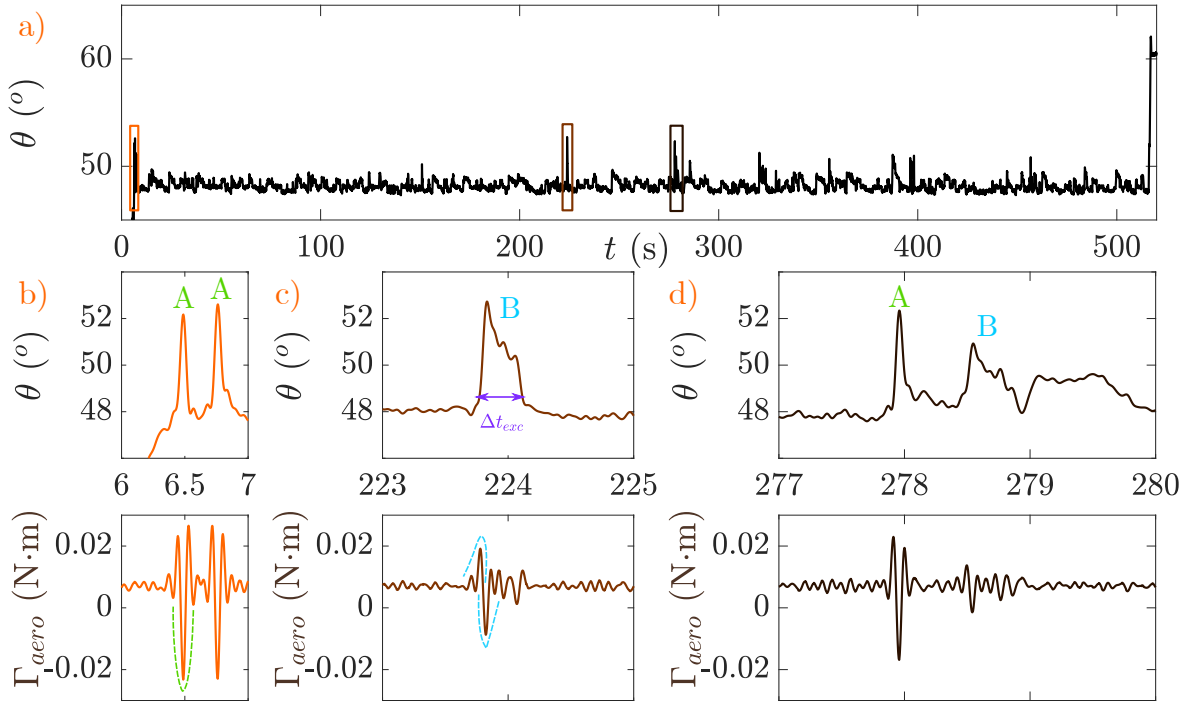

Figure 4.10: a) Example of a complete time series of a transition in laminar flow. b-d) Zoom on particular excursion events, with the reconstruction of the aerodynamic torque Γ_{aero} represented in the bottom figures. Experiments carried out in the wind tunnel at LEGI in Grenoble.

Two types of excursions can be identified from the angular time series in Fig. 4.10.a:

- *Type A excursions* are short, $\Delta t_{exc} \leq 0.2\,\mathrm{s}$, almost symmetric in the initial and final motions, as in Fig. 4.10.b.
- *Type B excursions* on the contrary are of longer duration, $\Delta t_{exc} \simeq 0.5 - 1\,\mathrm{s}$, with a quick motion to its extremum and then a slow return to the initial equilibrium position, as in Fig. 4.10.c.

Through the reconstruction of the aerodynamic torque using equation 5.4, $\Gamma_{aero}(t) = J\ddot{\theta} - mgl\sin(\theta)$[2], we can observe the aerodynamic torque variations during an excursion, shown in Fig. 4.10 bottom row. From this, we can extract the signature of the two types of excursions. Type A excursions present a sharp "V" shape in the torque evolution, with intense negative torque (Fig. 4.10.b). On the other hand, Type B excursions show a torque evolution with more of an "N" shape. A last observation is that despite attaining similar angles, about 4° above the mean angle, the intensity of the synchronous torque fluctuations is quite different between the two types of excursions.

Due to this particularity, it might be possible that these two excursions emanate from separate aerodynamic mechanisms. For instance, with a typical time Δt_{exc} of about 0.1 s, Type A excursions occur over the time of a vortex shedding event, as a frequency of 10 Hz is close to the Strouhal frequency for the disk, as mentioned in Chapter 0. With duration $\Delta t_{exc} \simeq 0.5\,\mathrm{s}$, a Type B excursion seems to correspond more to a natural response of the pendulum, as if the pendulum were disturbed by incident turbulence, for instance, but would relax to its initial position through its own dynamics almost unrestrained by aerodynamic considerations. Type A excursions on the contrary would result from abnormal vortex shedding events, possibly of the leading-edge vortex, which tends to be the most stable vortex in the wake and would thus generate strong pressure fluctuations when shedding abnormally.

The mechanisms of the excursions are, however, only speculative at this point and a thorough study of a higher number of events, ideally completed with PIV measurements in the mean wake, is fundamental to gain a better understanding of this phenomenon. *Preliminary PIV measurements have been carried out and will be presented in Chapter 5.*

We can find an equivalent of the excursion we present here in the geomagnetic field. An excursion is then usually defined as a deviation of the virtual geomagnetic pole resulting in a reduction of the magnetic field projected onto its initial axis by a factor less than $1/\sqrt{2}$ [23]. Examples of such magnetic excursions have been recorded on Earth [24] and in dynamo experiments and numerical simulations [18, 19, 25, 26]. In rotational spherical Couette flow, excursions, as incursions in the bistable region, are also observed [10].

2 $\ddot{\theta}$ is calculated by differentiating twice the angular time series, which however requires a strong filtering on the signal to smooth the acquisition noise.

4.6 CONCLUSION

In this chapter, we have presented a bestiary of various temporal dynamics observed for the pendulum in the bistable zone. We made the choice of keeping this bestiary mostly descriptive as the following chapter, Chapter 5, will enter more into the details of transitions, in particular one-way transitions. In that chapter, the time distribution of the transitions will be discussed and a model will be proposed based on the transition to turbulence.

The diversity of dynamics of the pendulum exposed in this chapter is a good example of how a simple pendulum can show dynamics as complex as that of natural systems. The pendulum can be used as a toy system to explore dynamical system properties in addition to probing intricate aerodynamic couplings, as we presented in Part i.

REFERENCES

[1] P. Varkonyi and G. Domokos. "Static Equilibria of Rigid Bodies: Dice, Pebbles, and the Poincare-Hopf Theorem." In: *Journal of Nonlinear Science* 16.3 (June 2006), pp. 255–281.

[2] P. L. Várkonyi and G. Domokos. "Mono-monostatic bodies." In: *The Mathematical Intelligencer* 28.4 (Sept. 2006), pp. 34–38.

[3] E. Feireisl, A. Novotný, and H. Petzeltová. "On the Existence of Globally Defined Weak Solutions to the Navier—Stokes Equations." In: *Journal of Mathematical Fluid Mechanics* 3.4 (Nov. 2001), pp. 358–392.

[4] A. F. Vasseur and C. Yu. "Existence of global weak solutions for 3D degenerate compressible Navier–Stokes equations." In: *Inventiones mathematicae* 206.3 (Dec. 2016), pp. 935–974.

[5] P. Antonelli and S. Spirito. "Global existence of weak solutions to the Navier–Stokes –Korteweg equations." In: *Annales de l'Institut Henri Poincaré C, Analyse non linéaire* 39.1 (Feb. 2022), pp. 171–200.

[6] K. Borońska and L. S. Tuckerman. "Extreme multiplicity in cylindrical Rayleigh-Bénard convection. I. Time dependence and oscillations." In: *Physical Review E - Statistical, Nonlinear, and Soft Matter Physics* 81.3 (2010), pp. 1–13.

[7] M. Grandemange, M. Gohlke, and O. Cadot. "Bi-stability in the turbulent wake past parallelepiped bodies with various aspect ratios and wall effects." In: *Physics of Fluids* 25.9 (Sept. 2013), p. 095103.

[8] M. Berhanu et al. "Dynamo regimes and transitions in the VKS experiment." In: *Eur. Phys. J. B* 77.4 (2010), pp. 459–468.

[9] F. Ravelet et al. "Multistability and memory effect in a highly turbulent flow: Experimental evidence for a global bifurcation." In: *Phys. Rev. Lett.* 93.16 (2004), p. 164501.

[10] D. S. Zimmerman, S. A. Triana, and D. P. Lathrop. "Bi-stability in turbulent, rotating spherical Couette flow." In: *Phys. Fluids* 23.6 (2011), p. 065104.

[11] M. J. Schmeits and H. A. Dijkstra. "Bimodal behavior of the Kuroshio and the Gulf Stream." In: *J. Phys. Oceanogr.* 31.12 (2001), pp. 3435–3456.

[12] E. Simonnet, J. Rolland, and F. Bouchet. "Multistability and rare spontaneous transitions in barotropic β-plane turbulence." In: *Journal of the Atmospheric Sciences* 76.6 (Apr. 2021), pp. 1889–1911.

[13] B. Dubrulle et al. "Bifurcations and dynamo action in a Taylor–Green flow." In: *New Journal of Physics* 9.8 (Aug. 2007), pp. 308–308.

[14] S. G. Huisman et al. "Multiple states in highly turbulent Taylor–Couette flow." In: *Nature Communications* 5.1 (Sept. 2014), p. 3820.

[15] D. Barkley. "Theoretical perspective on the route to turbulence in a pipe." In: *J. Fluid Mech.* 803 (Sept. 2016), P1.

[16] M. Obligado, M. Puy, and M. Bourgoin. "Bi-stability of a pendular disk in laminar and turbulent flows." In: *J. Fluid Mech.* 728 (2013), R2.

[17] D. Barros et al. "Forcing symmetry exchanges and flow reversals in turbulent wakes." In: *Journal of Fluid Mechanics* 829 (Oct. 2017), R1.

[18] G. A. Glatzmaier and P. H. Roberts. "A three-dimensional self-consistent computer simulation of a geomagnetic field reversal." In: *Nature* 377.6546 (Sept. 1995), pp. 203–209.

[19] M. Berhanu et al. "Magnetic field reversals in an experimental turbulent dynamo." In: *Epl* 77.5 (2007).

[20] A. Kamenev. *Field Theory of Non-Equilibrium Systems*. Cambridge: Cambridge University Press, 2011.

[21] G. Bonnavion and O. Cadot. "Unstable wake dynamics of rectangular flat-backed bluff bodies with inclination and ground proximity." In: *J. Fluid Mech.* 854 (2018), pp. 196–232.

[22] Y. Haffner et al. "Mechanics of bluff body drag reduction during transient near-wake reversals." In: *Journal of Fluid Mechanics* 894 (July 2020), A14.

[23] A. P. Roberts. "Geomagnetic excursions: Knowns and unknowns." In: *Geophysical Research Letters* 35.17 (Sept. 2008), p. L17307.

[24] D. Vandamme. "A new method to determine paleosecular variation." In: *Physics of the Earth and Planetary Interiors* 85.1-2 (1994), pp. 131–142.

[25] M. Bourgoin et al. "An experimental Bullard-von Kármán dynamo." In: *New J. Phys.* 8 (2006), pp. 1–14.

[26] R. Monchaux et al. "The von Kármán Sodium experiment: Turbulent dynamical dynamos." In: *Physics of Fluids* 21.3 (Mar. 2009), p. 035108.

5 RARE-EVENT TRIGGERING FOR SPONTANEOUS TRANSITIONS

What triggers the spontaneous transitions of the pendulum, ambient turbulence or vortex-induced events?

5.1 INTRODUCTION

Spontaneous transitions in multistable systems are always shrouded in mystery as to what might trigger such events. Sometimes ambient noise is responsible for the change of stability, sometimes on the contrary its absence.

To understand what kind of trigger lies behind spontaneous transitions, a few steps are usually required, common throughout the diversity of multistable systems.

First, an analysis of the statistics of the transitions is often useful. By observing a large number of transitions, similarities or invariants may come to light, precursor events appear and well-documented statistical properties may arise. A standard statistics in the study of transitions between stable states is the distribution of waiting/survival times. The *waiting time* ahead of a transition is defined by the time in a given initial state before the transition occurs. For systems presenting two mirror stable states, geometric like a bluff-body wake [1], or scalar like a magnetic field (projected onto a reference axis) in a dynamo [2], the waiting time can be seen as the time before reversal. For transient systems, the waiting time is closer to a lifetime of the transient state, such as puffs in the transition to turbulence [3]. For independent events, the probability distribution of the waiting times is an exponential law. Such distributions are found throughout physical systems, from turbulent lifetimes [4] to climate events return times [5] and radioactive degeneracy [6]. Not all phenomena are bound to exponential distribution. For instance, in the case of earthquakes, long-time correlations between two events are observed, thus the return time distribution is found to follow a power law exponential (or heuristic) probability distribution [7]. From the time distributions, characteristic values can be extracted such as the mean, the standard deviation or the skewness. The mean is usually considered to define a *characteristic time* τ_c of the phenomenon. Exponential distributions have the particularity of having equal mean and standard deviation.

After collecting enough statistics for a given set of control parameters, it is possible to look at the evolution of the characteristic time with a parameter. For instance, in a von-Kármán flow driven by two counter rotating disks, the characteristic time of spontaneous symmetry breaking is observed experimentally to follow a -6 power law scaling of the dimensionless frequency shift between the two disks [8]. For the transition to turbulence, a double-exponential scaling is observed for the lifetime of turbulent puffs as a function of the Reynolds number in pipe, plane Couette flows and forced

isotropic turbulence [9–11].

From there on, two things come to mind: looking for a model or looking for a trigger. Each can lead to the other, as a model can provide insights on the intrinsic phenomenon, while identifying a trigger can orient the search for a model.

In bistable systems, a common modeling approach is based on energy potential wells and transitions are stimulated by a noise intensity kT, exceeding the potential energy barrier ΔE set by the energy of the unstable fixed point between the two stable positions. The characteristic time then follows an Arrhenius law, $\tau_c = \tau_0 \exp(-\Delta E/kT)$. This was, for instance, observed for climate models [12], glass transition [13] and sometimes for the transition to turbulence [14]. Other models supported by extreme or rare events are found in magneto-hydrodynamic dynamo [15] and transition to turbulence [16], among others.

In aerodynamic wake bifurcations, it is widespread to look for a mechanism or trigger to the transition as it occurs within the structure of the wake itself. Indeed, experimental observations of the transition often already encompass flow visualization and force or local pressure measurements so that there is a direct access to local variables instead of integrated ones like turbulence rate or thermal noise. In particular, the flow dynamics of wake reversals have been thoroughly investigated both numerically and experimentally and precursor events on the drag force measurements have been reported [17, 18].

In this chapter, we will follow the same path towards a better understanding of the spontaneous transitions observed for the pendulum and described in Chapter 4. At first, we will investigate the statistics of waiting times ahead of transitions for a given initial angle, before comparing the characteristic times obtained. Inspired by studies on the transition to turbulence, a model will be proposed to provide insights on the possible aerodynamic mechanisms at work. Finally, preliminary flow visualization during transitions will be presented with the identification of potential precursors to the transition in the wake of the pendulum.

This chapter is based mainly on a published article [19].

5.2 EXPERIMENTAL PROTOCOL

The standard pendulum described in Chapter 0 presents a large bistability between the drag-dominated branch (D-branch) and the lift-dominated branch (L-branch), as shown in Fig. 5.1. The observed transitions were all one-way in this configuration, as discussed in Chapter 4. Thus, to accumulate a substantial number of transitions for this system, a specific experimental protocol had to be designed. Note that the transitions presented earlier for the fly-swatter were observed both ways and could be recorded at fixed flow velocity over a long period of time, provided that no atmospheric pressure drift exists as discussed in the interlude of this chapter.

The protocol implemented is sketched in Fig. 5.1 for the case of upwards (D→L) transitions. As previously mentioned, when the pendulum jumps from the D to the L-branch at $U = 6.4\,\mathrm{m}\cdot\mathrm{s}^{-1}$, it stays in the L-branch as long as the control parameter is kept constant. Therefore, we modulate the flow velocity to aggregate the statistics of thousands of transitions.

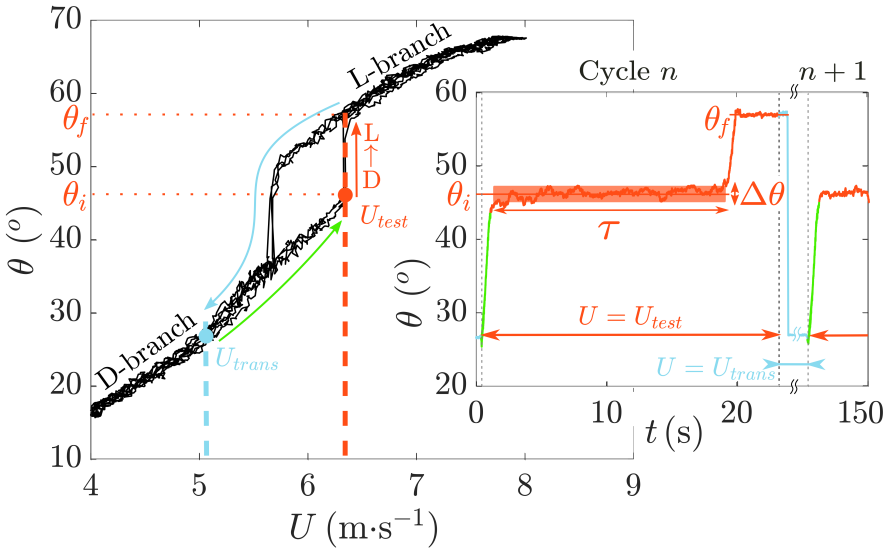

Figure 5.1: Left: Angular position θ of the pendulum as a function of U. Right: time series illustrating the protocol used to probe the statistics of spontaneous jumps from the the D- to the L-branch, at $U_{\text{test}} = 6.4\,\text{m}\cdot\text{s}^{-1}$ (see text for details)

At time $t = 0$, the wind velocity, initially at $U_{trans} = 5\,\text{m}\cdot\text{s}^{-1}$, below the bistable region, is rapidly increased to a fixed test velocity U_{test}, within the bistable region (e.g. $6.4\,\text{m}\cdot\text{s}^{-1}$) . After a short transient (dynamics displayed in green in Fig. 5.1), the pendulum reaches the initial average equilibrium angle θ_i (in the D-branch), and spontaneously jumps to the L-branch after a time τ, finally reaching a final average equilibrium angle θ_f (displayed in orange in Fig. 5.1). A few seconds after the transition, the flow velocity is decreased back to U_{trans} where it is maintained for typically two minutes in order to restore the global flow structure in the wind tunnel (displayed in light blue in Fig. 5.1) before repeating the cycle. During the time interval τ, the equilibrium position of the pendulum fluctuates around the average equilibrium angle θ_i, with a standard deviation $\Delta\theta$. Note that $\Delta\theta \ll |\theta_f - \theta_i|$, so that there is no ambiguity between the occurrence of a transition and simple natural fluctuations.

This protocol is repeated hundreds of times (typically 200 times) for several values of the test velocities U_{test}, allowing to analyse the statistics of the waiting times τ as a function of the control parameter of the bifurcation. A similar protocol is used for probing the L→D transition, for which U_{trans} lies in the L-branch, above the bistable region (e.g. $7\,\text{m}\cdot\text{s}^{-1}$), and is decreased down to a prescribed test velocity U_{test} within the bistable region (e.g. $5.7\,\text{m}\cdot\text{s}^{-1}$).

As this protocol can be kept running for long periods of time, temperature drifts are likely in the wind tunnel due to turbulence, as the wind turbines provide the system with constant energy. To avoid such drifts, it is possible to add a third velocity stop in the protocol. Before returning to the transient flow velocity U_{trans}, either a complete halt of the wind tunnel is possible for a few minutes to stabilize the temperature to the room temperature or a high flow velocity is set to stabilize the temperature at a higher level, thus diminishing the air density. This, for instance, could be used for keeping a velocity instruction U_{test} constant while slightly changing the initial angle θ_i. Indeed,

the equilibrium position θ_i is set by the dynamic pressure ρU_{test}^2 from the following equation:

$$-\Gamma_{weight_i} = mgl\sin(\theta_i) = \frac{1}{2}\rho LSU_{test}^2 C_N(\theta_i) = \Gamma_{aero_i} \tag{5.1}$$

With this consideration, it appears that while the practical control parameter of the experimental is U_{test}, the physical one is the aerodynamic torque which is ultimately related to θ_i. We thus chose to present our experimental results as a function of the initial angle θ_i, a better proxy for the physical control parameter than the flow velocity U_{test}. Indeed, because of small variations of atmospheric pressure P and temperature T, and hence air density $\rho = \frac{PM}{RT}$, the aerodynamic torque varies over a series of measurements at constant velocity U_{test}, resulting in a series of θ_i values typically spanning 0.14° around a mean value $\overline{\theta_i}$.

In the following, the test velocity will be simply referred to as U, as the transient velocity U_{trans} does not play any role in the temporal dynamics of the transitions.

5.3 WAITING TIME PROBABILITY

5.3.1 *Survival function*

By reproducing the protocol about 800 times for the upwards (D→L) transitions and 1800 times for the downwards (L→D) transition, we obtained well-converged probability distributions for the waiting times τ ahead of transition for different values of $\overline{\theta_i}$ (namely six for the D→L transitions and eight values for the L→D transitions). For a better characterization of the probability distribution, we chose to look at the survival function $P_{\overline{\theta_i}}(\tau \geq t)$, which in the case of an exponential distribution is an exponential, rather than the cumulative density function which is $P_{\overline{\theta_i}}(\tau < t) = 1 - \exp\left(-t/\tau_c(\overline{\theta_i})\right)$.

In Fig 5.2, the survival functions are presented for the 14 tested initial positions $\overline{\theta_i}$, sorted by the D→L and L→D transitions. As represented by the dotted lines, the experimental distributions $P_{\overline{\theta_i}}(\tau \geq t)$ are fitted by $\exp\left(-t/\tau_c(\overline{\theta_i})\right)$ with a very good agreement, just as observed in other multi-stable systems [20–23].

A striking feature brought to light by Fig. 5.2 is that the characteristic time-scale τ_c strongly depends on $\overline{\theta_i}$. It spans nearly four orders of magnitude when $\overline{\theta_i}$ spans only a few degrees for both D→L and L→D transitions.

A closer look at Fig. 5.2 shows deviations from the exponential law for some experiments, in particular in the long term behavior (e.g. $\overline{\theta_i} = 46.9°$ for the D→L transition) – likely due to finite size sampling, as observed for similar distributions [9] or small deviations of the physical control parameter ρU^2 during a series of measurements at constant velocity U due to environmental variations.

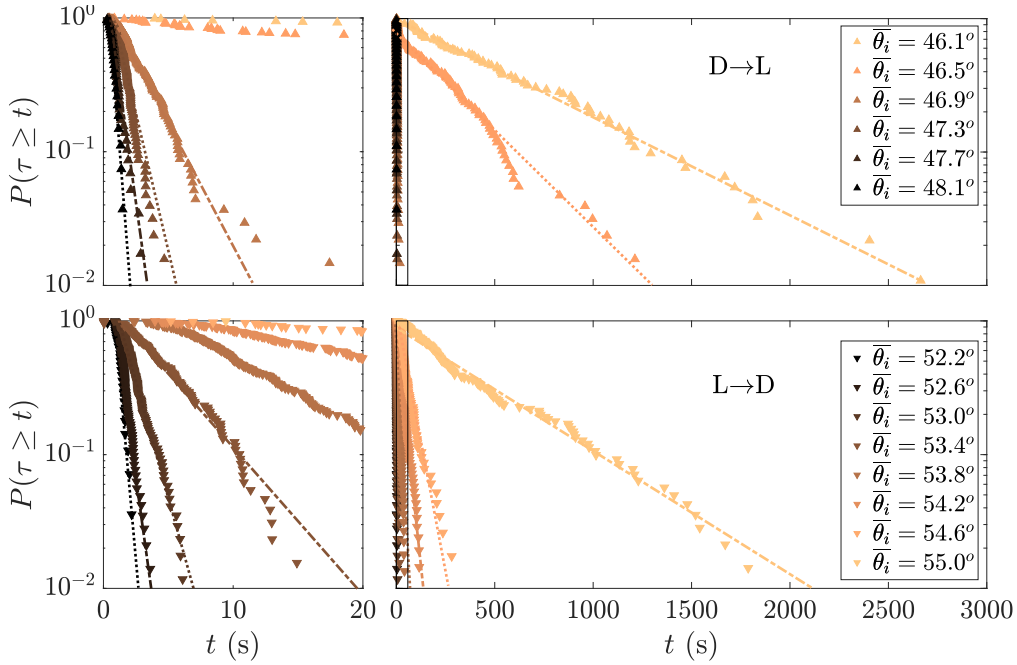

Figure 5.2: Survival distribution function of the waiting time τ for different values of $\overline{\theta_i}$ for the (top) D→L and (bottom) L→D transition. Dotted lines represent the exponential fits.

Interlude

During long experimental runs, it appeared that the time of the transition would evolve towards longer or shorter time over the duration of the run. This led to non exponential survival functions at first for a given flow velocity. In particular, during one run, a storm passed above Lyon and the time statistics resulting from that run were especially far from an exponential distribution.

The explanation for this was that, instead of simply using U as the control parameter, the true control parameter is in fact ρU^2 and as $\rho = P_{atm}M/RT$, the atmospheric pressure P_{atm} and the ambient temperature T are fundamental to correctly estimate the aerodynamic torque on the pendulum. From this consideration, the measurement of the temperature and the atmospheric pressure in the wind tunnel were added to the acquisition.

An example of a long experimental run for the fly-swatter with a consequent meteorological drift is shown below, with close to proportionality between ρ and θ and between θ and P_{atm}, as the temperature remained constant. In the first few hours, the bistable switching (see Chapter 4) is observed, but, by $t = 20\,\text{h}$, the lower branch could no longer subsist for the measured value of ρU^2.

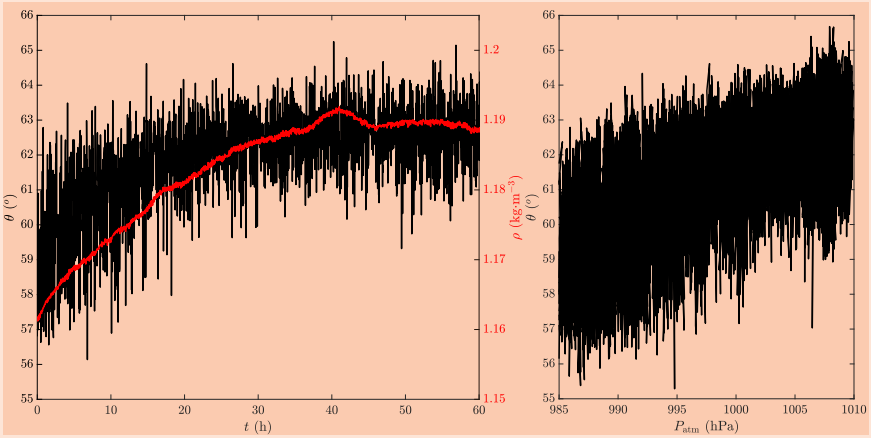

Left: Angular time series over 60 h with the corresponding air density ρ measured simultaneously. Right: drift of the angle θ with the atmospheric pressure P_{atm}.

5.3.2 *Double-exponential distribution*

Reducing 2596 recorded spontaneous transitions into 14 characteristic times can be a bit extreme to try to understand how the characteristic times depend on the initial angle, especially as the initial angle presents fluctuations over a series and not all series are converged to the same extent. In particular, series with a long characteristic time have fewer experimental points than series with a short one.

In order to take a step back and consider the entirety of the experimental data, Figure 5.3 presents the waiting time τ as a function of the initial angle $\sin(\theta_i)$. Note that according to Eq. 5.1, $\sin(\theta_i)$ is a accurate proxy for the aerodynamic torque. The colorbar corresponds to the joint probability of the variables $\sin(\theta_i)$ and τ, computed as the local density of the experimental points in the $(\sin(\theta_i), \tau)$ space, through a 2D-Voronoï computation. The characteristic times $\tau_c(\overline{\theta_i})$ computed from the exponential fits for several values of $\overline{\theta_i}$ are located close to the brightest spots in Fig. 5.3 (not displayed for the legibility of the figure).

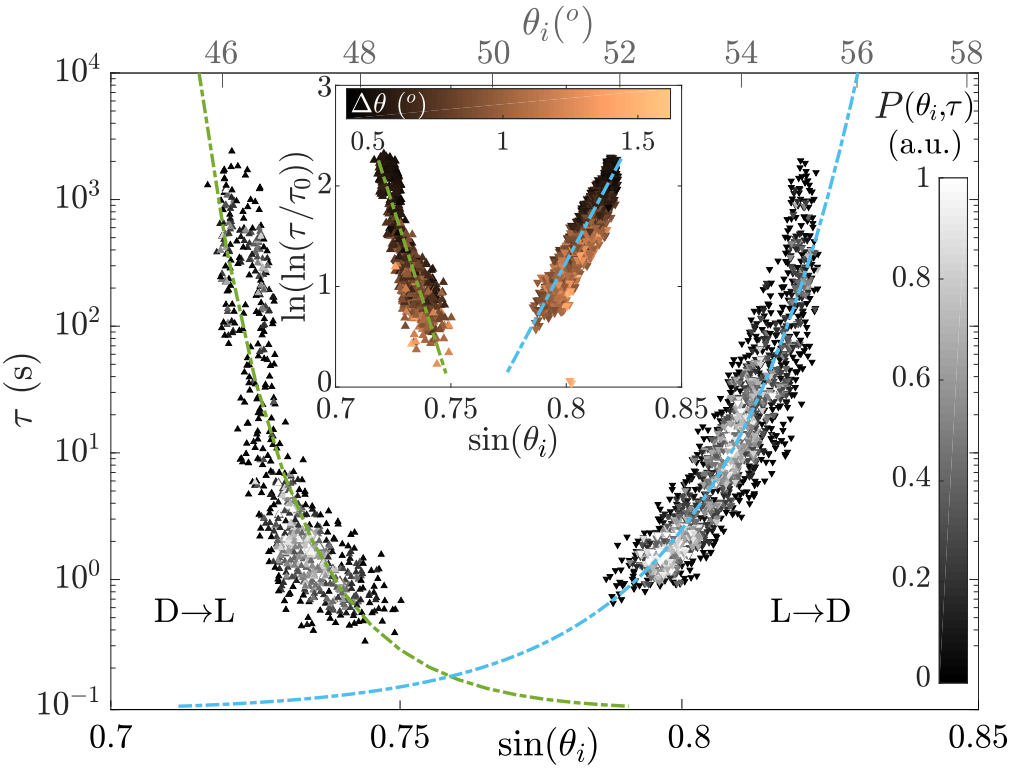

Figure 5.3: Waiting time τ as a function of $\sin(\theta_i)$ for the two transitions. Dash-dotted corresponds to the best fits according to Eq. 5.2. Inset: Evolution of $\ln(\ln(\tau/\tau_0))$ as a function of $\sin(\theta_i)$. See text for details.

Weighting the experimental points with their joint probability, the waiting times for each transition T (D→L or L→D) are fit with excellent agreement by a double-exponential function as:

$$\tau = \tau_0^T \exp\left[\exp\left(\frac{\sin(\theta_i) - \sin(\theta_0^T)}{\eta^T}\right)\right]. \tag{5.2}$$

Following the previous studies in which double-exponential dependency was found, the fitting parameter τ_0^T is expected to be a characteristic time scale of the system, which stems here from the spectral signature of the pendulum. $1/\tau_0^T$ is taken as the frequency of the first peak in the power spectral density of θ. In particular, $\tau_0^{D\to L} \simeq 0.11\,\mathrm{s}$ and $\tau_0^{L\to D} \simeq 0.09\,\mathrm{s}$. These times might be interpreted as vortex shedding characteristic times as we will detail further later. In the fitting procedure, only $\sin(\theta_0^T)$ and η^T are free fitting parameters. The best fits are shown as dash-dotted lines in Fig. 5.3 for both transitions. We will also discuss later a potential interpretation of both $\sin(\theta_0)$ and η.

5.4 RARE-EVENT TRIGGERING MODEL

We present in the following a rare-event phenomenology for this behavior, inspired by a model previously proposed in the context of transition to turbulence.

5.4.1 *Transition to turbulence*

As we previously mentioned, similar double-exponential statistics were reported for the characteristic lifetime of turbulent puffs as a function of the Reynolds number Re during the transition to turbulence in pipe flows [3, 24] and were analyzed in the framework of rare-event dynamics [25, 26]. After a brief description of this framework for the transition to turbulence, we will present a model for the pendulum transitions following the same steps to explain double-exponential dynamics.

In pipe flows, for Reynolds numbers between laminar and fully turbulent states, turbulence develops as turbulent puffs that may evolve in three different manners. They can remain, decay or split. The double exponential statistics are found for the time to decay and time to split as a function of the Reynolds number, as shown in the opposite figure [3, 4].

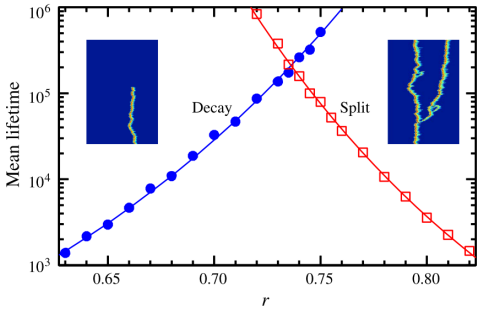

Mean lifetime of turbulent puffs before decaying or splitting in pipe flow with double-exponential statistics from [3].

The rare-event-based phenomenology proposed first by Goldenfeld *et al.* in 2010 [25] assumes that the turbulent state cannot be sustained when the turbulent kinetic energy $\langle u^2 \rangle$ lies below a given threshold B_c for a certain time τ_0, which depends on the Reynolds number. In other words, turbulence dies if all local maxima of the kinetic energy lie below this threshold B_c during at least τ_0. This can be reduced again to the fact that the global maximum of the kinetic energy in the puff lies below the threshold during a time τ_0. In the transition to turbulence phenomenology, the characteristic time scale τ_0 was proposed to be the correlation time of the flow fluctuations. It represents the memory lapse of the flow after which the flow "forgets" its previous state.

From the gaussian distribution of the velocity fluctuations, the maxima of the turbulent kinetic energy follow a Gumbel distribution [25]. The probability that the maximum

of kinetic energy is below the threshold is the cumulative probability for all possible maximum values below the threshold:

$$P(\langle u^2 \rangle_{max} < B_c) = \exp\left[-\exp\left(-\frac{B_c - \mu}{\beta}\right)\right] \tag{5.3}$$

with μ and β characteristic parameters of the Gumbel distribution, which we will describe in more detail for the pendulum.

By directly linking the probability of decay τ_0/τ_c to the probability $P(\langle u^2 \rangle_{max} < B_c)$, the double-exponential statistic is recovered by a Taylor-expansion of B_c around Re_0 the Reynolds number for which the turbulent puffs are observable for the first time, $B_c = B_{c_0} + B_{c_1}(Re - Re_0) + O((Re - Re_0)^2)$ [25].
Note that when the characteristic time of transition τ_c is above 2 τ_0, the threshold lies in the sub-gaussian part of the Gumbel distribution. It follows that it is not extreme events (on the over-gaussian tail of the Gumbel) that are responsible for the decay, but rather rare events.

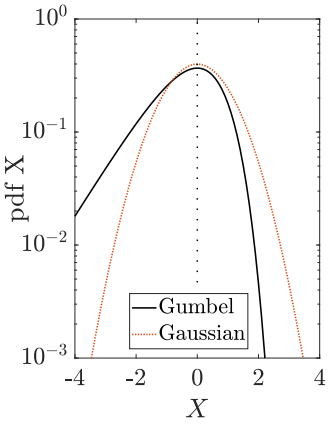

5.4.2 *A model for the pendulum*

Let us extend this approach to the bistable pendulum by focusing first on the L→D transition.

We propose the following mechanism: the pendulum jumps when the L state cannot be sustained, or equivalently when all maxima of the aerodynamic torque Γ_{aero} lie below a given threshold over a certain time τ_0. The lift (L) state is thus only maintained thanks to enough upwards fluctuations of the pendulum. As soo, as these fluctuations are no longer sufficient, the pendulum falls towards the drag (D) state, like the relaminarization of the turbulent puff. To support this phenomenology and its implications on the time statistics, we first need to verify that the torque fluctuation maxima follow a Gumbel distribution.

To compute the instantaneous aerodynamic torque $\Gamma_{aero}(t)$, we use the momentum equation of the pendulum (Chapter 0, Eq. 0.1) without assuming a model for the aerodynamic forces:

$$J\ddot{\theta} = -mgl\sin(\theta) + \Gamma_{aero}(t), \tag{5.4}$$

with J the moment of inertia of the pendulum.

The aerodynamic torque $\Gamma_{aero}(t)$ is retrieved from the time series $\theta(t)$ following Eq. 5.4. The probability density functions (pdf) of the torque fluctuations $\delta\Gamma = \Gamma_{aero}(t) - \langle\Gamma_{aero}(t)\rangle$ (where $\langle\Gamma_{aero}(t)\rangle$ is the time-averaged torque) display exponential tails, as shown in Fig. 5.4.a.

Exponential-tailed distributions present Gumbel distribution for their extrema. This leads to the rare-event statistical approach [27].

To support this, the maxima $\delta\Gamma_{max}$ of $\delta\Gamma$ are computed over disjoint time intervals $\tau_0^{L\to D}$ (as in Section 5.3.2), for each realization during the waiting time (of length

$\tau \gg \tau_0^{L\to D}$) before the transition to the D-branch. For each $\overline{\theta_i}$, accumulating statistics over all realizations leads to more than 10^5 samples of maxima measurements, whose pdf are displayed in Fig 5.4.c.

These pdf are fitted as Gumbel distributions $P(\delta\Gamma_{max}) = \frac{1}{\beta}\exp\left[-X/\beta + \exp\left(-X/\beta\right)\right]$, where $X = \delta\Gamma_{max} - \mu$ and μ and β are calculated from the mean and the standard deviation of the distribution. The mean value is $\mu + \beta\gamma$, with $\gamma \simeq 0.577$ the Euler-Mascheroni constant and the standard deviation is $\beta\pi/\sqrt{6}$. For each value of $\overline{\theta_i}$, β and μ have been extracted from experimental signals. The agreement between the pdf and the Gumbel distribution is excellent over three decades as shown in Fig. 5.4 and further checked on the cumulative distribution function in Annex B.1.

Assuming that a L→D transition occurs when the maximum $\delta\Gamma_{max}$ of torque fluctuations lies below a threshold $\delta\Gamma_c$ during a time $\tau_0^{L\to D}$, we now apply the statistical model developed for turbulent puffs [25] to our experimental data in order to compute $\delta\Gamma_c$ as a function of $\sin(\overline{\theta_i})$. For a given value of $\overline{\theta_i}$, the probability p that the transition occurs during $\tau_0^{L\to D}$ is given as $p = \tau_0^{L\to D}/\tau_c(\overline{\theta_i})$, and is linked to the pdf of the maxima of $\delta\Gamma$ as $p = P(\delta\Gamma_{max} < \delta\Gamma_c)$.

Using the parameters β and μ extracted from the pdf of $\delta\Gamma_{max}$, the threshold $\delta\Gamma_c$ can then be estimated from the relation 5.3 [25]:

$$p(\overline{\theta_i}) = \frac{\tau_0}{\tau_c(\overline{\theta_i})} = \exp\left[-\exp\left(-\frac{\delta\Gamma_c(\overline{\theta_i}) - \mu(\overline{\theta_i})}{\beta(\overline{\theta_i})}\right)\right]. \tag{5.5}$$

The evolution of $\delta\Gamma_c/\beta$ as a function of $\sin(\overline{\theta_i})$ is shown in Fig. 5.4.d. The best linear regression (dash-dotted lines) matches the slope of the double-exponential fit following Eq. 5.2. As such, η appears to be intrinsically determined by the system as both a purely statistical approach on the waiting time and its estimation based on dynamical criteria give similar values.

The linear evolution of $\delta\Gamma_c$ is, moreover, understood from the fact that $\mu(\overline{\theta_i})/\beta(\overline{\theta_i})$ is observed constant for the L→D transition (see Fig. 5.4.e). From the definition of μ and β, we can rewrite this as the fact that for the whole angular range, the standard deviation of the torque fluctuation maxima is proportionnal to its mean value, by a constant factor, recalling a homogeneous dilatation. We have no explanation for now on this homothetic property of the Gumbel distribution, but it might either be coincidental or resulting from aerodynamic effects.

This translates into the following. As $\sin(\overline{\theta_i})$ decreases from 0.82 to 0.79, the threshold normalized to the torque standard deviation decreases, which corresponds to more probable transitions, and thus shorter waiting times. On the other hand, the standard deviation of the torque fluctuations strongly increases as $\sin(\overline{\theta_i})$ decreases (see Fig. 5.4.e), which is reminiscent of the increase of standard deviation of the pendulum angular position $\Delta\theta$, color-coded as in the inset of Fig. 5.3).

While we detailed the whole analytic process for the L→D transition, it applies also to the D→L transition symmetrically. A transition occurs when the D state cannot be sustained anymore i. e.when the minimum aerodynamic torque during time $\tau_0^{D\to L}$ lies

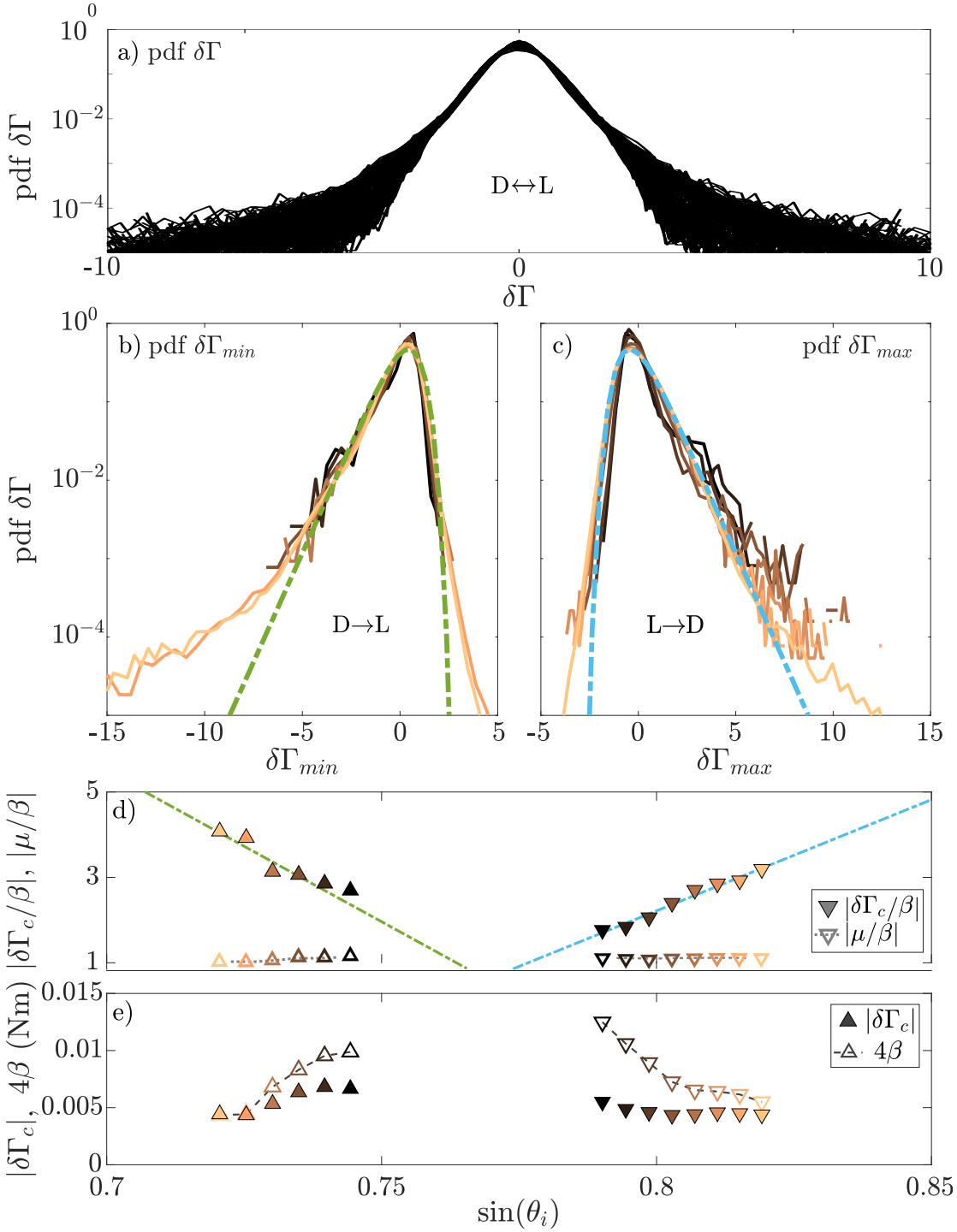

Figure 5.4: Normalized and centered pdf of the torque-fluctuation a) $\delta\Gamma$, b) minima $\delta\Gamma_{min}$ and c) maxima $\delta\Gamma_{max}$ and associated fitted Gumbel distributions (dash-dotted lines). d) Evolution of $\delta\Gamma_c/\beta$ and μ/β, as a function of $\sin(\overline{\theta_i})$ and linear fit (dash-dotted lines). e) $\delta\Gamma_c$ and β as a function of $\sin(\overline{\theta_i})$.
μ/β is observed to be independent of $\overline{\theta_i}$. $\delta\Gamma_c$ unexpectedly increases as $\overline{\theta_i}$ approaches the edges of the bistable zone. Yet as β shows a stronger increase, τ_c gets smaller. The color code for $\overline{\theta_i}$ is identical to that of Fig. 5.2.

above a given threshold. This transition is thus controlled by the pdf of the minima $\delta\Gamma_{min}$ of $\delta\Gamma$, computed over $\tau_0^{\mathrm{D}\to\mathrm{L}}$, and displayed in Fig. 5.4.b), in excellent agreement with Gumbel distributions for the same reasons as the pdf of the maxima. A similar application of the rare-event statistical model leads to conclusions similar to those drawn for the L→D transition and summarized in Fig. 5.4.d) for $\sin(\overline{\theta_i})$ between 0.725 and 0.745, see also Fig. 5.5.e. Here again, the linear best fits of $\delta\Gamma_c/\beta$ as a function of $\sin(\overline{\theta_i})$ shown as dash-dotted lines in Fig. 5.4.d) are in excellent agreement with those shown in the inset of Fig. 5.3, a strong asset for the validity of the proposed phenomenology.

5.4.3 *What can we tell from this rare-event model*

From the model presented above, though no direct information on the possible trigger to the transition is exposed, a few points can give insight on the transition mechanisms.

First, the characteristic times $\tau_0^T \simeq 0.10\,\mathrm{s}$ identified for the double-exponential fit correspond to Strouhal numbers $\mathrm{St} = \frac{d_{disk}}{U\tau_0} \simeq 0.07$ and recall values reported in previous studies for transverse vortex shedding (in the $x-y$ plane) for a disk at non zero incidence [28]. In contrast, the correlation time of the incoming flow is $\tau_{flow} \simeq 0.95\,\mathrm{s}$, based on the hot-wire measurement. This separation of time scales suggests that the mechanisms behind the transition should be found in the wake of the disk rather than in the ambient turbulence in the incoming flow.

Secondly, as we already expect the transition dynamics to be strongly associated with the C_N coefficient, we can propose a possible interpretation of the $\sin(\theta_0)$ and η parameters from the double-exponential fit (Eq. 5.2). In the transition to turbulence, the equivalent to $\sin(\theta_0)$ is a Reynolds number Re_0. Re_0 is suggested to be the minimal Reynolds number above which turbulent puffs are visible, in the sense that their lifetime is long enough for an experimental or numerical observation. As such, $\sin(\theta_0)$ may represent the extremal θ for which the bistability can be observed. If we consider the C_N coefficient to be fully continuous, $\sin(\theta_0)^T$ would correspond to the angles θ_{meta} for which $\frac{\mathrm{d}C_N}{\mathrm{d}\theta}|_{\theta_{meta}} = C_N(\theta_{meta})\cot(\theta_{meta})$, limit cases for the existence of the angular bistability for the dynamical system point of view (see Interlude in Chapter 2).

For η, the interpretation is more difficult, in particular as we lack estimates for this fitting parameter in different configurations and no interpretation is proposed in the model for the transition to turbulence. It is only seen as the first-order coefficient from the Taylor-expansion of the threshold. If, however, we try to combine the rare-event transition model to a double-well energy-based model like an Arrhenius law, the parameter η might be linked with the potential energy landscape. For instance, it might be related to the depth or width of the mean potential well of the initial position. In that sense, we might expect this parameter η to be a function of the curvature of the potential well, thus a linear combination of $\cos(\theta_i)$ and $\frac{\mathrm{d}C_N}{\mathrm{d}\theta}|_{\theta_i}$. This however is just a hypothesis and further investigations are required to confirm or reject it.

A last point can be extracted from the value of the threshold of torque fluctuations for the transition relative to the mode μ of the Gumbel distribution. As we already mentioned, the threshold is in the rare-event (sub-gaussian) part of the Gumbel distribution.

This means that the threshold corresponds to a lack of upward fluctuations for a L→D transition (resp. downward fluctuations for a D→L transition). Therefore, the transition does not require an extreme downward (resp. upwards) fluctuation to occur. Looking at the wake structure from Chapter 1, we go from a quasi-periodic vortex shedding in the D-branch towards a more plane-like quite stable wake with two wingtip vortices in the L-branch. A possible interpretation for the mechanism of the downwards transition would for instance be that the two vortices connect close enough to the disk so that the wake temporarily forms a ring vortex limiting upward torque fluctuations from the leading-edge vortex. For the upwards transition, right after its shedding, the ring vortex might take time to regrow and the two wingtip vortices have time to roll-up without the formation of the trailing-edge vortex and thus limit the downward torque fluctuations.

5.5 PRECURSORS EVENTS IN THE WAKE?

5.5.1 *Transition and PIV in the experiment*

As we have conjectured that a major part of the mechanism to transition lies in the wake dynamics, we have tried to identify structural changes in the wake using PIV measurements synchronized with the detection of the transition. To this end, due to experimental constraints for transverse PIV (see 0.4.1.5 for more details), we changed from the 4 cm disk pendulum to the 6 cm disk pendulum for which $U_{L\to D} \simeq 2.8\,\mathrm{m}\cdot\mathrm{s}^{-1}$ and $U_{D\to L} \simeq 3.4\,\mathrm{m}\cdot\mathrm{s}^{-1}$, thus much lower than the velocities for the initial pendulum detailed in Fig. 5.1. The same protocol as previously is used for the transition but with an added part. The detection of the transition also triggers the PIV camera and the triggering signal is back-acquired to synchronize both acquisitions. The signal acquisition is done at a frequency of 10 000 Hz (only three transitions were acquired at only 1000 Hz) with the PIV acquisition at 4000 fps. The plane of visualization is taken about 4 cm behind the disk. This induces a delay of visualization if anything happens in the near wake. As the advection velocity within the wake is not yet completely determined experimentally right behind the disk, we chose to keep the synchronization at the trigger point.*A synchronous evolution of the wake structure and of the angular position corresponds to a wake modification born at the location of the disk occurring before the motion of the pendulum*.

Event	D→L	L→D	L→L
Number of realizations	4	6	2
Mean initial angle θ_i	48.5°	52.5°	53.5°
Mean final angle θ_f	53.5°	48°	53.5°
Excursion angle θ_{exc}	–	–	51.2°
Total duration	∼6.5 s	∼7.7 s	∼2.0 s
Number of images	∼ 26000	∼ 30800	∼ 8000

Table 5.1: PIV and angular characteristics of the different recorded transition events. Total duration and number of images cover for the transition or excursion only, though sometimes the definition of the start and end of the transition was difficult on the experimental angular signal.

In total, 10 transitions have been recorded with both angular and PIV measurements, summarized in Table 5.1. Among those are six L→D and four D→L transitions. For each transition, the video lasts 3.15 s with the detection of the transition between $t = 1.5\,\mathrm{s}$ and $t = 2.5\,\mathrm{s}$. In addition to these transitions, two excursions L→L were recorded with PIV measurements. One excursion, of type B (see Chapter 4), has been recorded standalone, as its large amplitude over a long duration triggered the acquisition system like a transition. The other excursion is of type A (see Chapter 4) and is much shorter. It was recorded right after an upward transition. These excursions have yet to be analyzed thoroughly and will thus only be mentioned succinctly in the next section 5.6, as a perspective to this study.

5.5.2 *Wake structure on both sides of the transition*

For simplicity, we will first present only one example of a D→L transition in this section, while the next section will detail both D→L and L→D transitions. As the initial and final angles on both directions of transitions are almost identical, we can expect a strong symmetry of the two cases in particular in the wake structure, before and after the transition.

Figure 5.5 shows the mean wake structure behind the disk before and after the transition.

At the lower angle, before the transition on the D-branch, the wake presents intense flow velocity fluctuations (more than $1\,\mathrm{m}\cdot\mathrm{s}^{-1}$), with two large regions of transverse velocity fluctuations v_{rms} and a large horse-shoe region of fluctuations for the vertical component w_{rms}. The intense fluctuation at the bottom of the horse-shoe is the signature of a strong trailing-edge vortex separation. The two symmetric regions on fluctuations around $z = 20\,\mathrm{mm}$ corresponds to the location of the wingtip vortices. Their fluctuation both in the transverse and vertical directions is a marker of the transverse vortex shedding.

On the contrary, after the transition, on the L-branch, the wake fluctuates much less, with about only $0.6\,\mathrm{m}\cdot\mathrm{s}^{-1}$ standard deviations. The regions of fluctuation are both also reduced, with a rounder shape for the vertical velocity fluctuations. The maximum of the vertical velocity fluctuations is no longer at the bottom but rather on the side, meaning that the trailing-edge vortex is less intense not only compared to the D-branch but also compared to the vertical fluctuations of the wingtips vortices.

This change of structure confirms that something happens in the wake during the transition and to this end, let us have a closer look at the temporal dynamics of the wake in the strong-fluctuation regions.

5.5.3 *Events in the wake*

To look at the temporal dynamics of the wake during a transition, we decided to focus on the strong-fluctuation zones identified in Fig. 5.5. By visualizing the flow velocity at a constant height or abscissa over the duration of the transition, we can observe interesting behaviors as shown in Fig. 5.7.c-f) for a D→L transition and 5.8.c-f) for a L→D transition.

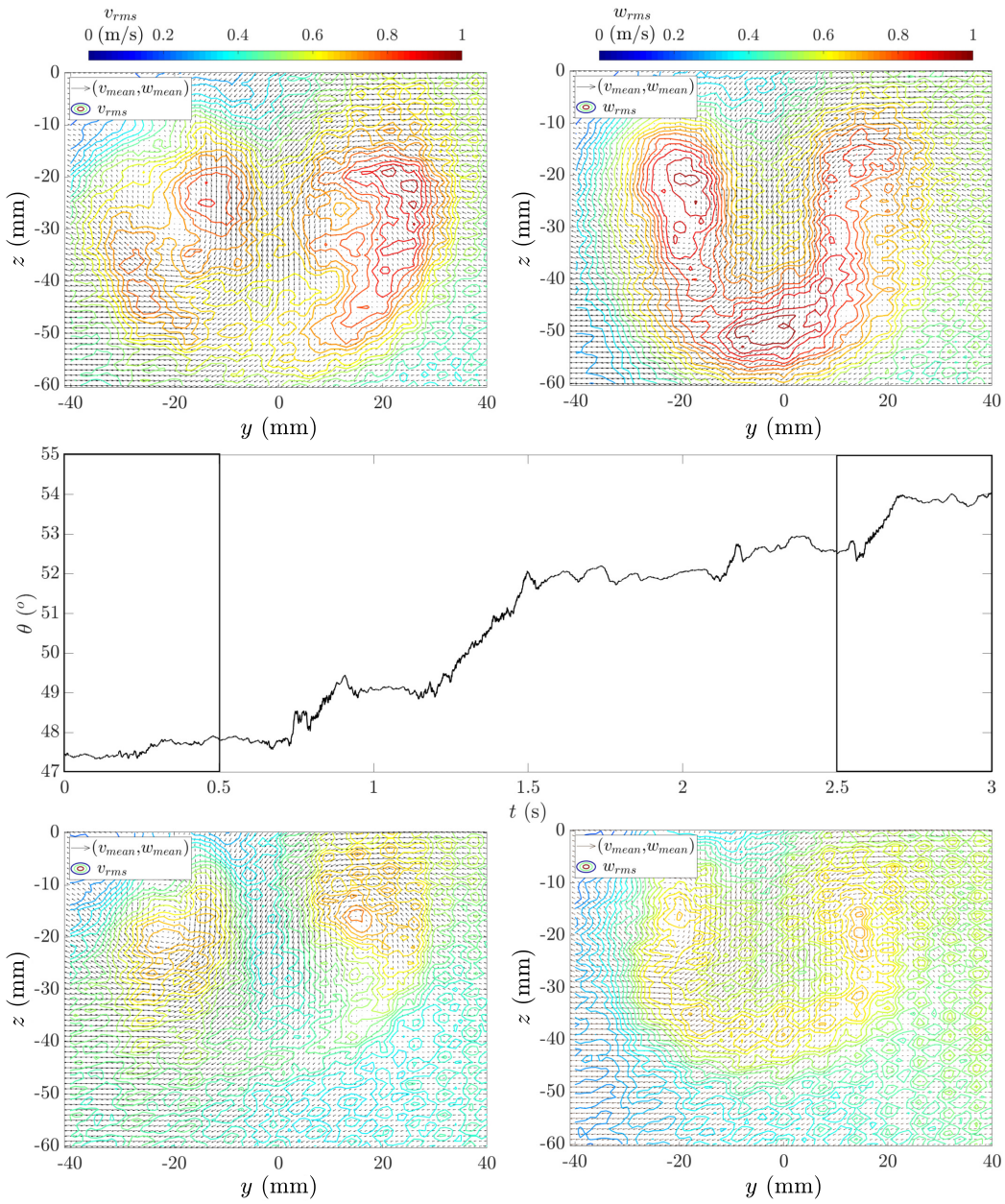

Figure 5.5: Wake structure before and after a D→L transition.
Top: time-averaged flow structure before the transition, on the D-branch. Middle: Angular time series of the D→L transition. Bottom: time-average flow structure after the transition, on the L-branch. Left: standard deviation of the transverse velocity v_{rms}. Right: standard deviation of the vertical velocity w_{rms}.

For instance, by looking at the time evolution of the vertical velocity along a horizontal line in the region of intense fluctuation, we can partially reconstruct the trailing-edge vortex (TEV). Signatures such as the presence or absence of the TEV or the Strouhal number can be extracted from the spatio-temporal diagram.

Indeed, when a vortex of direction co-planar with the plane of visualization goes through it, it modifies the flow velocity in one direction first before its core crosses the plane and then in the other direction.

In particular, in the case of a detached trailing-edge vortex going through a transverse plane, its signature is a starting upward flow velocity w followed by a downward motion, as shown in Fig. 5.6, due to its vorticity along $-\mathbf{e}_y$. We can identify such trailing-edge vortices in Fig. 5.7.e-f.

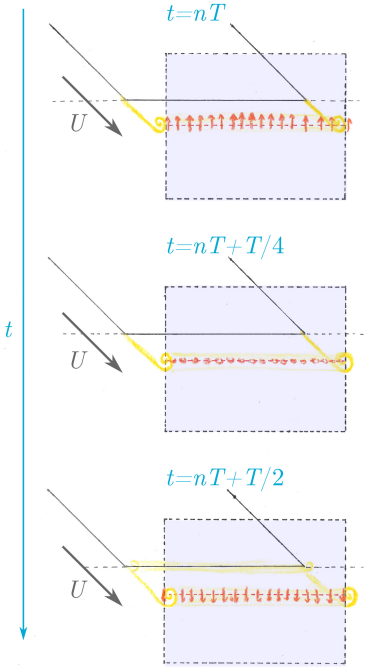

Figure 5.6: Trailing-edge vortex going through a transverse visualization plane over half a Strouhal period T.

For vortices that present a vorticity normal to the plane of visualization, the temporal fluctuations of velocity can indicate the displacement of the center of the vortex, without the calculation of the vorticity and finding the location of its peak. In Fig. 5.7.c, the time series of the position of the center of the vortex along the y-axis is estimated from the spatio-temporal evolution of the vertical flow velocity w: it corresponds to the location where $w = 0$. This is shown by the white part in the figure. The z coordinate of the center of the vortex can similarly be estimated from the spatiotemporal evolution of the horizontal flow velocity v.

Thanks to these considerations, even without computing the vorticity quantitatively, we can observe structural modifications of the wake during the transition, as shown for a D→L in Fig. 5.7 and for a L→D in Fig. 5.8.

In Fig. 5.7.c), a precursor[1] to the upward transition seems to be a reduction of the intensity, as well as a slow-down, of the oscillation of the center of the wingtip vortex at $t = 2\,\text{s}$,. Conjointly with a slight delay at $t = 2.1\,\text{s}$, a trailing-edge vortex goes through the plane at the altitude corresponding to the upper angle region of fluctuation, in Fig. 5.7.e. At the same time, the trailing-edge vortex shedding at the altitude for the initial position dies down in Fig. 5.7.f. Time landmarks are shown by white lines throughout Fig.5.7.c-f.

For the downward transition in Fig. 5.8.d, the precursor to the transition seems to be on the contrary the disappearance of the trailing-edge vortex at $t \simeq 1\,\text{s}$, in Fig. 5.8.e. Later at $t = 1.4\,\text{s}$, the trailing-edge vortex reappears in its lower final position, in Fig. 5.8.f. At about $t = 1.5\,\text{s}$, the fluctuations of the center of the wingtip vortex increase to the intensity of the ones observed in the lower angles for the upward transitions (Fig.

1 As we already mentioned, thus a wake event synchronous with the angular evolution

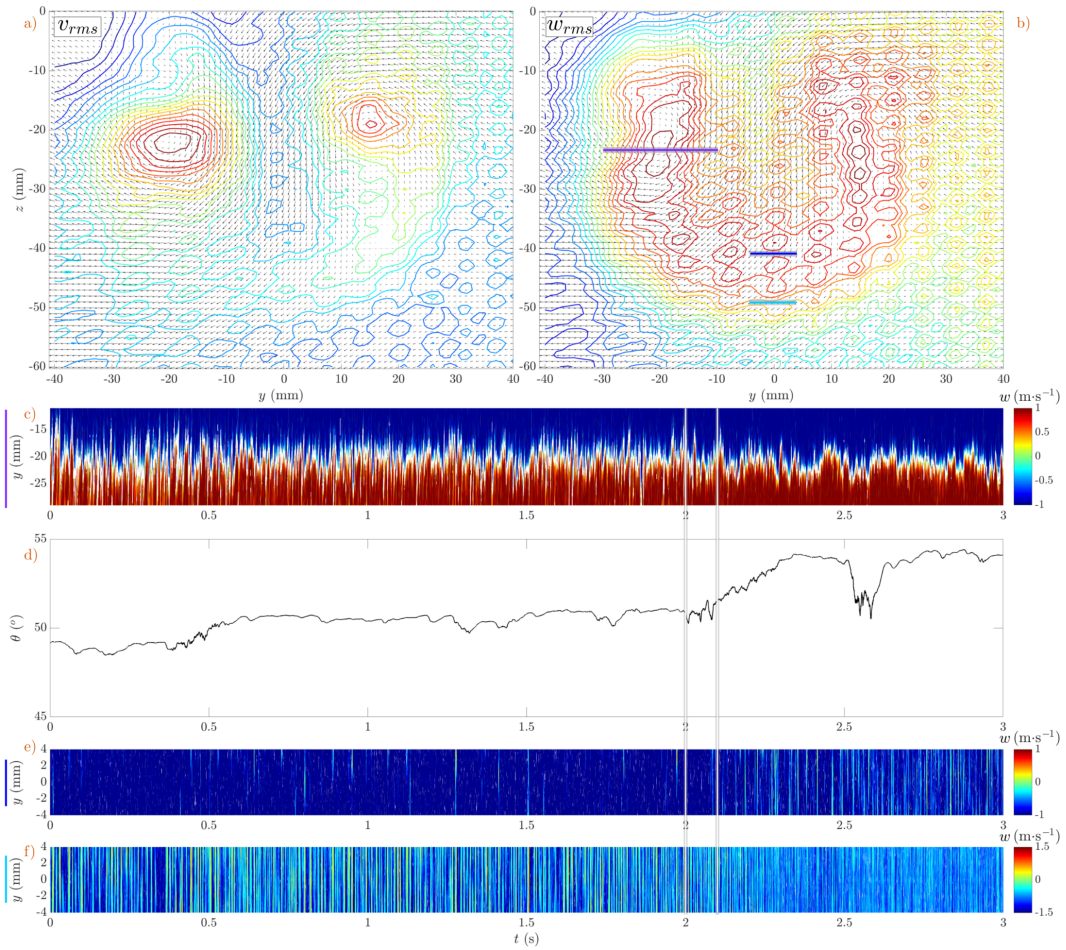

Figure 5.7: Details of the temporal dynamics in the wake for a D→L transition. a-b) Average flow structure and fluctuations over the whole duration of transition (a: v_{rms}, b: w_{rms}). d) Angular time series. c,e-f) Spatio-temporal evolution of w along a horizontal segment. The corresponding segments for each spatio-temporal diagram are represented with matching colors in panel b.

5.8.c and 5.7.c). Time landmarks are shown by white lines throughout Fig.5.8.c-f.

Interestingly, it seems that despite moving early in the transition process, the trailing-edge vortex directly attains its final position for both transitions. The change of dynamics for the center of the wingtip vortex also happens around the start of the transition. Hence, we have not yet identified a possible "closing" mechanism to the transition to assist the complete travel, compared to an excursion which comes back to the same branch. It might also be that the three observations of modification of the wake are alone to initiate the transition, so that as soon as the transition starts with these wake restructurings, it will conclude in a change of branch. As such, excursions would not be aborted transitions but a different mechanism.

5.6 PERSPECTIVES

In this chapter, we have presented the temporal statistics of the spontaneous transitions observed in our pendulum system. As it exhibits a double-exponential distribution, we

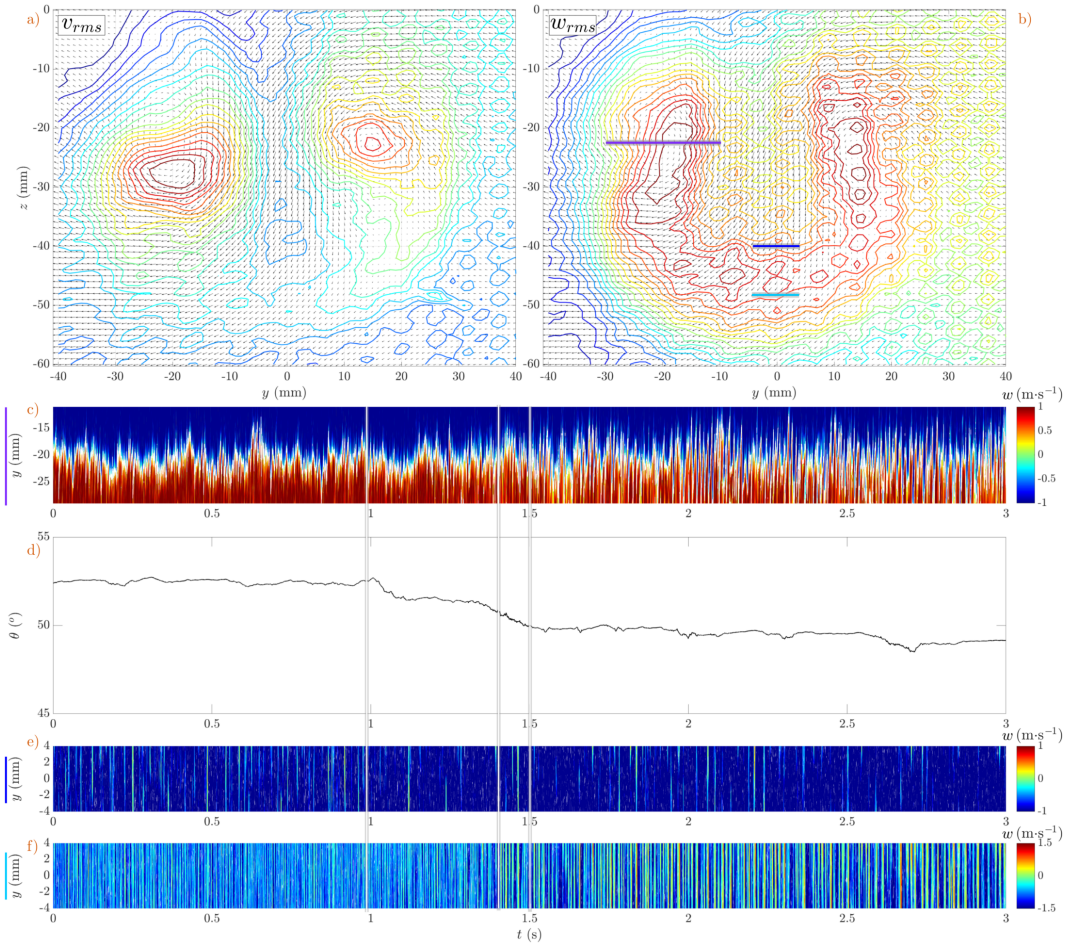

Figure 5.8: Details on the temporal dynamics in the wake for a L→D transition. a-b) Average flow structure and fluctuations over the whole duration of transition (a: v_{rms}, b: w_{rms}). d) Angular time series. c,e-f) Spatio-temporal evolution of w along a horizontal segment. The corresponding segments for each spatio-temporal diagram are represented with matching colors in panel b.

have developed a phenomenological model inspired from the transition to turbulence, where such double-exponential statistics are common. The resulting phenomenology focuses on the fact that transitions are not triggered by extreme fluctuations towards the final position but rather by a rare lack of fluctuations leading back to the initial position.

The preliminary analysis of the synchronized PIV measurements brought up some possible triggers to the transition, in particular in the trailing-edge vortex. However, a more thorough study is necessary to fully understand the global changes happening during the transition and its chronology, in a similar fashion as has been done for bluff body wake reversals [18]. The vorticity analysis in particular, as initiated in Chapter 1, might provide insight on the balance between the vortices during the transition.

The comparison of the wake structure evolution during a transition and an excursion will also be central in the comprehension of both phenomena. With the short duration of type A excursions, structural changes are expected to be minute due to the flow time response, which is why it might be difficult to observe them in the vorticity, as

it requires a rather strong spatial filtering. To overcome this flaw, proper orthogonal decomposition (POD) analysis applied to the raw velocity field might be an interesting method to try out on the PIV measurement, as it has already proved its effectiveness on bluff body wakes [18, 29].

Complementary investigations on various pendulum configurations remain also to be pursued, to document in particular the physical meaning of η, θ_0 and confirm the choice of τ_0 in the double-exponential fit and model.

REFERENCES

[1] G. Bonnavion and O. Cadot. "Unstable wake dynamics of rectangular flat-backed bluff bodies with inclination and ground proximity." In: *J. Fluid Mech.* 854 (2018), pp. 196–232.

[2] M. Berhanu et al. "Magnetic field reversals in an experimental turbulent dynamo." In: *Epl* 77.5 (2007).

[3] D. Barkley. "Theoretical perspective on the route to turbulence in a pipe." In: *J. Fluid Mech.* 803 (Sept. 2016), P1.

[4] B. Hof et al. "Finite lifetime of turbulence in shear flows." In: *Nature* 443.7107 (2006), pp. 59–62.

[5] F. Ragone, J. Wouters, and F. Bouchet. "Computation of extreme heat waves in climate models using a large deviation algorithm." In: *P. Natl. Acad. Sci. USA* 115.1 (2018), pp. 24–29.

[6] E. Rutherford and F. Soddy. "LX. Radioactive Change." In: *The London, Edinburgh, and Dublin Philosophical Magazine and Journal of Science* 5.29 (May 1903), pp. 576–591.

[7] V. Carbone et al. "Unified scaling law for waiting times between seismic events." In: *Europhysics Letters* 71.6 (2005), pp. 1036–1042.

[8] F. Ravelet et al. "Multistability and memory effect in a highly turbulent flow: Experimental evidence for a global bifurcation." In: *Phys. Rev. Lett.* 93.16 (2004), p. 164501.

[9] M. Avila, A. P. Willis, and B. Hof. "On the transient nature of localized pipe flow turbulence." In: *J. Fluid Mech.* 646 (2010), pp. 127–136.

[10] S. Gomé, L. S. Tuckerman, and D. Barkley. "Statistical transition to turbulence in plane channel flow." In: *Phys. Rev. Fluids* 5.8 (2020), p. 083905.

[11] M. F. Linkmann and A. Morozov. "Sudden relaminarization and lifetimes in forced isotropic turbulence." In: *Phys. Rev. Lett.* 115.13 (2015), p. 134502.

[12] R. Benzi et al. "Stochastic resonance in climatic change." In: *Tellus* 34.1 (Jan. 1982), pp. 10–15.

[13] Y. J. Lü and W. H. Wang. "Single-particle dynamics near the glass transition of a metallic glass." In: *Physical Review E* 94.6 (Dec. 2016), p. 062611.

[14] O. Dauchot and E. Bertin. "Subcritical transition to turbulence: What we can learn from the physics of glasses." In: *Physical Review E* 86.3 (Sept. 2012), p. 036312.

[15] D. Faranda et al. "Robust estimate of dynamo thresholds in the von Kármán sodium experiment using the extreme value theory." In: *New J. Phys.* 16 (2014), p. 083001.

[16] T. Nemoto and A. Alexakis. "Extreme events trigger turbulence decay: numerical verification of extreme value theory in pipe flows." In: (2020).

[17] Y. Fan et al. "Experimental and numerical analysis of the bi-stable turbulent wake of a rectangular flat-backed bluff body." In: *Physics of Fluids* 32.10 (2020).

[18] Y. Haffner et al. "Mechanics of bluff body drag reduction during transient near-wake reversals." In: *Journal of Fluid Mechanics* 894 (July 2020), A14.

[19] A. Gayout, M. Bourgoin, and N. Plihon. "Rare Event-Triggered Transitions in Aerodynamic Bifurcation." In: *Physical Review Letters* 126.10 (2021), p. 104501.

[20] A. De La Torre and J. Burguete. "Slow dynamics in a turbulent von Kármán swirling flow." In: *Phys. Rev. Lett.* 99.5 (2007), p. 054101.

[21] K. R. Sreenivasan, A. Bershadskii, and J. J. Niemela. "Mean wind and its reversal in thermal convection." In: *Phys. Rev. E* 65.5 (2002), p. 056306.

[22] K. Sugiyama et al. "Flow reversals in thermally driven turbulence." In: *Phys. Rev. Lett.* 105.3 (2010), p. 034503.

[23] P. K. Mishra et al. "Dynamics of reorientations and reversals of large-scale flow in Rayleigh-Bénard convection." In: *J. Fluid Mech.* 668 (2011), pp. 480–499.

[24] B. Hof et al. "Repeller or attractor? selecting the dynamical model for the onset of turbulence in pipe flow." In: *Phys. Rev. Lett.* 101.21 (2008), p. 214501.

[25] N. Goldenfeld, N. Guttenberg, and G. Gioia. "Extreme fluctuations and the finite lifetime of the turbulent state." In: *Phys. Rev. E* 81.3 (2010), p. 035304.

[26] T. Nemoto and A. Alexakis. "Method to measure efficiently rare fluctuations of turbulence intensity for turbulent-laminar transitions in pipe flows." In: *Phys. Rev. E* 97.2 (2018), p. 022207.

[27] E. J. Gumbel. "Les valeurs extrêmes des distributions statistiques." In: *Annales de l'institut Henri Poincaré* 5.2 (1935), pp. 115–158.

[28] S. Gao et al. "Flow around an inclined circular disk." In: *J. Fluid Mech.* 851 (Sept. 2018), pp. 687–714.

[29] B. Podvin et al. "Proper orthogonal decomposition analysis and modelling of the wake deviation behind a squareback Ahmed body." In: *Physical Review Fluids* 5.6 (June 2020), p. 064612.

Part III

BACK TO SLEEP

6 THE STABILIZATION OF WIND-INDUCED SELF-OSCILLATIONS

Knowing the static aerodynamic coefficients of an object, can we predict its dynamics or do we have to define dynamical coefficients?

6.1 INTRODUCTION

Fundamental aerodynamic characteristics, the drag and lift coefficients have been mostly identified for static objects, and time-averaged to reduce the influence of vortex shedding on the measurements. However, in nature, it might be interesting and of great importance to be able to define dynamical aerodynamic coefficients. In particular, two fluid-structure-interaction domains come to mind on that regard, wind-induced structural oscillations and flapping flight.

These two situations possess in common that, through movement, a new coupling between vortex and structure can arise. The movement is either forced for flight or free in the case of wind-induced oscillations. Yet in both, two timescales exert utmost influence on the coupling. One is due to vortex shedding $t_{vs} = 1/f_{vs} = D/\mathrm{St}U$, with St the Strouhal number, D the characteristic length of the system and U the flow velocity. The other is the characteristic time of the system t_{self}; it can relate to the flapping frequency in flight or the elastic-response frequency for a vibrating structure. From these two timescales, a dimensionless parameter, the reduced velocity Ur, can be extracted:

$$\mathrm{Ur} = \frac{1}{\mathrm{St}}\frac{t_{self}}{t_{vs}} = \frac{U}{Df_{self}}. \tag{6.1}$$

This parameter gauges how the vortex shedding and the characteristic oscillation are close to one another and as such what kind of interaction is expected. For instance, when Ur is high, the vortex shedding happens on a much shorter time scale than the system oscillation and as such, a quasi-steady approach might be possible to model the system dynamics [1]. On the contrary, when Ur is close to $1/\mathrm{St}$, the oscillation and vortex shedding synchronize and a lock-in in frequency may arise, so that the vortex shedding deviates from its original pulsation to unfold coincidentally with the system oscillation [2].

Quasi-steadiness is here understood as the negligibility of fluid memory effect, so that the aerodynamic moment and forces are solely dependent on the motion of the system [3].

An intriguing trait of the definition of Ur is the factor $1/\mathrm{St}$ which is also a dimensionless parameter. Its presence can be interpreted by the fact that the vortex shedding may be influenced by the dynamics of the mobile system and as such, both t_{vs} and St may vary from an *a priori* estimation with handbook tables or theory for static situations.

With these considerations, various interpretations of the reduced velocity are possible:

- it compares the vortex shedding and self-oscillation without prior approximation on the vortex shedding, and can be used to define St by how variables, like added mass or damping, evolve as function of Ur.
- it defines a Strouhal number based on the self-oscillation frequency rather than the vortex shedding, $\mathrm{Ur} = 1/\mathrm{St}_{\mathrm{self}}$.
- it quantifies the number of oscillations during the period a fluid particle crosses the object, and as such compares self-oscillation with flow advection.

While the reduced velocity Ur is common in self-oscillating fluid-structure interactions studies, it is scarcely spread in the flapping flight community, where frequency ratios are usually solely taken as Strouhal numbers [4]. In the case of plunging or pitching airfoils, the standard parameter to quantify the vortex-movement interaction is rather the inverse of the reduced velocity, the reduced frequency $k = \pi f_{self} D/U$ [5, 6].

In this chapter, for simplicity, only the reduced velocity Ur, defined in Eq. 6.1, will be considered, as, in the following, models will be based on self-oscillating fluid-structure interactions. A point that will be discussed later is that in our system, Ur is yet independent from the flow velocity U due to the self-oscillation having a frequency proportionnal to U.

However, estimating Ur is only the first step to understand the fluid-structure coupling and to build dynamical aerodynamic coefficients. The key to our objective is the model of the vortices, responsible for most of the unsteadiness. On that aspect, a common approach to both flight and structural oscillations is added mass, that corrects flow influence at 2nd order time derivative. While in periodically oscillating motion of wings and airfoils, standard calculation of added mass is based on Theodorsen's theory and potential flow [6–9], for wind-induced oscillations, due to the onset of flow instabilities, added mass is more difficult to estimate and complements to it such as added stiffness are often introduced [10].

In the latter case, the question of a dynamical aerodynamic coefficient is yet less important than the real dynamics of the system, in particular as wind-induced oscillations can be destructive, such as in the Tacoma Narrows Bridge flutter incident. Thus more classical approaches on the subject encompass global mode analysis [11], linear stability analysis [12] and time-domain expansion [13]. This goes especially for flutter instability, also known as galloping instability in civil engineering. A criterion has been proposed for the onset of flutter by Nakamura in 1979 [3], as a condition on the phase difference between the movement and the aerodynamic torque. This condition also depends on the distance between the center of rotation and the center of mass. Hence, Blevins summarizes the apparition of flutter when the center of mass is ahead of the center of rotation while divergence occurs when the aerodynamic center is in front of the center of rotation. In addition to that, flutter is observed to exist mostly for Ur above 10 for which the quasi-steady approximation is valid, whereas below this value, another regime is expected, vortex-induced vibrations (VIV) [1].

In this chapter, we investigate the dynamics of a balanced disk pendulum acting as a weathercock, subject to cross flow as initial conditions towards its alignment to the flow. Due to the balancing of the pendulum (placing the center of rotation at the center of mass), the condition to flutter is undefined, as the center of rotation and

the center of mass coincide, and as the aerodynamic center is far from the rotation point, no divergence is expected and the torsional motion should be governed by quasi-steady effects [1, 3]. By covering a wide range of angles of attack, our aim is to propose models that enable the reconstruction of the dynamics over the whole angular landscape of the system. Towards that end, two approaches are presented, one based on VIV time-domain expansion and the other empirical and closer to flapping flight with the definition of dynamical aerodynamic coefficients.

Similar configurations have been explored for different purposes. Pendula have since long been used for the estimation of fluid friction as described in Chapter 0, among which a recent study has been the investigation of the galloping instability and its control using a filament behind the pendulum [14]. This work is yet very different from ours as the pendulum is heavy and possesses a natural frequency independent from aerodynamic considerations and as such experiences unstable regimes above a certain threshold flow velocity, modeled by galloping instability. A closer investigation is that of a freely rotating disk placed in a flow [15]. The aim is to research wake symmetry-breaking at small amplitudes with an equilibrium position normal to the flow. A stochastic model is then proposed to reconstruct experimental pressure and angle measurements with good agreement especially on the variations of the location of the center of pressure. While the angular amplitude in that study [15] is much smaller (up to 10° around the equilibrium) than the one presented in this section-chapter (up to 90°), some experimental techniques such as the pressure measurement array placed in the disk would be very interesting to implement to provide a finer quantification of the fluid movement impacting on the pendulum dynamics we model in the following.

6.2 MATERIAL AND METHODS

6.2.1 *Experimental setup*

For these experiments, the wind tunnel is set as referred to in Chapter 0, while the pendulum is attached at its center of mass to an air bushing equipped with a rotary contact-less encoder that records the angular position α of the blade with minimal damping. For cross-reference between chapters, α is defined here as $\alpha = \theta - 90^\circ$, and would correspond to the opposite of the angle of attack in the literature.

In addition to the balancing of the pendulum, few modifications have been made to the initial setup (see Fig.6.1). The size of the disk d_{disk} and its material have been varied throughout the experiments. The change of materials, from Aluminium to Vivak® polyester, was imposed by the weight of the disk that would only allow for a short distance L to the attach point, in order to balance the pendulum. This would however increase the sensibility of the system to the attach and its own vortex shedding. Due to the elasticity of the polyester, the thickness has also been increased for the larger disks to compensate for potential aeroelastic effects, which are not quantified here.

As detailed later (Eq. 6.9), the change in disk diameter throughout the study enabled the probing of a wide range of reduced velocity Ur. Such exploration is necessary as we expect behavioral variations depending on this particular parameter coding for the relative relevance of vortex shedding on the dynamics. A simple sweep in the flow velocity U, as done in classic flutter experiments [10], is not sufficient for the variation

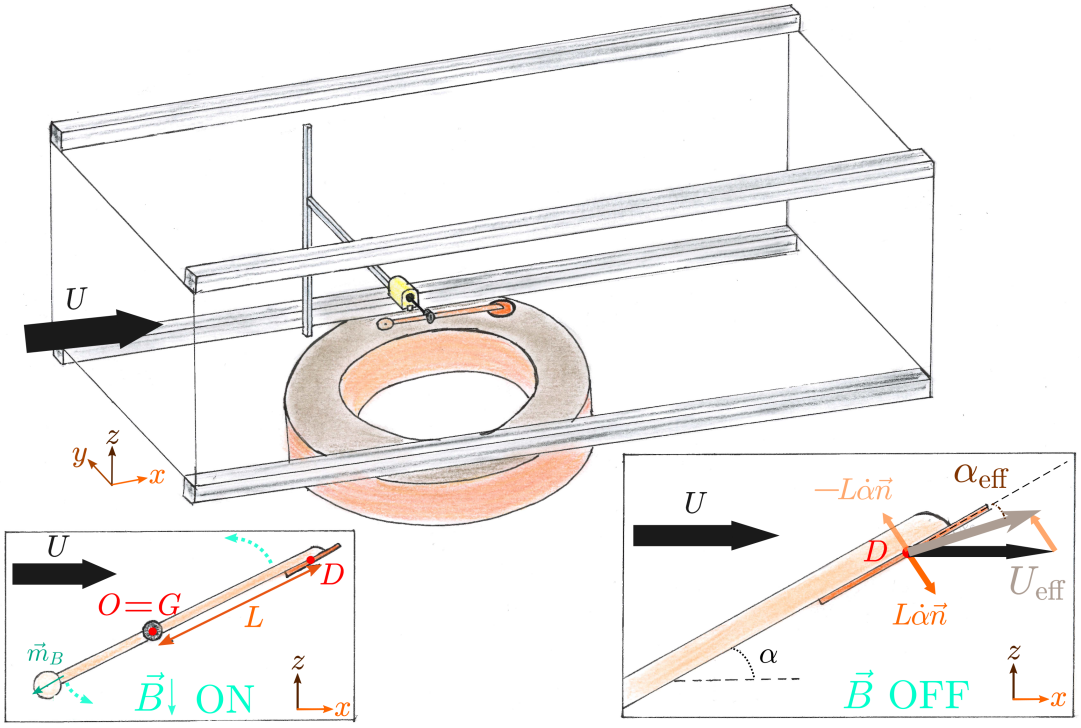

Figure 6.1: Experimental setup showing the test section of the wind-tunnel, the pendulum made of a thin disk and the coil for setting the pendulum to the vertical. A detailed view on the pendulum presents the effective flow velocity U_{eff} and angle of attack α_{eff} acting on the moving disk.

of Ur, due to the fact that the self-oscillation frequency is proportional to U and with it Ur is independent in the flow velocity as we will see in section 6.3.1.

For each of the 7 tested disk diameters, two configurations were tested: one balanced on its own and the other balanced using a thin circular magnet opposite to the disk and aligned to the wind (all 14 configurations are detailed in Table 6.1). This magnet was first placed on the system to ensure reproducibility of initial conditions. Indeed a coil was placed below the pendulum, outside the wind tunnel, which recoils the magnet between each experiment and maintains the pendulum close to the vertical before the start of the next experiment. Turning the coil off acts then as a starting point for the acquisition and movement of the system. The recoiling is achieved by taking advantage of the magnetic torque $\vec{m}_B \wedge \vec{B}$, and magnetic force $\nabla(\vec{m}_B \cdot \vec{B})$, with $\vec{m}_B$ the magnetic moment of the magnet and $\vec{B}$ the magnetic field produced by the coil (Fig.6.1). No quantitative study has been done on this magnetic setup, due to the complexity of interactions and its sole purpose to help automatize the experiment.

However, due to the aerodynamic moment at the vertical rapidly overcoming the magnetic torque, this method could only be used for small flow velocities and the smaller disks. For the larger disks and higher flow velocities, the pendulum was set vertical manually, and maintained to position by a long beam released at the start of each experiment. Despite the human intervention, no particular bias has been observed on the pendulum trajectories and each experiment conducted multiple times to reduce such uncertainty, as described later. The magnet was still used to vary the inertia

momentum J of the balanced pendulum, thus helping exploring an even wider range of the parameter space, in particular for the reduced velocity Ur, which is proportional to $\sqrt{J}$.

Diameter d_{disk} (cm)	3	4	5	6	8	9	10
Material	Al	Al	Al	Al	Al	Vivak®	Vivak®
Thickness e (mm)	0.3	0.3	0.3	0.3	0.3	0.6	0.6
Distance L (cm)	13.5	13.8	13.3	12.9	11.8	12.5	12.1
Inertia J (kg · cm^2)	1.34	1.57	1.66	1.89	2.24	2.57	2.90
Equivalent Ur	91.2	55.0	36.9	27.8	17.8	14.6	12.8
L with magnet (cm)	17.4	17.5	17.3	16.9	16.2	16.5	16.0
J with magnet (kg · cm^2)	2.36	2.63	2.86	3.25	3.95	4.31	4.82
Equivalent Ur	107	63.3	42.5	31.8	20.1	16.5	14.3

Table 6.1: Physical characteristics of the different pendula used in the experiment. Each disk enables for two sets of experiments, one with a magnet at the blade's opposite end and the other without. Al stands for aluminium.

An experimental run progresses as follows. Once the pendulum is placed at the vertical using one of the two methods presented before, the flow velocity is increased to the desired test value. Once the flow is stable, after typically 1 min, the pendulum is set free and left to oscillate around its equilibrium position, which by static considerations is at the horizontal. This run is then repeated for about 10 times for one given value of U. The process is then replicated for around 8 to 14 values of U for each pendulum configuration, totaling 751 runs all configurations included.

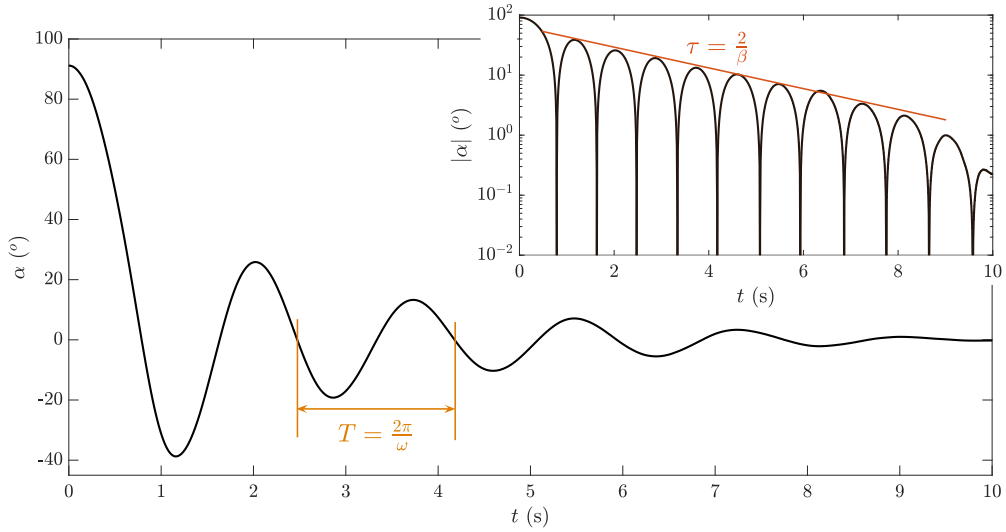

Figure 6.2: Example of an experimental signal: the pendulum is set to the vertical and left to oscillate. Inset: Semi-log presentation of the signal amplitude over time. A pulsation ω can be defined from the period T of oscillation and a damping coefficient β can be extracted from the exponential decrease of amplitude of characteristic time τ.

Fig. 6.2 shows typical time series obtained following the aforementioned protocol. Presenting periodic oscillations and exponential decay (inset), this signal can be pa-

rameterized by to characteristic times, its period $T = 2\pi/\omega$ and its attenuation time $\tau = 2/\beta$, with ω the pulsation of oscillation and β the damping coefficient, so that the system may be described by a damped harmonic oscillator equation:

$$\ddot{\alpha} + \beta\dot{\alpha} + \omega^2\alpha = 0 \tag{6.2}$$

Interlude

When looking at an exponentially damped oscillating time series, the urge to model it with a linearly damped harmonic oscillator equation like Eq. 6.2 is great but might be hasty. A double-checking can be done through the use of a phase portrait. Indeed, the phase portrait of a damped harmonic oscillator possesses some well-defined properties.

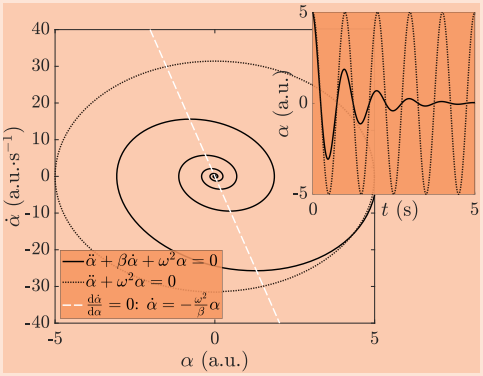

Time series and phase portrait of a damped harmonic oscillator, its non-damped equivalent, and the solutions of $\frac{d\dot{\alpha}}{d\alpha} = 0$.

In particular, while the two-fold symmetry of the envelop is commonly known, a less-known property which is however interesting is found on the derivative of the phase portrait.
The points $(\alpha_i, \dot{\alpha}_i)$ verifying the condition $\frac{d\dot{\alpha}}{d\alpha} = 0$ are aligned along a line whose slope is function of the frequency and damping ratio, $-\frac{\omega^2}{\beta}$.
It results from a simple calculation based on the expression of $\frac{d\dot{\alpha}}{d\alpha}$ as $\frac{d\dot{\alpha}}{dt}\frac{dt}{d\alpha}$ and the expression of $\ddot{\alpha}$ from Eq. 6.2.

6.2.2 *Momentum equation*

While a damped harmonic oscillator equation seems a good approach to the system dynamics, the momentum equation of the pendulum can be written in the absence of any weight nor forcing forces through the torque balance:

$$J\ddot{\alpha} = \Gamma_{aero}(t, \alpha, \dot{\alpha}) \tag{6.3}$$

with Γ_{aero} being the instantaneous aerodynamic torque.

A standard expression for Γ_{aero} based on dimensional analysis for the Reynolds number $\mathrm{Re} \sim 10^3 - 10^4$ is $\Gamma_{aero} = \frac{1}{2}\rho S U^2 L C_N(\alpha, \dot{\alpha}, t)$, with ρ the air density and $S = \pi d_{disk}^2/4$, U and L previously introduced. C_N is the normal aerodynamic coefficient which can be written as $C_N = -C_L\cos(\alpha) - C_D\sin(\alpha)$.

As the system moves in the flow, one needs to consider its retro-action on the flow and a common approach consists in adjusting the flow velocity U_{eff} in the reference frame of the disk and the angle of attack to this corrected flow velocity α_{eff}, see Fig. 6.1. The disk velocity being estimated as $L\dot{\alpha}$, U_{eff} and α_{eff} can be defined as in Eq. 6.4 [2, 4, 5].

$$\begin{cases} U_{\text{eff}}^2 &= U^2 + 2LU\dot{\alpha}\sin(\alpha) + L^2\dot{\alpha}^2 \\ \alpha_{\text{eff}} &= \alpha + \arctan\left(\frac{L\dot{\alpha}\cos(\alpha)}{U+L\dot{\alpha}\sin(\alpha)}\right) \end{cases} \tag{6.4}$$

Combining the above equations and considering that angular velocity only affects the aerodynamic coefficient in α_{eff}, the momentum equation becomes Eq. 6.5.

$$J\ddot{\alpha} = \frac{1}{2}\rho SLU_{eff}^2 C_N(\alpha_{eff}, t) \tag{6.5}$$

Through a Taylor expansion in α around the equilibrium position $\alpha = 0°$, a damped harmonic oscillator equation is obtained, involving $\frac{dC_N}{d\alpha}|_0$, the angular derivative of the C_N coefficient at $\alpha = 0°$ (details of the Taylor expansion in Annex C):

$$\ddot{\alpha} + \frac{\rho SL^2U}{2J}\left|\frac{dC_N}{d\alpha}|_0\right|\dot{\alpha} + \frac{\rho SLU^2}{2J}\left|\frac{dC_N}{d\alpha}|_0\right|\alpha = O(\alpha^3) \tag{6.6}$$

The similarity between Eq. 6.6 and Eq. 6.2 supports the characterization of the signal by the pulsation and attenuation, described in Fig. 6.2.

6.3 RESULTS

6.3.1 *VIV-inspired time domain expansion*

In order to quantitatively compare the dynamics resulting from Eqs. 6.2 and 6.6, the normal C_N coefficient is required.

A first approximation for it is to take the static coefficient $C_{N_{st}}$ as C_N in Eq.6.5. For a disk, it depends strongly on α, but is almost linear for α spanning from about $-\pi/4$ to $\pi/4$ [16]. Using the Taylor expansion (Eq. 6.6), we can define a pulsation ω_{st} and a attenuation β_{st}, whose expressions are $\omega_{st}^2 = \frac{\rho SLU^2}{2J}\left|\frac{dC_{N_{st}}}{d\alpha}|_0\right|$ and $\beta_{st} = \frac{\rho SL^2U}{2J}\left|\frac{dC_{N_{st}}}{d\alpha}|_0\right|$.

Figure 6.3 compares the experimental values for ω^2 and β with their static coefficient approximations ω_{st}^2 and β_{st}. While the order of magnitude for both ω^2 and β is correct in the static approximation, it does not capture the experimentally computed values, in particular when ω_{st}^2 is high, which corresponds to large disks and high flow velocity. Hence, the static approximation does not recover the real dynamics, despite the consideration of non-stationarity in U_{eff} and α_{eff}, commonly introduced in various fluid-structure interaction fields.

When observing frequency shift in unsteady aerodynamics, a standard theoretical approach is the addition of stiffness and mass to the dynamics equation, thus taking into account vortex shedding effects on the free dynamics [2, 10]. In our case, an added mass would correspond to an added inertia due to the rotational environment.

Also known as time-domain expansion, this method consists in appending supplementary time derivatives of a relevant variable (for us α), $a_0\alpha$, $a_1\dot{\alpha}$, $a_2\ddot{\alpha}$, etc... to the governing equation of a system.

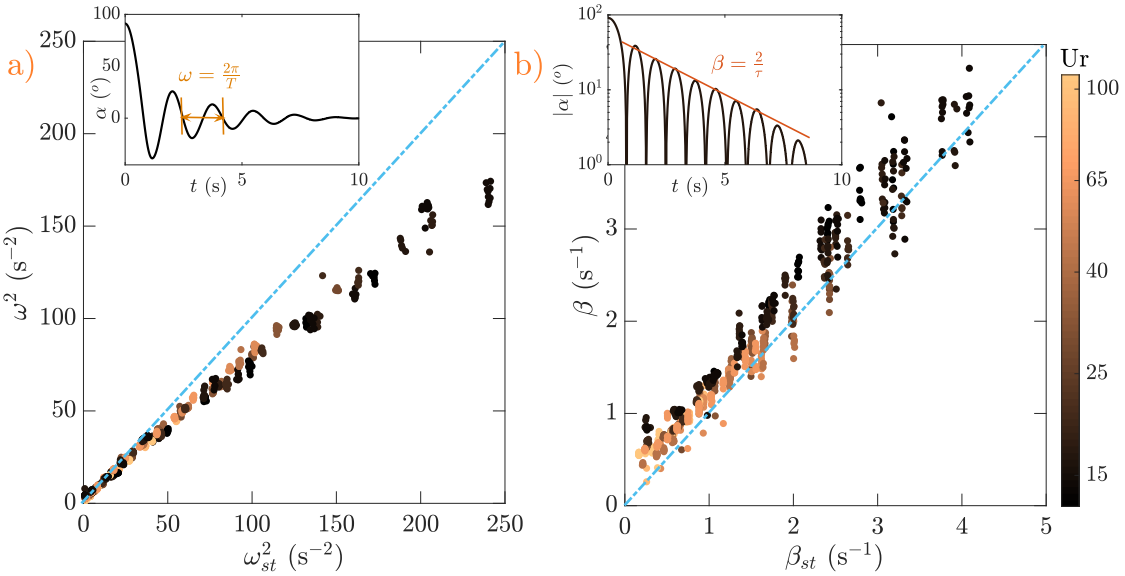

Figure 6.3: a) Experimental measured pulsation ω^2 with respect to the static estimated pulsation ω_{st}^2. b) Experimental measured damping coefficient β with respect to the static estimated damping β_{st}. Dash-dotted lines represent identity and the color codes for the Ur parameter of each experiment on both graphs.

In vortex-induced vibration (VIV) models, added mass, stiffness and damping are appended to the system equation in the simplest way possible, which writes from Eq. 6.6 as follows:

$$(1+m)\ddot{\alpha} + (\beta_{st} + \gamma U)\dot{\alpha} + (\omega_{st}^2 + k)\alpha = 0 \tag{6.7}$$

with m the added mass, γU the added damping and k the added stiffness.

For Eq. 6.7 to reconstruct the experimental dynamics, whose equation may be expressed by Eq. 6.2, an identification of both the pulsation and the attenuation is necessary. As such, m, γU and k can be defined by the following relations:

$$\begin{cases} \omega^2 &= \frac{\omega_{st}^2 + k}{1+m} \\ \beta &= \frac{\beta_{st} + \gamma U}{1+m} \end{cases} \tag{6.8}$$

To estimate m and k, a linear fit of ω^2 as a function of ω_{st}^2 is done. Then γ is obtained by inverting Eq. 6.8: $\gamma = (1+m)\frac{\beta}{U} - \frac{\beta_{st}}{U}$, with m taken from the previous fit. An example of the linear fit is shown in Annex C. This computation is done using the whole range of flow velocity for each tested disk configuration, giving only one value for m, γ and k per disk, *as ω_{st}/U is constant by calculation*.

Stemming from the VIV framework, behavioral dynamics likely depend on the ratio between the vortex shedding frequency and the frequency of natural oscillation of the system, the reduced velocity Ur, which was previously introduced but not yet defined in our particular case.

As it is a control parameter and should be known *a priori*, the self-oscillation frequency in the definition of Ur (Eq. 6.1) is taken as the one from the static approximation $\omega_{st}/2\pi$, which from the Figure 6.3 is not that different from ω. It follows that:

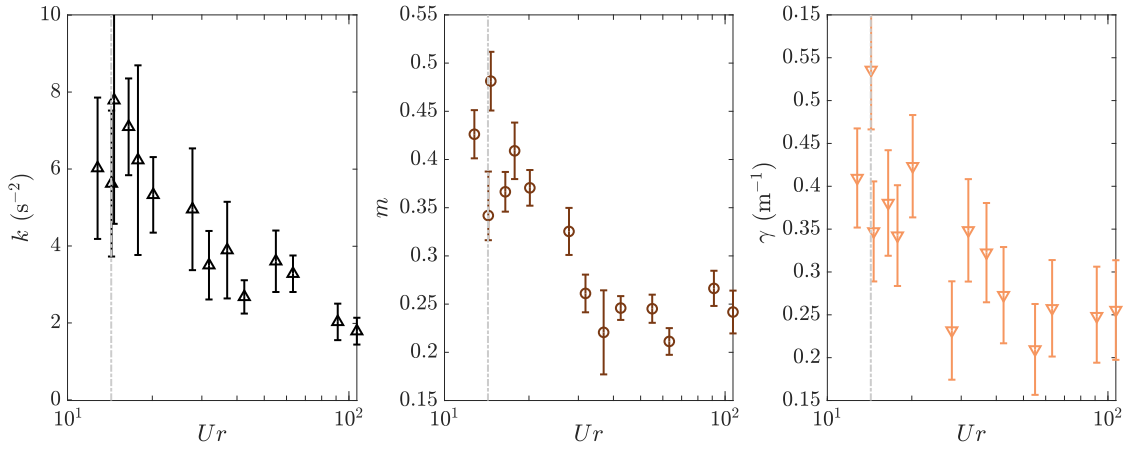

Figure 6.4: Added stiffness k, mass m and damping γ obtained for each Ur parameter in the experiments. Dash-dotted line represents 1/St with St $\simeq$ 0.07.

$$\mathrm{Ur} = \frac{1}{\mathrm{St}}\frac{f_{vs}}{f} = \frac{U}{d}\frac{2\pi}{\sqrt{\frac{1}{2}\frac{\rho S U^2 L}{J}\left|\frac{\mathrm{d}C_N}{\mathrm{d}\alpha}|_0\right|}} = \frac{4}{d^2}\sqrt{\frac{2\pi J}{\rho L\left|\frac{\mathrm{d}C_N}{\mathrm{d}\alpha}|_0\right|}} \tag{6.9}$$

In view of the particularity of wind-induced self-oscillation, observed in Eq. 6.9, Ur is independent of the flow velocity U. As such, Ur is varied in the experiments by the modifications of geometrical parameters (d, J, L). The range of explored Ur in this study is spanning from 12 to 110, as introduced in Table 6.1.

As previously mentioned, a condition to apply quasi-steady models is to have Ur>10, which here is thus respected for all configurations.

Now that we have a proper definition of Ur and a way of estimating m, γ and k for one configuration, Figure 6.4 shows the evolution of these three added terms as functions of the parameter Ur.

The three of them exhibit the same overall tendency with its maximum around Ur $\simeq$ 15 and a decrease to a constant value as Ur tends to higher values. The maximum corresponds to a value of St $\simeq$ 0.07, represented in Fig. 6.4 by a dash-dotted line, and estimated in the literature to be linked with a transverse vortex shedding for a disk [17]. Such divergence around UrSt $\sim$ 1 is expected in VIV systems, for which the oscillations couple together due to the similarity of frequencies, leading to lock-in synchronicity between vortex shedding and natural oscillations. Another observation is that the maximum of the added mass is close to 0.5, which relates to the added mass coefficient found in particle-laden flows for a sphere immersed in fluid [18, 19]. A possible interpretation for this value would thus be that at synchronization, the disk and its wake form a "sphere" of fluid that does only detach at a specific step in the oscillation cycle.

6.3.2 *Dynamical C_N coefficient*

Contrary to the VIV approach for which a strong hypothesis of damped-harmonic oscillator behavior is done, we propose an empirical model which does not require any

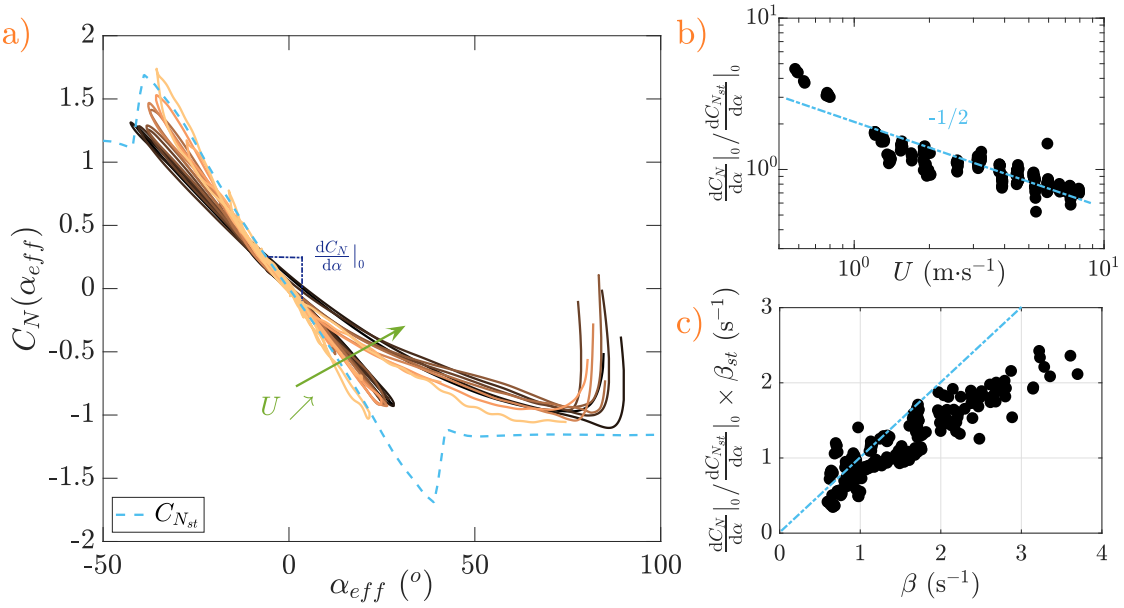

Figure 6.5: a) Dynamic (solid lines) vs static (dashed line) C_N coefficients as function of the angular position α_{eff} given by Eq. 6.4 for various flow velocities U, which color codes as follows: the lighter the color, the smaller U. b) Ratio between the slope of the dynamic $C_{N_{in}}$ coefficient and the static coefficient $C_{N_{st}}$ with respect to flow velocity. c) Damping estimated from the empirical correction on the $C_{N_{st}}$ coefficient compared to the experimental damping β.

hypothesis of the sort. Going back to Eq. 6.5, it is possible to invert the momentum equation to extract an instantaneous $C_{N_{in}}(\alpha_{\text{eff}}, t)$ coefficient.

$$C_{N_{in}}(\alpha_{\text{eff}}, t) = \frac{2J\ddot{\alpha}}{\rho S L U_{\text{eff}^2}} \tag{6.10}$$

The thus-obtained experimental instantaneous $C_{N_{in}}$ coefficient is presented in Fig. 6.5.a) for one disk configuration together with its static $C_{N_{st}}$ equivalent known for a disk [16], as a function of the effective angle of attack α_{eff}. The color codes for the flow velocity U: the lighter the line, the lower the velocity. A first observation is the strong dependency of the linear section of the C_N coefficient around $\alpha = 0°$ on flow velocity. This dependency is less marked on the constant part of the signal ($\alpha_{\text{eff}} \gtrsim 50$), which corresponds to the initial oscillation starting at $\alpha = 90°$. While it might seem unusual to look at $C_{N_{in}}$ as a function of α_{eff} rather than α, $C_{N_{in}}$ has to be defined in the reference frame of the disk. Appendix C presents how α_{eff} is important for the correct definition of $C_{N_{in}}$.

With this consideration, we expect an empirical model to be simply a multiplicative factor correction to the static model, especially as α_{eff} enables the C_N reconstructions to collapse on a single line over time (see Annex), accounting for the change in the slope of $C_{N_{in}}$ compared to that of $C_{N_{st}}$ around $\alpha_{\text{eff}} = 0$.

$$J\ddot{\alpha} = \frac{1}{2}\rho S L U_{eff}^2 C_{N_{st}}(\alpha_{eff}) \times \frac{\frac{dC_{N_{in}}}{d\alpha}|_0}{\frac{dC_{N_{st}}}{d\alpha}|_0} \tag{6.11}$$

When looking at the slope of the linear section of the dynamic $C_{N_{in}}$ coefficient with respect to the slope of the static $C_{N_{st}}$ coefficient as a function of the flow velocity U, (Fig. 6.5.b), a trend compatible with a $-1/2$ power law scaling is observed. This power law reminds of the skin friction drag coefficient dependency in Reynolds number, around $\mathrm{Re} \sim 10^3 - 10^4$, corresponding to the range we cover in our experiments [20]. By adding this correction into the equation 6.5 however, the damping is also modified by the same factor $\frac{\mathrm{d}C_{N_{in}}}{\mathrm{d}\alpha}\big|_0 / \frac{\mathrm{d}C_{N_{st}}}{\mathrm{d}\alpha}\big|_0$, especially visible when the Taylor expansion is done as in Eq. 6.6. In Fig. 6.5.c), the newly computed damping term is plotted against the experimental damping coefficient. It is thus clear that this multiplicative factor in the equation does not entirely reconstruct the dynamics and another damping $\chi\dot{\alpha}$ has to be added into this empirical model for better results. While it is not yet understood, it appears that the needed damping to be added in this case is close enough to the added damping γU from the previous model, so that $\gamma U\dot{\alpha}$ can just be appended to Eq. 6.11 to recover the experimental behavior.

$$J\ddot{\alpha} + \chi\dot{\alpha} = \frac{1}{2}\rho S L U_{eff}^2 C_{N_{st}}(\alpha_{eff}) \times \frac{\frac{\mathrm{d}C_{N_{in}}}{\mathrm{d}\alpha}\big|_0}{\frac{\mathrm{d}C_{N_{st}}}{\mathrm{d}\alpha}\big|_0} \tag{6.12}$$

The validity of this complete model will be tested in the following, by comparison between the two approaches both in terms of time series and phase portrait.

6.4 DISCUSSION

6.4.1 *Physical interpretations to the models*

Now that the two models have been presented, a physical interpretation for each complementary term is welcome.

In particular, the added mass (or inertia) can be interpreted, like in particle-laden flows and VIV, as the mass of fluid displaced and dragged by the disk in its movement. We can therefore compute the diameter d_{air} of an equivalent air sphere around the disk centered at the center of the disk and of inertia momentum mJ:

$$d_{air}^3(L^3 + \frac{d_{air}^2}{10}) = \frac{6mJ}{\pi\rho} \tag{6.13}$$

As shown in Fig. 6.6.a), this diameter d_{air} is almost linear in the diameter of the disk d_{disk} with a plateau at the smaller values probably due to the influence of the rod holding the disk.

With regards to the added stiffness, it is difficult to conclude on a phenomenological interpretation. Yet we hypothesized that it transcribes into the momentum equation the rolling of the wingtip vortices that have to change their rotation between positive and negative angles of attack, leading to a restoring spring-like torque $-k\alpha$ with their coupling to the leading- and trailing-edge vortices.

On the other hand, for the added damping, we can define a factor $\epsilon = \frac{\gamma U}{(1+m)\beta_{st}}$ which considers it in the reference frame of the static coefficient equation 6.6 corrected in added mass, so that $\beta = \frac{\beta_{st}}{1+m} + \epsilon$. ϵ is therefore the correction required with respect to the static description of the system. In Fig. 6.6.b), the ϵ estimate for each pendulum

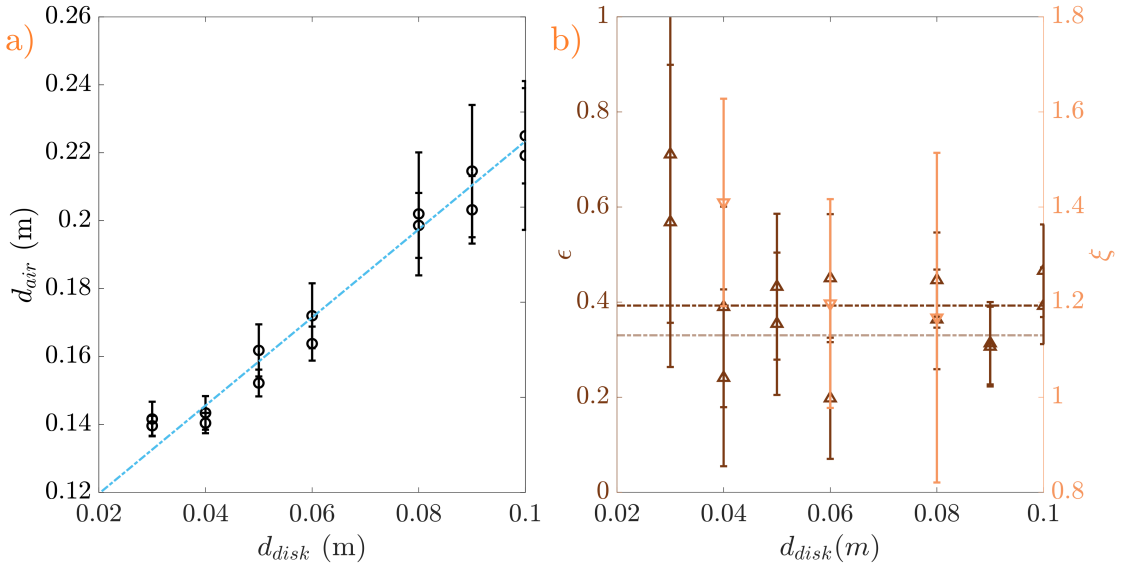

Figure 6.6: Evolution of the interpreted added terms d_{air} (a), ϵ (b left axis) and ξ (b right axis) as functions of the diameter of the disk d_{disk}.

configuration is presented versus the pendulum diameter d_{disk}. Though the value for the smaller disk is close to 0.7, ϵ tends to converge at higher d_{disk} towards a constant value ϵ_c, represented by the dash-dotted lines. A good candidate for this value is $\epsilon_c = \frac{\pi}{8}$ (dark line) which can be related to the potential flow theory and has been described as damping in unsteady aerodynamic flutter models [1, 21]. A refinement of the formula from Fung 1969 in our specific case would be $\epsilon_c = \frac{2\pi-1}{16}$ (light line).

For the empirical model, there is also a need for additional damping as presented previously. However, rather than introducing it as a $+\chi\dot{\alpha}$ in Eq. 6.12, it is possible to implement it directly into the dynamical equation Eq. 6.11 without changing its form, as a correction on α_{eff} and U_{eff}, though for the latter, it would only result in a 3rd order correction. It can indeed be noticed that the damping β_{st} emanates from the $L\dot{\alpha}/U$ in Eq. 6.6, which is the approximation taken for the relative velocity of the counter flow in response to the pendulum movement (Fig. 6.1). By impending a modification of the damping through the modification of the $C_{N_{st}}$ coefficient, it can be balanced by simply varying this relative velocity by a factor $\xi = \frac{\beta}{\beta_{st}} \frac{\frac{dC_{N_{st}}}{d\alpha}|_0}{\frac{dC_{N_{in}}}{d\alpha}|_0}$, as introduced in Eq. 6.14.

$$\begin{cases} J\ddot{\alpha} &= \frac{1}{2}\rho S L U^{*2}_{eff} C_{N_{st}}(\alpha^*_{eff}) \times \frac{\frac{dC_{N_{in}}}{d\alpha}|_0}{\frac{dC_{N_{st}}}{d\alpha}|_0} \\ U^{*2}_{eff} &= U^2 + 2\xi L U \dot{\alpha}\sin(\alpha) + \xi^2 L^2 \dot{\alpha}^2 \\ \alpha^*_{eff} &= \alpha + \arctan\left(\frac{\xi L \dot{\alpha}\cos(\alpha)}{U + L\xi\dot{\alpha}\sin(\alpha)}\right) \end{cases} \tag{6.14}$$

Estimated values for ξ are presented in Fig. 6.6.b), for three different configurations as examples, though the uncertainty on the damping and empirical correction makes it difficult to conclude on this part. An observation to be made yet is that ξ appears to be higher than 1, meaning that when the aerodynamic coefficient is pondered by a dynamical term, the air around the pendulum moves at a higher velocity than the pendulum its self. This could be explained by the fact that not only the air behind the

pendulum is dragged away but the air ahead is deviated as well, and may induce an supplementary advection for the air behind.

6.4.2 *Comparison of models*

When proposing models to reconstruct experimental dynamics, the natural thing to do is estimating the match of the model to the experiment. To quantify this, we have computed the quadratic angular error $\sqrt{\langle \Delta\alpha^2 \rangle}$ between the solution of the modeling equation and the experimental signal for the same initial conditions $\alpha(0)$ and $\dot{\alpha}(0)$. The corresponding signals are shown in Fig. 6.7. (top), with the initial conditions taken close to the vertical at rest. Here, while the VIV-inspired model collapses almost on the experiment with $\sqrt{\langle \Delta\alpha^2 \rangle} \leq 2°$, the empirical model is quite wrong as $\sqrt{\langle \Delta\alpha^2 \rangle} \simeq 10°$, due to the lack of restitution of the transient dynamics. Even the static model only exhibits a deviation of about $\sqrt{\langle \Delta\alpha^2 \rangle} \simeq 5°$ from the experimental signal despite the lack of fidelity in both frequency and damping.

However, the phase portrait match is greater for the empirical model, especially in the flow velocity dependence (Fig. 6.7.a-d). When looking at the $\dot{\alpha} = 0$ line, the empirical model is the only one that shows the same evolution in flow velocity as the experiment. Hence it confirms that the reconstruction for this model is correct at smaller amplitude, as the transient needs not to be considered. To support this, finally, the solutions of both models collapses with $\sqrt{\langle \Delta\alpha^2 \rangle} \simeq 1°$ to the experimental signal for initial conditions taken at the first minimum of oscillation (i. e.$\alpha(t = 0) \simeq 40°$), which takes place in the linear part of the C_N coefficient, ahead of stall (Fig. 6.7. bottom).

6.5 PERSPECTIVES

This chapter presents two very different approaches to incorporate dynamical effects into the static aerodynamic coefficient. Despite the seemingly verified condition on Ur (see 0.1), the quasi-steady approximation is not sufficient in this particular case of a weathercock-like pendulum. A possible explanation to this is the peculiar form of Ur, which though considered a reduced velocity is independent of the flow velocity U. Such particularity is yet not very common in fluid-structure interactions.

Yet the simplicity and versatility of the system, with only a balanced pendulum placed in a wind tunnel, offers first an ideal framework to investigate the geometrical dependencies of dynamical corrections for aerodynamic forces. For instance, here we propose added mass, damping and stiffness for a disk. As these three terms help reconstructing the dynamics, it is natural to think they code for vortex interactions. As seen in the previous chapters, such vortices are highly dependent on the geometry already in static so we can expect strong influence on the dynamical retroaction.

A simple comparison for this can be found in the literature on flutter and VIV. All kinds of objects have been tested, from cylinders [22, 23] to flags [24, 25], with civil engineering models of bridges and towing cables [26–28]. Although the models are diverse and the research in the various fields similar in many aspects, no single model encoding the geometrical dependency has yet been proposed and the added mass, stiffness and damping coefficients are only determined in compiled handbooks for each particular situation. On the contrary, in static configuration, at least in 2D, some transforms, such as Joukowski's, enable the calculation of aerodynamic forces for almost

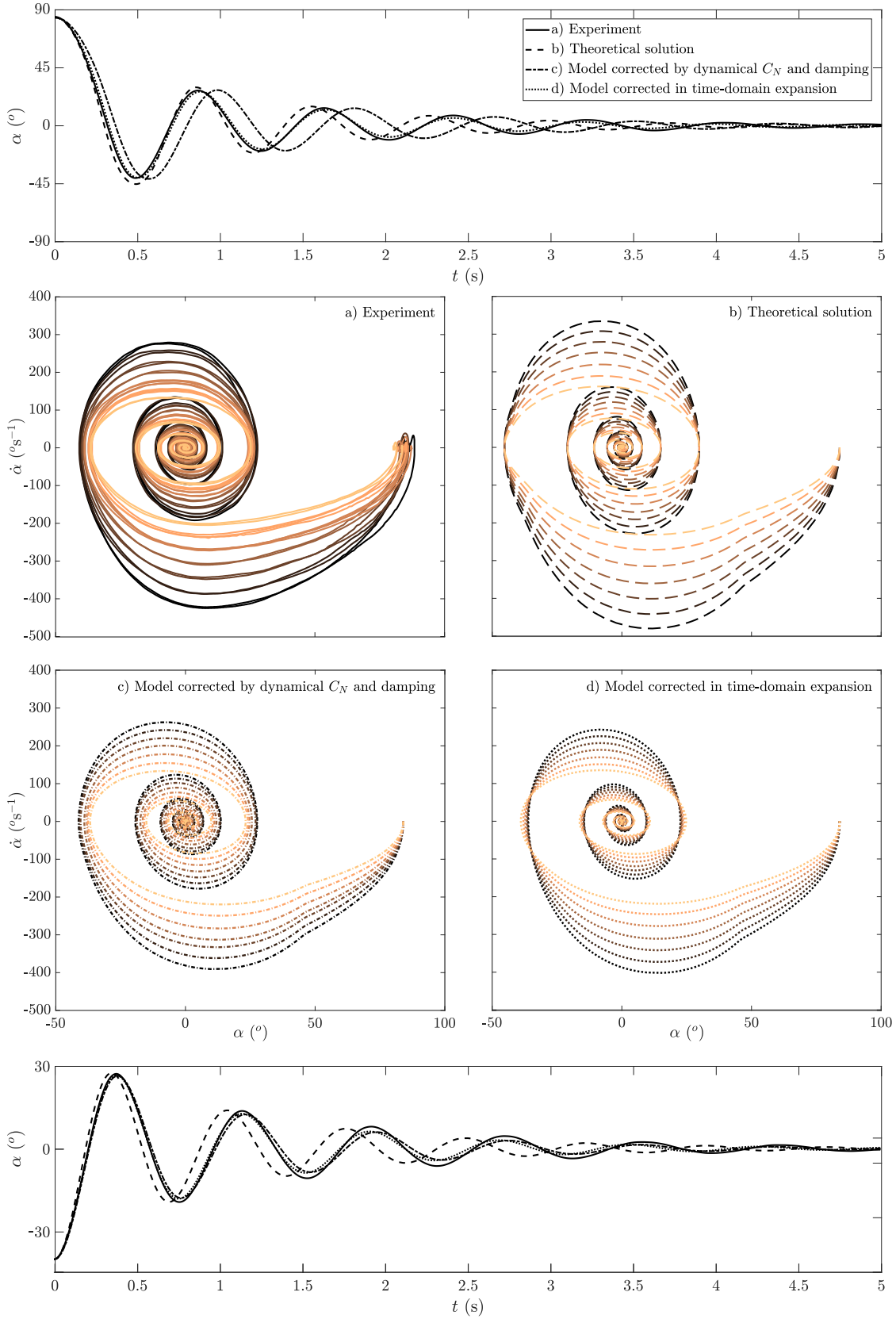

Figure 6.7: Comparison between the experiment a) and the various models proposed here: b) static coefficient model, c) empirical dynamic coefficient model with added damping and d) VIV-based model. Top: experimental signal with the model signals with initial conditions at the vertical. Bottom: models with initial conditions at the first minima of oscillation. Middle: phase portraits for the experiment and models. The color codes for the flow velocity, with the lighter being the smaller velocity. All presented curves were obtained from the 4 cm pendulum with magnet attached, similar results were obtained for the other pendula.

any shape of airfoils [8]. In flapping flight, one limitation to such standardization is the Reynolds number, which spans from 10 to 10^4, from insects to birds [29]. This range overlaps with the change in flow velocity dependence for the aerodynamic forces and Strouhal numbers usually vary notably over that range, rendering the scaling difficult to choose for comparison across situations.

On another note, the determination of the empirical dynamic C_N coefficient may help on a different domain than the two previously mentioned, that also makes use of wind-induced oscillations. Knowing the aerodynamic coefficients is enssential in the design of wind-induced energy-harvesters that are under development as new renewable energy sources [30–32]. These harvesters collect energy from vortex shedding and aerodynamic forces link with the collected energy levels [33]. So a better understanding of dynamical effects in fluid-structure interactions is key to the enhancement of wind energy extraction, as already proven for wind turbines and the use of dynamic stall to enable energy production at lower wind speeds [34].

REFERENCES

[1] R. D. Blevins. *Flow-induced Vibration*. Van Nostrand Reinhold, 1990.

[2] M. P. Païdoussis, S. J. Price, and E. de Langre. *Fluid-Structure Interactions: Cross-Flow-Induced Instabilities*. Cambridge University Press, 2011, p. 414.

[3] Y. Nakamura. "On the aerodynamic mechanism of torsional flutter of bluff structures." In: *Journal of Sound and Vibration* 67.2 (Nov. 1979), pp. 163–177.

[4] Z. J. Wang. "Vortex shedding and frequency selection in flapping flight." In: *Journal of Fluid Mechanics* 410 (2000), pp. 323–341.

[5] N. Chiereghin, D. J. Cleaver, and I. Gursul. "Unsteady lift and moment of a periodically plunging airfoil." In: *AIAA Journal* 57.1 (2019), pp. 208–222.

[6] J. W. Edwards, H. Ashley, and J. V. Breakwell. "Unsteady aerodynamic modeling for arbitrary motions." In: *AIAA Journal* 17.4 (Apr. 1979), pp. 365–374.

[7] T. Theodorsen. *General Theory of Aerodynamic Instability and the Mechanism of Flutter*. Tech. rep. 496. 1949, p. 55.

[8] T. von Kármán and W. R. Sears. "Airfoil Theory for Non-Uniform Motion." In: *Journal of the Aeronautical Sciences* 5.10 (Aug. 1938), pp. 379–390.

[9] K. Ramesh et al. "An unsteady airfoil theory applied to pitching motions validated against experiment and computation." In: *Theoretical and Computational Fluid Dynamics* 27.6 (2013), pp. 843–864.

[10] S. Chen, S. Zhu, and Y. Cai. "An unsteady flow theory for vortex-induced vibration." In: *Journal of Sound and Vibration* 184.1 (July 1995), pp. 73–92.

[11] J. Moulin and O. Marquet. "Flow-induced instabilities of springs-mounted plates in viscous flows: A global stability approach." In: *Physics of Fluids* 33.3 (2021).

[12] G. Bartoli and C. Mannini. "A simplified approach to bridge deck flutter." In: *Journal of Wind Engineering and Industrial Aerodynamics* 96.2 (2008), pp. 229–256.

[13] D. D. Bueno and E. H. Dowell. "A note on the state space representation of aeroelastic systems for time domain analysis." In: *Journal of Fluids and Structures* 104 (2021), p. 103294.

[14] A. Orchini, H. Kellay, and A. Mazzino. "Galloping instability and control of a rigid pendulum in a flowing soap film." In: *Journal of Fluids and Structures* 56 (2015), pp. 124–133.

[15] E. Boujo and O. Cadot. "Stochastic modeling of a freely rotating disk facing a uniform flow." In: *Journal of Fluids and Structures* 86 (Apr. 2019), pp. 34–43.

[16] O. Flachsbart. "Messungen an ebenen und gewölbten Platten." In: *Ergebnisse der Aerodynamischen Versuchsanstalt zu Göttingen - IV. Lieferung*. München und Berlin: Verlag von R. Oldenburg, 1932, pp. 96–100.

[17] S. Gao et al. "Flow around an inclined circular disk." In: *J. Fluid Mech.* 851 (Sept. 2018), pp. 687–714.

[18] S. D. Poisson. "Mémoire sur les mouvements simultanés d'un pendule et de l'air environnant." In: *Mémoires de l'Académie Royale des Sciences de l'Institut de France*. Vol. 11. 1831, pp. 521–581.

[19] G. G. Stokes. "On the Effect of the Internal Friction of Fluids on the Motion of Pendulums." In: *Mathematical and Physical Papers*. Vol. 88. 2208. Cambridge: Cambridge University Press, 1912, pp. 1–10.

[20] S. F. Hoerner. *Fluid-Dynamic Drag*. 1965.

[21] Y. C. Fung. *An Introduction to the Theory of Aeroelasticity*. Dover Books on Aeronautical Engineering. Dover Publications, 2008.

[22] S. C. Luo et al. "Stability to translational galloping vibration of cylinders at different mean angles of attack." In: *Journal of Sound and Vibration* 215.5 (1998), pp. 1183–1194.

[23] M. Horowitz and C. H. K. Williamson. "Vortex-induced vibration of a rising and falling cylinder." In: *Journal of Fluid Mechanics* 662 (Nov. 2010), pp. 352–383.

[24] M. Argentina and L. Mahadevan. "Fluid-flow-induced flutter of a flag." In: *Proceedings of the National Academy of Sciences of the United States of America* 102.6 (2005), pp. 1829–1834.

[25] S. Alben and M. J. Shelley. "Flapping States of a Flag in an Inviscid Fluid: Bistability and the Transition to Chaos." In: *Physical Review Letters* 100.7 (Feb. 2008), p. 074301.

[26] M. Matsumoto et al. "Effects of aerodynamic interferences between heaving and torsional vibration of bridge decks: The case of Tacoma Narrows Bridge." In: *Journal of Wind Engineering and Industrial Aerodynamics* 91.12-15 (2003), pp. 1547–1557.

[27] Z. Q. Chen et al. "Flutter, Galloping, and Vortex-Induced Vibrations of H-Section Hangers." In: *Journal of Bridge Engineering* 17.3 (2012), pp. 500–508.

[28] C. Mannini, A. M. Marra, and G. Bartoli. "Journal of Wind Engineering VIV – galloping instability of rectangular cylinders : Review and new experiments." In: *Jnl. of Wind Engineering and Industrial Aerodynamics* 132 (2014), pp. 109–124.

[29] D. D. Chin and D. Lentink. "Flapping wing aerodynamics: From insects to vertebrates." In: *Journal of Experimental Biology* 219.7 (2016), pp. 920–932.

[30] J. Allen and A. Smits. "Energy harvesting eel." In: *Journal of Fluids and Structures* 15.3-4 (Apr. 2001), pp. 629–640.

[31] S. Olivieri et al. "Fluttering conditions of an energy harvester for autonomous powering." In: *Renewable Energy* 105 (2017), pp. 530–538.

[32] N. Wu et al. "Performance of a bistable flow-energy harvester based on vortex-induced vibration." In: *Journal of Wind Engineering and Industrial Aerodynamics* 217.January (2021), p. 104733.

[33] T. Shi et al. "Performance of an omnidirectional piezoelectric wind energy harvester." In: *Wind Energy* 24.11 (2021), pp. 1167–1179.

[34] E. J. Stamhuis. *Biomimetic Wind Turbine Design with Lift Enhancing Periodic Stall*. Patent. 2017.

CONCLUSION

7 CONCLUSION

The goal of this thesis was to deeply understand the dynamics of wind-swept pendulums and the relation between these and the wake dynamics of the pendulum, from both fundamental aerodynamic considerations and complex system approaches.

Indeed, despite its simplicity, previous experiments with a disk pendulum placed in a wind tunnel had brought up rich aerodynamic behaviors such as the bistability of the equilibrium position for a range of flow velocities [1]. Although the bistability could be explained by the shape of the aerodynamic C_N coefficient, this shape and its possible impact on other dynamical properties were not yet understood. In particular, the bistability is induced by the presence of a sharp stall between two regimes: one drag-dominated regime of constant C_N, and the other lift-dominated regime of linear increase of C_N with the angle of attack $\alpha = 90° - \theta$.

As such, Part i researches the three-way coupling between the aerodynamic coefficient, the wake and the geometry of the pendulum, to try understanding 3D stall.

First in Chapter 1, the wake of a fixed inclined disk was investigated, to try understanding how the flow around the disk could lead to the particular shape of the C_N coefficient. We observed a clear change of the wake structure between the two regimes, from a ring vortex when drag dominates to a two-vortex plane-like wake when lift carries the pendulum. Together with this, the vortex intensity was shown to follow a comparable angular evolution to that of the C_N coefficient. This provides a first clue towards the understanding of the stall origin in the restructuring of the wake.

Chapter 2 then centers around the question of the aspect-ratio of the pendulum. In Nature, disks and similarly squares are quite rare and more common objects tend to present an oblong structure, with one dimension larger than the others. By varying the aspect ratio of a rectangular plate, we have observed the disappearance of the bistability, coming from the leveling of stall. Only aspect ratios close to 1 present a sharp stall and thus a bistability in the pendulum configuration. Complementary to this, we extended the definition of the stall angle to any profile of C_N coefficient and observed that this angle varies almost linearly with the arc-tangent of the aspect ratio, corresponding to the angle formed by the diagonal of the rectangular plate with the chord. This gives a rule-of-thumb estimate of the stall angle of a rectangular plate of any aspect ratio.

Like the aspect-ratio, a second geometrical property of an object that is important in Aerodynamics is the porosity. To understand its influence on the aerodynamic coefficient and the stall, Chapter 3 makes use of a most common everyday object: the fly-swatter. By tuning the filling of the holes of a fly-swatter, we have been able to some extent to control the appearance of a sharp stall. Comparing the configuration of bistability with minimal filling and the configuration of non-bistability with maximal filling, we have observed that the stability of the leading-edge vortex (LEV) was necessary to the existence of the bistability but not sufficient as the wingtip vortices are also needed to

initiate the sharp stall in their interaction with the LEV.

These first chapters suggest that the main wake structures responsible to a sharp 3D stall are the wingtip vortices, whose interaction with either the leading-edge or trailing-edge vortex change the amplitude of stall. This would thus mean that the mechanism of stall already dependent on the camber and thickness of an airfoil in 2D presents another phenomenology in 3D.

Another aspect of the bistable pendulum which has not been tackled in Part i is the dynamics of bistable pendulum itself, as Part i concentrated on a static approach of the system only. The second part of this thesis (Part ii) thus explores the temporal dynamics of the pendulum in the bistable zone.

Throughout Chapter 4, 5 different behaviors of the pendulum are identified: transitions (both one-way and both-ways), wanderings around the unstable position, overshoots and excursions. By first describing the possibilities of our pendulum to behave like other multistable systems, we have dug in this chapter a few trenches to use the pendulum as a toy system to study not only the aerodynamics of the disk or rectangle but also more theoretical and universal aspects of stochastic multistable systems.

In Chapter 5, one of these trenches is followed: the time statistics of the one-way transitions. As double-exponential statistics were observed, we have developed in this chapter a model inspired from the transition to turbulence. The underlying phenomenology points towards a rare-event triggering of the transition in the wake, that preliminary PIV measurements seem to support as well.

These two chapters leave many doors open in their trail, as we will further develop in the next section.

Finally in Part iii, a simple question was asked: what would happen if our wind-swept pendulum were not subjected to any other force than the aerodynamic efforts.

Chapter 6 thus delves into the unsteady aerodynamics of the balanced pendulum returning to the horizontal, as a quasi-steady approach to this weathercock problem was lacking. In transcribing the experimental dynamics, we propose in this chapter two models to complement the static C_N coefficient in a dynamical manner. One relies on classical fluid-structure interaction modeling while the other is empirical.

This final chapter forms a bridge connecting the static/steady aspects of aerodynamics to the forced aerodynamics of flight, by exploring the range of freely-moving but not restrained nor forced objects, as the only frequency of the system is induced by the wind itself. This first step into unsteady aerodynamics is followed by another bigger one in the following, Part iv, with the development of a project on butterfly flight in parallel of this thesis centered around a pendulum.

7.1 PERSPECTIVES

As we already mentioned throughout the various chapters, many things are still to be achieved on the subject of the bistable pendulum.

7.1.1 *On the wake of the pendulum*

The characterization of the wake structure is a large part of the questions we left opened in this thesis. As the pendulum itself provided us with much information, flow visualization, which is both resource- and time-consuming, has been kept to the minimum[1], but the closure of our interrogations on the stall and on dynamical aspects may only be achieved through flow visualization or numerical simulations.

On that matter, a few directions of research can be explored:

- The conducted PIV measurement in Chapter 1 was only two-dimensional while the wake is three-dimensional. Thus a natural extension is the 3D visualization of the wake through tomographic Particle Image Velocimetry (PIV) or Particle Tracking Velocimetry (PTV) for instance. As this requires complex experimental development, a small step can be achieved by visualizing first the longitudinal wake to reconstruct the leading-edge and trailing-edge vortices. Then, a simultaneous recording of both longitudinal and transverse plane would provide preliminary insight on the 3D structure in a given region, before implementing fully resolved 3D flow measurements.

- A second aspect is the investigation of the coupling between the wake dynamics and the object dynamics. For the pendulum, this means a synchronous acquisition of the angle with the PIV. Though it was initiated during this PhD, the analysis of the preliminary experiments is still lacking, thus leaving room to further development both in the experiments, with only a few angles recorded, and in the interpretation through the reconstruction of the wake with the vorticity structure. A similar study would be to simultaneously acquire two-plane PIV, as proposed before, and force measurements on static plates as a first step towards the comprehension of the wake/force coupling.

- The wake of the rectangular plates would be interesting to visualize as well, in order to try our hypothesis on the origin of 3D stall proposed in Chapter 2. While PIV measurements would provide insight on the 3D structure, surface flow measurements might be a good complement to our study on the stall angle. In particular, the variation of the leading-edge vortex expansion on the surface with the angle of attack and aspect ratio may be key to understanding the linear relation between the stall angle and the arc tangent of the aspect ratio.

- For the fly-swatter in Chapter 3, like for the rectangular plates, a thorough study of the wake is also necessary to complete our understanding of the role of the upper corners in the existence of the bistability and of the sharp stall. A complementary aero-acoustic study over the various configuration would also add to the understanding of porosity.

1 Part of this choice was due to Covid pandemic that delayed the installation of the PIV setup.

- The dynamical investigation of the wake is also important to refine both the model for the transitions in Chapter 5 and the models for the unsteady aerodynamic coefficient in Chapter 6, and extend the phenomenological and empirical approaches with instantaneous flow dynamics.

Lastly on the wake aspects, much of the analysis of the PIV measurements remains also to be completed, in particular for the spontaneous transitions and excursions. Though we have presented preliminary results on that aspect, a quantitative analysis of the evolution of vorticity for instance could add to the understanding of the aerodynamic trigger for the transition.

7.1.2 *On the model of the bistable dynamics*

On the transitions and excursions, the model we proposed only covers the transitions and as we concluded on the possibility of excursions not being aborted transitions but a different phenomenon, it would be interesting to develop a conjoint model for the excursions as well, following a similar approach.

The interpretation of the parameters of the double-exponential distribution η and $\sin(\theta_0)$ in Chapter 5 requires many more statistics of transitions with different pendulum configurations, especially ones that present both-ways transitions. Some experimental data has already been acquired on that regard but their analysis is still under progress.

Introduced in Chapter 4, ΔU is, for instance, a first parameter that is convenient to vary by simply playing on the attachment of the pendulum in order to get insight on the physical interpretation of η and $\sin(\theta_0)$.

7.1.3 *On the influence of turbulence*

An additional subject left aside in this thesis in the characterization of the C_N coefficient is the influence of the turbulence rate. Preliminary experiments were conducted, extending partially previous results from [1] with the disappearance of the bistability with increasing turbulence rate, by the narrowing of the flow velocity range but with the extension of the forbidden angles. This aspect was originally planned for this thesis, but the Covid pandemic delayed greatly the installation of an active grid for turbulence in the wind tunnel in Lyon and set aside opportunities of extra-laboratory collaboration for experiments.

As the turbulence rate is increased, the bistability disappears in a yet different way to what is observed when holing a square into a fly-swatter. This might result from the destabilization of the wake structure from the outside by the incoming vortices, just like holes destabilize the vortices from the inside. The turbulence rate would act, for instance, like a pressure on the wake, leading to a thermodynamic analogy, whose development is in progress.

7.1.4 *On flying itself*

The first lines of this thesis, rewritten here as *"[The comprehension of] flying might not be all plain sailing but the fun of it is worth the price"*, give a final hint on a potential direction to pursue.

Indeed, as we reduced the whole problem of flight into a wind-swept pendulum, we have yet to come back to flight itself, by reintroducing the complexity of living beings into the system. Though the first part proposed parallels between animal flight and the different questions we asked in the chapters, it still remains to complete the analogy and try our findings on the living characteristics of birds and insects, for the wake, the aspect ratio and the porosity.

This part will hopefully be one of the directions pursued in my postdoctoral research, on both insects and birds.

REFERENCES

[1] M. Obligado, M. Puy, and M. Bourgoin. "Bi-stability of a pendular disk in laminar and turbulent flows." In: *J. Fluid Mech.* 728 (2013), R2.

Part IV

IN THE ARMS OF MORPHEUS

8

PHOEBUS

This chapter is not directly a part of my PhD thesis but rather a work I initiated during my time as a PhD student.

As the reader may have noticed by now while going through this manuscript, Zoology, and more particularly Ornithology, is a central and quite omnipresent interest of mine[1].

During this thesis, I had the opportunity to develop my own project on animal flight, parallel to the project presented in the first 6 chapters. First as a Junior Laboratory from the ENS de Lyon, this project **PHOeBUS**, which stands for *Flight ObsErvation of Butterflies Under Space-like gravity*, grew during my 1st year of PhD into a funded CNES (French Space Agency) project for parabolic flights.

As its name implies, project PHOeBUS focuses on the flight adaptation of butterflies to various gravity levels. It aims at understanding the fundamental aerodynamic mechanism behind the generation of lift in flapping flight.

1 If not, the reader is invited to read Chapter 0 (again).

APPENDIX

APPENDIX: SHAPING THE BISTABILITY

A

A.1 BIRD NOMENCLATURE

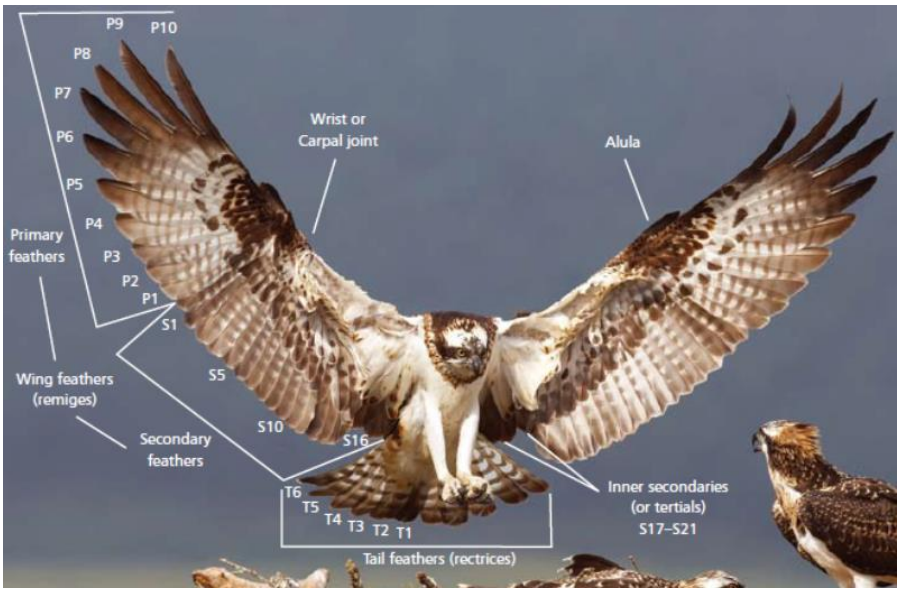

Figure A.1: Bird nomenclature for the numbering of feathers (from S. Espin, *et al.*, "Sampling and contaminant monitoring protocol for raptors", 2016).

A.2 EFFECT OF THE SQUARE ORIENTATION ON THE ANGULAR BISTABILITY

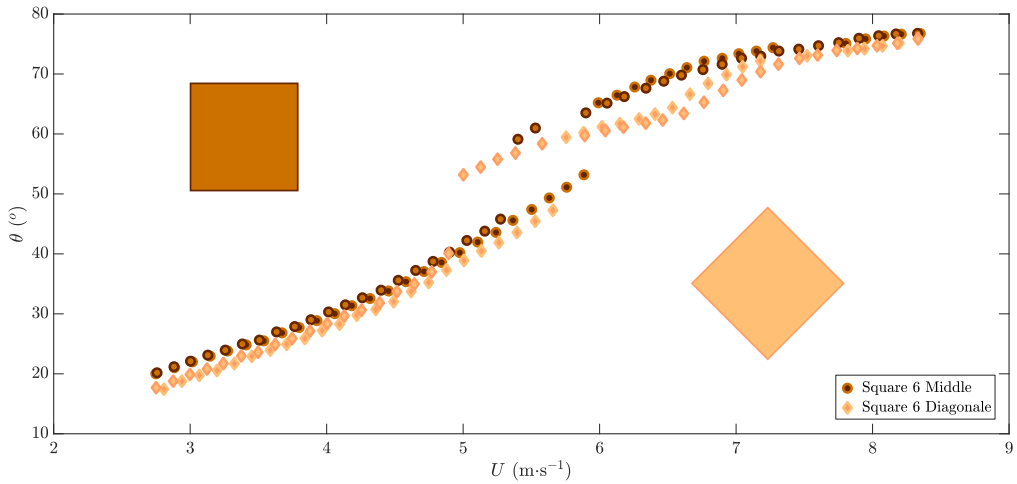

Figure A.2: Angular equilibrium position θ as a function of the flow velocity U for two configurations of square plates.

B

APPENDIX: RARE-EVENT TRIGGERING FOR SPONTANEOUS TRANSITIONS

B.1 CUMULATIVE DISTRIBUTION FUNCTION FOR $\delta\Gamma_{min/max}$

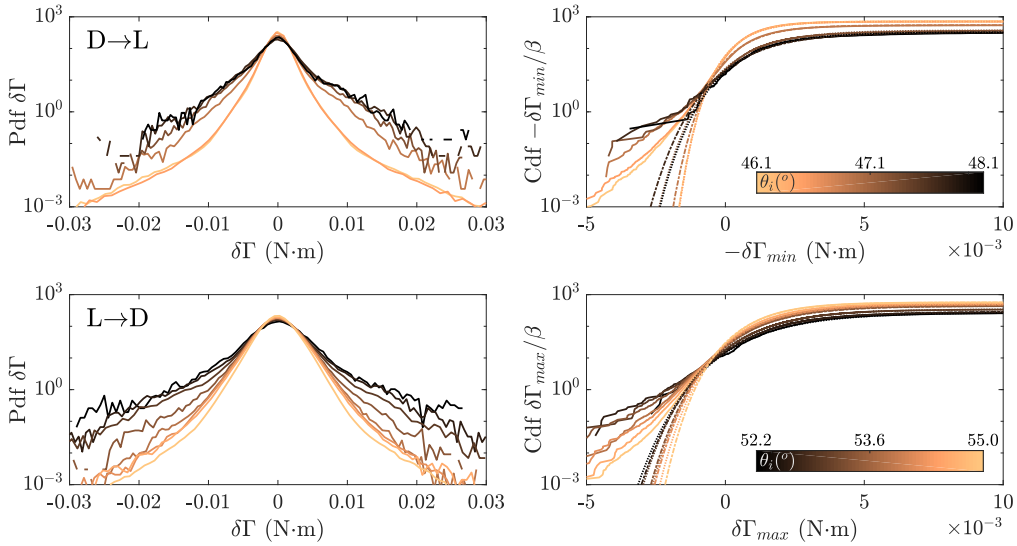

Figure B.1: Left: Probability distribution functions (pdf) of torque fluctuations $\delta\Gamma$ ahead of (top) D→L transitions and (bottom) L→D transitions. The exponential tails allow the application of rare-event statistics.
Right: Cumulative distribution functions (cdf) of the minima $-\delta\Gamma_{min}$ and maxima $\delta\Gamma_{max}$ of torque fluctuations, rescaled by the standard deviation. The Gumbel distribution best fits are represented by continuous lines (dotted or dash-dotted lines for clarity).
The color code for the angle $\overline{\theta_i}$.

C

APPENDIX: THE STABILIZATION OF WIND-INDUCED SELF-OSCILLATIONS

QUANTIFYING HUMAN BIAS ON THE EXPERIMENT

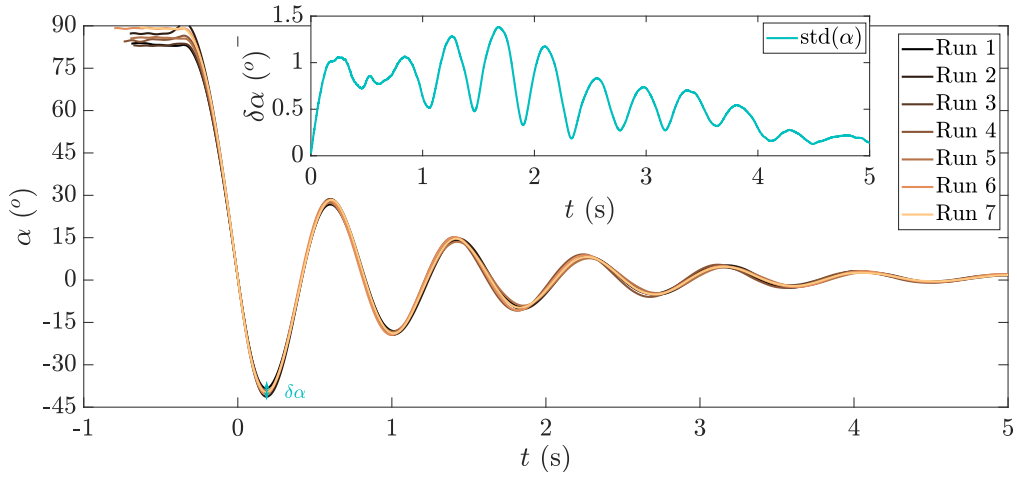

Figure C.1: Angular time series for different experimental runs for a given configuration. These runs are set off manually, inducing a slight uncertainty on the starting condition. Inset: standard deviation std(α) of the angular time series over the different runs.

In Fig. C.1, we present the time series of a series of experiments corresponding to the flow velocity $U = 7.3\,\mathrm{m}\cdot\mathrm{s}^{-1}$ and the pendulum of 4 cm weighted with the magnet with manual set-off. We observe that the maximal standard deviation at any time for a given pendulum configuration is std$(\alpha) \simeq 1.4°$, with a mean standard deviation of 0.62°.

DETAILS ON THE TAYLOR EXPANSION

To carry out the Taylor expansion, two assumptions are made:

- $\alpha \ll \pi$ ($\alpha < \pi/4$ is sufficient in our case)
- $L\dot{\alpha} \ll U$

$$\begin{cases} J\ddot{\alpha} &= \frac{1}{2}\rho S L U_{eff}^2 C_N(\alpha_{eff}, t) \\ U_{eff}^2 &= U^2 + 2LU\dot{\alpha}\sin(\alpha) + L^2\dot{\alpha}^2 \\ \alpha_{eff} &= \alpha + \arctan\left(\frac{L\dot{\alpha}\cos(\alpha)}{U + L\dot{\alpha}\sin(\alpha)}\right) \end{cases} \tag{C.1}$$

Starting from Eq. C.1, a first expansion is carried out on α_{eff} and U_{eff}.

$$\begin{cases} U_{eff}^2 & = U^2 + 2LU\dot{\alpha}\alpha + L^2\dot{\alpha}^2 \\ \alpha_{eff} & = \alpha + \frac{L}{U}\dot{\alpha}(1 - \frac{\alpha^2}{2})(1 - \frac{L}{U}\dot{\alpha}\alpha)) \end{cases} \tag{C.2}$$

OBTAINING m AND k FROM THE EXPERIMENT

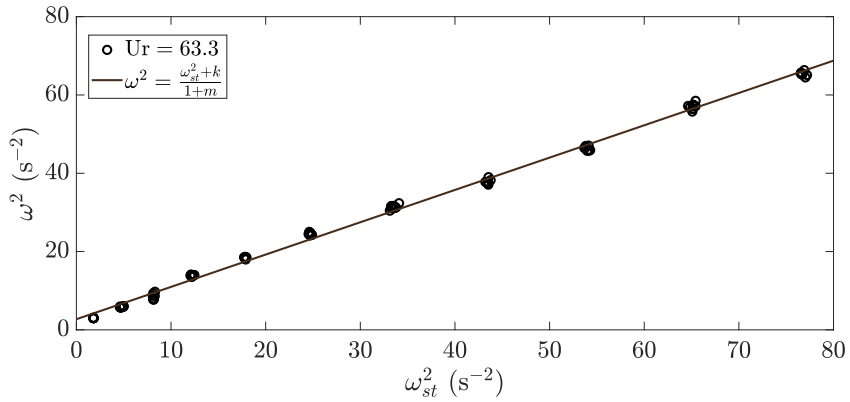

Figure C.2: Determination of the added mass m and added stiffness k for one particular reduced velocity Ur = 63.3 corresponding to the pendulum of of 4 cm weighted with the magnet.

TAKING INTO ACCOUNT α_{eff} IN C_N INVERSION

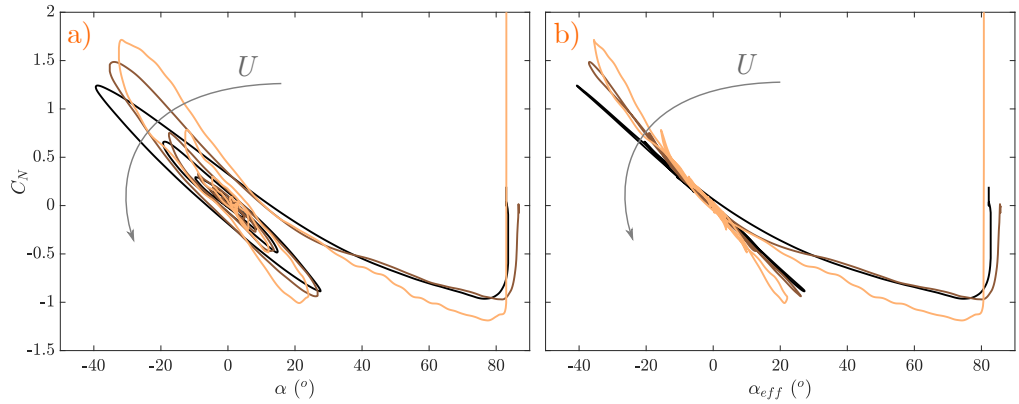

Figure C.3: Reconstitution of the dynamical C_N coefficient: (a) with the angle α and (b) taking into account the effective angle of attack α_{eff}. We observe a collapse of the spiraling $C_N(\alpha)$ curves for $C_N(\alpha_{eff})$.

ARTICLES

I - Gayout A., Bourgoin M., & Plihon N.
(2021). *Rare-event triggered transitions in aerodynamic bifurcation*. Physical Review Letters, 102.
https://doi.org/10.1103/PhysRevLett.126.104501

II - Gayout A., Gylfason A., Plihon N., & Bourgoin M.
(under review). *Fluidelastic modelling of a weathercock stabilization in a uniform flow*. Journal of Fluid and Structures.